

Second harmonic wave loads as springing excitation of a large cruise ship in short and steep head waves

Satu K. Hänninen

Second harmonic wave loads as springing excitation of a large cruise ship in short and steep head waves

Satu K. Hänninen

A doctoral dissertation completed for the degree of Doctor of Science in Technology to be defended, with the permission of the Aalto University School of Engineering, at a public examination held in Auditorium K216 at the Aalto University School of Engineering (Espoo, Finland) on 30 May 2014 at 12 noon.

**Aalto University
School of Engineering
Department of Applied Mechanics
Marine Technology**

Supervising professor

Professor Jerzy Matusiak

Thesis advisors

Professor Jerzy Matusiak

D.Sc. Tommi Mikkola

Preliminary examiners

Professor Armin W. Troesch, University of Michigan, United States

Professor Bettar O. el Moctar, University of Duisburg Essen,
Germany

Opponents

Professor Bettar O. el Moctar, University of Duisburg Essen,
Germany

D. Sc. Patrik Rautaheimo, Finland

Aalto University publication series

DOCTORAL DISSERTATIONS 61/2014

© Satu K. Hänninen

ISBN 978-952-60-5668-5

ISBN 978-952-60-5671-5 (pdf)

ISSN-L 1799-4934

ISSN 1799-4934 (printed)

ISSN 1799-4942 (pdf)

<http://urn.fi/URN:ISBN:978-952-60-5671-5>

Unigrafia Oy

Helsinki 2014

Finland



Author

Satu K. Hänninen

Name of the doctoral dissertation

Second harmonic wave loads as springing excitation of a large cruise ship in short and steep head waves

Publisher School of Engineering

Unit Department of Applied Mechanics

Series Aalto University publication series DOCTORAL DISSERTATIONS 61/2014

Field of research Naval Architecture

Manuscript submitted 10 January 2014

Date of the defence 30 May 2014

Permission to publish granted (date) 14 April 2014

Language English

Monograph

Article dissertation (summary + original articles)

Abstract

Ship springing is an important topic for the ship building industry, because it can cause fatigue damage and, in the case of large cruise ships, endanger the comfort of the passengers onboard. The existing literature presents different excitation mechanisms for springing. However, detailed descriptions of the development of springing excitation along the length of a hull are lacking.

This study focuses on one classical theory of springing excitation, which states that the resonant second harmonic wave loads cause vibration of the two-node vertical mode of a hull. A thorough analysis of such wave loads is presented for one study case of a large cruise ship advancing in short and steep head waves. The ship is assumed to be rigid and the structural responses are not considered.

The wave loads to be analysed were obtained using an unsteady Reynolds-Averaged Navier-Stokes (RANS) solver with a volume-of-fluid method (VOF) for free-surface flows. Before the actual analysis of the springing excitation, the reliability of the computed results was studied with a solution accuracy assessment and with a comparison of local pressure histories against the respective experimental results. The experimental data were obtained by conducting dedicated model tests in the towing tank of the Department of the Applied Mechanics at Aalto University. The study on the reliability of the results shows that a RANS-VOF solver can give reliable results at a detailed level in short and steep waves. The present study case differs from most of the previously validated RANS computations on ship wave loads by having very short encountered waves ($L_{wave}/L_{ship} = 0.16$) and by studying the loads at a detailed level.

The results show that the second harmonic vertical loads mostly originate from the foremost part of the bow. The importance of the second harmonic vertical force at different stations depends both on the ratio of the rise and the fall times of individual local pressures and on the phase difference between local pressures at different depths. The behaviour of the local loading relates to the local hull form. The relevant factors of the hull form are, in particular, the bow bulb, the form of the buttock lines, and the local entrance angle at the level of the design waterline. In future work, the generality of these findings should be studied for different hull forms and wave conditions.

Keywords Ship wave loads, Second-order resonant springing, Hull form, RANS, Volume-of-fluid method, Model tests

ISBN (printed) 978-952-60-5668-5

ISBN (pdf) 978-952-60-5671-5

ISSN-L 1799-4934

ISSN (printed) 1799-4934

ISSN (pdf) 1799-4942

Location of publisher Helsinki

Location of printing Helsinki

Year 2014

Pages 212

urn <http://urn.fi/URN:ISBN:978-952-60-5671-5>

Tekijä

Satu K. Hänninen

Väitöskirjan nimi

Aaltokuorman toinen harmoninen komponentti suuren matkustajalaivan springing-herätteenä lyhyessä ja jyrkässä vasta-aallokossa

Julkaisija Insinööritieteiden korkeakoulu**Yksikkö** Sovelletun mekaniikan laitos**Sarja** Aalto University publication series DOCTORAL DISSERTATIONS 61/2014**Tutkimusala** Laivatekniikka**Käsikirjoituksen pvm** 10.01.2014**Väitöspäivä** 30.05.2014**Julkaisuluvan myöntämispäivä** 14.04.2014**Kieli** Englanti **Monografia** **Yhdistelmäväitöskirja (yhteenvedo-osa + erillisartikkelit)****Tiivistelmä**

Springing on tärkeä aihe laivanrakennuksessa, koska se voi aiheuttaa laivan rakenteiden väsymistä ja matkustajalaivan tapauksessa häiritä matkustajien mukavuutta. Kirjallisuudessa on esitetty erilaisia teorioita springing-värähtelyn heräämisestä, mutta yksityiskohtaiset kuvaukset herätteen kehittymisestä laivan rungolla puuttuvat.

Tämä tutkimus keskittyy yhteen klassiseen teoriaan, jonka mukaan springing-värähtely herää, kun aaltokuorman toinen harmoninen komponentti resonoi rungon alimman pystysuuntaisen taivutusmuodon kanssa. Työssä esitetään perusteellinen analyysi aaltokuormasta yhdessä tilanteessa, jossa suuri matkustajalaiva etenee lyhyessä ja jyrkässä vasta-aallokossa. Laiva oletetaan jäykäksi, eikä sen rakenteiden vasteita tarkastella.

Analysoitavat aaltokuormat on saatu laskennallisesti Reynolds-keskiarvoitetulla Navier-Stokes (RANS) virtausratkaisijalla, joka käyttää volume-of-fluid menetelmää (VOF) vapaanpinnan käyttäytymisen ennustamiseen. Laskentatulosten luotettavuutta on tarkasteltu sekä ratkaisun numeerista käyttäytymistä analysoimalla että vertaamalla laskettuja paineita mittauksiksi. Mittaukselliset tulokset ovat peräisin tämän tutkimuksen yhteydessä tehdyistä mallikokeista Aalto-yliopiston Sovelletun mekaniikan laitoksen hinasaltaassa. Esitetty laskentatulosten luotettavuuden arviointi osoittaa, että RANS-VOF ratkaisija voi antaa luotettavia tuloksia yksityiskohtaisella tasolla lyhyissä ja jyrkissä aalloissa. Esitetty tapaus eroaa useimmista kirjallisuudessa aikaisemmin esitetyistä validoiduista RANS-laskennoista kohdatavien aaltojen lyhyden ($L_{wave}/L_{ship} = 0.16$) ja aaltokuorman yksityiskohtaisen tarkastelun perusteella.

Tulokset osoittavat, että laivan kohtaaman pystysuuntaisen aaltokuorman toinen harmoninen komponentti syntyy pääosin laivan keulan etuosassa. Tämän voimakomponentin merkittävyys eri kaarien kohdalla riippuu sekä paikallisten paineiden nousu- ja laskuajan suhteesta että eri syväyksillä vaikuttavien paineiden keskinäisistä vaihe-eroista. Esitetyt tulokset selittävät, kuinka paikallisen kuormituksen käyttäytyminen liittyy paikalliseen runkomuotoon. Olennaisia tekijöitä runkomuodossa ovat etenkin keulabulbi, rungon vertikaalien muoto ja rungon paikallinen avautumiskulma vesiviivan korkeudella. Näiden johtopäätösten yleispätevyyttä on syytä tutkia tulevaisuudessa erilaisille runkomuodoille ja aallokko-olosuhteille.

Avainsanat Laivan aaltokuormat, Toisen kertaluvun springing, Runkomuoto, RANS, Volume-of-fluid menetelmä, Mallikokeet

ISBN (painettu) 978-952-60-5668-5**ISBN (pdf)** 978-952-60-5671-5**ISSN-L** 1799-4934**ISSN (painettu)** 1799-4934**ISSN (pdf)** 1799-4942**Julkaisupaikka** Helsinki**Painopaikka** Helsinki**Vuosi** 2014**Sivumäärä** 212**urn** <http://urn.fi/URN:ISBN:978-952-60-5671-5>

Preface

This research was carried out within the research project *Laivan springing-ilmion herätteet*, funded by Tekes, the Finnish Funding Agency for Technology and Innovation, and Aker Yards (now STX Europe) and within the research project *Breaking wave loads*, funded by the Academy of Finland. The work was partly funded by the Finnish Graduate School in Computational Fluid Dynamics and by the Aalto University School of Engineering, too. The financial support is gratefully acknowledged. Apart from the financial support, the project *Laivan springing-ilmion herätteet* was an important springboard for this work. Several people from the industry contributed to the realisation of the project. Furthermore, they provided information on springing from a practical point of view. Special thanks are due to Dr. H.C. Kai Levander, D. Sc. Patrik Rautaheimo, Mr. Karno Tenovuo, Mr. Ari Niemelä, and Mr. Raimo Hämäläinen.

Professor Jerzy Matusiak was the supervisor and one instructor of this work. I thank him for having first instructed me on springing at the beginning of my doctoral studies and for having showed interest in my research over the years. I greatly appreciate his guidance, support, and valuable discussions.

D. Sc. Tommi Mikkola was the other instructor of this work. I greatly appreciate his support, valuable discussions, and advice on several aspects of this study. Tommi's strong background in computational fluid dynamics has been a considerable asset for my work, too.

Professor Armin W. Troesch and Professor Bettar O. el Moctar acted as the pre-examiners of this thesis. I greatly appreciate their valuable comments.

Dr. Ing. Jacek Pawlowski acquainted himself with my study before this manuscript was written. I greatly appreciate his interest in my research and thorough discussions on several aspects of this work.

Professor Michel Visonneau read this manuscript before the preliminary examination. I greatly appreciate his feedback and the related discussions. Furthermore, I am grateful for several previous discussions on the ISIS-CFD flow solver, which was used in this study.

I wish to express my gratitude to the other developers of the flow solver, in particular Dr. Ganbo Deng and Dr. Patrick Queutey, too. Moreover, I thank the personnel of Numeca for their practical advice on the use of FineTM/Marine.

The computations and most of the analysis of the results were conducted with the machines of CSC – the Finnish IT Center for Science. The computational resources provided are gratefully acknowledged.

The model tests of this study were conducted with the help of the personnel of the Marine Technology Unit in the towing tank of the Department of the Applied Mechanics at Aalto University. I greatly appreciate the contribution of the laboratory manager, Keijo Hanhiova, Mr. Pentti Tukia, Mr. Teemu Päivärinta, Mr. Jarmo Leinonen, Mr. Seppo Poimuvirta, Mr. Rüdiger von Bock und Polach, Mr. Eero Karri and Mr. Juha Alasoini. Furthermore, I wish to express my gratitude to Mr. Teemu Manderbacka, who shared the knowledge he had gained from the previous model tests on measuring local wave loads in short waves. In addition, I thank Mr. Timo Lehti from VTT Technical Research Centre of Finland for the advice on the choice of the pressure sensors.

I wish to thank all my colleagues in Otaniemi for the inspiring working atmosphere. In addition to the persons mentioned above, several others have advanced my study through professional or less professional discussions and by doing their work. In particular, I thank my fellow doctoral students Mr. Otto Puolakka and Ms. Maria Hänninen for refreshing discussions; Ms. Leila Silonsaari, Ms. Soile Mäkelä, Ms. Pirkko Suominen, Ms. Seija Latvala, and Ms. Sanna Tossavainen for taking care of several practical matters; and Professor Pentti Kujala for his support.

Finally, I warmly thank my friends, my parents, my sister, and her family for their support and encouragement.

Espoo, April 10, 2014,

Satu Hänninen

Contents

Preface	7
Contents	9
Nomenclature	13
1. Introduction	19
1.1 What is springing?	19
1.2 On springing excitation from a general point of view	22
1.3 Second-order resonant springing excitation	24
1.4 Predicting ship wave loads with interface-capturing methods	27
1.5 Scope of the work	30
1.6 Structure of the thesis	33
2. Study case	35
3. Computational approach	39
3.1 Mathematical model	39
3.2 Setup for the flow solver	42
3.3 Analysis of the computational results	47
3.3.1 Averages	47
3.3.2 Characteristics of the waves encountered	47
3.3.3 Forces	48
3.3.4 Non-dimensional results	49
3.3.5 Applied discrete Fourier transformation	50
3.3.6 Computational results compared with the experimen- tal ones	51
3.3.7 Local entrance angle	51
3.3.8 Rise and fall times of the time histories	52

4. Experimental approach	53
4.1 Instrumentation	53
4.2 On the calibration of the pressure sensors	55
4.3 Analysis of the measured data	56
5. Reliability of the results	59
5.1 Solution accuracy assessment	59
5.1.1 Wave conditions	59
5.1.2 Local pressures	61
5.1.3 Vertical force at stations	67
5.2 Validation data (measured data)	76
5.2.1 Wave conditions	76
5.2.2 Local pressure histories	77
5.3 Comparison of the computational and experimental results .	86
5.3.1 Wave conditions	86
5.3.2 Local pressure histories	87
5.4 Summary	92
6. Development of the wave loads on the hull	95
6.1 Description of the flow behaviour	95
6.1.1 Approach of the freely propagating wave to the bow .	95
6.1.2 Propagation of the wave on the hull	98
6.1.3 Propagation of the loading on the hull	99
6.1.4 Propagation of the loading at the design waterline . .	104
6.1.5 Behaviour of the free surface at the longitudinal sec-	
tions	108
6.1.6 Summary	113
6.2 Springing excitation	114
6.2.1 Propagation of the distribution of vertical loading on	
the hull	114
6.2.2 Vertical loading and its second harmonic contribu-	
tion at certain stations in the area of the bow	119
6.2.3 Distribution of the amplitude of the second harmonic	
vertical force in the area of the bow	131
6.2.4 Accumulation of the second harmonic component of	
the global vertical force	133
6.2.5 Summary	137
7. Discussion	139

7.1 On the reliability of the results	139
7.2 On the springing excitation	142
8. Conclusions and recommendations for future work	149
References	151
A. Turbulence model	157
B. Second harmonic vertical force at the stations	159
C. Instantaneous pressure distributions at the level of the design waterline	161
D. Pressure histories at six stations in the area of the bow	163
E. Measured waves	171
F. Measured pressures	177

Nomenclature

Abbreviations

BRICS	Blended reconstructed interface capturing scheme
DFT	Discrete Fourier transformation
DWL	Design waterline
GDS	Gamma differencing scheme
RANS	Reynolds-averaged Navier-Stokes equations
VOF	Volume-of-fluid method

Greek symbols

α	Local entrance angle of the hull
β	Deadrise angle; Model coefficient
δ	Kronecker's delta
γ	Model coefficient
κ	Constant of STT $K - \omega$ model
μ	Dynamic viscosity
Ω	Vorticity
ω	Frequency; Turbulent frequency
$\Delta\omega$	Spacing in the frequency domain
ϕ	Generic quantity
ρ	Density
σ	Model coefficient

Nomenclature

τ	Stress
Θ	Mode shape of the vertical two-node mode
ξ	Amplitude

Roman symbols

A	Wave amplitude
a	Total mass of a vibratory system; Fourier cosine coefficient; Constant
B	Breadth
b	Total damping of a vibratory system; Fourier sine coefficient
C	Coefficient
Co	Courant number
c	Stiffness of a vibratory system; Volume fraction
d	Distance between the free surface at rest and the bottom of the domain; Wall distance
F	Wave excitation force; force; auxiliary function
dx	Width of a x -span
G	Generalised force
g	Acceleration of gravity
\vec{g}	Gravity vector
H	Wave height
h	Instantaneous wave height
ix	Index of a station
iy	Index of a computational point at a station
j	Index of an encounter
K	Turbulent kinetic energy
k	Wave number; k^{th} component of a Fourier series
L	Length

N	Number
n	Integer; Number; Surface normal
\vec{n}	Outwards-directed unit normal vector
P	Production term
p	Pressure
R	Radius
S	Surface of a control volume; Mean strain-rate tensor
\bar{T}	Stress tensor
t	Time, Period
Δt	Time step
\vec{U}	Velocity field
u	The first cartesian velocity component in the xyz coordinate system
V	Control volume, Velocity
w	The third cartesian velocity component in the xyz coordinate system
x	Response of a vibratory system; the first cartesian coordinate in the xyz coordinates system
y	The second cartesian coordinate in the xyz coordinates system; Cell height; Distance from the wall
z	The third cartesian coordinate in the xyz coordinates system

Subscripts and superscripts

*	Nondimensional quantity; Constant of STT $K - \omega$ model
+	Dimensionless distance from the wall
∞	Free-stream values
0	Location of the free surface at the beginning of the computation
1	First cell height; Constant of STT $K - \omega$ model

Nomenclature

2	Second harmonic component
ω	Number of points in the frequency domain; Production term; Model coefficient
<i>air</i>	Properties of air
<i>boundary</i>	Quantity related to boundary
$b_{1,1}$	Lower boundaries of the refinement box b_1
$b_{1,2}$	Upper boundaries of the refinement box b_1
$b_{2,1}$	Lower boundaries of the refinement box b_2
$b_{2,2}$	Upper boundaries of the refinement box b_2
<i>cell</i>	Quantity related to cell
<i>cum</i>	Cumulative
d	Velocity of a surface
e	Quantity related to encounter
<i>fall, n%</i>	Fall time that corresponds to the n percent of the peak-to-peak amplitude of the time history
<i>FPP</i>	Location of the fore perpendicular of the ship
<i>hull</i>	Natural frequency of the vertical two-node mode of a hull
ij	ij component of a tensor
<i>input</i>	Input value
j	j^{th} cartesian coordinate
k	Model coefficient
l	Viscous stress
<i>max</i>	Upper boundaries of the computational domain
<i>mean</i>	Mean value
<i>min</i>	Lower boundaries of the computational domain
P	Quantity related to pressure
p	Piezometric pressure

<i>peak</i>	Peak value
<i>p, f</i>	Number of points within a vertical section
<i>rel</i>	Relative quantity
<i>rise</i>	Rise time
<i>rise, n%</i>	Rise time that corresponds to the n percent of the peak-to-peak amplitude of the time history
<i>sensor</i>	Quantity related to pressure sensor
<i>ship</i>	Quantity related to ship
<i>single</i>	Corresponds to the second harmonic encounter frequency
<i>span</i>	Corresponds to the frequency span of width ω_e around the second harmonic encounter frequency; Time span
<i>station</i>	Quantity related to the stations
<i>t</i>	Quantity related to time; Eddy viscosity; Reynolds stress
<i>x</i>	Longitudinal component
<i>y</i>	Horizontal component
<i>z</i>	Vertical component
<i>wave</i>	Quantity related to wave
<i>water</i>	Properties of water

1. Introduction

1.1 What is springing?

Ship springing means the resonant wave-induced vibration of a ship hull. Conventionally, it concerns only the vibration of the vertical two-node mode of the hull; see Figure 1.1. In practice, the vibration of a two-node mode means that the ship starts to vibrate along its whole length from bow to stern. The springing vibration can be described by saying that it is long-lasting after it has first started and that its amplitude is rather constant. Springing can also be described by pointing out its difference from whipping vibration, which rises quickly to its maximum level as a result of the impact of a single wave, and usually dies away rather quickly, too.

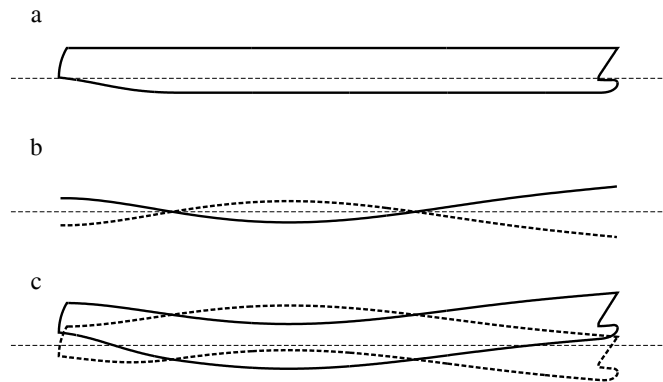


Figure 1.1. **a** Profile of a ship **b** Shape of the vertical two-node mode of a large cruise ship **c** Profile of a ship that is deformed.

Springing became an important matter for the shipbuilding industry in the latter half of the 20th century as a result of the constantly increasing size of ships. The larger size of ships increases the risk of wave-induced vibrations for two reasons. First, the eigenfrequencies of the hull decrease

as a function of the increasing length of the ship. As a consequence, they become closer to the frequency content of the wave loads that the ship undergoes. Then the resonance between the mode shape of the hull and different parts of the wave loading becomes possible. Second, the rigidity of the hull in relation to the mass of the hull becomes smaller with the increase in the size of the ship. Reduced rigidity makes the amplitude of flexural vibration larger.

The motivation to study springing typically relates to fatigue damage to a ship or to the comfort of the people on board. In the context of the previously published scientific studies, springing-type vibration is usually seen as a serious risk for fatigue damage to freighters. In the context of the present research, it is relevant that long-lasting vibration may affect the comfort of the passengers on a large cruise ship. Passenger comfort is a significant factor in the design and construction of large cruise ships.

Springing is a complex hydroelastic phenomenon. In practice, this means that the coupled interaction between the related hydrodynamics and structural behaviour must be taken into account in order to acknowledge the phenomenon in its entirety. The hydroelasticity also implies that springing includes aspects that are more related either to hydrodynamics or to structural behaviour. One way to sort out the hydrodynamic and structural parts of the problem is to discuss the different factors in a basic spring-mass system. The equation below describes a simple spring-mass system, e.g. (Lloyd, 1989):

$$a\ddot{x}(t) + b\dot{x}(t) + cx(t) = F(t). \quad (1.1)$$

If Eq. (1.1) was to represent the springing vibration of a ship, $x(t)$ would present the vibratory response of the ship, a the total mass of the vibratory system, which includes the mass of the ship and the added mass, b the total damping, which consists of the structural and hydrodynamic damping, c the stiffness of the ship, and $F(t)$ the wave loads that excite the springing vibration. Another way of expressing the content of Eq. (1.1) would be to have the effects of the added mass and damping (radiation forces) on the right-hand side of the equation together with the wave excitation forces.

A simple way to sort out the hydrodynamic and structural parts of springing would be to say that the left-hand side of Eq. (1.1) is the structural part and the right-hand side the hydrodynamic part. However, as the previous description of the different terms has already indicated, the left-

hand side of Eq. (1.1) is affected by hydrodynamic aspects, because the term a includes the added mass and the term b the hydrodynamic damping.

The literature includes examples which illustrate the importance of the hydrodynamic aspects on the left-hand side of Eq. (1.1). As an example, the numerical study of Vidic-Perunovic (2012) demonstrates how the depth of the water affects the springing response in finite depths of water through the mass and damping terms and the value of the natural frequency of the system, besides having an effect on the excitation force. The effect of the depth of the water on the natural frequency of the hull has been observed in the full-scale measurements too (Moe et al., 2005).

On the other hand, a relevant question is whether the structural behaviour affects the wave excitation on the right-hand side of Eq. (1.1). The magnitude and the behaviour of the excitation force $F(t)$ can be affected by the springing vibration, especially if the vibratory amplitude is large. Thus, solving the excitation force accurately is not always possible without taking the structural behaviour into account at the same time. The work of el Moctar et al. (2011) and Oberhagemann and el Moctar (2012) is an example of a sophisticated numerical prediction of springing excitation which is fully coupled with the structural behaviour of a ship hull. The existing knowledge about the effect of the springing vibration on its own excitation force is still limited, but some examples in the literature indicate that such an effect can matter. For instance, Storhaug and Moan (2007a) reported that springing can cause whipping. If such a connection exists, the deformation of the hull as a result of springing can affect its own excitation force as well.

The present study focuses on springing excitation. In other words, the focus is in the term $F(t)$ in Eq. (1.1). It is assumed that the structural response does not affect the magnitude or the behaviour of the excitation force significantly. There are two reasons for this assumption. First, the present study concerns large cruise ships, which are relatively rigid. Their rigidity is high especially in comparison with the other ships (containers and bulk carriers) in the published literature on springing. Second, the aim of this study is to go deep into springing excitation. Achieving that goal is simplified by excluding the structural behaviour from this study.

Next, Sections 1.2-1.3 describe the previous findings that deal with springing excitation. It is considered from the point of view of the springing

excitation $F(t)$. The aspects that relate more to the left-hand side of Eq. (1.1) have been excluded from this literature survey. Previous authors, e.g. Storhaug (2007), have presented literature surveys on springing from other points of view that suit their studies.

Even though the rest of this work focuses on springing excitation, it is important to keep in mind the fact that most of the previous studies present the results on springing as structural responses. Thus, the phenomena on the left-hand side of Eq. (1.1) play a remarkable role in the previous studies, even if they are presented from the point of view of springing excitation in the literature survey of this work. Understanding and predicting structural behaviour has its own challenges in the case of springing, but these lie outside the scope of this work.

1.2 On springing excitation from a general point of view

Ship springing became an important topic in the published literature in the second half of the 20th century after it had been observed as vibration on board full-scale ships in operation. The first publications give the impression that such vibration was not expected. By that time, the main questions seemed to be these: What causes this vibration? What is the source of the excitation?

The paper of Bell and Taylor (1968) is one of the first publications to present observations on the vibration of the vertical two-node mode on board a ship as a result of wave excitation without evidence of slamming. Such a vibration was later named springing. The important observation in the paper is that significant wave-excited hull vibration can be set up in moderate sea conditions. The authors do not manage to explain the excitation mechanism, but they set a starting point for the later studies. They say that “the observations appear to be consistent with the vibration being excited by impulsive forces acting on the bow, even if the precise nature of the excitation is not understood”. The ship in question was a tanker of 47,000 tons deadweight in a normal ballast condition.

Soon after that, theories were presented on the origin of springing. First, a linear excitation mechanism was assumed, e.g. (Goodman, 1971), and demonstrated, e.g. (Hoffman and van Hooff, 1973) and (Hoffman and van Hooff, 1976). In the case of this *linear springing*, the vibration is caused by the wave components of the sea spectrum which correspond to the natural frequency of the hull. Next, the concept of non-linear springing was

presented. Non-linear springing includes two excitation mechanisms according to e.g. Slocum and Troesch (1983) and Troesch (1984). The two definitions can be explained using two different frequencies of the incident waves $\omega_{e,1}$ and $\omega_{e,2}$, the natural frequency of the hull ω_{hull} , and the integer n . One definition of non-linear springing states that springing vibration occurs when $\omega_{e,1} + \omega_{e,2} = \omega_{hull}$. This excitation mechanism is often called *sum frequency springing*. The other definition states that springing vibration occurs when $n \cdot \omega_e = \omega_{hull}$. In more recent publications, this excitation mechanism is sometimes called *n^{th} -order resonant springing*. Further, *n^{th} -order resonant springing* is sometimes considered as a special case of *sum frequency springing*. All these explanations of the excitation mechanism rely on the assumption of a state of resonance between the wave loads and the two-node mode of the hull. In fact, several studies have indicated or even demonstrated the importance of the resonant wave loads in comparison with the off-resonant wave loads on springing, e.g. (Troesch, 1980), (Slocum and Troesch, 1983), (Hoffman and van Hooff, 1973), (Storhaug, 2007), and (Oberhagemann and el Moctar, 2012). In the 21st century, the wave conditions in the studies on springing are often selected according to the above-mentioned excitation mechanisms (especially $n \cdot \omega_e = \omega_{hull}$ with $n \geq 1$), e.g. (Storhaug, 2007), (Storhaug and Moan, 2007b), (Storhaug and Moan, 2007a), (Miyake et al., 2008), (Hu et al., 2012), (Lee et al., 2012), (Kim et al., 2012), (Oberhagemann and el Moctar, 2012), and (Shao and Faltinsen, 2012).

As for the new aspects of springing in the 21st century, the development of the measurement devices has enabled more to be learned from full-scale measurements. The related findings do not necessarily make it easier to define the source of the springing excitation itself, but they increase the general understanding of the topic in realistic sea states. One aspect to acknowledge is that distinguishing springing and whipping from the measured data is difficult, e.g. (Storhaug et al., 2003), (Moe et al., 2005), (Storhaug et al., 2007). Even if this aspect makes extracting springing excitation in realistic sea states challenging and can even be irrelevant from the point of view of the total fatigue damage, Storhaug and Moan (2007a), for instance, presented an example of a method for distinguishing springing and whipping. Another outcome of the more detailed data of full-scale measurements is the possibility of judging the capability of the existing numerical methods for predicting springing-type vibration against authentic full-scale data. The benchmark study of Storhaug et al. (2003)

on this topic concluded that the traditional sea-keeping methods are not capable of predicting springing response in realistic sea states, even if the wave-bending responses that occurred simultaneously at lower frequencies were fairly well predicted. The sea-keeping methods that were tested included four different strip theories and one linear 3-D Rankine method. The ship in question was a bulk carrier. Soon afterwards, Vidic-Perunovic (2005) and Vidic-Perunovic and Jensen (2005) showed that the prediction of the springing response is improved when the effect of the bi-directional waves is included in a second-order strip theory. Recently, the significance of the linear excitation caused by diffracted waves has been pointed out in the case of a container ship in (Vidic-Perunovic, 2010). The importance of diffracted waves may bring into question the capability of strip theories to predict springing.

On the basis of the previous findings concerning the capability of the sea-keeping methods of predicting springing in realistic sea states, it is reasonable to argue that the origin of the springing excitation needs to be understood better. Understanding the origin of the excitation enables sophisticated choices to be made with regard to the prediction tools applied. In order to increase the knowledge, the first step to be taken is to explain the origin of the above-mentioned excitation mechanisms of springing in regular wave conditions.

The present study focuses on the origin of the second-order resonant springing excitation ($2 \cdot \omega_e = \omega_{hull}$) in the case of a large cruise ship advancing in one head wave condition. Next, the previous findings on the second-order resonant springing excitation are described in Section 1.3. Then the aim and the content of this study are addressed in detail in Sections 1.4 - 1.5.

1.3 Second-order resonant springing excitation

The second-order resonant springing has been addressed in several studies through model tests and numerical approaches. Model tests have been conducted within the studies of e.g. Troesch (1980), Slocum and Troesch (1983), Storhaug and Moan (2007b), Storhaug and Moan (2007a), Miyake et al. (2008), and Hu et al. (2012). Numerical approaches have been applied in (Hu et al., 2012), (Kim et al., 2012), (Lee et al., 2012), (Oberhagemann and el Moctar, 2012), and (Shao and Faltinsen, 2012). In addition, Troesch (1984) presented numerical results which were obtained with a

method that utilised experimental values for certain terms of an empirical equation of motion. Furthermore, Kalske (2010) and Manderbacka et al. (2008) addressed springing-type excitation by studying local second harmonic wave loads with a ray theory and measured data, respectively.

In the above-mentioned studies, the springing excitation on the total hull surface was predicted numerically either with 3-D potential solvers including different non-linear terms (Kim et al., 2012), (Lee et al., 2012), (Shao and Faltinsen, 2012) or with RANS, (Oberhagemann and el Moctar, 2012). The validations that were presented focused on comparing the predicted structural response with the corresponding result from a model test. Such validations are presented in (Kim et al., 2012), (Lee et al., 2012), and (Oberhagemann and el Moctar, 2012) for a container ship. Kim et al. (2012) reported that the results of a 3-D Rankine panel method with a Timoshenko beam agree well with the experimental results. Lee et al. (2012) reported that the results of a 3-D hydroelastic code with a 2-D beam model are comparable with the experimental results. Oberhagemann and el Moctar (2012) reported that the results of a RANS solver coupled with a model decomposition approach are in good agreement with the experimental results. Thus, the above-mentioned methods with the 3-dimensional approaches to wave excitation are reported as being capable of predicting second-order resonant springing in some regular wave conditions.

An essential question is what is the origin of the second-order springing excitation. The definition $2 \cdot \omega_e = \omega_{hull}$ implies that the second harmonic wave loads are the source of the springing excitation. As for a very basic aspect, the experimental results of Troesch (1980) show that the second-order springing excitation is not linear and that it does not follow a similar hump-hollow pattern as a function of the ratio of the ship and wave length to the linear excitation in his study.

Another fundamental aspect of second-order resonant springing is that it becomes more important with an increase in the speed of the ship and steepness of the wave. The effect of the speed of the ship is demonstrated with experimental results in (Storhaug and Moan, 2007b) and with numerical results in (Shao and Faltinsen, 2012). Further, the theoretical analysis in (Shao and Faltinsen, 2012) specifies how the velocity affects the second-order resonant springing excitation in the case of wave diffraction. The conclusion reached is that the contribution of the second-order velocity potential is predominant in comparison with the contribution of

the quadratic effects of the linear velocity terms. As for the wave height, the importance of the increasing wave height in second-order resonant springing was demonstrated in the experimental studies of Slocum and Troesch (1983) and Miyake et al. (2008). The results in (Slocum and Troesch, 1983) suggest that the springing response is quadratic to wave amplitude. At least in theory, high ship velocities and wave steepnesses can lead to impact-type loading.

The connection of impact-type loads and second-order resonant springing has received some attention in the literature, in (Hu et al., 2012) and in (Lee et al., 2012). Hu et al. (2012) report that besides the continuous springing in regular waves, whipping occurred repeatedly in the model tests of an ultra-large tanker. They comment that separating the springing- and whipping- induced responses is difficult because of the low level of damping and slow decay of the whipping response. Lee et al. (2012) studied the second-order resonant springing of a container ship in regular waves using a 2D slamming model and reported that the magnitude of the slamming force is very small. Overall, the existing knowledge on the relationship between the impact-type loads and second-order resonant springing still seems to be very scattered. On the other hand, an interesting example is presented in (Oberhagemann and el Moctar, 2012) regarding 4th- and 5th-order resonant springing. Their numerical results show that the 4th- and 5th-order resonant springing response becomes significant with steeper incident waves. The authors suggest that the higher response as a result of steeper waves relates to resonant vibration, which is probably initiated with small but periodic impacts.

The fullness of a ship bow is typically considered as a relevant parameter for springing. This topic is touched on through the results of the second-order resonant springing in (Storhaug and Moan, 2007a), (Miyake et al., 2008), and (Shao and Faltinsen, 2012). Storhaug and Moan (2007a) analysed the second-order springing from the model experiments in irregular waves for different bow forms of a bulk carrier in ballast condition. They report that the second-order springing was reduced but still displayed when a wedge-shaped bow was utilised instead of the bow of a bulk carrier. On the other hand, the study of Miyake et al. (2008) demonstrates that the bluntness is not a necessary parameter e.g. for second-order resonant springing. Their experimental results show that a slender hull without a bulbous bow (Wigley) can suffer springing when its rigidity corresponds to that of a mega-container ship. The numerical results

of Shao and Faltinsen (2012) on a Wigley hull with two widths show that the second-order springing excitation becomes more important with the blunter (wider) hull. The authors suggest, without showing an analysis, that the blunt ship generates a stronger scattered wave, which in return interacts with the incident wave and itself to give second-order effects. Thus, the previous studies indicate that the fullness of a ship bow increases the importance of the second-order resonant springing. On the other hand, it has been pointed out that springing can occur in the case of a slender ship, too.

In addition to the fullness of the bow, considering the effect of the bulb on springing is relevant from the point of view of the present study. Previously, the experimental study of Storhaug and Moan (2007a) tested the effect of a bow bulb on the second-order springing of a bulk carrier in ballast condition in irregular waves. They do not report a difference in the results with and without the bulb. The full-scale study of Bell and Taylor (1968) may support this finding by reporting that the increase in the level of vibration with the speed of the ship behaves similarly both with and without a ram bow.

To conclude the consideration of the second-order resonant springing excitation, the previous studies have made serious efforts to increase the knowledge of the phenomenon. Often, the findings have been obtained by varying a parameter that affects the excitation and by observing the related changes in the springing response. However, detailed descriptions of the propagation of the loading on hulls are missing. Analysing the loading along a hull at a detailed level can increase the understanding of the origin of the springing excitation.

1.4 Predicting ship wave loads with interface-capturing methods

The aim of this study is to analyse the behaviour of the wave loads on the hull at a detailed level in order to learn more about springing excitation. In practice, such an analysis requires a numerical method to be applied for the springing excitation, because the numerical methods can provide detailed information on the loading in both the spatial and time domains. In the case of both the full and model-scale experiments, practical aspects limit the amount of information. For instance, the sizes of the measurement devices limit the spatial resolution with which the behaviour of the loading on the hull can be observed.

In the present study, the information on the wave loads is obtained with a Reynolds-averaged Navier-Stokes (RANS) solver that uses an interface-capturing method for the free-surface flows. This choice was made because such methods can predict arbitrary free-surface behaviour, e.g. wave breaking, and the related loads. The aim of the work is to learn more about the origin of second harmonic excitation. In order to have a distinct contribution of higher harmonic loading, the waves that are encountered have been chosen to be very steep and the form of the bow is rather full. These selections can lead to a serious deformation of the free-surface level near the hull, which requires the use of a method that can predict arbitrary free-surface behaviour.

The aim of analysing the origin of the springing excitation from the computations imposes high requirements on the reliability of the computational results. Performing such analysis means that the computational results must be reliable on various levels. The various levels of loading in the present case cover e.g. local pressure histories at different locations of the hull, instantaneous pressure distributions on the hull, the time histories of the forces that cover different extents of the hull, and their second harmonic amplitudes and phases. Before the actual analysis of springing excitation, the reliability of these results needs to be shown.

Previously, Oberhagemann and el Moctar (2012) studied springing using a similar flow solver (RANS-VOF) for the wave excitation. In addition, they coupled the flow solver with a model decomposition approach in order to get the results as structural responses. Their study is an encouraging reference as they conclude that the computed structural responses are in good agreement with the measured ones. As a difference from the present study, Oberhagemann and el Moctar (2012) do not present direct wave loads at any level. In their case, the given responses depend on the behaviour of the structural model, too. In order to learn more about the applications of similar flow solvers to the prediction of wave loads, the previous studies on other wave loads than springing excitation are addressed next.

In the case of predicting ship wave loads with interface-capturing methods, several previous studies have already addressed the validity of the computational results, e.g. (Sato et al., 1999), (Orihara and Miyata, 2003), (Hino, 2005), (Klemt, 2005), (Carrica et al., 2006), (Carrica et al., 2007), (Oberhagemann et al., 2008), (Visonneau et al., 2008), (Zwart et al., 2008), (Deng et al., 2009), (Larsson et al., 2010), (Oberhagemann et al., 2009),

(Carrica et al., 2011), (Castiglione et al., 2011), (Orihara, 2011), and (Guo et al., 2012). Most of these studies have addressed global ship wave loads, e.g. (Sato et al., 1999), (Orihara and Miyata, 2003), (Hino, 2005), (Carrica et al., 2006), (Carrica et al., 2007), (Visonneau et al., 2008), (Zwart et al., 2008), (Deng et al., 2009), (Larsson et al., 2010), (Oberhagemann et al., 2009), (Carrica et al., 2011), (Castiglione et al., 2011), and (Guo et al., 2012). Additionally, a few of the studies have addressed local loads, such as pressure histories; see e.g. (Klemt, 2005), (Oberhagemann et al., 2008), (Oberhagemann et al., 2009), and (Orihara, 2011). Even though all these previous studies exist, more work is and will be needed regarding the validation of the ship wave loads that are predicted with interface-capturing methods. Every time a different wave condition, a different hull form or a different level of detail of the analysis is presented, the need to validate the computation may be considered. This is despite the fact that interface-capturing methods themselves are not known to impose any limitations on the cases of ship wave loads that are allowed. (Hänninen et al., 2014)

The primary purpose of validating these kinds of computations is to ensure that a method is correctly applied in a particular flow case. The challenge is that the correct application of a field method depends on the behaviour of the flow, which is seldom known in advance at an adequate level of detail. User-made choices which can seriously affect the solution are the discretisation resolution (both grid spacing and time steps) and the level of the iterative convergence for each time step. Before the actual comparison of computational results against the corresponding experimental ones, the effects of these matters on the flow solution need to be studied. The literature includes two main options regarding the level of detail with which the solution behaviour is studied as a function of the resolution. One option is defining quantified numerical uncertainties. Then the solution should be in the vicinity of the asymptotic range. In the case of ship wave loads, reaching the asymptotic range is a challenge even for the lowest harmonic components. Nevertheless, quantified uncertainties have been presented for mean and first harmonic global loads in (Carrica et al., 2006), (Carrica et al., 2007), (Castiglione et al., 2011), and (Guo et al., 2012) and for the first to third harmonic components of the vertical force acting on a ship frame in (Hänninen et al., 2012). As for quantifying the uncertainties for time histories such as (impact-type) pressure histories in this study, the scientific literature seems not to have presented practical examples yet. Another way of addressing the solution behaviour

as a function of the resolution is to study qualitative solution behaviour. Then the computational results which are obtained with different resolutions are compared. In the case of ship wave loads, such analyses have been presented in (Orihara and Miyata, 2003), (Klemt, 2005), and (Deng et al., 2009). As for studying the solution behaviour of local pressure histories, a qualitative approach was applied in (Klemt, 2005). (Hänninen et al., 2014)

Thus, in comparison with the previous studies, both the solution accuracy assessment and the validation in this study are challenging because of the detailed level needed in the springing analysis. Further, the present study differs from most of the previous studies in having a low ratio of the wave and ship lengths, 0.16. The corresponding ratio in most of the previous publications was 0.6-1.09. On the other hand, the lowest ratio in the study of Oberhagemann and el Moctar (2012) was slightly lower than in the present study.

In this study, the solution behaviour as a function of the resolution is studied qualitatively. The primary reason is that a qualitative analysis coheres with the description of the present findings on the qualitative behaviour of the flow. A quantified analysis would focus its attention on numerical values and their correctness, whereas within the scope of this work it is sufficient that the simulation predicts the correct physical behaviour in a qualitative sense. Nevertheless, the option of using a quantitative approach was seriously considered and even applied when the possibility of computing the present study case was first studied (Hänninen et al., 2012).

1.5 Scope of the work

This study addresses the second harmonic wave loads that can cause springing excitation. In other words, the wave conditions are such that the previously mentioned condition of the second-order resonant springing $2 \cdot \omega_e = \omega_{hull}$ applies. The study case is a large cruise ship that is advancing in short and steep regular head waves. A single wave condition with one speed of the ship is considered. The springing excitation is analysed from the results given by a Reynolds-averaged Navier-Stokes solver that uses a volume-of-fluid method for the free-surface flows.

This work includes two parts. The first part concerns the reliability of the computed results and the second part the springing excitation.

Studying the reliability of the computed results is done with two approaches. The reliability of the computed results is addressed first through a solution accuracy assessment and second through a validation against experimental results. The solution accuracy assessment is based on the qualitative comparison of the computed results with different resolutions. The goal of this assessment is to ensure that the chosen resolution does not affect the conclusions of the work. Further, the solution accuracy assessment demonstrates that the selected iteration number does not affect the results. This part of studying the reliability of the computed results covers the wave loads to the same extent as the analysis that explains the origin of the springing excitation. The validation is based on a qualitative comparison of the computed results and the corresponding experimental results. The experimental data comes from the model tests which were conducted and analysed as a part of this study. The experimental data includes point-wise pressures at ten locations in the bow area of the hull.

The second part of this work concerns the wave loads that can cause resonant springing in the present study case. The analysis of the wave loads includes two steps and the related results are analysed qualitatively. First, the behaviour of the flow is described at a general level. Second, the features that matter for the second-order resonant springing excitation are underlined.

Within the first step, the aim of analysing the behaviour of the flow at a general level is to point out the phenomena which lead to the observed behaviour of the wave loads on the hull. The related description starts with the analysis of the deformation of the approaching wave in the vicinity of the hull. For this perspective, the significance of the bow bulb is explained. The description of the behaviour of the flow continues with analysing the propagating wave and the related local loads on the hull surface in the area of the bow. For this perspective, the connection between the behaviour of the local loads and the local hull form is described.

Within the second step, the analysis of the results connects the behaviour of the local loading to the resulting global springing excitation. First, the analysis of the results explains how the features of the local vertical loads at different stations lead to the second harmonic vertical force at the station in question. In this respect, the changes in the features of the local loads which are favourable for the second harmonic vertical force are stressed. Second, the accumulation of the global second harmonic vertical force along the length of the hull is described. In this respect, the

effect of the variations in both the second harmonic amplitude and phase of the vertical force between different stations is pointed out.

The main contribution of the present work can be summarised as follows:

1. showing that the present method is capable of predicting the ship wave loads at a detailed level in very short and steep waves. The solution accuracy assessment shows the reliability of the computed wave loads at different levels of detail, which cover the range needed in the analysis of the springing excitation. The validation of the computed results against the results of the model tests that were conducted goes into a detailed level by considering local pressures in the time domain at ten different locations;
2. explaining the origin of the second harmonic wave loads that can cause springing vibration in the case of the ship and wave condition being investigated;
3. showing how the local features of the ship hull relate to the resulting loading in the case of the hull form and wave condition being investigated.

To the best of the author's knowledge, there are no previous published studies that present the analysis of the origin and development of springing excitation along the length of a ship hull at this detailed level.

Parts of this work have been published in two peer-reviewed journal papers, (Hänninen et al., 2012) and (Hänninen et al., 2014). The literature survey on the validation of the ship wave loads predicted with interface-capturing methods (Section 1.4) is presented in (Hänninen et al., 2014). The study case (Chapter 2) was originally described in (Hänninen et al., 2014) in a shorter form. The description of the computational approach was published in (Hänninen et al., 2014) with regard to the mathematical model (Section 3.1), the setup of the flow solver (Section 3.2), and the analysis concerning the pressure histories in Section 3.3. The calculation of the vertical force at a station and the calculation of the second harmonic component in Section 3.3 were originally presented in (Hänninen et al., 2012). The description of the experimental approach (Chapter 4) was mainly published in (Hänninen et al., 2014). The study on the relia-

bility of the results was originally published in (Hänninen et al., 2014). It is taken further regarding the analysis of the wave conditions in the computations (Section 5.1), the analysis of the measured results (Section 5.2), and the comparisons of the computed and measured results (Section 5.3 of this thesis). The discussion on the reliability of the computed results in Section 7.1 includes some aspects which were originally presented in (Hänninen et al., 2014), but they are elaborated further here.

The full research and the reporting of this work were performed independently by the author. The supervisor and the instructor of the thesis and any other individuals contributed to the work only through discussions and by providing comments on the related journal papers and on the manuscript of the thesis.

1.6 Structure of the thesis

Chapter 2 describes the flow case and the general assumptions that are made on the physics of the flow.

Chapters 3 and 4 present the methods that were applied. Chapter 3 describes the numerical approach. The description includes the mathematical model that was applied (Section 3.1), the setup for the flow solver (Section 3.2), and the methods used for analysing the computational results (Section 3.3). Chapter 4 describes the experimental approach. The description includes the instrumentation in the model tests (Section 4.1), the calibration of the pressure sensors (Section 4.2), and the methods used for analysing the experimental results (Section 4.3).

Chapters 5 and 6 present the results of this work. Chapter 5 focuses on the reliability of the results. The related analysis starts with the solution accuracy assessment of the computational results in Section 5.1. Next, the validation data (or the results of the model tests) are presented and analysed in Section 5.2. Last, the validity of the computational results is judged through the comparison against the experimental results in Section 5.3. Chapter 6 focuses on the origin of the springing excitation using the computational results. The behaviour of the flow is described at a general level in Section 6.1. The features of the loading which matter for the second harmonic wave loads (or springing excitation) are pointed out in Section 6.2.

The outcome of this work is addressed in Chapters 7 and 8. Chapter 7 presents a discussion of the results. First, the reliability of the results

is in focus in Section 7.1. Second, the present findings on the springing excitation are elaborated in Section 7.2. Chapter 8 concludes this work and gives recommendations for future studies.

2. Study case

This chapter is partly based on (Hänninen et al., 2014).

The study case of this work describes a large cruise ship that is advancing in short and steep head waves. The scale that is applied is 1:49. The selected encounter period is such that the second harmonic component of the wave loads resonates with the two-node vertical mode of a passenger ship roughly 300 m long. The ship frames are given in Figure 2.1 and the case parameters are presented in Table 2.1. The origin of the coordinate system locates at the aft perpendicular of the ship at the level of the design waterline. The positive z -axis points upwards and the positive x -axis from the stern towards the bow of the ship.

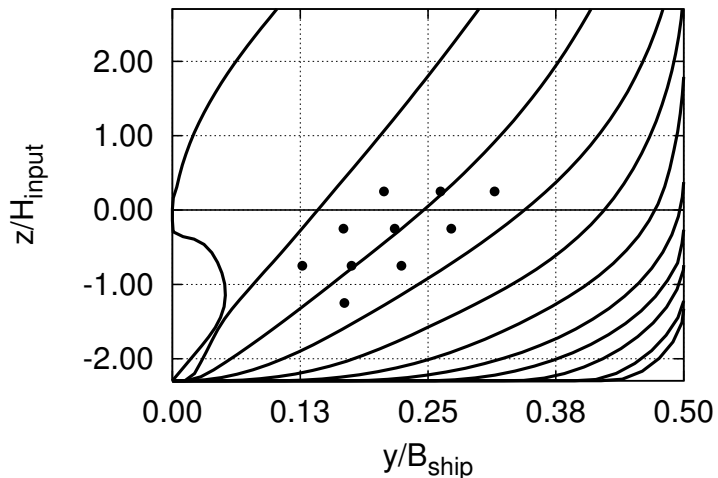


Figure 2.1. Ship frames between the fore perpendicular and the midship and the locations of the pressure sensors.

The setup applied in studying this case includes two assumptions about the physics of the flow. First, it is assumed that the deformation of the hull (springing vibration) does not significantly affect the main features

Table 2.1. Ship and wave particulars in the model scale. L_{ship} denotes the length between the perpendiculars of the ship. The draught is the draught at the model velocity. (Hänninen et al., 2014)

Length L_{ship}	6.69m	Wave length L_{wave}	1.05m
Breadth B_{ship}	1.10m	Wave height $H_{input} = 2A$	0.08m
Draught	0.184m	Wave steepness kA	0.24
Block coefficient	0.72	Encounter period t_e	0.38s
Velocity V_{ship}	1.47m/s		
Froude number	0.181		
Reynolds number	$0.982 \cdot 10^7$		

of the flow. As a consequence, the hull is considered rigid. The reasoning that underpins this assumption is that the order of magnitude of the vibration amplitude is about 1% of the wave height in this case. Second, it is assumed that ship motions are negligible, which implies that the effect of the radiation forces can be ignored. The validity of this assumption is confirmed by the measured data of the ship motions in the model tests in Subsection 5.2.1.

As for the analysis of the results, this study focuses on the behaviour of the wave loads on the surface of the hull. The area of the bow is the main focus of interest, although the contribution of the loading on the other parts of the hull to the global second harmonic loading is addressed, too. Figure 2.2 shows the six stations ($0.82 \leq x/L_{ship} \leq 0.98$) that are used as examples to study the flow behaviour in detail. In addition, Figures 2.1-2.2 give the locations of the pressure sensors in the model test. At these locations, the computational results are compared with the experimental ones.

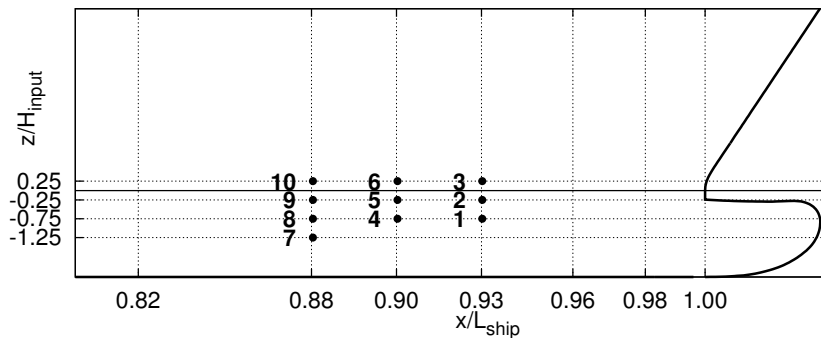


Figure 2.2. Pressure sensors and their numbering seen from the starboard side of the hull.

As Figures 2.1-2.2 show, the validation data from the model tests originate from a small area of the hull. When studying the reliability of the computed results, it is assumed that the validity of the present computation (modelling accuracy) can be assessed on the basis of these data. Furthermore, the reliability of the computed results is studied with a solution accuracy assessment (numerical accuracy). This assessment covers the second harmonic amplitude of the vertical force at the stations along the whole length of the hull and a more detailed analysis of the wave loads in the area of the bow.

3. Computational approach

This chapter addresses the computational approach. Section 3.1 describes the mathematical model, Section 3.2 the setup for the flow solver and Section 3.3 the analysis of the computational results.

The main parts of Sections 3.1 and 3.2 were presented previously in (Hänninen et al., 2014) or are based on (Hänninen et al., 2014), but they also include some additional information. The origin of the information in Section 3.3 (Hänninen et al., 2012) or (Hänninen et al., 2014) is indicated when needed.

3.1 Mathematical model

The computations are performed using the ISIS-CFD flow solver, which is distributed by Numeca International under the name FINETM/Marine. This section describes the mathematical model of the flow applied in this study. First, the governing equations are described. Second, the boundary conditions are given. Last, the assumptions and the limitations of the mathematical model are mentioned.

The description of the governing equations follows Queutey and Visonneau (2007). The conservations of mass, momentum, and volume fraction are modelled with the equation of continuity, the Navier-Stokes equations, and the transport equation of the volume fraction in Eqs. (3.1)-(3.3), respectively. Equations (3.1)-(3.3) are written for incompressible fluids in a moving grid system. In the case of the equation of continuity, distinct phases are assumed to have constant densities. In the case of a moving grid, a so-called space conservation law is satisfied.

$$\int_S \vec{U} \cdot \vec{n} dS = 0, \quad (3.1)$$

$$\frac{\partial}{\partial t} \int_{V(t)} \rho \vec{U} dV + \int_{S(t)} \rho \vec{U} (\vec{U} - \vec{U}_d) \cdot \vec{n} dS =$$

$$= \int_{V(t)} \nabla \cdot \bar{T} dV - \int_{S(t)} p \bar{n} dS + \int_{V(t)} \rho \bar{g} dV, \quad (3.2)$$

$$\frac{\partial}{\partial t} \int_{V(t)} c_i dV + \int_{S(t)} c_i (\vec{U} - \vec{U}_d) \cdot \bar{n} dS = 0, \quad (3.3)$$

where V is the control volume and S its closed surface. The velocity of the surface is denoted with \vec{U}_d and its outwards-directed unit normal vector with \bar{n} . \vec{U} represents the velocity field, p the pressure field, \bar{T} the stress tensor, \bar{g} the gravity vector, and c_i the volume fraction of the fluid i .

The coupling of the velocity and pressure fields is performed with a SIMPLE algorithm that takes into account the presence of a density discontinuity; see (Queutey and Visonneau, 2007).

The behaviour of the free surface is modelled with the volume-of-fluid method, which predicts the flows of both the water and the air in the computational domain using Eq. (3.3). This means that $i = air$ or $i = water$. In each computational volume, the volume fraction c_i indicates the presence of fluid i ($c_i = 1$) or its absence ($c_i = 0$) or a mixture of the two fluids ($0 < c_i < 1$). The value $c_{air} = c_{water} = 1/2$ is selected as the free surface. Using these volume fractions, the fluid density ρ and the fluid viscosity μ are defined for each control volume with

$$\rho = c_{water} \cdot \rho_{water} + c_{air} \cdot \rho_{air}, \quad (3.4)$$

$$\mu = c_{water} \cdot \mu_{water} + c_{air} \cdot \mu_{air}, \quad (3.5)$$

respectively. In this case, the volume fraction c_{air} can be defined as $c_{air} = 1 - c_{water}$. Only the volume fraction c_{water} is solved from Eq. (3.3).

The stress tensor T_{ij} in Eq. (3.2) consists of the viscous stress $\tau_{i,j}$ and of the turbulent Reynolds stress $\tau_{t,i,j}$, (Numeca, 2011a):

$$T_{ij} = \tau_{i,j} + \tau_{t,i,j}, \quad (3.6)$$

the definitions of which are

$$\tau_{i,j} = 2\mu S_{i,j}, \quad (3.7)$$

and

$$\tau_{t,i,j} = 2\mu_t S_{i,j} + 2\rho K \delta_{i,j} / 3, \quad (3.8)$$

where S_{ij} is the ij component of the mean strain-rate tensor, μ_t the eddy viscosity, K the turbulent kinetic energy, and δ_{ij} the ij component of the Kronecker's delta. The values of the eddy viscosity and the turbulent kinetic energy are solved from the turbulence model, which is Menter's STT $k - \omega$ model with wall functions. The turbulence model is described in Appendix A.

The boundary conditions that were applied are given in Table 3.1. They are described below according to (Numeca, 2011b). At the far-field boundary, the velocity is set to zero at the beginning of the computation. The variables that are imposed depend on the local flow direction with respect to the boundary patch. Depending on whether the flow enters or leaves the domain, a Dirichlet or a Neumann condition is applied. At the boundaries with the prescribed pressure, the pressure $p_{boundary}$ is set to the value

$$p_{boundary} = -\rho g (z_{boundary} - z_0), \quad (3.9)$$

where $z_{boundary}$ is the z -location of the boundary and z_0 the location of the free surface at the beginning of the computations. The fluid can both enter and exit at this boundary. At the boundary with the mirror condition, the geometry and the flow are assumed to be symmetric. Then the velocity field is assumed to be tangential to the mirror plane. At the boundary with the slip wall, the velocity component that is normal to the boundary is set to zero. Further, the turbulent production resulting from shear is neglected.

Table 3.1. Boundary conditions, (Hänninen et al., 2014)

x_{min}	Far-field condition	x_{max}	Wave generator, first order Stokes
y_{min}	Mirror condition	y_{max}	Mirror condition
z_{min}	Prescribed pressure	z_{max}	Prescribed pressure
Deck	Slip wall	Hull	Wall with wall-functions

The wave generation at the boundary x_{max} is based on the first-order Stokes wave theory. The flow solver receives the wave period t_{wave} , the wave height H_{input} , the x -location of the wave boundary, and the distance between the free surface at rest and the bottom of the domain d as input values (Numeca, 2011b). Additionally, the flow solver calculates the wave length L_{wave} from the dispersion relation with

$$\omega_{wave}^2 = gk \tanh(kd), \quad (3.10)$$

where $k = 2\pi/L_{wave}$ and $\omega_{wave} = 2\pi/t_{wave}$. According to the first-order Stokes wave theory, e.g. (Newman, 1977), the wave height h in deep water at the instant t and at the location x can be evaluated as

$$h(x, t) = \frac{1}{2} H_{input} \cdot \cos(kx + \omega_{wave} \cdot t) \quad (3.11)$$

when the wave propagates along the negative x -axis and the respective velocity components u and w as

$$u(x, t) = \frac{1}{2} H_{input} \cdot \omega_{wave} \cdot e^{kz} \cdot \cos(kx + \omega_{wave} \cdot t) \quad (3.12)$$

and

$$w(x, t) = \frac{1}{2} H_{input} \cdot \omega_{wave} \cdot e^{kz} \cdot \sin(kx + \omega_{wave} \cdot t), \quad (3.13)$$

respectively. At the beginning of the computation, the wave generator is started in such a way that the wave boundary condition does not induce horizontal velocity components (Numeca, 2011b). At the wave boundary, the velocity is imposed and the pressure is extrapolated (Deng, 2014).

The models which were selected for this study have three limitations. First, the model assumes that waves that are encountered can be modelled with a boundary condition that is based on the first-order wave theory. The suitability of this assumption is studied by comparing the time histories of the freely propagating waves in the computations and the time histories of the measured waves in the model tests. Second, the method applied for the free-surface flows, a volume-of-fluid method, assumes that the flow can be modelled as a mixture of water and air with a ratio that defines the properties of the fluid in a computational volume; see Eqs. (3.4)-(3.5). Third, the surface tension is not included in the mathematical model.

3.2 Setup for the flow solver

In this section, the discretisation schemes that were applied for the governing discretised equations are mentioned first. Second, the ways of studying the effect of resolution and the effect of the number of iterations within a time step are described. Third, the details of the setup of both the spatial and time domains are given.

The discretisations of the governing equations are explained in (Queutey and Visonneau, 2007). In this study, second-order discretisation schemes were selected as user-defined options. In the case of the time derivatives, a second-order backward scheme is used; see (Queutey and Visonneau, 2007). In the case of the convective terms of momentum and turbulence equations, the GDS gamma differencing scheme is used; see (Queutey and Visonneau, 2007). In the case of the convective term of the volume fraction conservation equation, the BRICS blended reconstructed interface capturing scheme is used; see (Wackers et al., 2011).

A set of six computations was performed in order to study both the effect of the resolution and the effect of the iteration number within a time step. This set includes three discretisation resolutions and two iteration numbers. The Courant number was fixed between the computations, which means that the effects of both the spatial and the temporal resolutions were studied simultaneously. The scaling ratios of both the spatial and the temporal resolutions were 1.25 (coarse/medium) and 1.20 (medium/fine); see Table 3.2. One way of estimating the general order of magnitude of the Courant number is to use the time steps Δt and the cell lengths L_{cell} in Table 3.2. This gives the Courant number $Co = V_{ship} \cdot \Delta t / L_{cell} = 0.13$. The refinement of the grids between the different resolutions was performed systemically, but the grids may have some differences as a result of the practical limitations of the grid generator.

The significance of the iterative error was tested on each resolution by repeating the computation with two different iteration numbers (10 and 20 iterations per time step), while the requirement for the decrease of the residuals (infinity norms) was set so high that practically it did not limit the iteration number. These present choices on the iteration within a time step check how the recommendations for the present solver work for the present flow case. According to the recommendations, 20 iterations and the decrease of the residuals by two orders of magnitude should be used for sea-keeping computations (Numeca, 2011b).

Table 3.2. Information on grids and time steps, (Hänninen et al., 2014)

	Number of cells	$t_e / \Delta t$	L_{wave} / L_{cell}	H_{wave} / H_{cell}	y_1
Coarse	2.29M	245.16	58.32	8.00	0.0020
Medium	3.71M	306.45	72.90	10.00	0.0016
Fine	6.53M	367.86	87.49	11.94	0.0013

The computational domain includes only one half of the ship hull because of the symmetric flow case. The computational domain moves with the ship. The locations of the domain boundaries are given in Table 3.3; see also Figure 3.1. The locations of the upper and the lower boundaries are slightly different between the three resolutions. This is accepted in order to ensure that the location of the initial free surface coincides with a cell face for each grid. With the hexahedral grid generator that was used, it is not possible to have both the same locations of the upper and the lower boundaries and the same location of cell faces coinciding with the initial

free surface for this set of grids. No special treatment is applied at the outlet boundary (x_{min}) for wave absorption. The grids were generated with the Hexpress hexahedral grid generator (version 2.11-1).

Table 3.3. Locations of the grid boundaries

	Coarse	Medium	Fine
x_{min}/L_{wave}	-8.32	-8.32	-8.32
x_{max}/L_{wave}	9.23	9.23	9.23
y_{min}/L_{wave}	0.00	0.00	0.00
y_{max}/L_{wave}	6.63	6.63	6.63
z_{min}/L_{wave}	-7.32	-8.75	-8.13
z_{max}/L_{wave}	2.44	1.01	1.63

The spatial domain has three sub-domains of local refinements: one to transport the waves in the computational domain (refinement box $b1$, Figure 3.1, Table 3.4); another one to refine the domain near the bow in the y -direction (refinement box $b2$, Figure 3.1, Table 3.4), and a third one near the hull surface for the boundary layer. The cell sizes in the refinement boxes $b1$ and $b2$ are given in Table 3.2. As for the boundary layer, the first cell heights y_1 are given in Table 3.2 and the stretching ratio is 1.20. The first cell heights were selected in such a way that the dimensionless distance from the wall y^+ gets the value of roughly 30 in the area of the stern of the ship.

Table 3.4. Locations of the boundaries of the refinement boxes $b1$ and $b2$

	$b1$	$b2$		$b1$	$b2$
$ x_{FPP} - x_{bi,1} /L_{wave}$	8.12	1.93	$ x_{FPP} - x_{bi,2} /L_{wave}$	2.86	0.13
$y_{bi,1}/L_{wave}$	0.00	0.00	$y_{bi,2}/L_{wave}$	6.63	0.95
$z_{bi,1}/L_{wave}$	-0.06	-0.12	$z_{bi,2}/L_{wave}$	0.06	0.21

Figure 3.2 shows some details of the resolutions of the three grids on the hull surface and on the symmetry plane $y = 0$ and on a plane near the design waterline depth.

At the beginning of the computation (0.00 s - 3.00 s), the ship accelerates according to an acceleration ramp of the form $0.5 - 0.5 \cos (t\pi / 3.00 \text{ s})$. The wave generation starts at the inlet boundary at the beginning of the simulation. The results to be analysed cover the time frame 6.98 s - 10.80 s, which includes ten encounter periods.

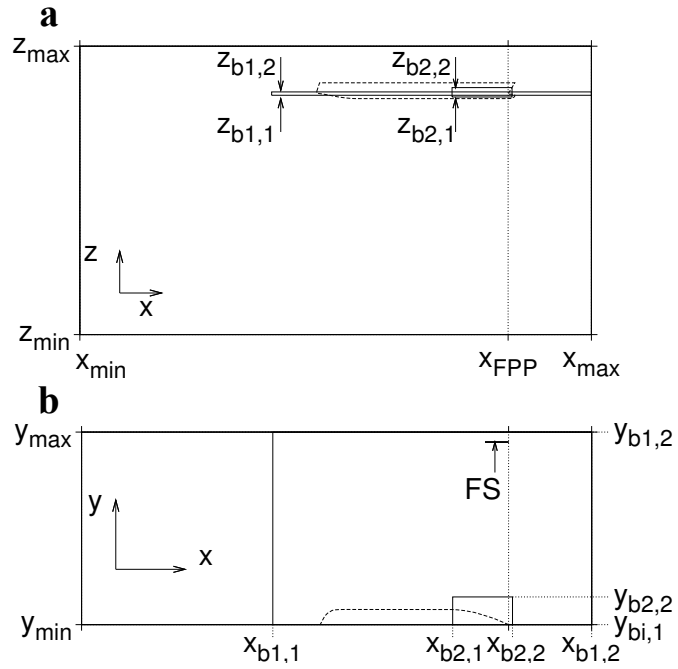


Figure 3.1. Coordinate axes, boundaries of the computational domain (x_{min} , x_{max} , y_{min} , y_{max} , z_{min} , z_{max}), boundaries of the refinement boxes $b1$ and $b2$ ($x_{b1,1}$, $x_{b1,2}$, $y_{b1,1}$, $y_{b1,2}$, $z_{b1,1}$, $z_{b1,2}$), location of the fore perpendicular (x_{FPP}). The origin on the coordinate system locates at the aft perpendicular of the ship at the level of the design waterline. **a** xz -level **b** xy -level, the line FS indicates the location of the analysis of the behaviour of the waves.

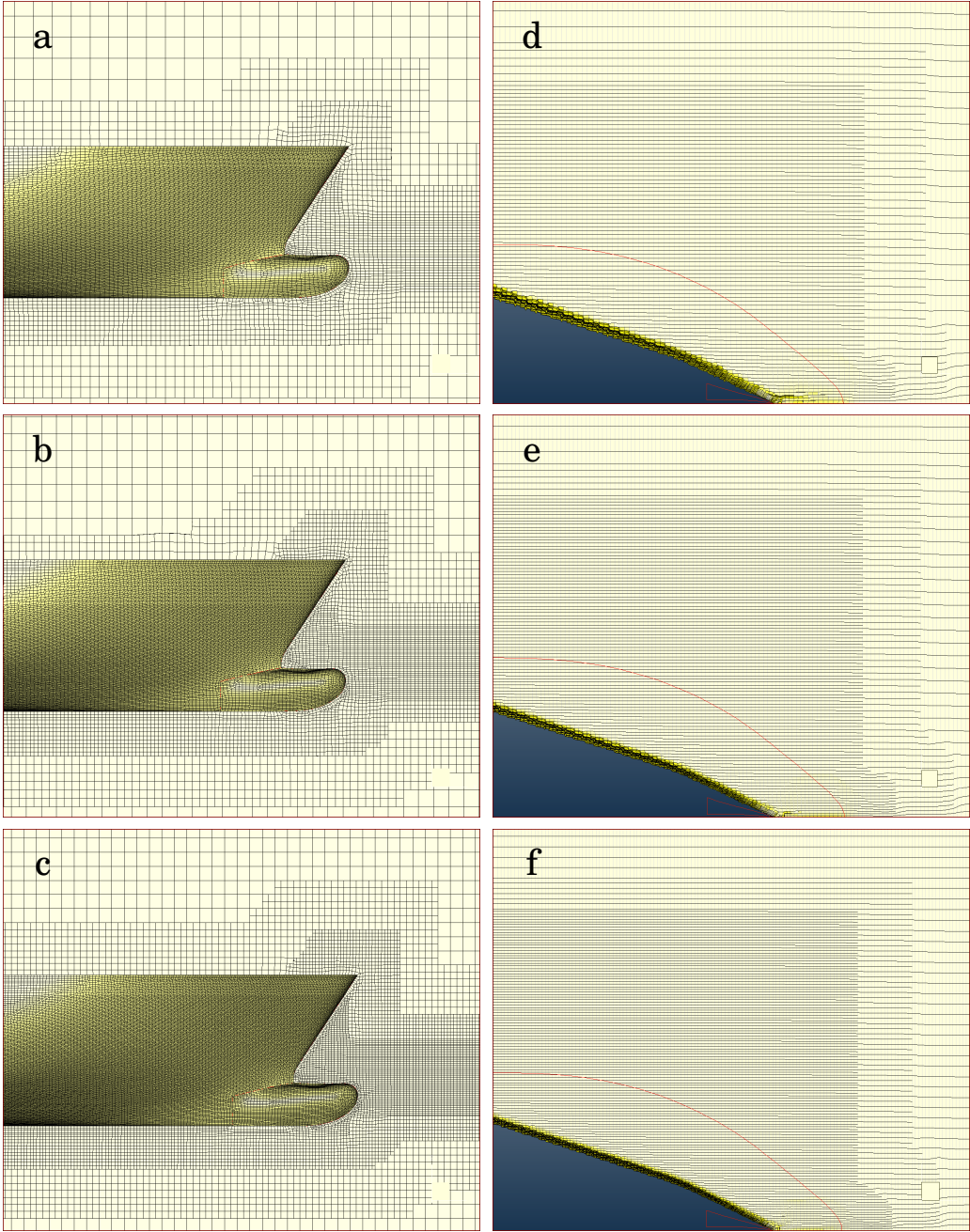


Figure 3.2. From top to bottom: coarse, medium, and fine grids. **a-c** hull surface and the symmetry plane $y = 0$, **d-f** z -directional plane near the design waterline.

Table 3.5 gives information on the fluid properties in the computations.

Table 3.5. Information on fluids, (Hänninen et al., 2014)

Water density ρ_{water}	998.1 kg/m ³	Air density ρ_{air}	1.2 kg/m ³
Water viscosity μ_{water}	0.001 kg/sm	Air viscosity μ_{air}	1.85×10^{-5} kg/sm
Standard gravity g	9.81 m/s ²		

3.3 Analysis of the computational results

This section describes the methods that are used in the analysis of the computational results.

3.3.1 Averages

The data to be analysed from the computations include ten encounter periods. The results that are presented (with the exceptions of Figures 6.1-6.6 and Figures 6.9-6.11) are the averages of these ten encounters. Thus, an instantaneous result of a quantity $\phi(t)$ is calculated with

$$\phi(t) = \frac{1}{10} \sum_{j=1}^{10} \phi_j(t), \quad (3.14)$$

where $\phi_j(t)$ is the corresponding instantaneous value of the j^{th} encounter.

3.3.2 Characteristics of the waves encountered

This subsection mainly follows Hänninen et al. (2014).

The characteristics of the waves encountered are studied at the y -location of the longitudinal cross-section FS in Figure 3.1. The wave characteristics at the y -location of FS are assumed to correspond to the characteristics of the waves that the ship encounters.

The wave characteristics are analysed from the time histories of the wave elevation, which are low-pass filtered with a threshold frequency of 3.5 times the encounter frequency.

The encounter period of one wave encounter is calculated as the time span between the zero crossing of the rising time history and the zero crossing of the following rising part of the time history.

The wave height of one wave encounter is calculated from the time history of the wave elevation as the distance between a local minimum and the following local maximum.

The encounter period and the wave height at a specific x -location for the whole period of the analysis is the average of the results of the ten distinct encounters at that specific location.

When the other computed results are made non-dimensional, the wave characteristics are calculated as averages between the x -location of the fore perpendicular of the ship and $x/L_{ship} = 0.88$ on the cross-section FS in Figure 3.1. The location $x/L_{ship} = 0.88$ corresponds to the location of the rear-most pressure sensors in the model tests; see Figure 2.2. Below, this average wave height is denoted as H .

3.3.3 Forces

The forces that are presented consist of the vertical force at the stations and of the vertical forces that accumulate along the length of the hull.

The calculation of the force at a station is presented first and it follows Hänninen et al. (2014). As unstructured grids are used, in practice the grid points are not located at the vertical intersections that represent stations. Instead, the points within thin vertical sections are selected and used to calculate the instantaneous force at a station. The number of the points within a vertical section is denoted as $N_{p,f}$.

The calculation of a vertical force history at a station consists of two steps. First, the points representing one half of the ship frame need to be organised. In general, the point closest to the centreline of the ship is chosen to be the point $i_y = 1$, the second closest point is $i_y = 2$, and so forth. The bulb area is an exception. There, the points closest to each other are adjacent. Second, the vertical force per unit ship length at a station is calculated using the trapezoidal rule:

$$F_{z,station}(t) = \sum_{i_y=2}^{N_{p,f}} (p_{i_y}(t) + p_{i_y-1}(t)) \cdot (y_{i_y} - y_{i_y-1}). \quad (3.15)$$

The force $F_{z,station}$ is called the vertical force at a station in this work.

The total force acting on the hull can be calculated by adding up all the vertical forces at the stations multiplied by the width of the x -span that a frame force represents. In this work, the development of this total force along the length of the hull is presented. This developing force is called the cumulative force $F_{z,cum}$. The definition of the cumulative force between the stem of the ship and an x -location downstream is:

$$F_{z,cum}(x, t) = \sum_{ix=1}^{n_{station}} F_{z,station,ix} \cdot dx, \quad (3.16)$$

where dx is the width of the x -span that a force at a station represents. The index $ix = 1$ indicates the foremost station and the index $ix = n_{station}$ indicates the rearmost station that is observed.

The generalised vertical excitation force of the 2-node vertical mode of a hull can be calculated by multiplying the distribution of the vertical force along the length of the hull by the vertical two-node mode of the hull $\Theta(x)$. In this work, the development of this generalised force along the length of the hull is presented. This developing force is called the cumulative generalised force $G_{z,cum}(x, t)$. The definition of the cumulative generalised force between the stem and an x -location downstream (index $n_{station}$) is:

$$G_{z,cum}(x, t) = \sum_{ix=1}^{n_{station}} F_{z,station,ix}(t) \cdot \Theta(ix) \cdot dx. \quad (3.17)$$

The mode shape is normalised so that it gets the value of one at the location of the fore perpendicular $x/L_{ship} = 1.0$.

3.3.4 Non-dimensional results

The results are presented in non-dimensional forms. The information on the pressure histories that are compared with the experimental results follows Hänninen et al. (2014).

The time domain is made non-dimensional by division by the average of the encounter period t_e . The time instant $t/t_e = 0.0$ is different for the comparisons of the pressure histories with the experimental results and for the other parts of the study. In the case of the comparisons with the experimental results, the results at each station are shifted in the time domain in such a way that the rising undisturbed wave crosses the still water level at the time instant $t/t_e = 0.0$. The wave elevation for this is obtained from the longitudinal cross-section FS (Figure 3.1). The negative time is defined as the time instants before the instant when the rising undisturbed wave crosses the still water level. In the other parts of the study, $t/t_e = 0.0$ is an instant before the front of the wave hits the hull; see e.g. Figure 6.1.

The local pressures p are made non-dimensional as follows:

$$p^* = \frac{p}{\rho g H}. \quad (3.18)$$

The forces at the stations $F_{z,station}$ are made non-dimensional as follows:

$$F_{z,station}^* = \frac{2F_{z,station}}{\rho g B_{ship} H}. \quad (3.19)$$

The cumulative forces $F_{z,cum}$ are made non-dimensional as follows:

$$F_{z,cum}^* = \frac{2F_{z,cum}}{\rho g L_{ship} B_{ship} H}. \quad (3.20)$$

3.3.5 Applied discrete Fourier transformation

The main parts of this subsection have been presented previously in (Hänninen et al., 2012) or are based on (Hänninen et al., 2012).

The force histories are subjected to discrete Fourier transformation DFT, e.g. (Chapra and Canale, 1988), in order to distinguish the effect of the second harmonic wave loads. The denotation F is used here for a force history from which its mean value F_{mean} has been subtracted.

From the point of view of the signal analysis, the time histories given by the computations are data sequences $F = F(n)$ of discrete times $n = 1, 2, \dots, N_t$. The length of the time history $L_t = N_t \Delta t$ defines the spacing $\Delta \omega$ of the frequency domain by $\Delta \omega = 2\pi/L_t$. The total number of points N_ω in the frequency domain is limited by the Nyquist frequency $\pi/\Delta t$.

The Fourier series of a real-valued time history F can be written as

$$F(n) = \sum_{k=1}^{N_\omega} a_k \cos\left(\frac{2\pi k}{N_t} n\right) + \sum_{k=1}^{N_\omega} b_k \sin\left(\frac{2\pi k}{N_t} n\right) \quad (3.21)$$

with

$$a_k = \frac{2}{N_t} \sum_{n=1}^{N_t} p(n) \cos\left(\frac{2\pi k}{N_t} n\right) \quad (3.22)$$

and

$$b_k = \frac{2}{N_t} \sum_{n=1}^{N_t} p(n) \sin\left(\frac{2\pi k}{N_t} n\right). \quad (3.23)$$

This study presents amplitudes that correspond to the second harmonic of the encounter frequency. As the length of the time histories is 10 times that of the encounter period, the respective index in the frequency domain is 20. Thus, the amplitudes $\xi_{2,single}$ corresponding to the second harmonic of the encounter frequency can be calculated with

$$\xi_{2,single} = \sqrt{a_{20}^2 + b_{20}^2}. \quad (3.24)$$

However, the second harmonic amplitudes, which are actually presented, include the energy in the frequency span of width ω_e around the second harmonic encounter frequency. These amplitudes are calculated with

$$\xi_{2,span} = \sqrt{\sum_{k=15}^{24} (a_k^2 + b_k^2)}. \quad (3.25)$$

The results in Appendix B show that the difference between the amplitudes $\xi_{2,single}$ and $\xi_{2,span}$ is negligible from a practical point of view. Nevertheless, the definition of the amplitude $\xi_{2,span}$ is more appropriate from the point of view of the springing excitation.

Further, this study presents low-pass filtered time histories, which consist either of the zeroth - first harmonic components or of the zeroth - second harmonic components. These filtered time histories are calculated with Eq. (3.21). Then N_ω in Eq. (3.21) is replaced with 14 in the case of the low-pass filtered time history of the zeroth - first harmonic components and with 24 in the case of the low-pass filtered time history of the zeroth - second harmonic components.

3.3.6 Computational results compared with the experimental ones

This subsection mainly follows Hänninen et al. (2014).

Before the computational results are compared with the experimental ones, the computational results are presented as similarly as possible to the experimental ones. First, the pressure histories are low-pass filtered with the threshold frequency of 30.5 times the encounter frequency in order to remove high-frequency noise.

Because of the unstructured grids, the computational points are located arbitrarily on the hull and their locations depend on the resolution. In order to have coherently selected observation areas for each sensor at each resolution, all the computational points within a distance of $1.33 \times R_{sensor}$ from the centre of a sensor are taken into account when estimating the pressure that acts on the surface area of one pressure sensor. In practice, there are 1-4 computational points within the selected observation area of one sensor depending on the resolution and on the location of the sensor. The pressure history, which is compared with an experimental result, is an average of the pressure histories of the individual points within the observation area of the sensor in question.

Moreover, the mean pressure is subtracted from the pressure signals in the case of constantly immersed sensors.

3.3.7 Local entrance angle

The distribution of the local entrance angle of the hull at the level of the design waterline is utilised when the computational results are being pre-

sented. This distribution is calculated from the distribution of the surface normal of the hull, which the flow solver gives. The local entrance angle α is evaluated as

$$\alpha = \text{atan} \left(\frac{n_x}{n_y} \right) \cdot \frac{180^\circ}{\pi}, \quad (3.26)$$

where n_x and n_y are the longitudinal and the horizontal components of the surface normal of the hull, respectively.

3.3.8 Rise and fall times of the time histories

In Subsection 6.2.2, the rise and the fall times of the time histories of the vertical forces $F_{z,station}$ and the rise times of the local vertical loads $p \cdot n_z$ are presented. The rise and the fall times are denoted with $t_{rise,n\%}$ and $t_{fall,n\%}$, respectively. These time spans correspond to the n percent of the peak-to-peak amplitude of the time history. In the case of the vertical forces, n equals 98. In the case of the local vertical loads, n equals 90. These choices are made to eliminate the possible creeping of the quantity in the vicinity of the maximum and minimum values of its time history.

The two instants that are used for the calculation of the rise time $t_{rise,n\%}$ are described below. The earlier instant occurs after the minimum value of the time history. It is the instant when the level of the quantity in question is slightly larger than the minimum value of the force history, which is $(50 - 0.5 \cdot n)\%$ of the peak-to-peak amplitude of the time history from the minimum value of the time history. The later instant occurs before the maximum value of the time history. It is the instant when the level of the quantity in question is slightly smaller than the maximum value of the time history, which is $(50 - 0.5 \cdot n)\%$ of the peak-to-peak amplitude of the time history from the maximum value of the time history. If the minimum value of a local pressure is smaller than zero and the vertical component of the surface normal positive (negative), the minimum (maximum) value of the time history of the corresponding local vertical load is considered zero in this analysis.

The fall times $t_{fall,n\%}$ are calculated similarly. Then, the earlier instant occurs after the maximum value of the time history and the later instant before the minimum value of the time history.

4. Experimental approach

This chapter addresses the experimental approach. Section 4.1 describes the instrumentation used in the model tests, Section 4.2 the calibration of the pressure sensors, and Section 4.3 the analysis of the measured data.

Most of what follows was originally presented in (Hänninen et al., 2014).

4.1 Instrumentation

The model tests were performed in the towing tank of the Department of Applied Mechanics of Aalto University; see Table 4.1. The tank has a plunger-type wave maker at one end and, for damping the waves, beaches at the other end. In order to minimise the wave reflection, floats were positioned at the beach end of the tank during these experiments. The movement of the wave maker was controlled with a sine signal. The water density was approximately 998 kg/m^3 on the basis of the measured temperature during the model tests and the acceleration of gravity is roughly 9.82 m/s^2 in Southern Finland.

Table 4.1. Characteristics of the towing tank and the wave maker, (Hänninen et al., 2014)

Tank Length	130m
Tank Depth	5.5m
Tank Breadth	11m
Plunger type wave maker with wedge inclination of 35°	

The characteristics of the ship model (Figure 4.1) are given in Table 2.1. The model was free to heave and pitch. The position of the model was balanced with weights in such a way that it was on an even keel at the selected model velocity. The draught given in Table 2.1 is the draught at the model velocity.

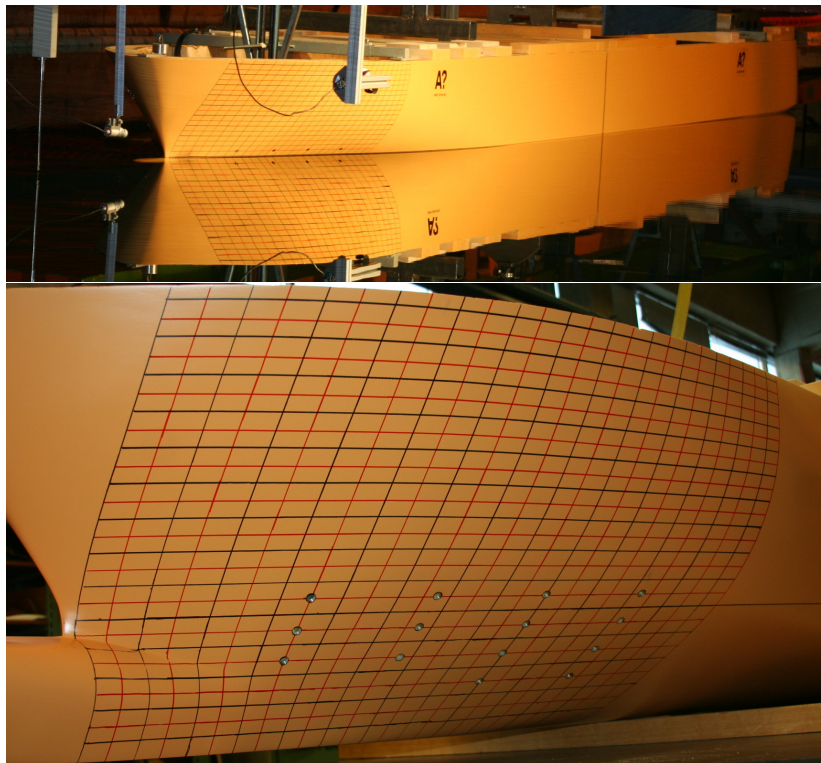


Figure 4.1. Above: the model in the towing tank. Below: the bow of the model.

The measured data consist of the local pressures, wave height, model velocity, and heave motion of the model. The local pressures were measured using 10 pressure sensors (Kyowa's PGM-02KG) on the port side of the bow area; see Figures 4.1 and 2.2. The sensors have a sensing diaphragm diameter of 12 mm (Kyowa). Their rated capacity is 20 kPa and the natural frequency is 2 kHz. The wave height was measured with a servo-mechanical wave height meter (Denshi Kogyo Co.'s VC-503). It was attached to the carriage 1.13 m in front of the fore perpendicular of the model and 0.15 m to port from the symmetry line. The velocity of the model was measured with a pulse encoder. The heave was measured near the aft and the fore perpendiculars of the model with potentiometers to ensure that the motions of the ship were minor in the wave conditions that were investigated. Further, the pitch motion was calculated from the heave measured at these two locations.

All the measured data were collected into a laptop computer via a National Instrument SCXI-1000 data acquisition box. The data acquisition box had one SCXI-1102B input module with an SCXI-1303 terminal block

and another SCXI-1520 input module with an SCXI-1314 terminal block. The output signals of the pressure sensors were amplified with a DC amplifier before the sensors were connected to a terminal block. The sampling frequency was 1007 Hz.

4.2 On the calibration of the pressure sensors

The calibration coefficients of the pressure sensors were determined with a specific calibration measurement in the towing tank. During a calibration, the forward speed of the model was zero and the hydrostatic pressure on the pressure sensors was altered. The responses of the pressure sensors were measured at six fixed levels of the hydrostatic pressure, which had a pressure difference corresponding to a depth of water of 2 cm between adjacent levels. In order to alter the hydrostatic pressure, the vertical position of the ship model was changed with the adjustable towing rig of the carriage. Before a calibration measurement, the ship model was pressed downwards so that all the pressure sensors were in the water.

Figure 4.2 shows an example of the calibration response in the case of Sensor 04 (below the design water line) and in the case of Sensor 06 (above the design waterline). The sensors above the design waterline were pressed under the water just before the calibration measurement started. The calibration measurement of the example in Figure 4.2 includes measuring the responses both when the ship model was pressed deeper into the water and when it was lifted back upwards. The response of the sensor above the design waterline has greater differences between the downward ($0 \text{ s} < t < 220 \text{ s}$) and upward ($260 \text{ s} < t < 500 \text{ s}$) movement compared with a sensor below the design waterline. This indicates that the response of the pressure sensors depends slightly on the time that they have been in water.

The calibration measurement was repeated several times in order to test the repeatability of the sensor behaviour. Some of the calibration measurements were performed both when the model was being pressed down and lifted up and some of them were performed only when it was being pressed down. It was found out that both the maximum variation of the calibration coefficient from its mean values and the respective standard deviation were of a magnitude of 1% for each sensor. Further, the linearity of the pressure sensors was good, the coefficients of determination being higher than 0.998 for each calibration of each sensor. These

numerical values indicate that the effect of the time that the sensors had been in the water (see the example above) is very minor in terms of the calibration coefficients.

Measuring the zero levels of the pressure sensors was performed without a forward speed.

4.3 Analysis of the measured data

The flow case was measured several times in order to have a representative sample of the waves that were encountered. As these steep waves are difficult to reproduce reliably over the length of the tank, the encounters corresponding to the target wave characteristics were selected afterwards. The selection criterion was that the wave height was within roughly $\pm 10\%$ of the target wave height. The wave height and the encounter periods of the individual encounters were calculated from the time histories of the wave elevation similarly as in the case of the computational results; see Section 3.3.

The purpose of the signal post-processing is to be able to compare the results of individual wave encounters easily with each other and with the computed results.

The pressure signals are low-pass filtered with the threshold frequency of 30.5 times the encounter frequency, as in the case of the computed results.

In practice, the selected data are from eight different runs and include 4-15 consecutive wave encounters from one run. The selected results from one run are treated separately before they are all presented together.

First, the average levels of the pressure signals are adjusted. In the case of the constantly immersed sensors, the mean value of the pressure is subtracted from the signal. In the case of the locations above the design water level, the signals are adjusted so that the air pressure gets the value of zero.

Second, the pressure signals are presented consistently with the signals of the wave elevation in the time domain. As in the case of the computed results, the basic idea is that the instant when the rising undisturbed wave crosses the still water level is moved to the value $t/t_e = 0.0$. In the case of the experimental results, this is done using the average encounter period of one run so that the selected wave encounters of one run fulfil this condition on average. The negative time is defined as the time in-

starts before the instant when the rising undisturbed wave crosses the still water level.

The selected pressure signals from one run are made non-dimensional with the respective average encounter period and average wave height.

As mentioned above, the data to be analysed are selected on the basis of the wave height measured in front of the bow. In addition to that, it is necessary to classify the selected pressure signals of the distinct encounters at each station for the sake of a more detailed analysis. As the information on the properties of the waves does not exist at the location of the pressure sensors, the properties of the measured pressures are utilised. At each station, the pressure signals of individual encounters are classified on the basis of the rise time of the signal in the second uppermost row of the pressure sensors. (See Figure 2.2 for the locations of the sensors.) The rise time t_{rise} is defined as the time span between the moment when the non-dimensional pressure gets the value of 0.02 and the moment when it is larger than 90% of the maximum pressure. The rise time is called fast if $t_{rise}/t_e < 0.1$, medium if $0.10 < t_{rise}/t_e < 0.15$, and slow if $t_{rise}/t_e > 0.15$. The present definition of the rise time and the selected boundaries of the three classifications are arbitrary, but they serve the purpose of comparing the rise times between different stations in this study. Further, they allow the classification of the results at a single station and a more detailed analysis of the behaviour of the pressure.

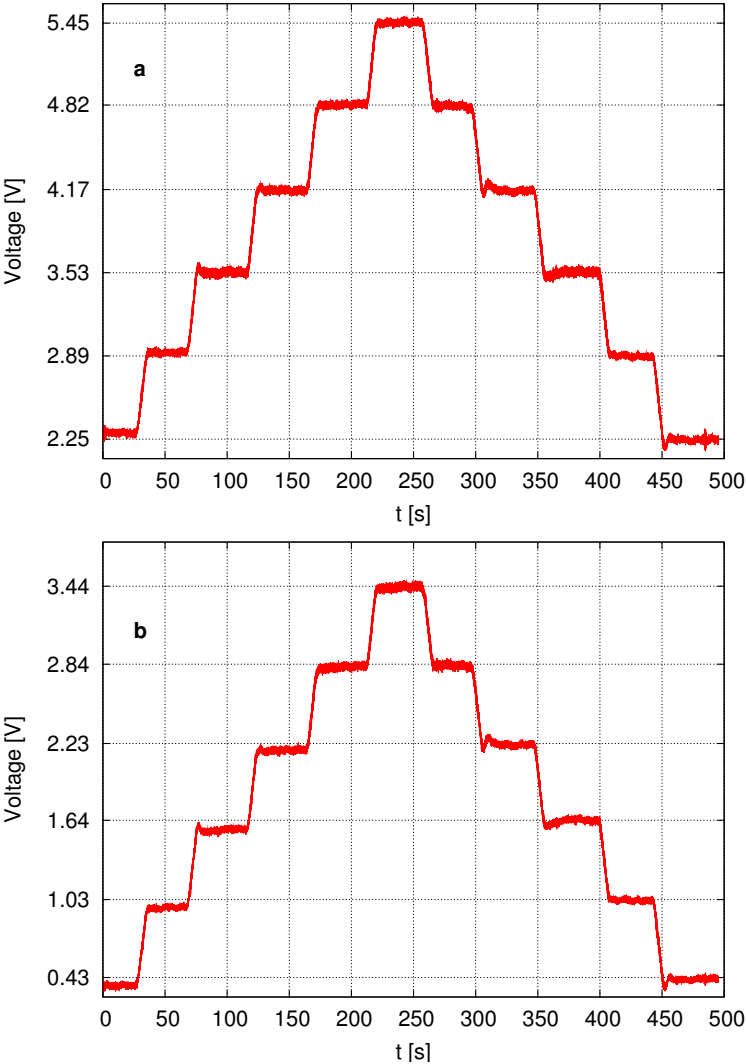


Figure 4.2. Responses of a calibration measurement. **a** Sensor 04 (located below design waterline) **b** Sensor 06 (located above design water line), (Hänninen et al., 2014)

5. Reliability of the results

This chapter addresses the reliability of the computational results. Section 5.1 presents the solution accuracy assessment of the computational results. Section 5.2 presents the measured data, which are used as the validation data. Section 5.3 addresses the validity of the computational results by comparing the computational and experimental results qualitatively.

The analysis of the results concerns wave conditions and wave loads. The levels of detail of studying the reliability of the computed wave loads are different between the solution accuracy assessment and the validation. The solution accuracy assessment in Section 5.1 concerns the reliability of the computed wave loads at several levels of detail, while the validation in Section 5.3 concerns the local pressure histories at ten locations in the area of the bow, which corresponds to the extent of the validation data presented in Section 5.2.

Parts of this chapter have been presented previously in (Hänninen et al., 2014). This concerns parts of Subsection 5.1.1, most of Subsection 5.1.2, and parts of Subsections 5.2.1 and 5.3.1.

5.1 Solution accuracy assessment

In this section, the computed results with the two different numbers of iterations and the three resolutions are compared. Section 5.1.1 addresses the wave conditions, Section 5.1.2 the pressure histories, and Section 5.1.3 the vertical forces in the area of the bow.

5.1.1 Wave conditions

Figure 5.1a gives the distribution of the average wave height in the computational domain. Each point in that figure gives the average wave

height of the ten waves encountered at the given x -location. These results show that the wave height oscillates as the distance to the wave boundary and the wave height increases downstream from the wave boundary. In the vicinity of the stern ($x/L_{ship} = 0.0$), the finer the grid is, the less the wave height increases. In Figure 5.1, the location $x_{b1,1}$, which indicates where the refinement box for the transportation of the waves in the computational domain ends, is given too.

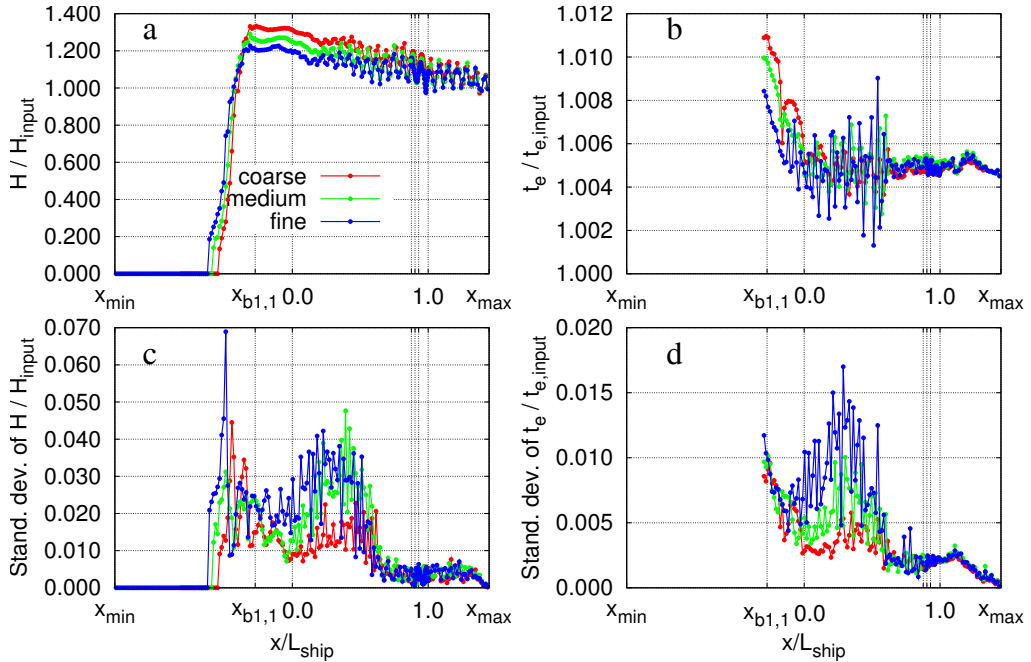


Figure 5.1. The characteristics of the waves at the y -location of the longitudinal cross-section FS in Figure 3.1. The computations with the coarse, medium, and fine resolutions with 20 iterations. The x -locations of the pressure sensors are given as three vertical lines behind $x/L_{ship} = 1.0$. **a** Average wave height **b** Average encounter period **c** Standard deviation of the wave height **d** Standard deviation of the encounter period.

The oscillation in the wave height is believed to be a consequence of the higher harmonic waves that the applied boundary condition creates. These waves travel more slowly than the main wave. Between the fore perpendicular of the ship and the location of the rear-most pressure sensors, for instance, the wave height varies as a function of x between 97% and 120% of the input value of the wave height. The standard deviation of the average wave height is less than 1% in the same area; see Figure 5.1c. The encounter periods are nearly constant and slightly larger than the input value; see Figure 5.1b. The standard deviation of the encounter period

is even smaller than that of the average wave height; see Figure 5.1d. This means that the wave conditions are fixed as a function of time at a constant distance to the wave boundary, but they vary with different distances to the wave boundary.

Figure 5.2 gives the time histories of the freely propagating wave at the same x -location as the pressure sensors on the longitudinal cross-section FS (Figure 3.1). The results of the three resolutions show similar behaviour at each x -location, despite small differences in the time histories. For instance, in the case of the middle cross-section, the behaviour of the uppermost part of the wave crest depends on the resolution. The variation in the wave heights between different cross-sections can be seen in Figure 5.1a.

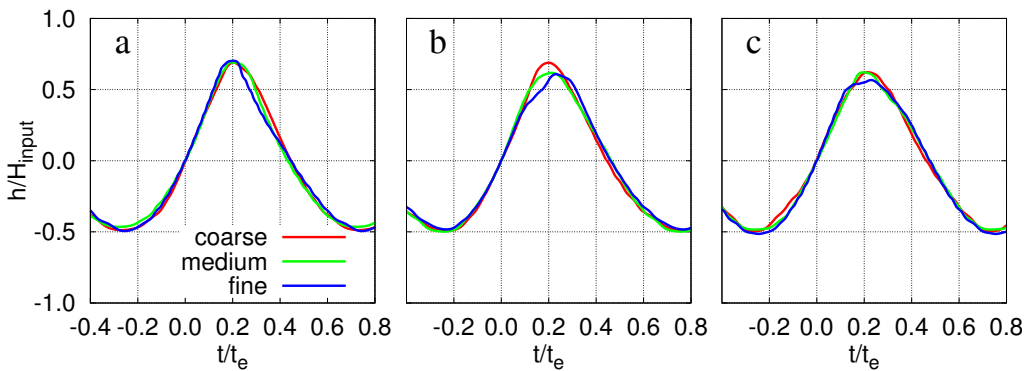


Figure 5.2. Computed wave histories with the coarse, medium, and fine resolutions with 20 iterations. **a** $x/L_{ship} = 0.88$ **b** $x/L_{ship} = 0.90$ **c** $x/L_{ship} = 0.93$ at the longitudinal cross-section FS in Figure 3.1.

5.1.2 Local pressures

In this section, the effect of the number of iterations and the effect of the resolution on the local pressures is studied. The present focus is on the time histories of the local pressures that correspond to the pressure histories obtained from the model tests. Appendices C and D show the local pressures with the different resolutions in a similar manner as in Chapter 6.

The order of this section is as follows. First, the effect of the number of iterations on the results is studied. Next, the effect of the arbitrarily distributed computational points on the results is observed and the repeatability of the results between different encounters is commented on. Then the effect of the resolutions on the results is analysed.

The effect of the number of iterations on the results is observed by comparing the results with 10 and 20 iterations. In general, this effect is minor from the practical point of view. In order to illustrate the greatest effect of the iteration number on the pressure histories, the pressure histories with the two iteration numbers at Sensor 04 are compared in Figure 5.3. The time span between the instants $t/t_e \approx 0.6$ and $t/t_e \approx 0.7$ shows the largest observed difference that the iteration number imposes on the results. The maximum difference is about 17% of the peak-to-peak amplitude of the pressure history (coarse 20) within that time span, while the difference is less or equal to 1% between $-0.06 < t/t_e < 0.55$, for instance. As the effect of the iteration number on the results is minor from the practical point of view, only the results with 20 iterations are presented below.

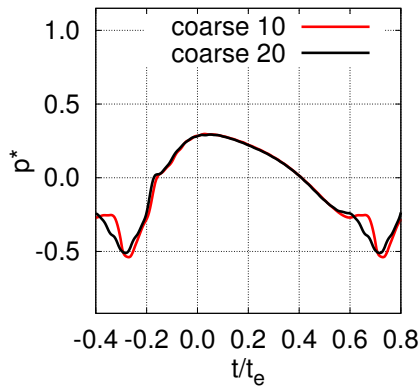


Figure 5.3. An example of the iterative error. Sensor 04. Coarse resolution with 10 and 20 iterations. Red and black lines, respectively. (Hänninen et al., 2014)

Before analysing the agreement of the computational results with the different resolutions, it is necessary to underline that the computational pressure histories, which represent the pressure histories that can be measured in model tests, are the averages of all the pressure histories within a surface area that represent a pressure sensor. Both the number and the locations of the computational points are different with the different resolutions, which can affect the agreement of the results of different resolutions in addition to the effect of the different resolutions on the flow solution. Thus, analysing the effect of the resolutions purely is not possible.

As one example of the effect of the locations of the computational points, Figure 5.4 gives the pressure histories for the distinct computational points of the fine resolution at Sensor 03. This example shows that the max-

imum value of the pressure can be very sensitive to the location of the computational points. In this example, the greatest difference between the maximum values of the pressures within the surface area that represent a pressure sensor is about 49% of the peak-to-peak amplitude of the respective pressure history that is calculated according to Subsection 3.3.6 and illustrated in Figure 5.5 (fine resolution at Sensor 03). This kind of variation in the behaviour of the pressures between the distinct computational points is typical for the sensors above $z/H_{input} = -0.5$. The largest effect is shown in this example. Another example (Figure 5.4) is the behaviour of the distinct pressure histories of the medium resolution at Sensor 04. In this case, both of the pressure histories show a spike at the instant $t/t_e \approx 0.7$. However, its importance is much more significant according to Point 01 than according to Point 02. The difference in the maximum value of this spike between these two points is about 35% of the peak-to-peak amplitude of the respective pressure history that is calculated according to Subsection 3.3.6 and illustrated in Figure 5.5 (medium resolution at Sensor 04). This second example illustrates that the importance which a detail in the flow solution gets can depend both on the locations and, as the average pressure histories of the computational points within a sensor are presented, on the number of the computational points within a sensor. Even if the results within the surface area of a sensor included several details, calculating an average from well-distributed computational points would smooth the solution.

As a further detail, the results in Figure 5.4 include all ten encounter periods for each distinct computational point with one colour. The results of the ten encounter periods are very close to each other. In the case of the results in Figure 5.4a, for instance, the variation of the ten encounters at each computational point is less than 1% of the peak-to-peak amplitude of the pressure history between $0.15 < t/t_e < 0.60$. Elsewhere the instantaneous variations are somewhat larger, the largest instantaneous value being 5% at one of the four locations. In the case of the results in Figure 5.4b, the variation behaves similarly as a function of time. The variation is less than 1% between $-0.05 < t/t_e < 0.65$, while the largest instantaneous value is 6%. This indicates an excellent repeatability of the encounters in the computations.

Next, Figure 5.5 gives the average pressure histories with the three resolutions for all the sensors. In general, the results with the different resolutions look alike on each sensor. Above the design waterline (Sensors 10,

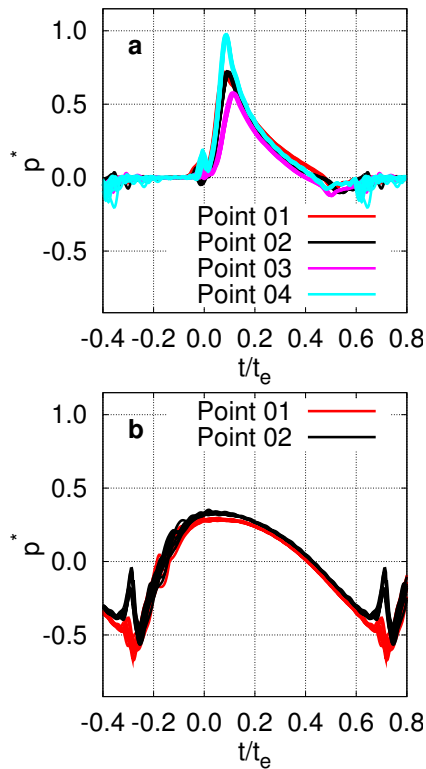


Figure 5.4. Examples of the effect of the location of the computational points within the surface area of a pressure sensor. **a** Fine resolution with 20 iterations, Sensor 03 **b** Medium resolution with 20 iterations, Sensor 04. (Hänninen et al., 2014)

06, 03, 09, 05, and 02), the shapes of the time histories at each sensor look alike between the three resolutions. To be more precise, the time histories have similar rises and descents in terms of both the length of the time and the shape of the time history. The main differences relate to the maximum peak values and the locations of these peaks in the time domain. In this regard, the results of Sensor 10 show the largest variation and the results of Sensors 03 and 9 the best agreement. Further, the behaviour of the pressure history close to the zero value can depend on the resolution. In this regard, the results of Sensor 09 show the largest variation.

Below the design water line (Sensors 08, 04, 01, and 07), the results of the three resolutions are fairly similar regarding both the amplitude and the shape of the time history in general. At a more detailed level, the shapes of the time histories of the fine and medium resolutions are more similar than the shapes given by the course resolution. This observation is the most distinct in the case of Sensors 07 and 08. Such finding can indicate the convergence of the solution with the refinements of the reso-

lution. On the other hand, the observation can indicate that these results are especially dependent on the distribution of the computational points within the surface area of a sensor.

The conclusion on the refinement study is that the general agreement of the results between the resolutions is good. The differences between the resolutions do not have an effect on the main behaviour of the pressure histories. From the practical point of view, these results indicate that the fine resolution adequately predicts the behaviour of the local pressures.

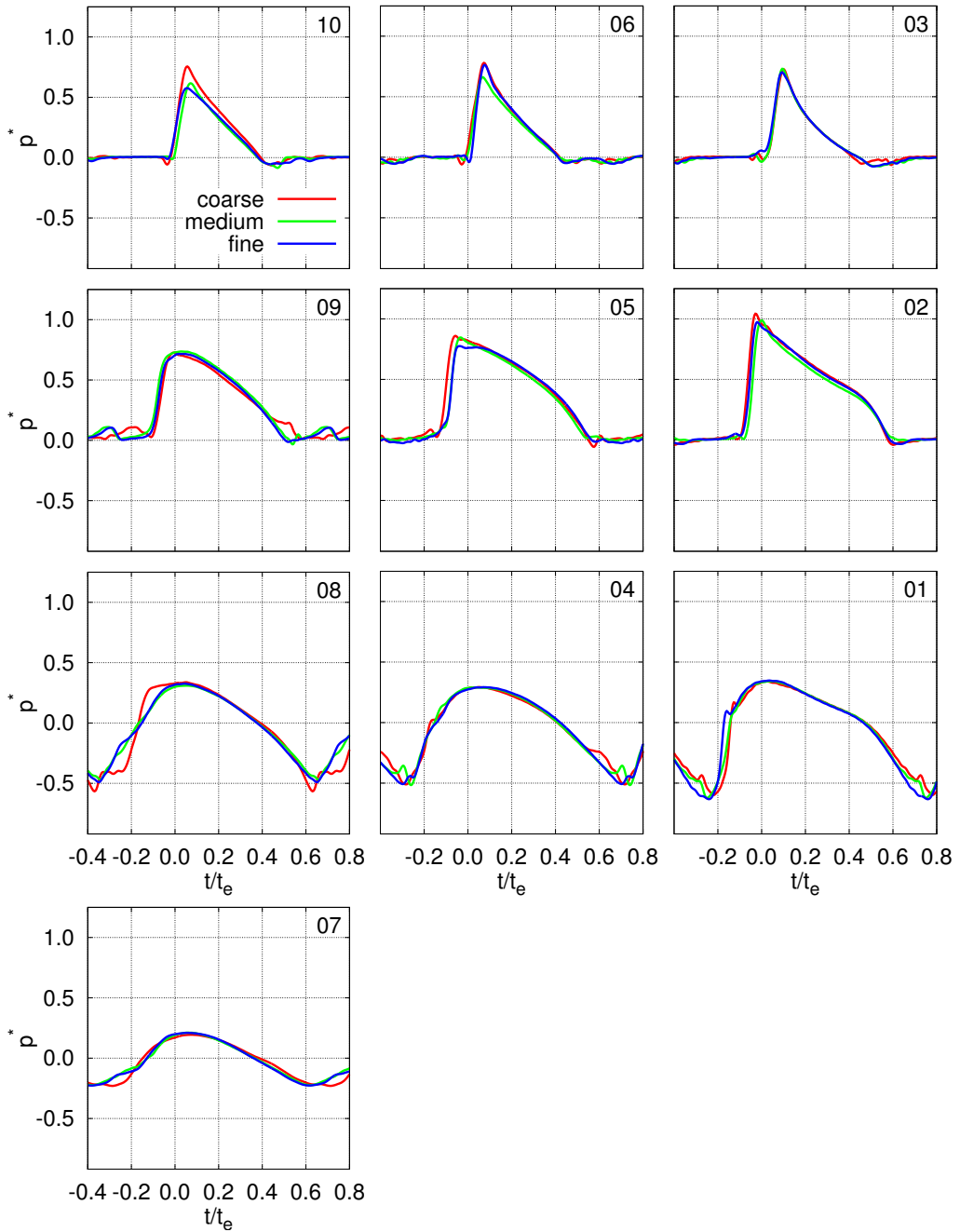


Figure 5.5. Computed pressure histories with 20 iterations. (Hänninen et al., 2014)

5.1.3 Vertical force at stations

This section addresses both the time histories of the vertical forces at stations and the distribution of their second harmonic component.

First, the effect of the resolution on the time histories of the vertical forces at the stations is studied using six examples. Both the unfiltered time histories and the low-pass filtered time histories with the zeroth - second harmonic components are considered.

The left-hand side of Figures 5.6-5.7 shows the effect of the resolution on the unfiltered force histories at six stations in the area of the bow. Overall, the three resolutions give similar time histories at each station. Further, the results with the fine and medium resolutions are very close to each other, while the result with the coarse resolution differs more. The largest difference between the coarse result and the other two results can be seen at the station $x/L_{ship} = 0.88$ during $0.4 < t/t_e < 0.6$.

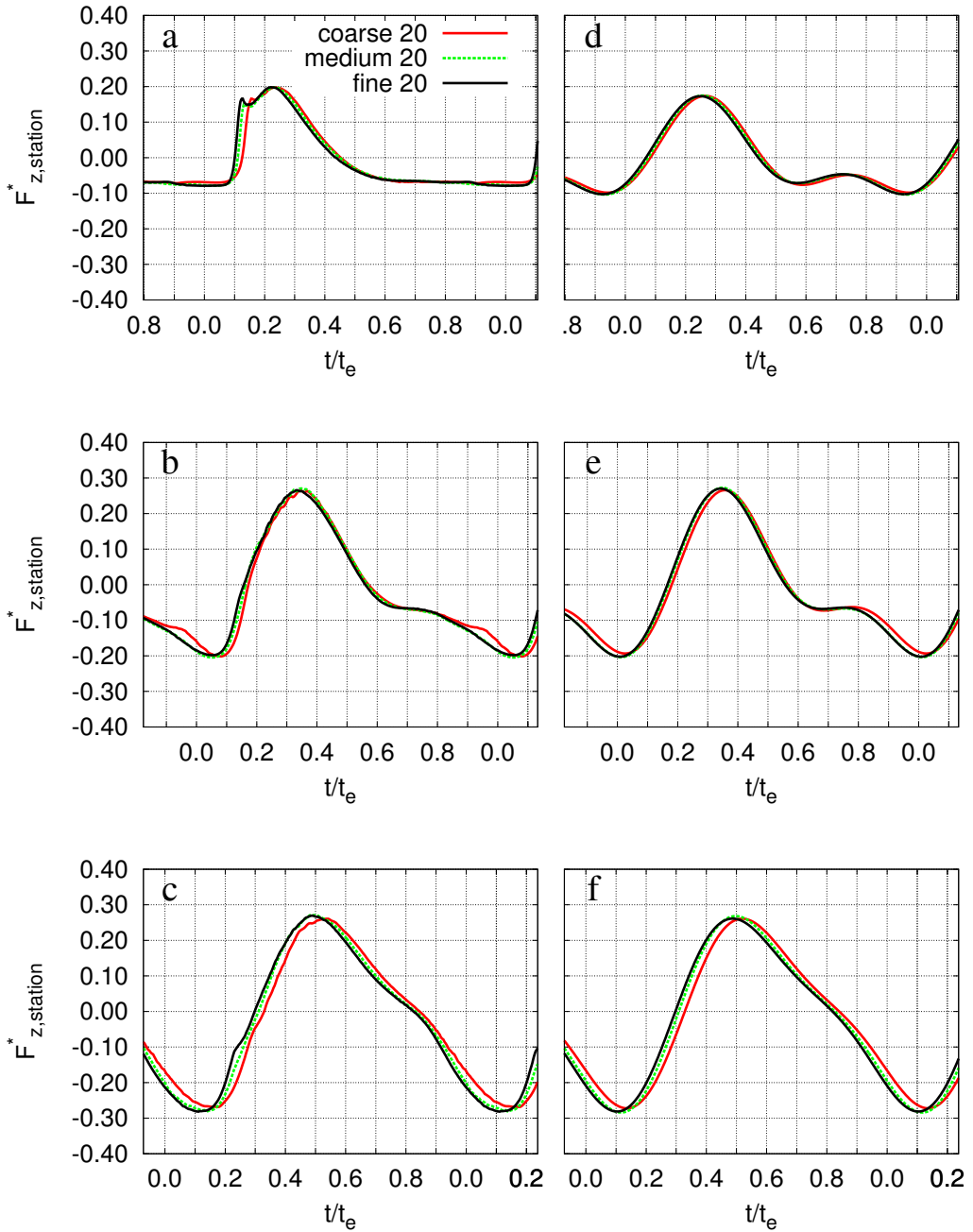


Figure 5.6. Vertical forces at stations with the three resolutions and 20 iterations. **a-c:** unfiltered time histories. **d-f:** low-pass filtered time histories with the zeroth - second harmonic components. From top to bottom: $x/L_{ship} = 0.98$, $x/L_{ship} = 0.96$ and $x/L_{ship} = 0.93$.

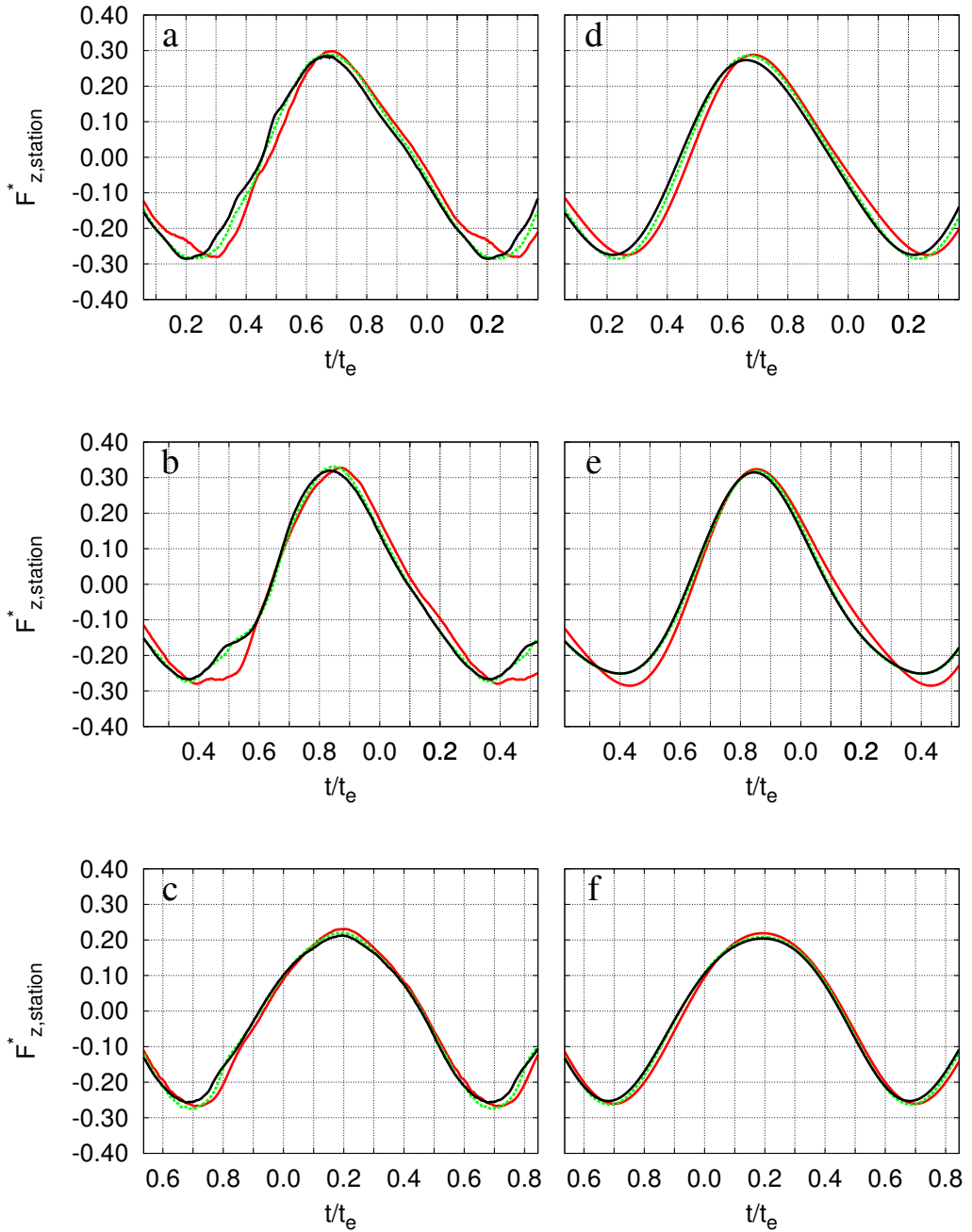


Figure 5.7. See the caption of Figure 5.6. From top to bottom: $x/L_{ship} = 0.90$, $x/L_{ship} = 0.88$ and $x/L_{ship} = 0.82$.

The right-hand side of Figures 5.6-5.7 shows the effect of the resolution on the low-pass filtered force histories with the zeroth - second harmonic components. In the case of these filtered time histories, the results with the three resolutions look even more similar than in the case of the unfiltered time histories, while the previous observations of the agreement of the result still hold.

In order to show the greatest effect which the number of iterations has on the force histories, the results at the station $x/L_{ship} = 0.88$ with both 10 and 20 iterations are given for all the resolutions in Figure 5.8. At this station, the number of iterations slightly affects the unfiltered time histories at all three resolutions during the time span $0.4 < t/t_e < 0.6$, when the coarse results differ most from the fine and medium results. Nevertheless, the effect of the number of iterations seems to be minor with all the resolutions.

The end part of this section addresses the distributions of the second harmonic vertical force at the stations.

Figure 5.9 gives the distribution of the second harmonic amplitude of the vertical force with the three resolutions with 20 iterations. The results with the fine and medium resolutions are similar from the practical point of view. The result with the coarse resolution is somewhat different around $x/L_{ship} \approx 0.88$ and $x/L_{ship} \approx 0.77$. At a general level, the distributions behave similarly with all three resolutions. Further, the results in this figure show that the importance of the loading is minor behind $x/L_{ship} \approx 0.65$. Therefore, only the results in front of that location are presented below.

In order to confirm the reliability of the distribution in Figure 5.9, the effect of the number of iterations on those results is checked for each resolution. Figure 5.10 shows that the effect of the number of iterations is minor. The most distinct effect can be seen around $x/L_{ship} \approx 0.87$ in the case of the coarse resolution. In all, increasing the number of iterations from 10 to 20 does not change the conclusions on the behaviour of the distributions in Figure 5.9.

Figures 5.11-5.12 give the respective results on the phase of the second harmonic vertical force. The conclusion is that the effect of the number of iterations is minor for the distribution of the second harmonic phase too.

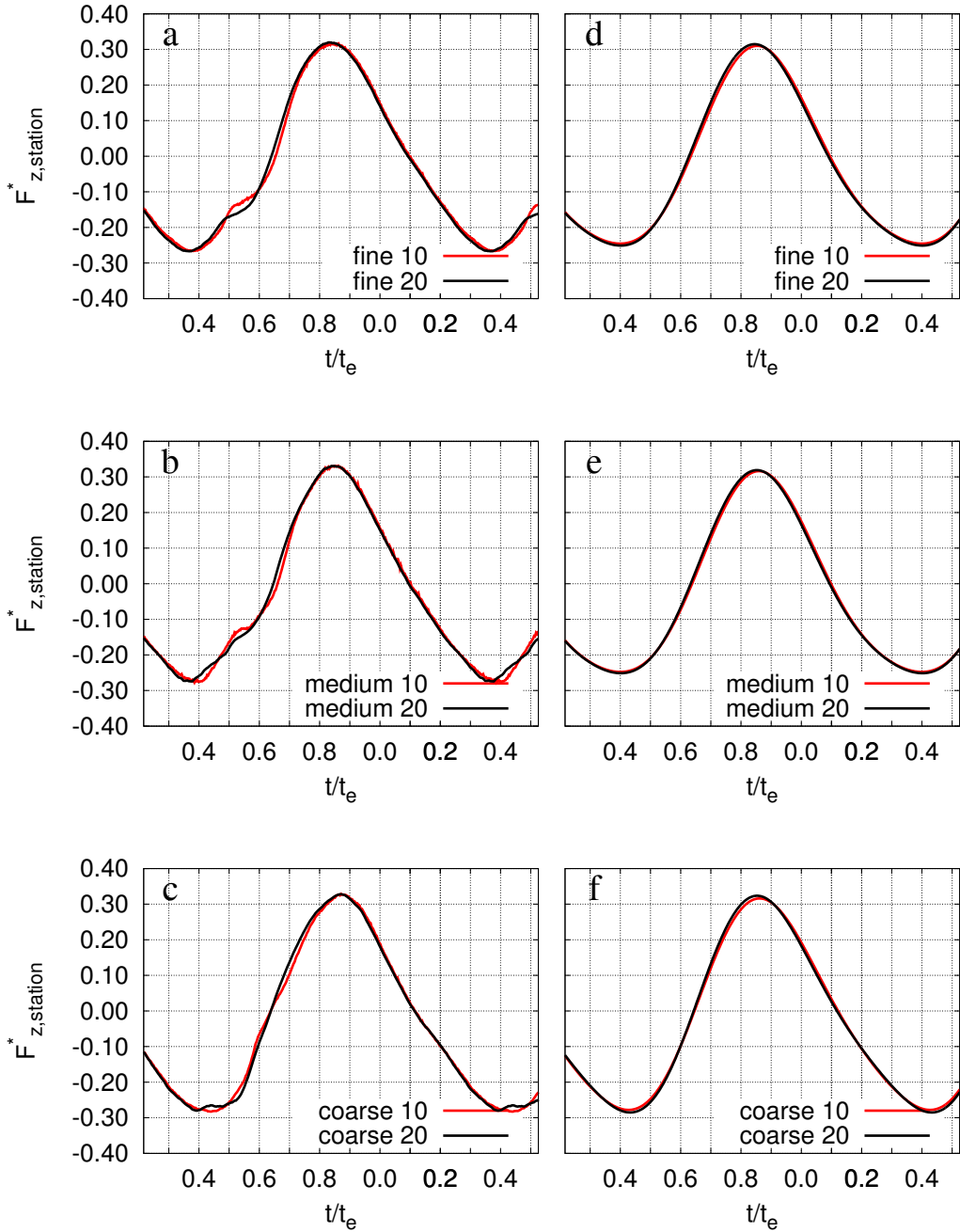


Figure 5.8. Vertical forces at $x/L_{ship} = 0.88$. The effect of the number of iterations. **a-c:** unfiltered time histories. **d-f:** low-pass filtered time histories with the zeroth - second harmonic components. From top to bottom: fine, medium, and coarse.

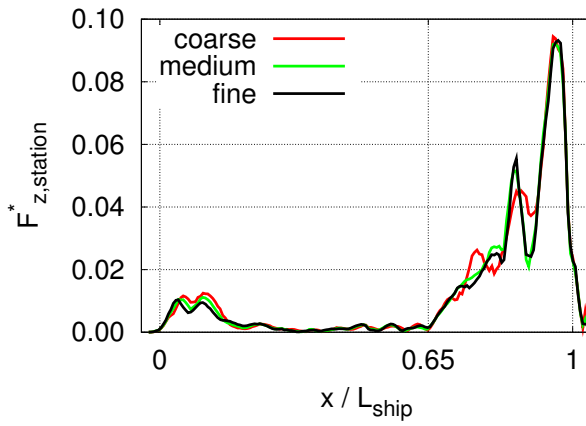


Figure 5.9. Distributions of the second harmonic amplitude of the vertical forces. The three resolutions with 20 iterations.

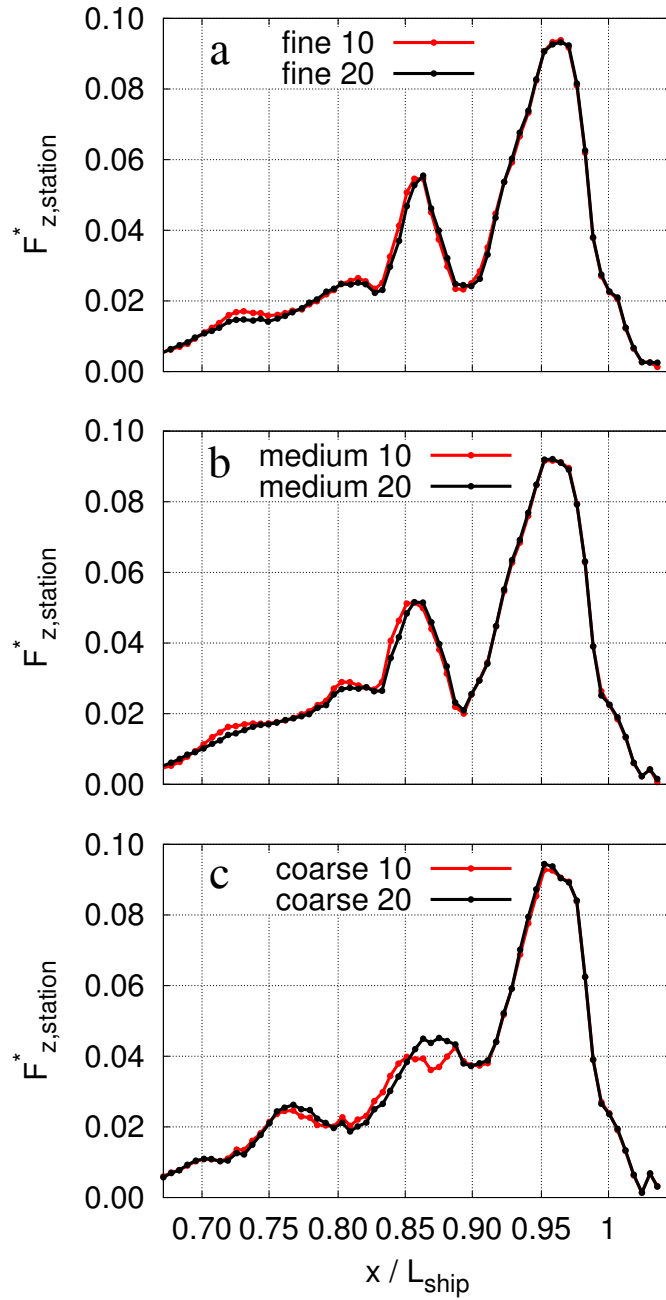


Figure 5.10. Distributions of the second harmonic amplitude of the vertical forces. 10 and 20 iterations. **a** fine, **b** medium, **c** coarse.

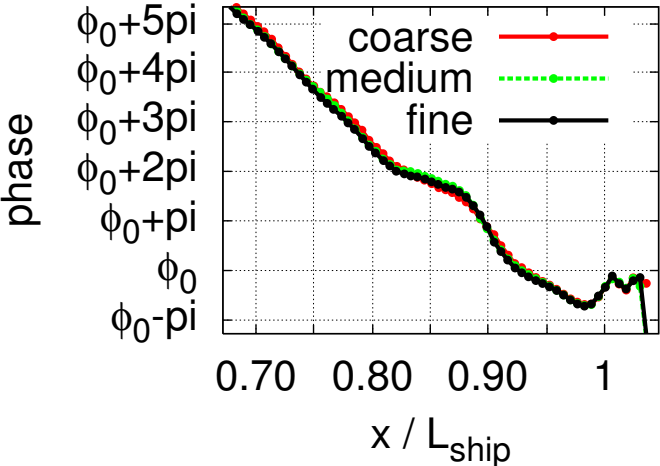


Figure 5.11. Distributions of the second harmonic phase of the vertical forces. The three resolutions with 20 iterations.

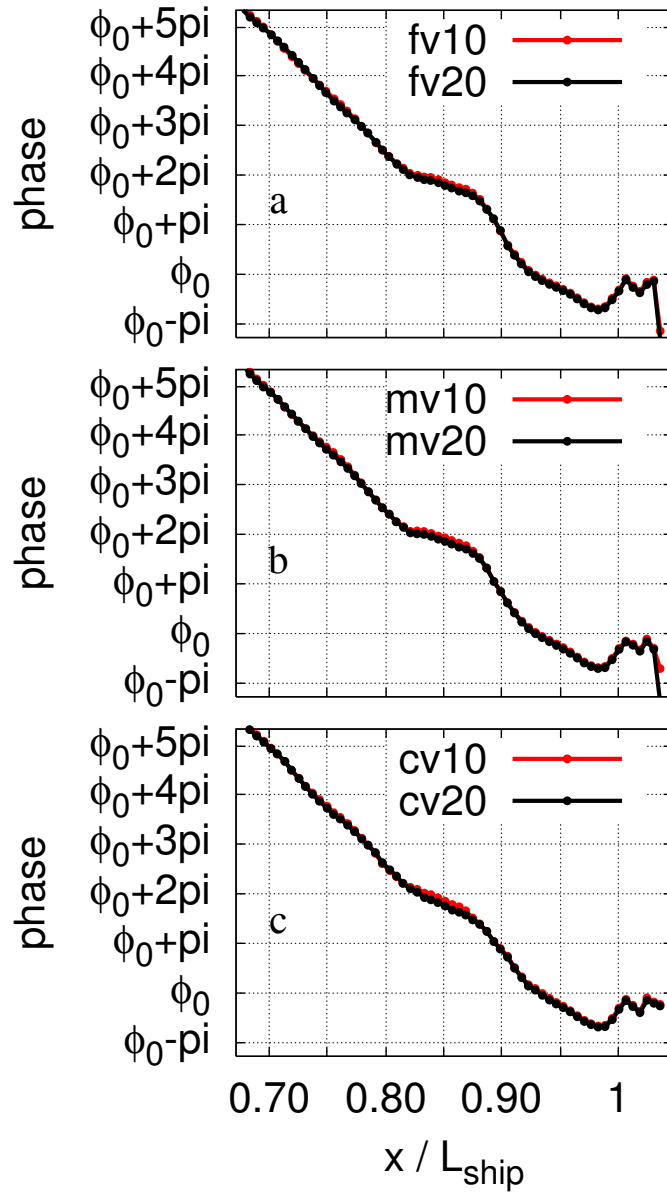


Figure 5.12. Distributions of the second harmonic phase of the vertical forces. 10 and 20 iterations. From top to bottom: fine, medium, and coarse.

5.2 Validation data (measured data)

The validation data are presented in this section. Section 5.2.1 gives the results relating to the wave conditions in the model tests and Section 5.2.2 the results relating to the pressure histories.

5.2.1 Wave conditions

First, this subsection addresses the properties of the freely propagating waves by giving statistical data and the time histories of the waves that were encountered. Second, it gives the results of the heave and pitch motions of the ship.

The model test data for the analysis were chosen according to the criterion of the wave height being within roughly $\pm 10\%$ from the target value. This results in 63 wave encounters. The statistical data of these selected encounters are given in Table 5.1 They show that the encounter periods are almost constant and slightly larger than the target value. The wave height varies notably but is very close to the target value on average.

Table 5.1. Statistical information on the wave data.

	Average / Target value	Standard deviation / Average
Encounter Period	1.03	0.02
Wave height	1.00	0.06

Figure 5.13 illustrates the time histories of the freely propagating waves that were encountered. The time histories of all the selected waves are given in one figure on top of each other in order to show the variation in the wave characteristics between different encounters. In general, the different waves look similar within a certain range of variation that relates to the different wave heights and encounter periods. The time histories of all the selected encounters are given separately in Appendix E.

The heave and pitch motions are negligible. The related data do not show any periodic variation in the heave or the pitch. Therefore, the order of magnitude of the ship motions is represented by the standard deviations of the time histories of the heave and pitch motions in Table 5.2.

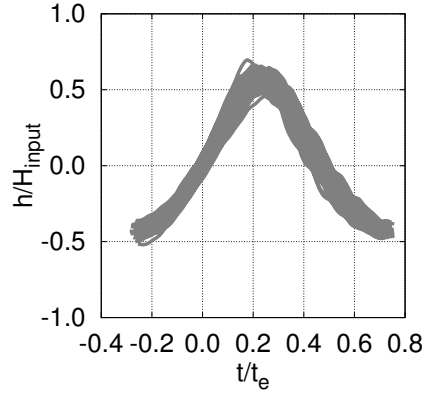


Figure 5.13. Signals of the selected waves encountered in the model tests.

Table 5.2. Standard deviations of the time histories of the ship motions

	Absolute value	Divided by L_{ship}
Heave at $x/L_{ship}=1.0$	0.2 mm	0.003%
Heave at $x/L_{ship}=0.0$	0.4 mm	0.006%
Pitch	< 0.004deg	

5.2.2 Local pressure histories

The subfigures in Figure 5.14 give all the measured pressure signals on top of each other for each sensor. In most of the cases, there are 63 signals per sensor. Sensor 03 is an exception, with 44 encounters, and Sensor 04 another one, with 57 encounters. These results give an overall idea of the pressure behaviour, even if the ranges of variation of the results are large.

Below, the behaviour of the local pressures is analysed using the signals of distinct encounters at each station. The analysis utilises the classification of the pressures described in Section 4.3. The focus is on three aspects of the behaviour of the signals of the representative encounters. One is the difference in the rise time of the pressure histories between the three stations. Another is the behaviour of the rising and falling parts of the pressure signal at each sensor. The third is the phase difference between the pressure signals at different depths of a single station. Further, the phase difference between the pressure signals and the wave is pointed out. Appendix F gives all the results at each station using the classification presented in Section 4.3.

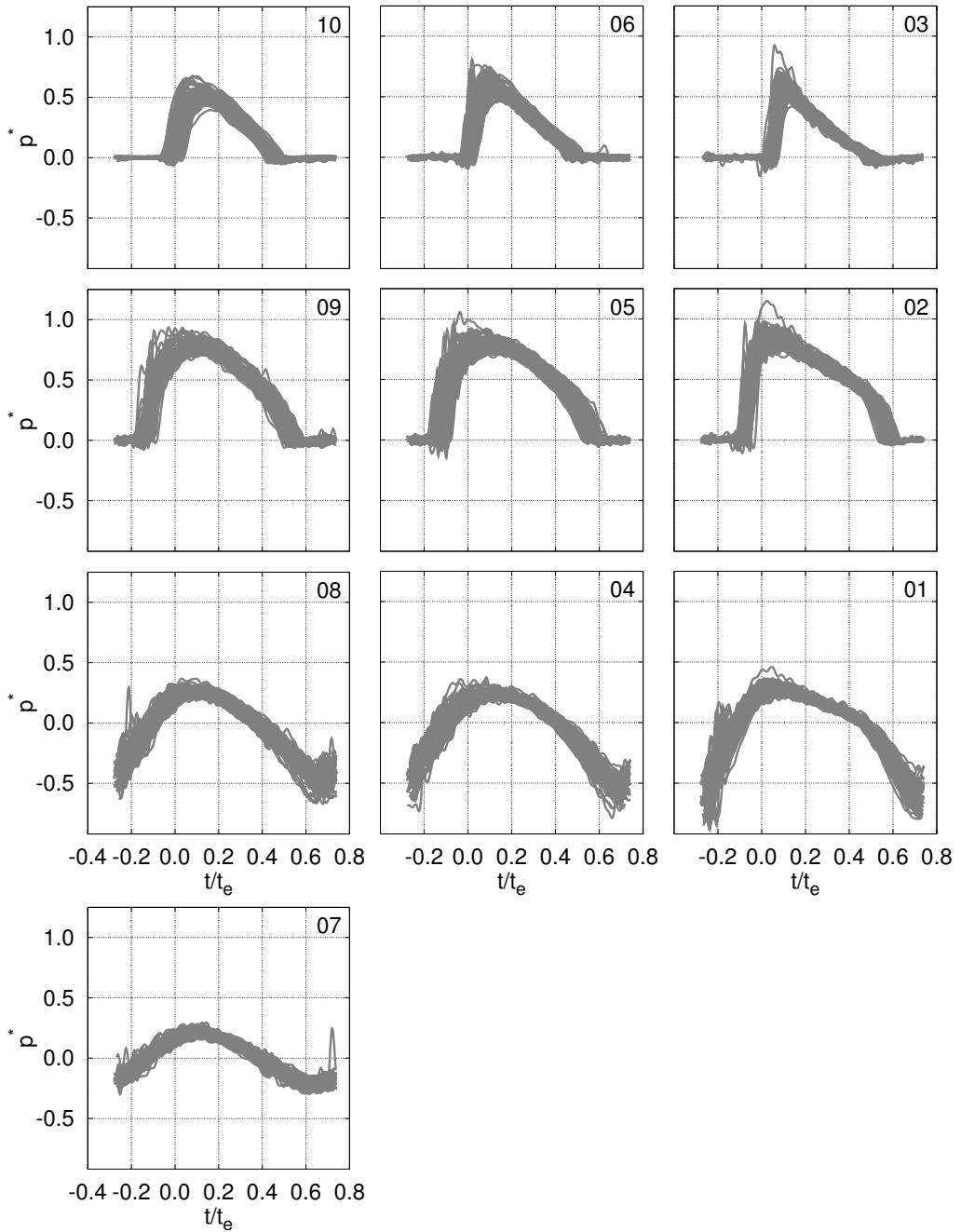


Figure 5.14. All pressure signals at the ten pressure sensors

Station at $x/L_{ship} = 0.93$ (foremost)

In the case of the foremost station, most of the encounters (51/63) belong in the fast rise time category. The numbers of encounters in the medium and slow rise time categories are 11/63 and 1/63 respectively. Thus, a clear majority of the results at this station has the so-called fast rise time and the results in that category are the most important.

Encounters 33, 34, and 4 in Figure 5.15 show the typical behaviour of the pressures at this station. In general, the changes in the pressure level happen nearly linearly at each sensor. At the two uppermost sensors, 03 and 02, the pressure rises linearly from the zero level to the maximum value like a fast impact. At the lowermost sensor, 01, the pressure rises linearly too but more slowly, especially in the case of Encounters 34 and 4. At the uppermost sensor, 03, the pressure falls linearly with a single slope. At the other sensors, 02 and 01, a rather linear fall occurs with two distinct slopes, first more slowly and then faster.

The phase difference between the signals at different depths is such that the rise at a sensor occurs after the rise at the sensor below has reached its maximum value. The first part of the fall of the pressure ends at different sensors at roughly the same time. The phase difference from the wave is such that the pressure at Sensor 02 starts rising slightly before the free-surface passes the level of the design waterline.

Encounters 29, 48, and 8 in Figure 5.16 illustrate the extremes of the behaviour of the measured pressure signals at this station. Encounter 29 belongs in the medium rise time category and the other two in the fast rise time category.

Station at $x/L_{ship} = 0.90$ (middle)

In the case of this station, the rise time of the second uppermost row (Sensor 05) mostly belongs in the medium rise time category (33/63), but the fast rise time category is important as well (23/63). There are some examples of the slow rise time category (7/63) too. Thus, the average rise time is longer than in the case of the previous station.

Encounters 12 and 54 in Figure 5.17 show typical results at this station. They belong in the medium and fast rise time categories, respectively. In general, the pressure signals at this station are slightly smoother than the ones at the previous station. At the two uppermost sensors, 06 and 05, the main rise in the pressure occurs linearly and is followed by a shorter and slower rise to the maximum value of the signal. At the lowermost sensor,

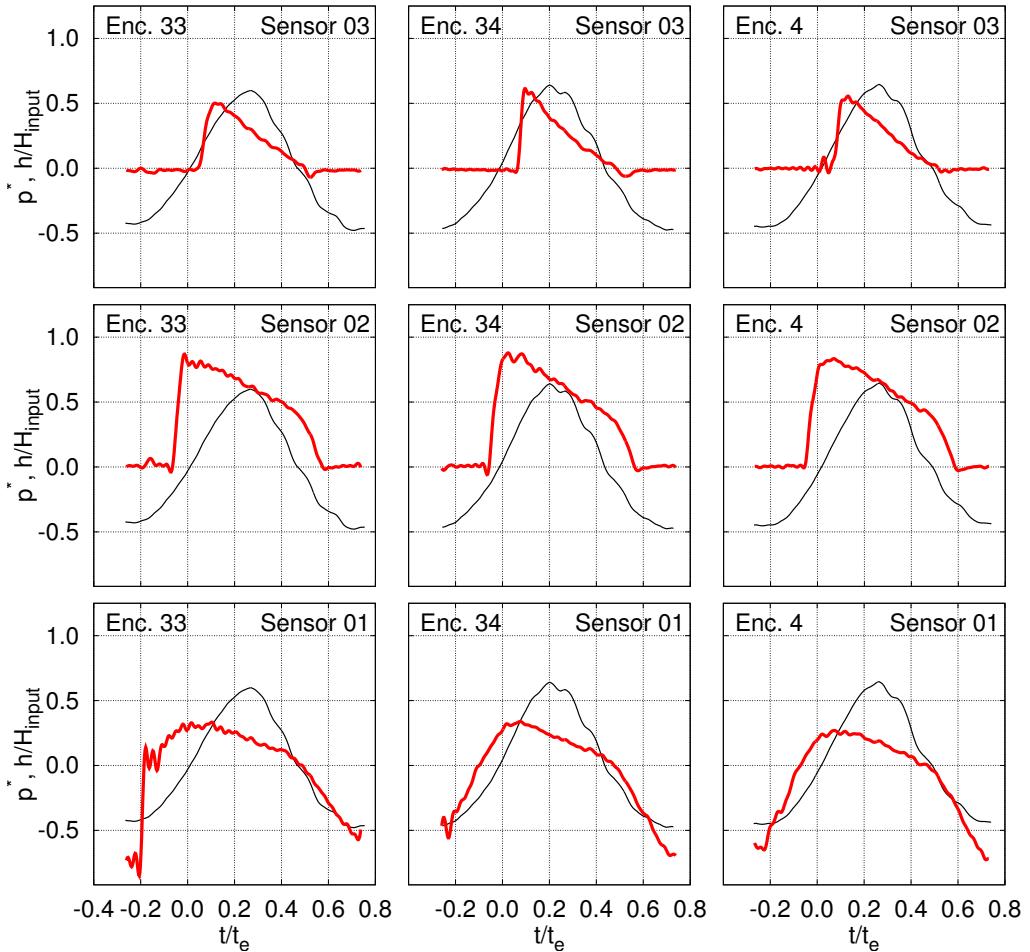


Figure 5.15. Examples (1/2) of pressure behaviour at the station $x/L_{ship} = 0.93$. From left to right: Encounters 33, 34, and 04. From top to bottom: Sensors 03, 02, and 01. Red line: pressure, black line: wave.

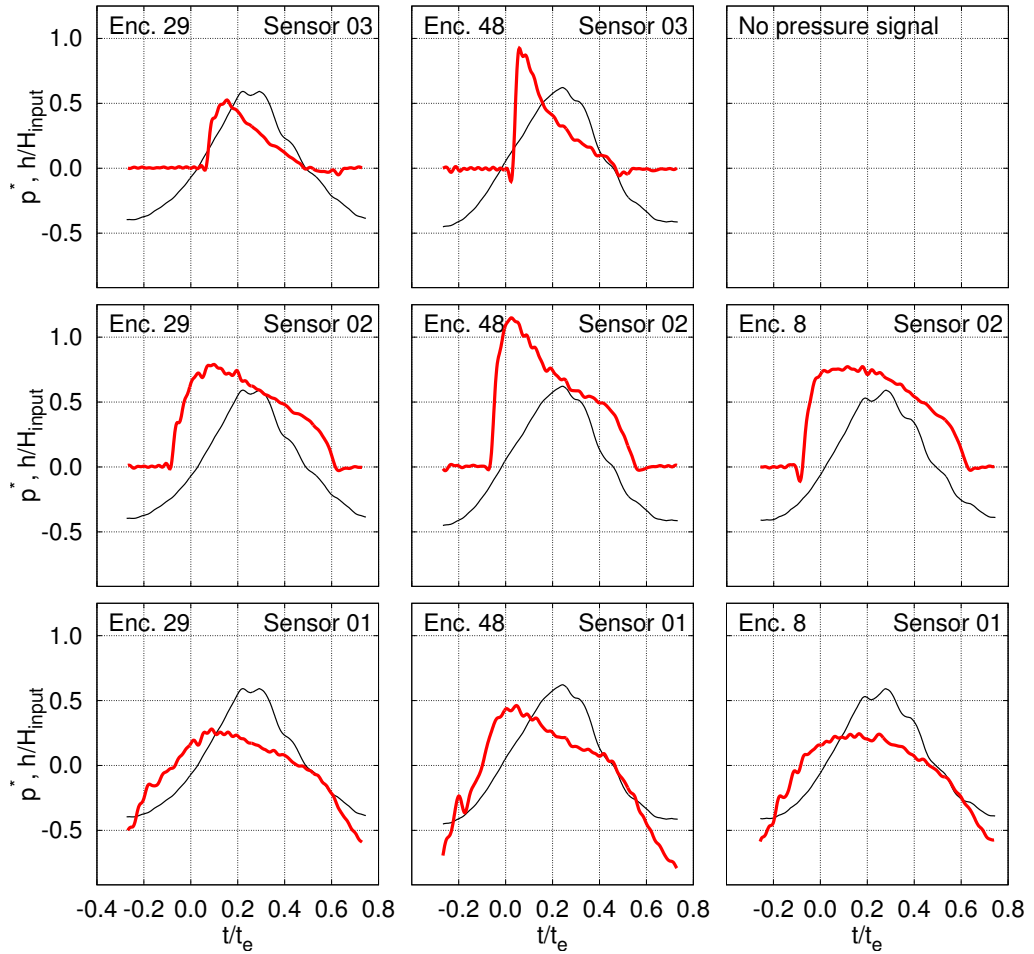


Figure 5.16. Examples (2/2) of pressure behaviour at the station $x/L_{ship} = 0.93$. From left to right: Encounters 29, 48, and 08. From top to bottom: Sensors 03, 02, and 01. Red line: pressure, black line: wave.

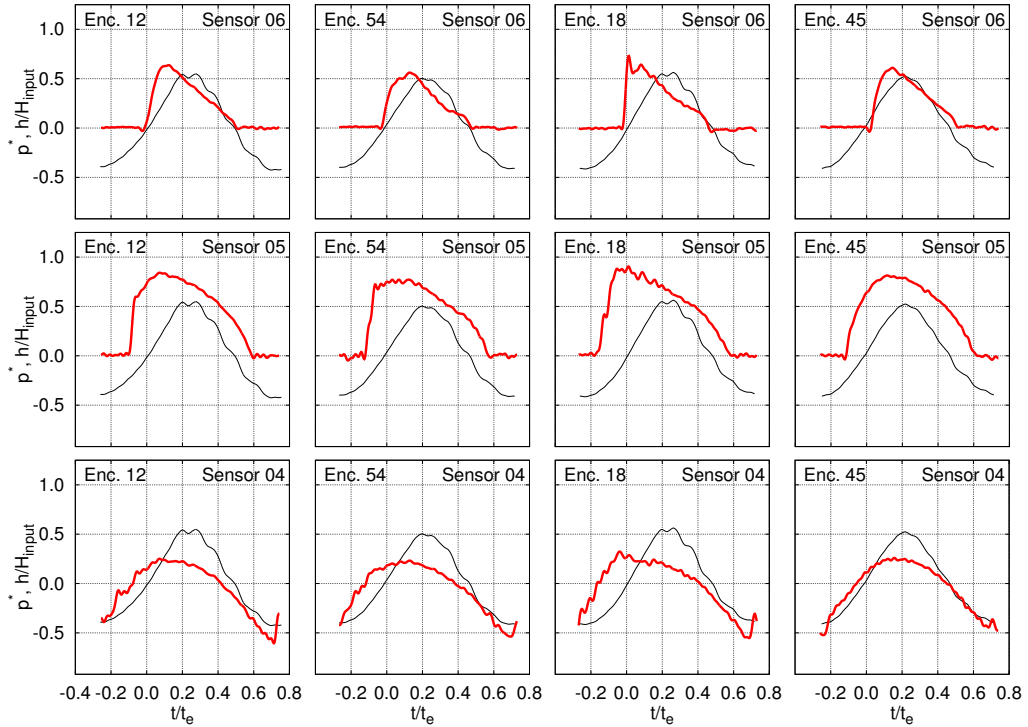


Figure 5.17. Examples of pressure behaviour at the station $x/L_{ship} = 0.90$. From left to right: Encounters 12, 54, 18, and 45. From top to bottom: Sensors 06, 05, and 04. Red line: pressure, black line: wave.

04, the rise in the signal follows a rather roundish shape. The fall of the signals is nearly linear only in the case of the uppermost sensor, 06. At the two lowermost sensors, 05 and 04, the pressure falls according to a roundish shape.

The rise in the pressure level at a sensor begins after the main rise at the lower sensor has ended. The maximum values at different sensors occur more simultaneously than at the previous station. Especially in the case of the two lowermost sensors 04 and 05, the pressure level starts to rise roughly when the front of the wave reaches the vertical location of the sensor.

Encounters 18 and 45 in Figure 5.17 show the extremes of the behaviour of the pressures at this station. They belong in the medium and slow rise time categories, respectively.

Station $x/L_{ship} = 0.88$ (rearmost)

In the case of this station, most of the encounters belong in the medium or slow rise time categories, 30/63 and 28/63 respectively. Thus, the average rise time is larger than in the case of the two previous stations.

Encounter 41 (medium rise time) in Figure 5.18 shows typical results at this station. The general impression is that the pressure signals are smoother than at the two previous stations. They all have rather roundish shapes. The signals are still somewhat asymmetric, with a shorter rise time and a longer fall time. The rise at a sensor starts after the most important rise at the sensor below has ended. The maximum values occur rather simultaneously. The phase difference from the wave is rather similar to that at the previous station.

Encounters 48 and 14 in Figure 5.18 show the extremes of the behaviour of the pressure at this station. They belong in the fast and slow rise time categories, respectively.

All three stations

To conclude Subsection 5.2.2, Figure 5.19 gives the iconic result of the behaviour of the pressure on each sensor with black lines and sketches the extreme behaviour of the pressure with grey lines. The most typical result was selected as an iconic result for the sake of clarity.

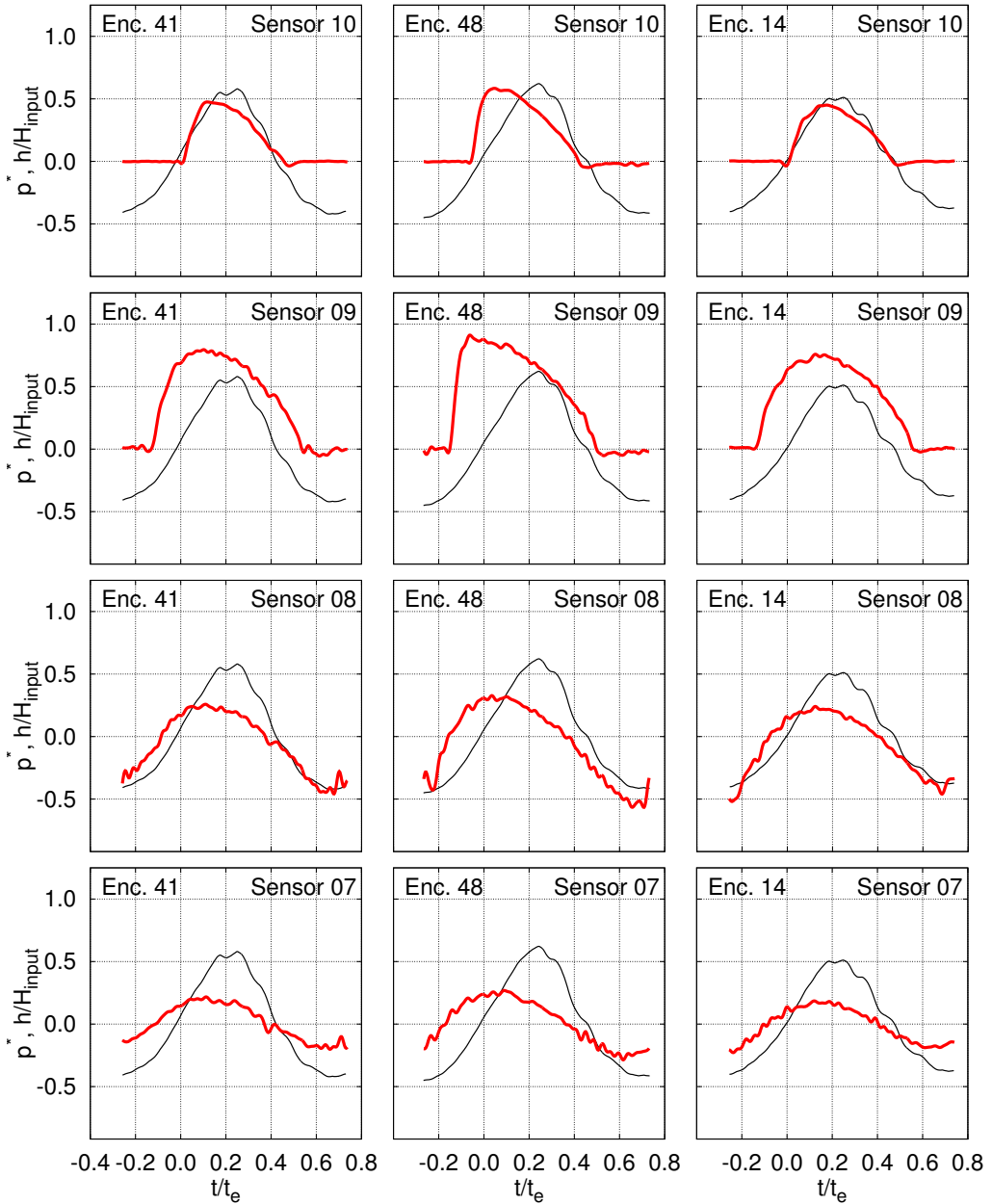


Figure 5.18. Examples of pressure behaviour at the station $x/L_{ship} = 0.88$. From left to right: Encounters 41, 48, and 14. From top to bottom: Sensors 10, 09, 08, and 07. Red line: pressure, black line: wave.

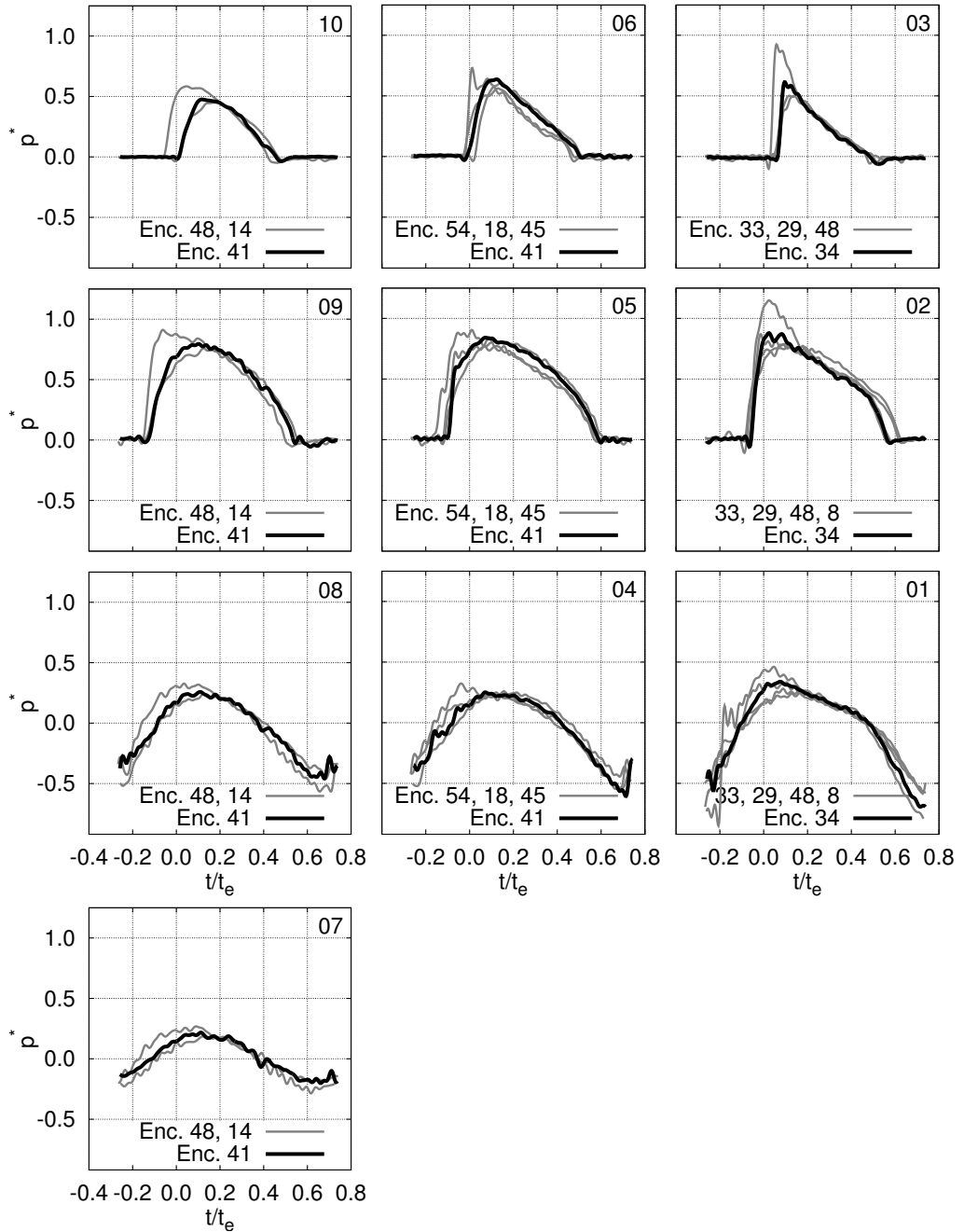


Figure 5.19. Signals at the ten pressure sensors. Black line: an iconic result. Grey lines: other results.

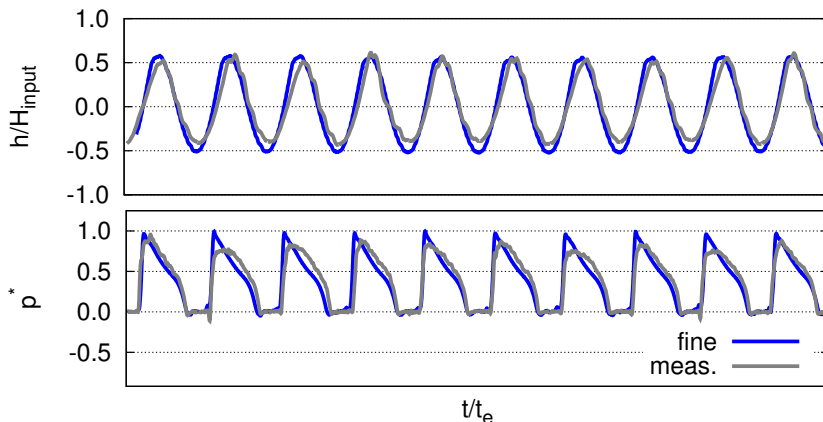


Figure 5.20. Examples of the computed (fine) and measured (meas.) time histories to be compared. Above: wave history. Below: pressure history at Sensor 02.

5.3 Comparison of the computational and experimental results

This section presents the validation of the computed results by comparing them against the experimental results. The wave conditions are addressed in Section 5.3.1 and the pressure histories in Section 5.3.2. The results in Sections 5.3.1 and 5.3.2 are presented according to the methods described in Sections 3.3 and 4.3. First, Figure 5.20 gives an example of the time histories to be compared.

5.3.1 Wave conditions

The wave conditions are observed at different locations between the computational and experimental results. The computational results are observed on the longitudinal cross-section FS (Figure 3.1) at the x -location, which corresponds to the locations of the pressure sensors on the hull. The experimental results are from the wave height meter in front of the bow. The reason why the wave conditions are observed at different locations relates to the different relative distance between the ship model and the wave generator. In the model tests, the ship model moves towards the wave generator and passes the wave field that is measured in front of the bow of the ship. In this respect, it is logical to use the information from the wave height meter in front of the bow. In the computations, the distance between the ship model and the wave boundary is fixed. In those, the wave conditions at a location which has a similar distance to the wave boundary as the area of interest on the hull are relevant.

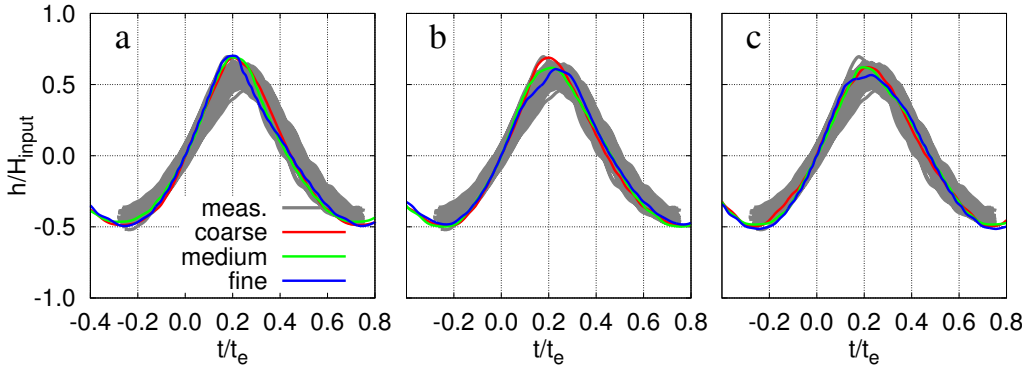


Figure 5.21. Wave histories in the computations and in the model tests. The subfigures give the computed results at different locations. **a** $x/L_{ship} = 0.88$ **b** $x/L_{ship} = 0.90$ **c** $x/L_{ship} = 0.93$. (Hänninen et al., 2014)

Figure 5.21 shows a comparison of the waves encountered in the computations and in the model tests. The shapes of the time histories in the computations and in the model tests are in reasonable agreement. Both the computational and the experimental waves are so-called Stokes waves with distinct non-linear features. Further, both of the results show that the shapes of the waves vary. Comparing the computed waves between the three x -locations shows that the wave height varies as a function of the x -location, too.

Figure 5.22 illustrates that the wave conditions in the computations and in the model tests result in a qualitative similar behaviour of the free surface in the bow area of the ship.

5.3.2 Local pressure histories

Figure 5.23 gives the computed pressure histories together with all the measured ones. It shows that the computed results are within the range of variation of the measured results.

Figure 5.24 allows a closer analysis of the characteristics of the rising and falling parts of the pressure histories and of the phase difference between the pressures at different depths at one station.

The pressure histories in the second uppermost row (Sensors 09, 05, and 02 in Figure 5.24) can be used for pointing out how the rise time between different stations behave in the computation and in the measurements. As for the starting point, the rise in the pressure level happens similarly between the computed and measured results at Sensor 02 at the foremost station $x/L_{ship} = 0.93$. The previous analysis of the measured results re-

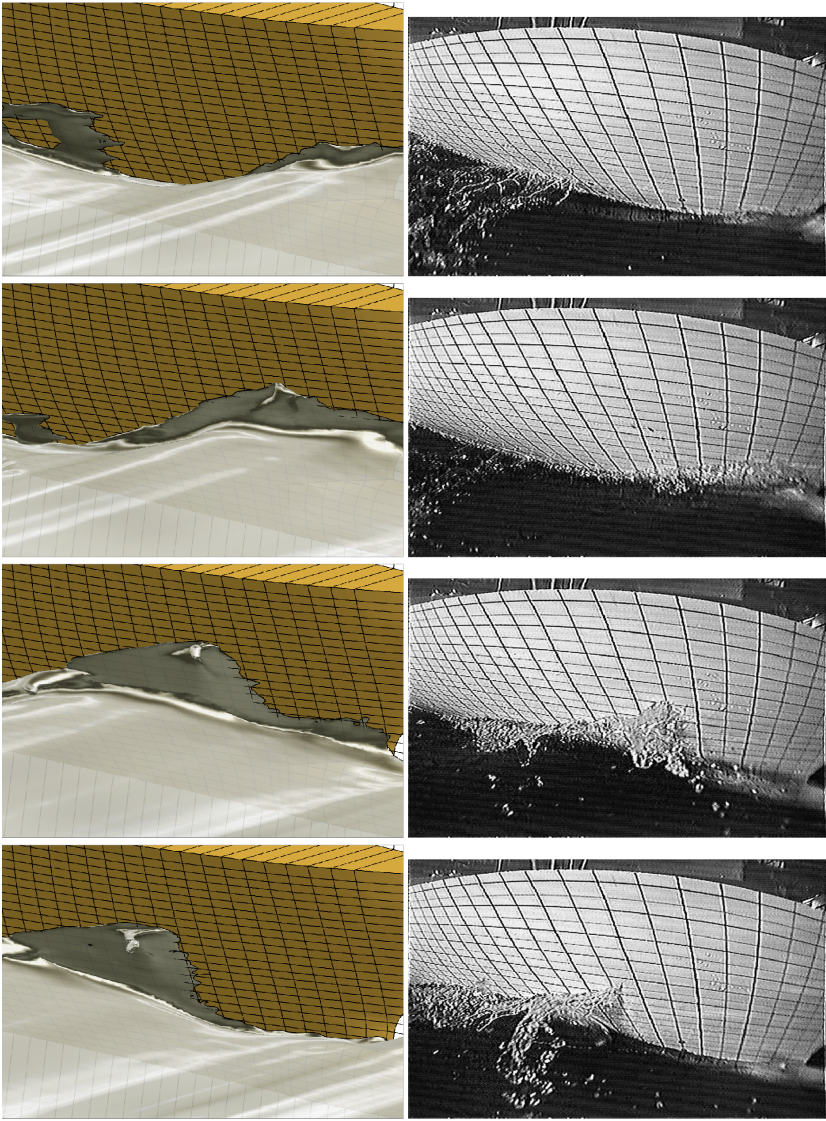


Figure 5.22. Behaviour of the free surface in the area of the bow. Left: computation with the fine resolution. Right: model tests. (Hänninen et al., 2014)

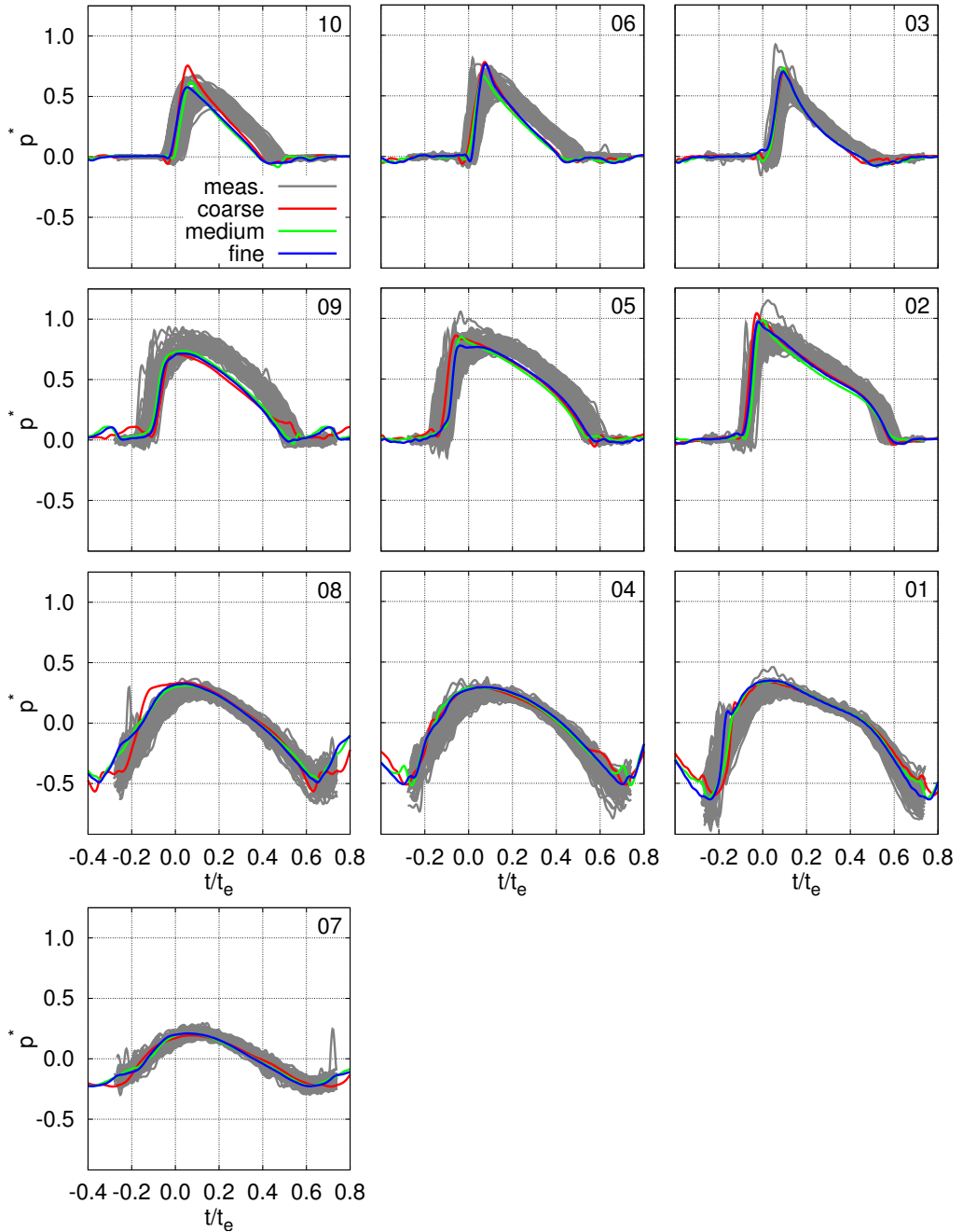


Figure 5.23. Pressure histories at the ten pressure sensors. Computed results with the coarse, medium, and fine resolutions (20 iterations). All the measured pressure signals.

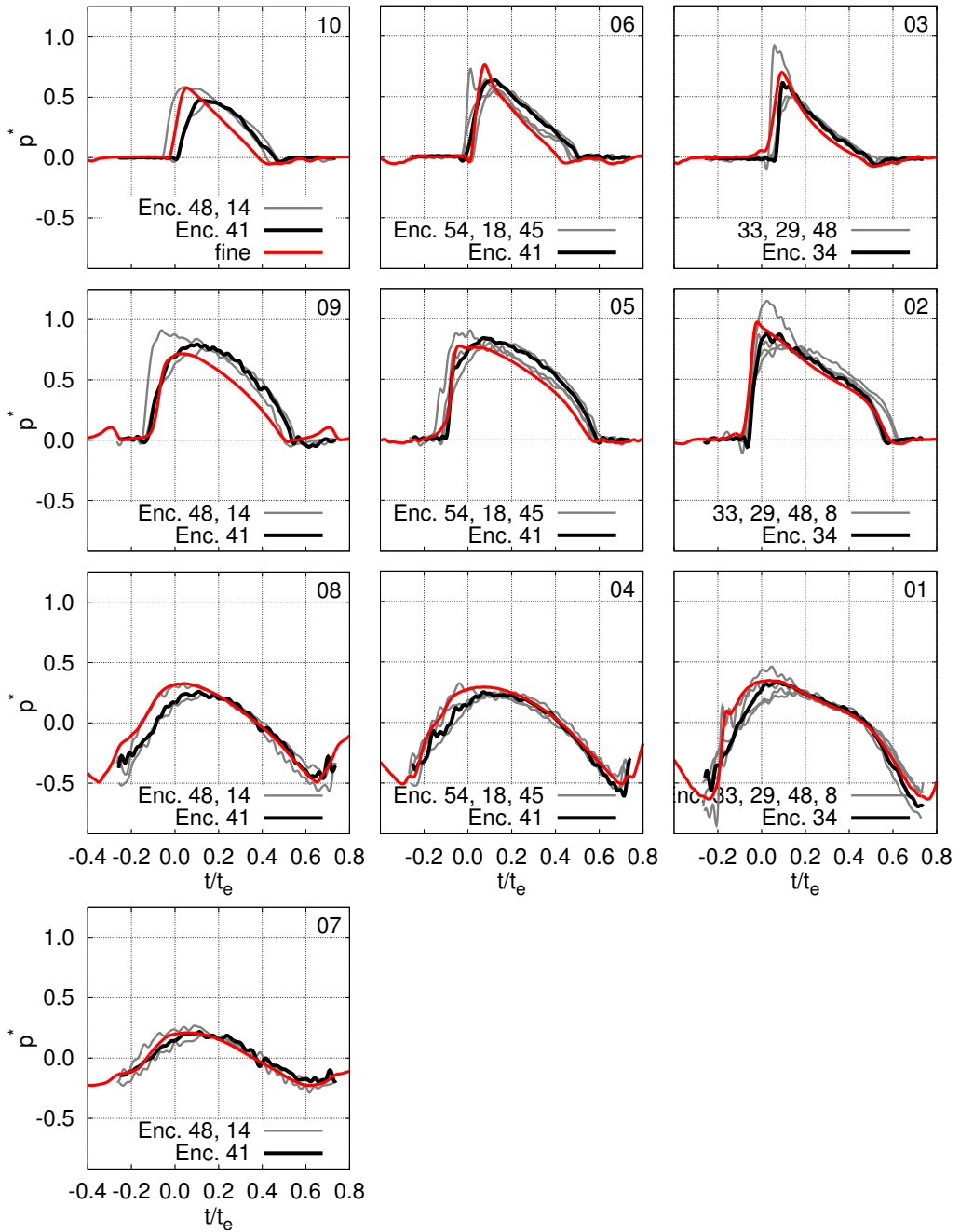


Figure 5.24. Pressure histories at the ten pressure sensors. Computed results with the fine resolution and 20 iterations (red line). Model test results: an iconic signal with black line and some other examples with grey lines (see Section 5.2.2).

vealed that the rise time increases on average when moving from the stem towards the fore shoulder of the ship; see Subsection 5.2.2. In comparison, the computed results show a slight increase in the rise time between the stations; see Figure 5.24. The increasing trend is not as distinct as in the case of the measurement when the measured results are considered in an average sense. However, as a result of the variation between the measured encounters, the individual encounters of the measured results at each station include shorter rise times, too. See Figure 5.24, for instance. From the point of view of the rise time in the second uppermost row, the computed results are most similar to the measured results with the shortest rise time at each station, which is logical as the wave height is somewhat greater in the computations.

Next, the agreement of the computed and measured pressure histories is studied at each station.

At the foremost station $x/L_{ship} = 0.93$, the computation and the measurement predict similar main characteristics of the pressure histories. Both the rise and fall of the time histories occur nearly linearly. The rises are fast and the falls of the two lowermost sensors, 01 and 02, occur with two different slopes. At the lowermost sensor, 01, the rise of the computed results is most similar to the measured results that have an impact-type rise. The phase differences between the pressures at different depths are similar between the computed and measured results.

At the middle station $x/L_{ship} = 0.90$, both the computed and measured results show that the pressure behaviour becomes smoother in comparison with the previous station. Nevertheless, both the computed and measured pressures at the two uppermost sensors, 05 and 06, have an impact-type rise, while the rise at the lowermost sensor, 04, has a more roundish shape. The falls of the computed and measured pressure histories are similar, too. In the case of the two lowermost sensors, 04 and 05, the fall has a roundish shape. In the case of the uppermost sensor, 05, the fall is nearly linear. As a further observation on the agreement of the results, the computed result at Sensor 04 most resembles the measured signals with the greatest pressure variation. On the other hand, at Sensors 05 and 06, the lengths of the computed pressure impulses are slightly shorter than those of the measured ones. The phase differences between the time histories at different depths are similar between the computed and measured results.

At the rearmost station $x/L_{ship} = 0.88$, both the computed and mea-

sured pressure histories become smoother than at the two previous stations. The computed results agree best with the measured signals whose maximum pressure value occurs rather shortly after the most important rise of the pressure level. Thus, the computed results are not as close to the symmetric time histories as the measured ones on average. It could be said that the computed results most resemble the measured results that are closest to the impact-type behaviour of the pressures. This seems to be a logical consequence of the greater wave height in the computations. As at the previous station, the computed pressures at the lowermost sensors, 07 and 08, are most similar to the measured ones that have the largest pressure variation. At the uppermost sensors, 09 and 10, the situation is the opposite, as the lengths of the computed pressure impulses seem to be slightly shorter than those of the measured ones. The phase differences between the pressure histories at different depths are similar.

In order to check the agreement of the phase difference between the wave and the pressures in the computed and measured results, the computed results in Figure 5.25 are given in a similar way to the measured ones (Figures 5.15-5.18). At each station, the phase between the pressures and the wave in the computed results is in rather good agreement with that in the measured results.

5.4 Summary

The analysis of the computed results in Section 5.1 shows that the computational results do not depend on the resolution that is selected or on the number of iterations selected at the level of detail that is needed for the analysis of the springing excitation. The comparison of the computed and measured results in Section 5.3 shows that the computation predicts the main characteristics of the local pressures and their evolution along the observed area. Further, the phase of the loads in relation to the phase of the wave is similar between the computed and measured results. Overall, the agreement between the computed and measured results is good.

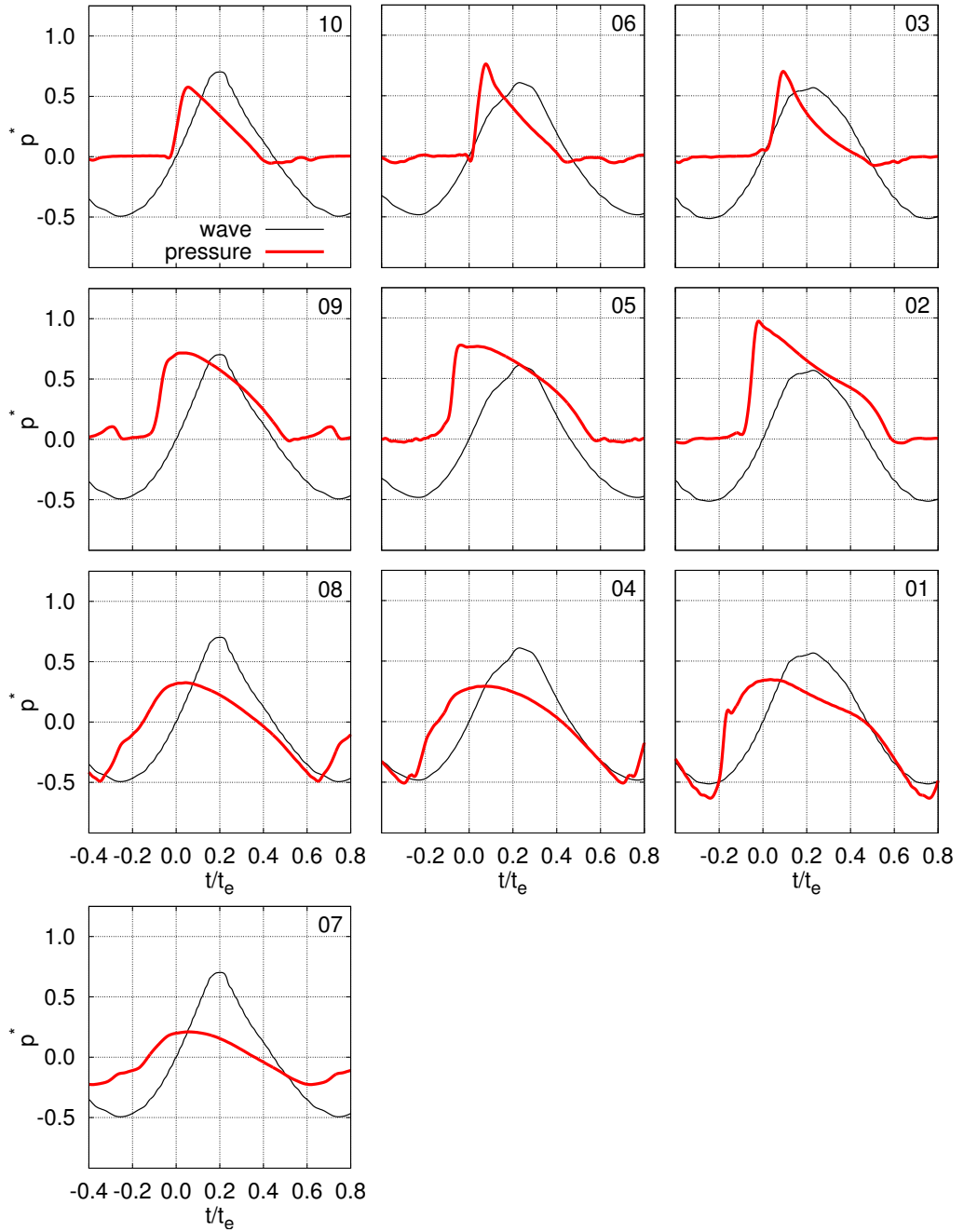


Figure 5.25. Computed pressure histories and the respective freely propagating wave. Fine resolution with 20 iterations.

6. Development of the wave loads on the hull

This chapter includes two sections. Section 6.1 gives a general description of the behaviour of the flow. Section 6.2 points out which features of the flow matter for the springing excitation.

6.1 Description of the flow behaviour

This section describes the main features of the behaviour of the flow. First, the behaviour of the approaching wave is observed at the symmetry plane in front of the bow in Subsection 6.1.1. Then the deformation of this wave is followed when it propagates along the hull in the area of the bow in Subsection 6.1.2. Next, the propagation of the related loading along the hull in the same area is described in Subsection 6.1.3. The propagation of the loading is studied in more detail at the level of the design waterline in Subsection 6.1.4. In order to gain a better understanding of the findings of Subsection 6.1.4, the analysis of the free-surface behaviour is continued in Subsection 6.1.5. The findings are summarised in Subsection 6.1.6.

6.1.1 Approach of the freely propagating wave to the bow

This subsection observes the deformation of the wave that approaches the bow at the symmetry plane of the ship. The aim is to show what the approaching wave is like just before it first encounters the hull at the stem.

The present description utilises Figures 6.1-6.2. In the figures, the profile of the approaching wave at the symmetry plane is given with a black line. In order to show how the wave actually deforms as a result of the proximity of the hull, the freely propagating wave further from the hull (turquoise line) is given too. The order of the subfigures in Figures 6.1-6.2 is the same as that of the subfigures at the respective instants in Subsec-

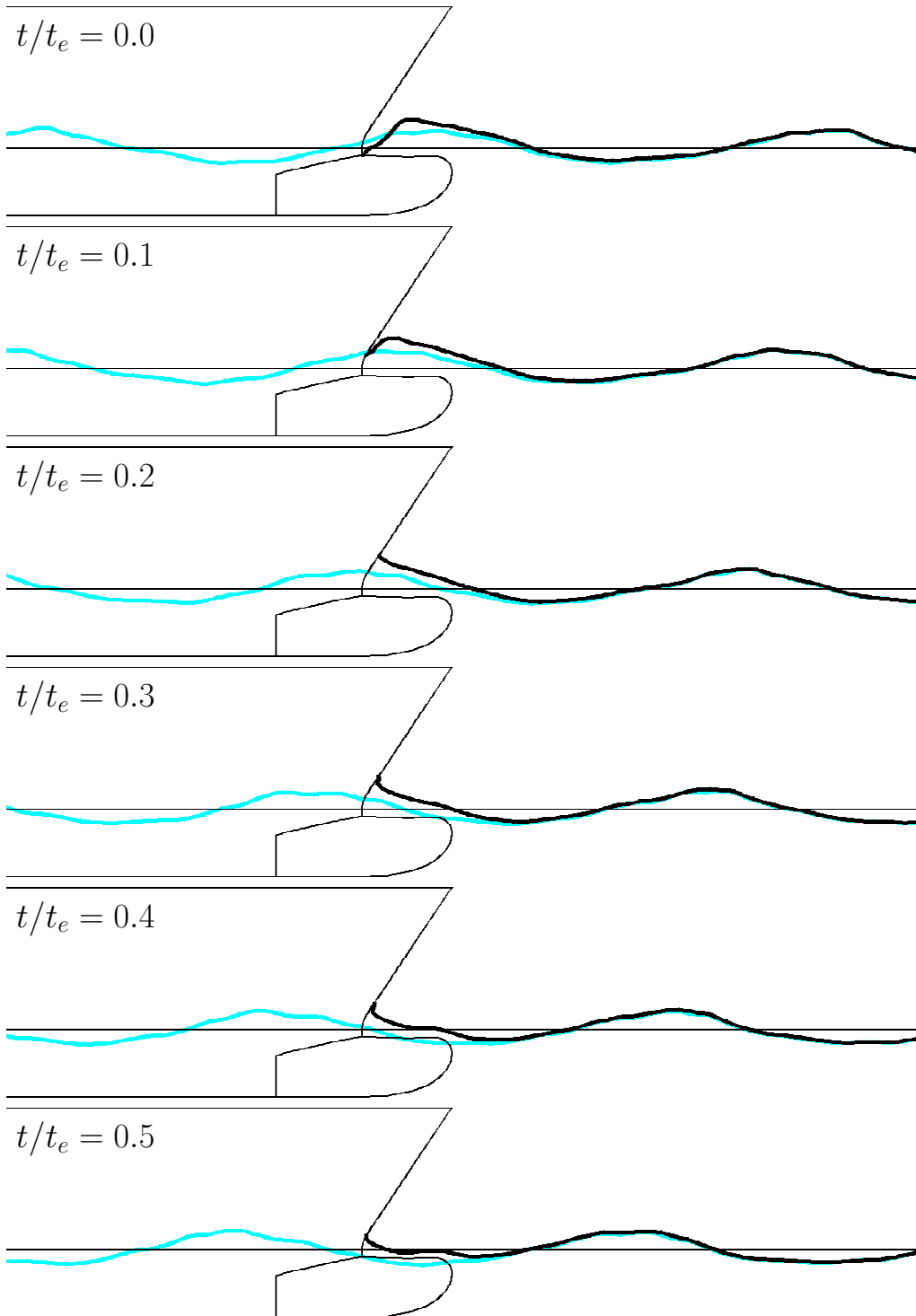


Figure 6.1. Propagation of the waves encountered in front of the bow. The waves at the symmetry plane $y/B_{ship} = 0.0$ with the black line and the waves at the cross-section $y/B_{ship} = 6.0$ with the turquoise line. $t/t_e = 0.0 - 0.5$.

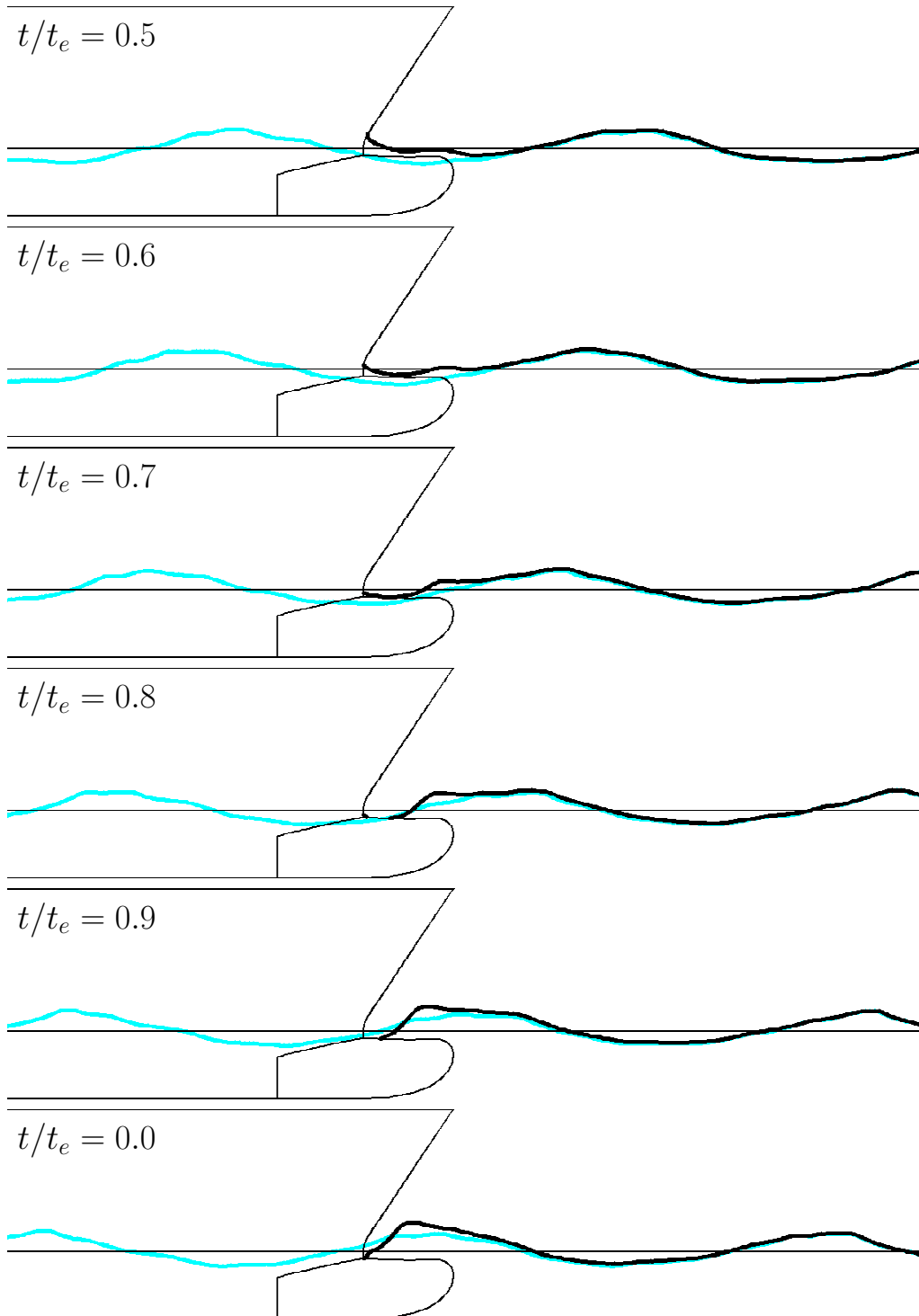


Figure 6.2. See the caption of Figure 6.1. $t/t_e = 0.5 - 0.9$ and $t/t_e = 0.0$. The uppermost subfigure is the same as the lowermost subfigure in Figure 6.1 and the lowermost subfigure is the same as the uppermost subfigure in Figure 6.1.

tions 6.1.2-6.1.5, but it does not correspond to the order of the explanation in this section.

In Figure 6.2, at $t/t_e = 0.6$, the front of the approaching wave is reaching the level of the bulb. Simultaneously, a local wave crest starts to form on the top of the front of the approaching wave at the level of the tip of the bulb. From $t/t_e = 0.7$ onwards, the whole front of the approaching wave becomes higher and steeper. In addition, the uppermost part of the bulb in front of the stem comes out of the water; see e.g. $t/t_e = 0.9$. The stem is out of the water around the level of the design waterline, too. The instant $t/t_e = 0.0$ shows the approaching wave just before its encounter with the stem. The front of the wave is much steeper than the front of the freely propagating wave. In addition to the significant deformation of the shape of the wave, the encounter occurs later than the freely propagating wave further from the hull would cross the location of the stem at the level of the design waterline.

Thus, the approaching wave deforms seriously before encountering the stem because of the bulb. The bulb acts like a shallow beach that makes the front of the approaching wave very steep.

6.1.2 Propagation of the wave on the hull

This subsection continues to follow the propagation and the deformation of the wave when it passes the area of the bow. The wave is observed on the surface of the hull.

The explanation utilises Figures 6.3-6.4, which illustrate the propagation of the wave along the surface of the hull (light grey line). In addition, the figures include the freely propagating wave further from the hull (black line) in order to facilitate keeping track of the phase of the wave. The colour contours give the distributions of the volume fraction. The figures cover ten instantaneous results during one encounter period. Because the observation area in Figures 6.3-6.4 is longer than the wave length, following the propagation of the front of one wave, for instance, over the whole observation area requires this same set of figures to be looped more than once.

At the instant $t/t_e = 0.0$ (Figure 6.3), the approaching wave is located on top of the bulb and it is about to encounter the stem. Both the stem and the surface of the hull behind it are out of the water around the level of the design waterline. After the encounter, the hull surface right behind the stem around the level of the design waterline becomes wetted ($t/t_e = 0.1$).

The front of the wave on the hull is delayed in comparison to the freely propagating wave at the level of the design waterline. When the wave continues to propagate further, the wetted area on the hull continues to expand in both the longitudinal and vertical directions ($t/t_e = 0.2$). This expansion is extensive in comparison to the change in the surface area under the freely propagating wave. As a consequence, the front of the wave on the hull reaches the phase of the freely propagating wave at the level of the design waterline. The front of the wave on the hull surface takes the shape of the buttock line, which crosses the design waterline at the same x -location as the front of the wave.

From $t/t_e = 0.2$ onwards, the front of the wave on the hull keeps roughly the same phase as the front of the freely propagating wave at the level of the design waterline. Further, the front of the wave roughly keeps following the shape of the buttock lines. The extensive expansion of the wetted surface of the hull becomes less important around the front of the wave at the level of the design waterline. Instead, a strong expansion of the wetted hull surface continues between the location of the crest of the freely propagating wave and the stem ($t/t_e = 0.3 - 0.6$). Finally, the splash (wetted surface) on the rear face of the wave becomes smaller and the hull surface right behind the stem comes out of the water again ($t/t_e = 0.6 - 0.9$).

During $t/t_e = 0.9$ and $t/t_e = 0.0 - 0.4$, the front of the wave approaches the left-hand edge of the observation area. The further the wave profile on the hull propagates along the length of the hull, the more similar it becomes to that of the freely propagating wave. Simultaneously, the splash on the rear face of the wave stays behind and becomes smaller and smaller before vanishing.

6.1.3 Propagation of the loading on the hull

This section describes the propagation of the loading on the hull surface in the area of the bow.

The piezometric pressure is used to visualise the local loading in this section. Figures 6.5-6.6 give the distributions of the loading at the same instants as were used in Figures 6.3-6.4. The colour scale of the piezometric pressure that is applied enables a general description of the pressure behaviour to be given. On the other hand, the pressure ranges covered by the red and blue colours are so large that some details become hidden.

Right after the wave has encountered the stem, the pressure level rises

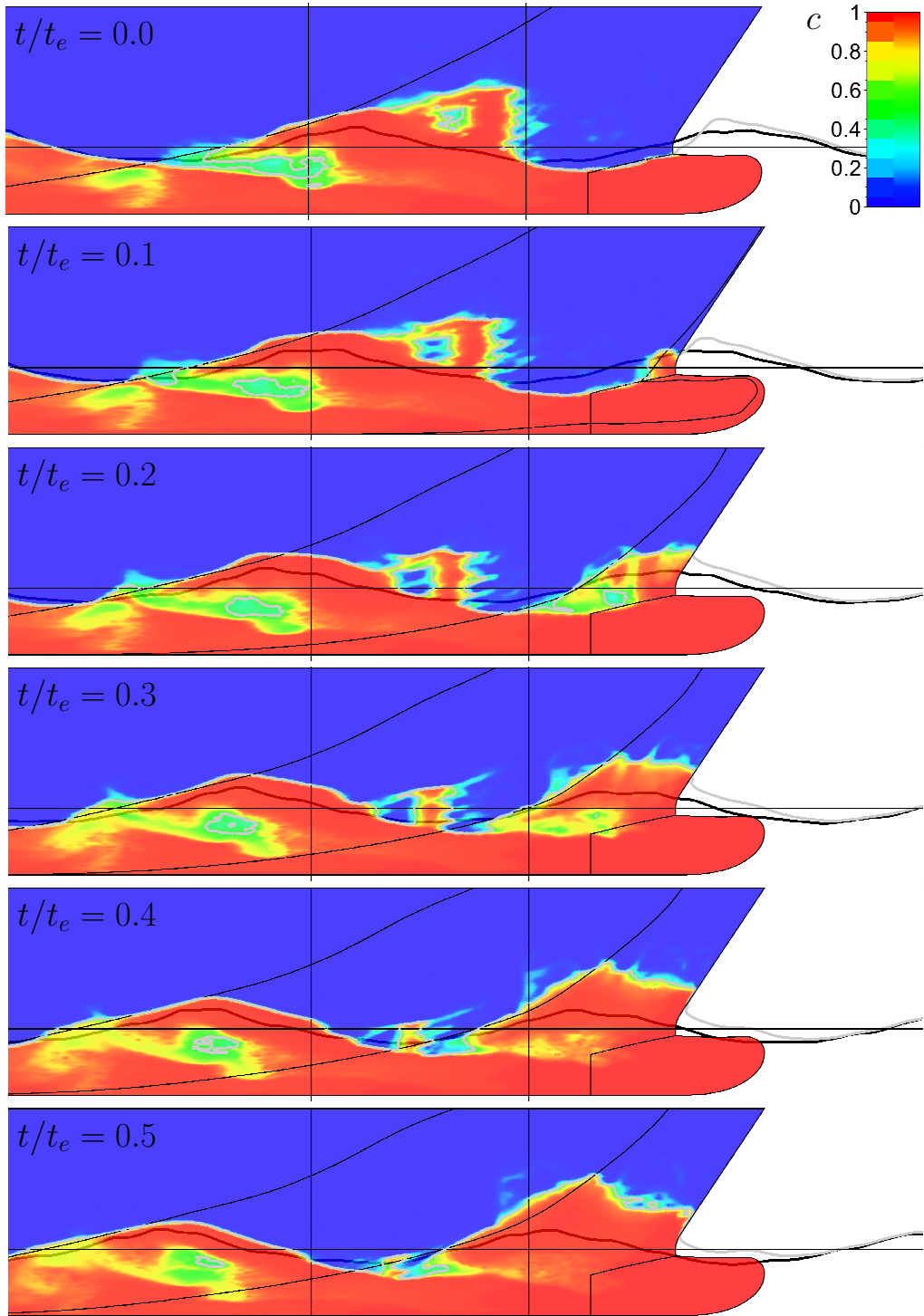


Figure 6.3. Propagation of the wave on the bow of the ship. $t/t_e = 0.0 - 0.5$. Grey line: the free surface on the hull and on the symmetry plane in front of the hull. Black line: the freely propagating wave at the cross-section $y/B_{ship} = 6.0$. Colour contours: the volume fraction c . Black horizontal line: design waterline. Black vertical lines: the local entrance angle is constant between these two x -locations. Further, buttock lines are given with black lines.

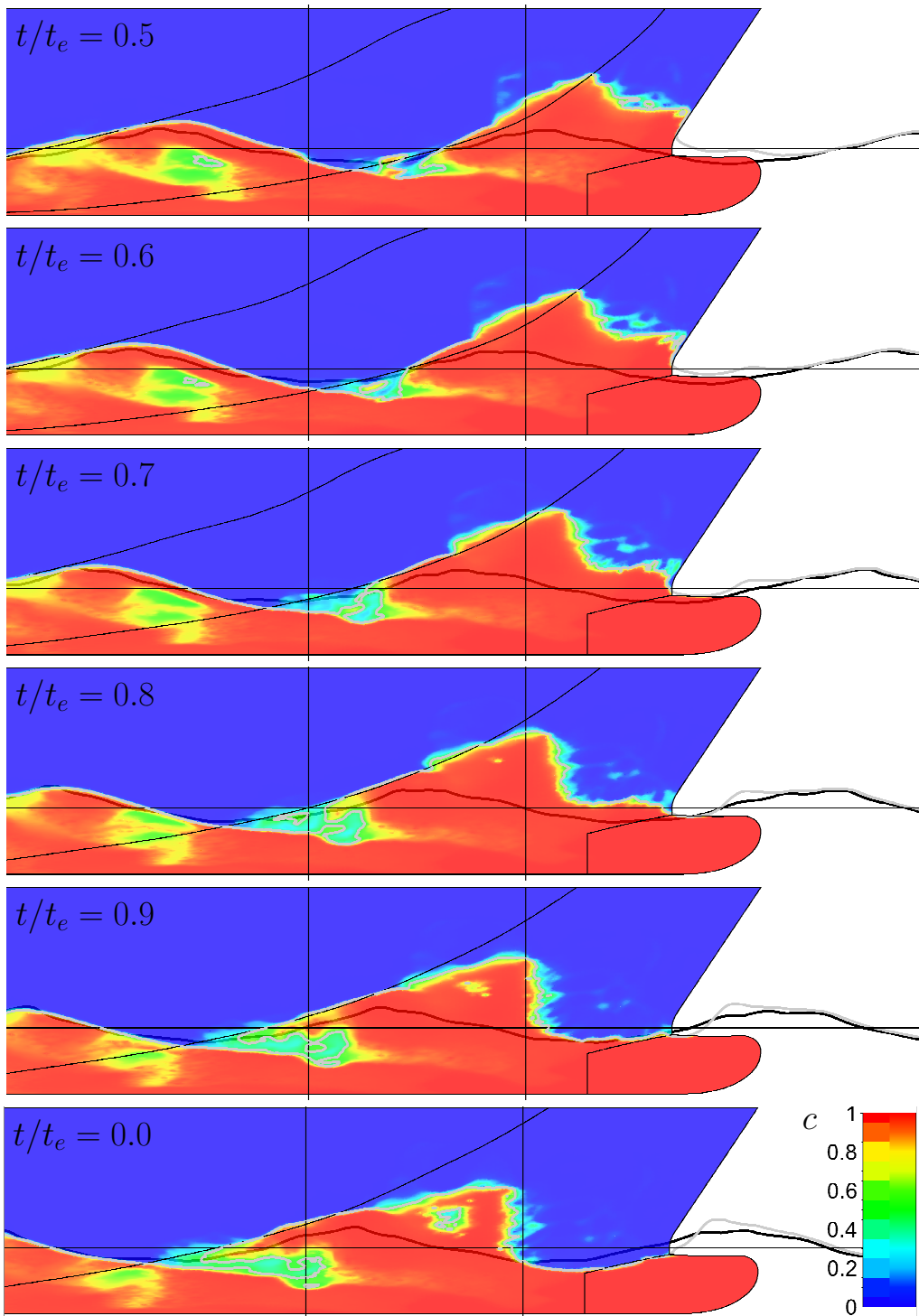


Figure 6.4. See the caption of Figure 6.3. $t/t_e = 0.5 - 0.9$ and $t/t_e = 0.0$. The uppermost subfigure is the same as the lowermost subfigure in Figure 6.3 and the lowermost subfigure is the same as the uppermost subfigure in Figure 6.3.

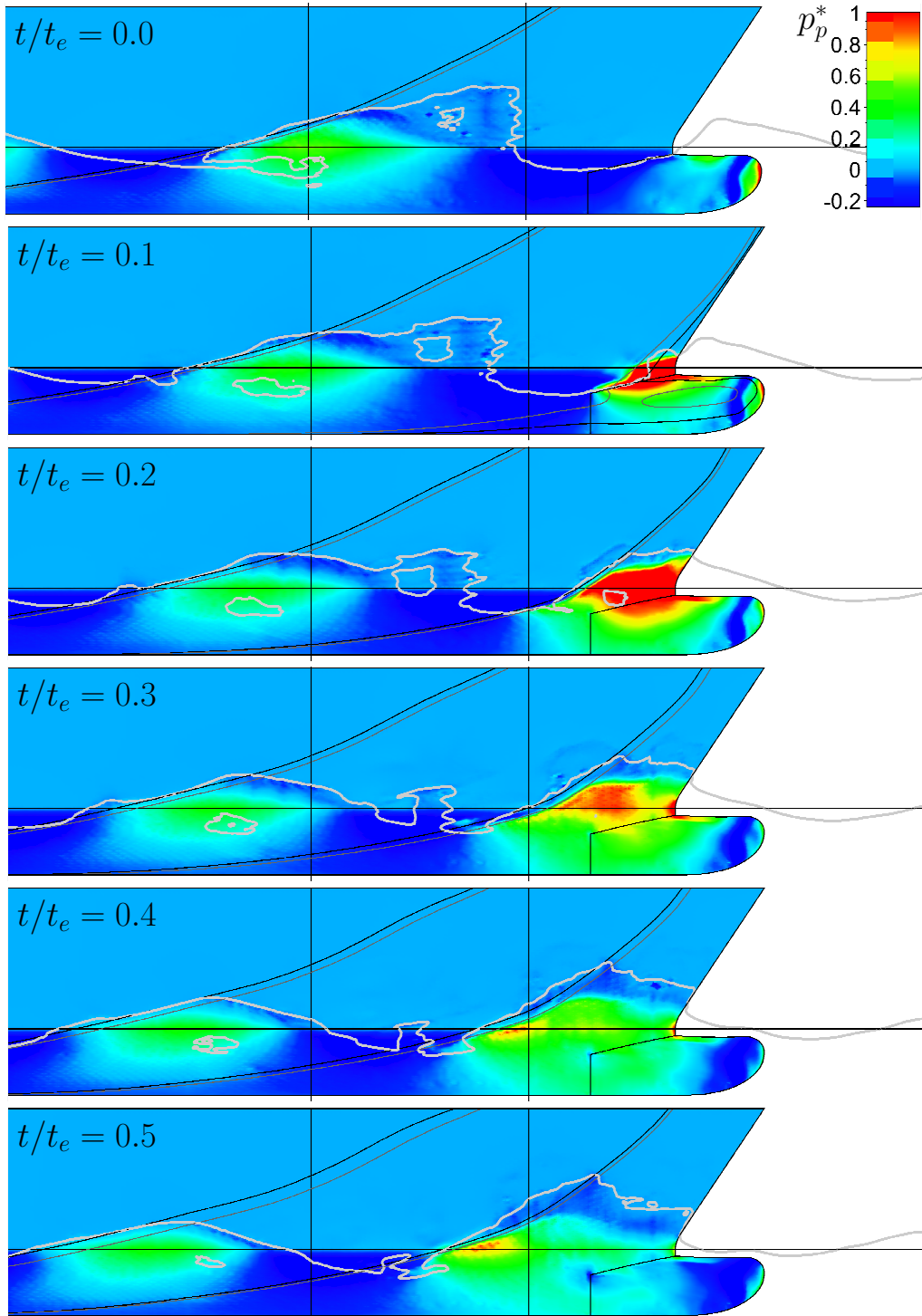


Figure 6.5. Propagation of the non-dimensional piezometric pressure p_p^* on the bow of the ship. $t/t_e = 0.0 - 0.5$. Colour contours: piezometric pressure p_p^* . Grey line: the free surface on the hull and on the symmetry plane in front of the hull. Black horizontal line: design waterline. Black vertical lines: the local entrance angle is constant between these two x -locations. The buttock lines of Figures 6.3-6.4 are given here in black and some additional buttock lines are given in dark grey.

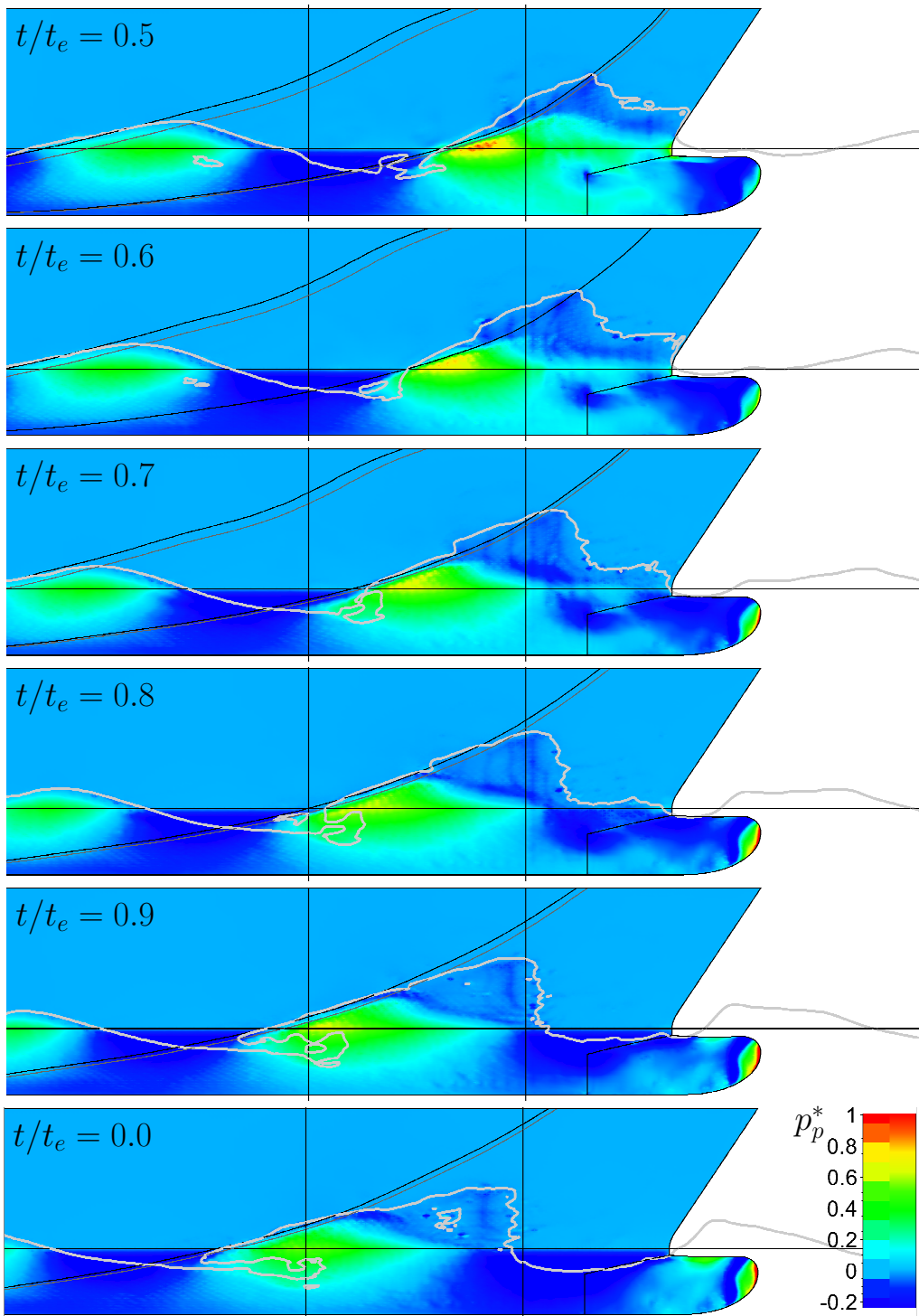


Figure 6.6. See the caption of Figure 6.5. $t/t_e = 0.5 - 0.9$ and $t/t_e = 0.0$. The uppermost subfigure is the same as the lowermost subfigure in Figure 6.5 and the lowermost subfigure is the same as the uppermost subfigure in Figure 6.5.

to a high level around the design waterline in the fore most part of the bow ($t/t_e = 0.1$). When the wave propagates a little further, the area of high pressure expands, especially in the longitudinal direction around the design waterline and slightly in the vertical direction ($t/t_e = 0.2$). This area extends in the longitudinal direction between the front of the wave at the design waterline and the stem. The front of the upper part of the area of elevated pressure follows the shape of a buttock line (dark grey), which is located slightly behind the front of the wave on the hull.

From $t/t_e = 0.3$ onwards, the area of the highest instantaneous pressure becomes smaller in size and the highest instantaneous pressure values become lower. Furthermore, the area of the highest instantaneous pressure moves further from the stem with the front of the wave. This area is located around the design waterline, behind the crossing point of the wave front and the design waterline. The front of the upper part of the area of elevated pressure follows the shape of the buttock lines.

From $t/t_e = 0.5$ onwards, it is possible to observe the pressure distribution below the total length of a wave crest (between the crossing of the front and the rear face of the free wave with the design waterline; see Figure 6.4. First, the pressure distributions below the crest of the wave are distinctly asymmetric ($t/t_e = 0.5 - 0.9$). The elevated pressure values below the front of the wave are larger than those below the rear face of the wave. Further, the vertical extent of the area of the elevated pressure (shown in green and yellow) is greater below the front than the rear face of the wave profile. The shape of the upper part of the area of elevated pressure follows the shape of the buttock lines as before. Next ($t/t_e \geq 0.0$), on the left-hand side of the figure, the elevated pressure values below the front and the rear face of the wave become similar, but the extent of the area of higher pressure is still larger below the front than the rear face of the wave.

All in all, these results show that the front of the upper part of the area of the elevated pressure follows the shape of the buttock lines.

6.1.4 Propagation of the loading at the design waterline

This subsection deepens the understanding of the evolution of the loading past the area of the bow by studying the pressure distributions more closely at the level of the design waterline.

The description of the pressure behaviour follows the distribution of the local entrance angle at the level of the design waterline. Figure 6.7 shows

that this distribution has three main parts in the area of the bow. Between $x/L_{ship} = 1.00$ and $x/L_{ship} \approx 0.96$, the entrance angle is largest with the values between $\sim 25^\circ$ and $\sim 28^\circ$. After a rapid decrease, the entrance angle is constant between $x/L_{ship} \approx 0.94$ and $x/L_{ship} \approx 0.85$ being $\sim 18^\circ$. In the third part, between $x/L_{ship} \approx 0.85$ and the fore shoulder, the entrance angle decreases linearly to zero.

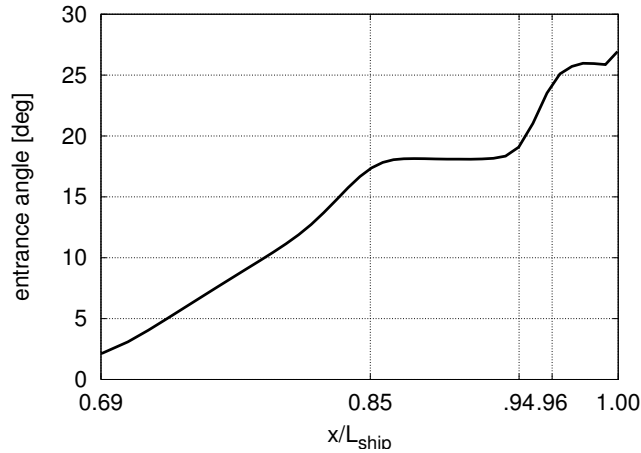


Figure 6.7. Local entrance angle at the level of the design waterline; see the definition of the local entrance angle in Subsection 3.3.7.

The description of the pressure behaviour utilises Figure 6.8, which gives the pressure distributions at the level of the design waterline. Further, Figure 6.8 shows the instantaneous wave profiles both on the hull and in free flow. In addition, it includes the form of the distribution of the local entrance angle at the level of the design waterline.

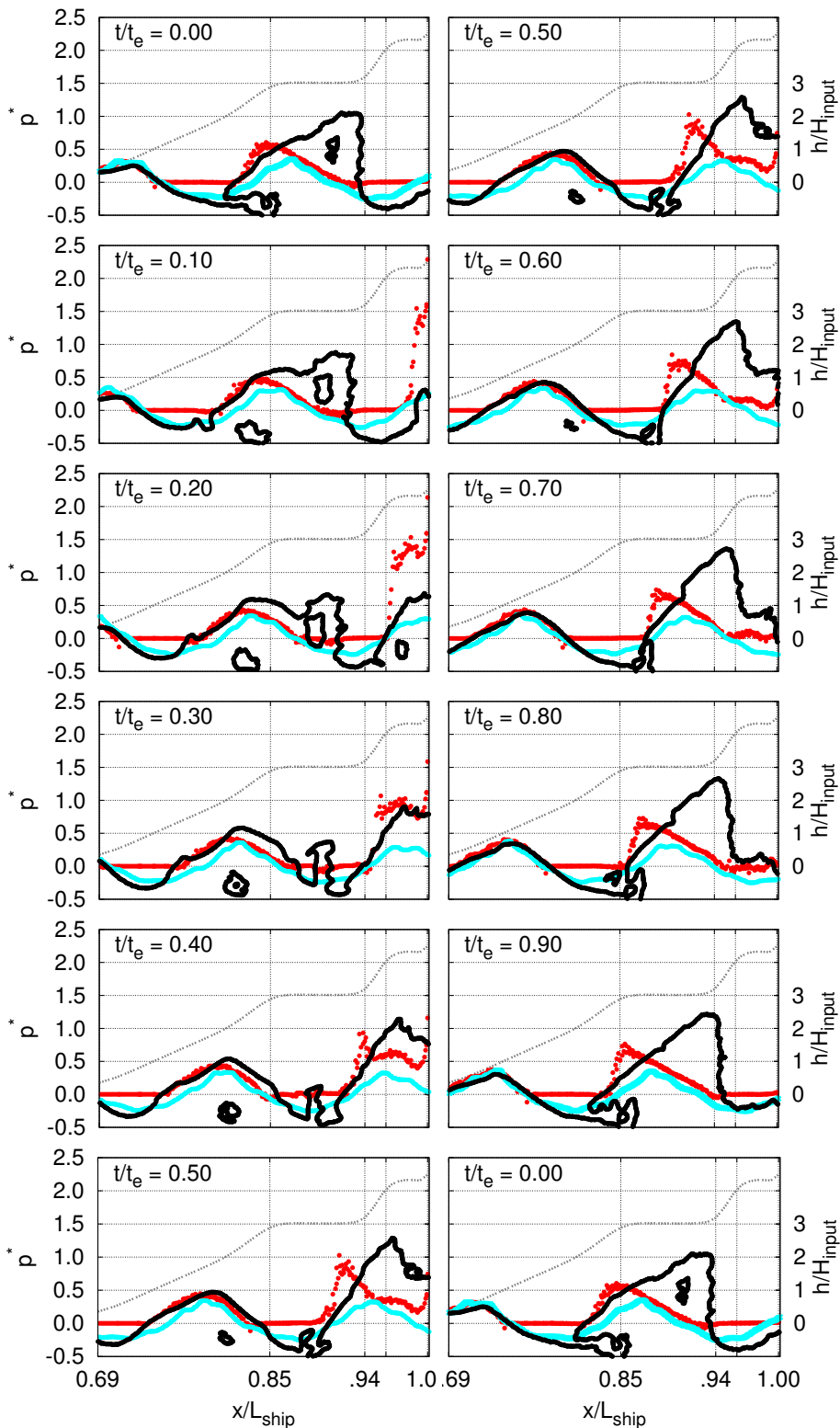


Figure 6.8. Pressure distributions (red) at the level of the design waterline. Free surface on hull (black). Freely propagating wave (turquoise). Entrance angle at the design waterline (grey).

First, the instantaneous pressure distributions are observed while the front of the wave passes the foremost area of the bow with the largest entrance angle ($x/L_{ship} > 0.96$). In this area, the pressure level rises sharply within a very short distance from zero to a high value right behind the front of the wave ($t/t_e = 0.1 - 0.2$). The pressure level is high for the whole area between the front of the wave and the stem. The highest value of the pressure occurs at the stem.

Next, the front of the wave passes the short part of the hull, where the entrance angle decreases by several degrees ($t/t_e = 0.3$). The instantaneous pressure distribution behaves similarly as at $t/t_e = 0.1 - 0.2$, except that the pressure level has clearly decreased.

Next, the instantaneous pressure distributions while the front of the wave passes the area of the constant entrance angle ($x/L_{ship} = 0.85 - 0.94$) are observed. Within this area, the pressure level rises linearly within a rather short distance from zero to a high level behind the front of the wave ($t/t_e = 0.4 - 0.8$). The rise occurs within a longer distance than in the area of the largest entrance angle. The value of the highest instantaneous pressure keeps decreasing while the wave passes this area. The fall in the pressure level happens nearly linearly within this area. Further, the fall occurs within a longer distance than the rise, e.g. $t/t_e = 0.8$. In the area of the larger local entrance angles ($x/L_{ship} > 0.94$), that part of the distribution decreases more slowly and not linearly.

Next, the instantaneous pressure distributions while the front of the wave passes the area where the entrance angle decreases linearly towards the fore shoulder, $x/L_{ship} < 0.85$, are observed. Again, the pressure level rises from zero to its maximum value around the location of the front of the wave ($t/t_e = 0.4 - 0.9$). However, the rise is not linear as before. Instead, the front of the pressure distribution becomes more and more roundish the further the wave propagates along the hull. Similarly, the shape on the rear face of the pressure impulse becomes more roundish within this area, too. As an example, compare the rear face of the distribution in the area of the constant entrance angle at e.g. $t/t_e = 0.0$ (linear) and in the area of the decreasing entrance at e.g. $t/t_e = 0.4$ (roundish). As a consequence, the pressure impulse becomes more symmetric in the area of the decreasing entrance angle, e.g. $t/t_e = 0.4$. All in all, the shape of the pressure distributions becomes somewhat similar to that of the wave profile, e.g. $t/t_e = 0.5$. The maximum values of the pressure are smaller in this area than in the previous areas.

To conclude, the results at the level of the design waterline show that the nature of the loading changes with the changing entrance angle. In practice, the pressure level rises with a very sharp impact in the foremost area of the bow. Behind that area, the rise occurs with a linear and less steep rise. And finally the rise takes a roundish and smooth form. The way the pressure level falls changes correspondingly.

6.1.5 Behaviour of the free surface at the longitudinal sections

This subsection studies whether the local entrance angle affects the behaviour of the free surface, too. This is done by studying the behaviour of the free surface at longitudinal sections in the area of the bow. One example is given for each of the three areas of the bow where the local entrance angle behaves differently at the level of the design waterline. The first example is within the area of the largest entrance angle, the second one in the area of the constant entrance angle, and the third one in the area of the decreasing entrance angle. See the distribution of the local entrance angle in Figure 6.7. For each of these longitudinal sections, the y -locations and the crossing with the design waterline are given in Table 6.1.

Table 6.1. The locations of the observed longitudinal sections with the three areas of the different entrance angle at the design waterline

x/L_{ship}	y/B_{ship}	Area of the entrance angle
0.98	0.05	Largest entrance angles
0.90	0.24	Constant entrance angle
0.82	0.39	Decreasing entrance angle

Figure 6.9 shows the behaviour of the free surface at the longitudinal section that crosses the design waterline in the area of the largest entrance angle; see Table 6.1. Above the bulb ($t/t_e = 0.6 - 0.9$ and $t/t_e = 0.0$), the behaviour of the front of the wave is similar to that at the symmetry plane described in Subsection 6.1.1. However, in the case of this longitudinal section, the front of the wave needs to propagate further before it encounters the hull at the level of the design waterline. During this propagation ($t/t_e = 0.0 - 0.1$), the front of the wave steepens significantly below and around the design waterline. The hull prevents the front of the wave from passing the hull smoothly with a less steep form. Instead, the water seems to pile up in front of the hull. After the front of the wave has encountered

the hull at the level of the design waterline between $t/t_e = 0.1 - 0.2$, the water keeps piling up in front of the hull. This kind of piling-up after the encounter, for its part, indicates that the local shape of the hull causes a blocking effect instead of letting the wave and the water pass the hull smoothly.

Figure 6.10 shows the behaviour of the free surface at the longitudinal section that crosses the design waterline in the area of the constant entrance angle; see Table 6.1. In the case of this longitudinal section, the front of the wave becomes steeper when it approaches the hull before $t/t_e = 0.5$. The steepening can be distinctly seen e.g. at $t/t_e = 0.4$ when the fronts of the approaching and freely propagating waves are compared. In addition, the front of the approaching wave has fallen slightly behind that of the freely propagating wave. The distinct splash at $t/t_e = 0.5$ may draw attention, but it is not relevant for this description because it originates from other parts of the hull. After the actual encounter of the approaching wave and the hull between $t/t_e = 0.5 - 0.6$, the wave profile in front of the hull is more elevated than the profile in the free flow. This behaviour indicates that the hull delays the propagation of the wave and the water past this buttock line. In all, the wave profile is deformed both before and after the encounter of the front of the wave with the hull. The effect is milder than at the previously observed longitudinal section.

Figure 6.11 shows the behaviour of the free surface at the longitudinal section that crosses the design waterline in the area of the decreasing entrance angle; see Table 6.1. In this case, the wave keeps both a form and a height that is almost similar to the freely propagating wave before the encounter with the hull ($t/t_e = 0.9 - 0.0$). The approaching wave is in a slightly later phase than the freely propagating wave. As a further detail, the profile of the approaching wave includes splashes that originate from other parts of the hull. After the encounter, from $t/t_e = 0.0$ onwards, the deformation of the free surface is minor while the wave continues to pass this buttock line. In all, the wave is able to pass this buttock line smoothly without serious deformation.

The three examples above show that the approaching wave behaves differently at the longitudinal sections that locate in the areas of the different local entrance angles of the hull. The larger the entrance angle is, the steeper the front of the wave becomes before encountering the hull. In addition, the larger the entrance angle is, the more important the piling of the water in front of the hull is after the front of the wave has encountered

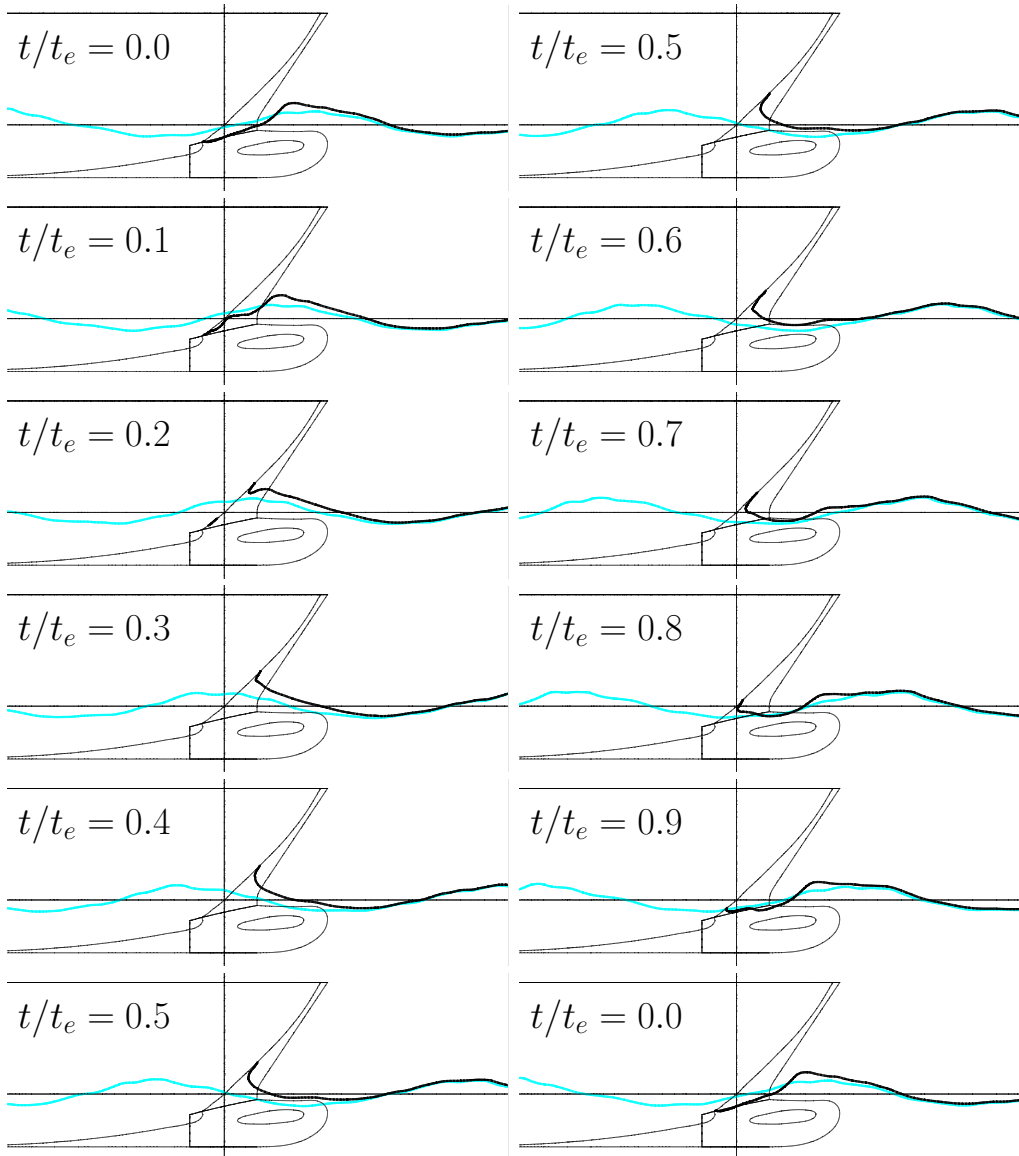


Figure 6.9. Free surface at the longitudinal section $y/B_{ship} = 0.05$, which crosses the design waterline at $x/L_{ship} = 0.98$. Black line: the free surface at the present longitudinal section. Turquoise line: freely propagating wave at the longitudinal section $y/B_{ship} = 6.0$. The location $x/L_{ship} = 0.98$ is indicated with the black vertical line and the level of the design waterline with the black horizontal line.

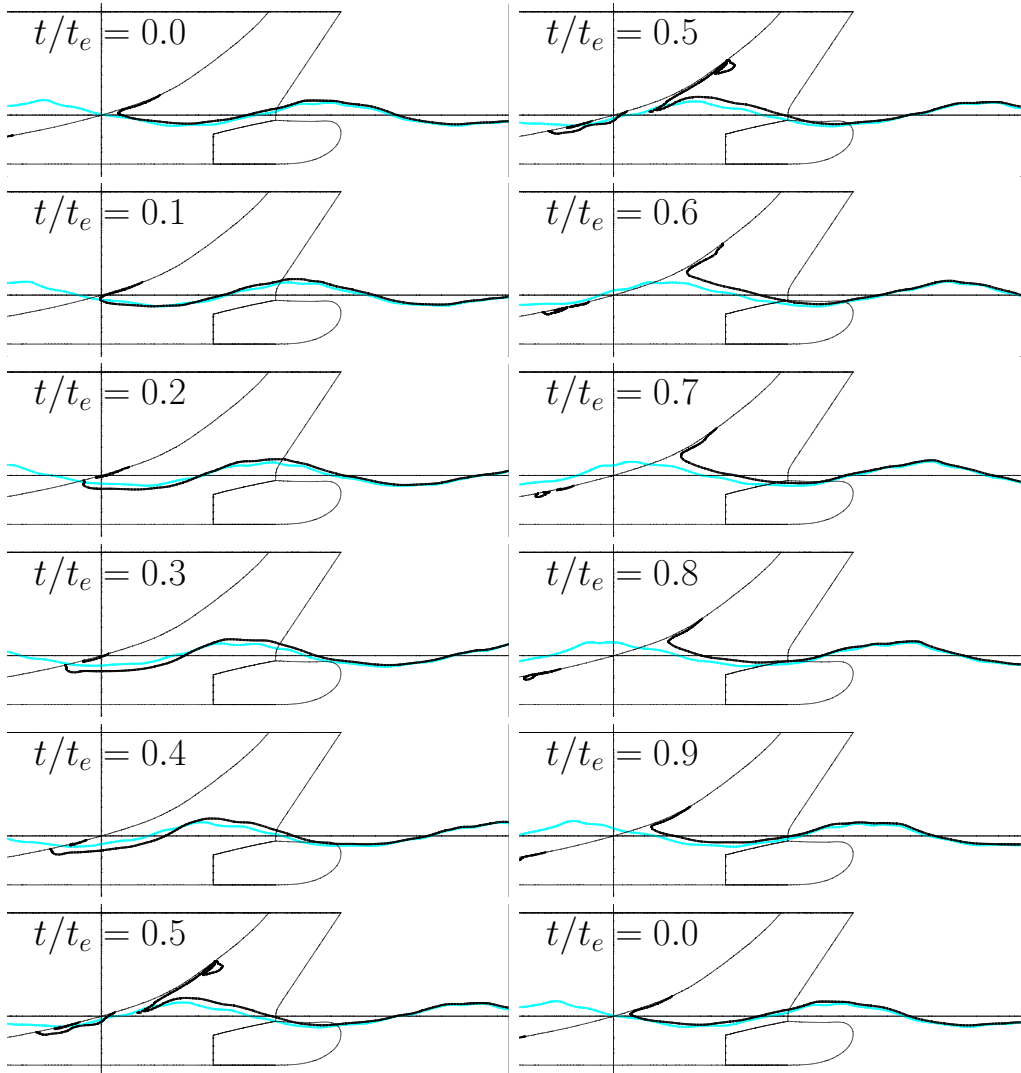


Figure 6.10. Free surface at the longitudinal section $y/B_{ship} = 0.24$, which crosses the design waterline at $x/L_{ship} = 0.90$. See the caption of Figure 6.9.

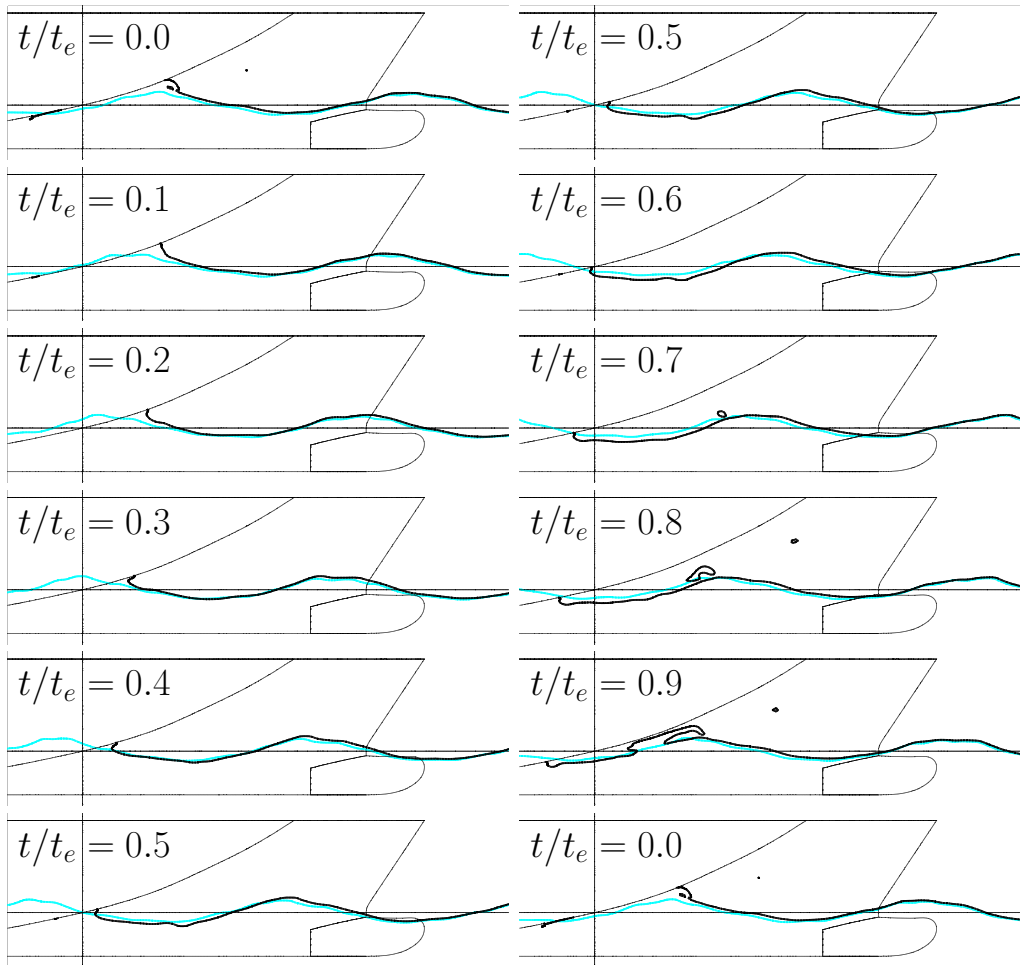


Figure 6.11. Free surface at the longitudinal section $y/B_{ship} = 0.39$, which crosses the design waterline at $x/L_{ship} = 0.82$. See the caption of Figure 6.9.

the hull at the level of the design waterline.

6.1.6 Summary

The results of this section explain how the pressure distribution evolves while the wave propagates in the area of the bow. Moreover, they explain how the local hull form affects the local behaviour of the loading. First, the approaching wave becomes very steep before hitting the stem as a result of the effect of the bow bulb. As a consequence of this blow, an impact with high pressure occurs in the foremost part of the bow. The impact-type behaviour of the local loads calms down within a short distance as the front of the wave propagates further along the hull. The behaviour of the local pressure becomes smoother and more symmetric towards the fore shoulder with the decreasing values of the local entrance angle at the level of the design waterline. In the z -direction, the upper part of the front of the propagating loading follows the shape of the buttock lines.

6.2 Springing excitation

The previous section gave a general description of the behaviour of the flow. This section focuses on two aspects, which matter for the springing excitation.

First, the ship is advancing in head waves in the case considered here. In head waves, only the vertical component of the wave loads can excite the vibration of a vertical mode. Therefore, one relevant aspect of the analysis is to distinguish the vertical component from the total wave loads (Subsection 6.2.1).

Second, the encounter period of the waves has been selected in such a way that the second harmonic component of the wave loads resonates with the two-node vertical mode of the hull. This means the second harmonic component of the vertical loading is the main origin of the springing excitation. Therefore, another important aspect of the analysis is to point out the features of the local vertical loads which result in the second harmonic component of the vertical loading (Subsections 6.2.2-6.2.3). The accumulation of the second harmonic component of the global vertical force along the length of the hull is described in Subsection 6.2.4.

6.2.1 Propagation of the distribution of vertical loading on the hull

As stated above, only the vertical component of the loading matters for springing in head waves. This section explains how the characteristics of the instantaneous distributions of local vertical loads differ from the distributions of pressure.

The distribution of the local vertical loads can be obtained from the distribution of the pressure by multiplying the local values of the pressure by the vertical component of the respective local surface normal.

The distribution of the vertical surface normal is given in Figure 6.12. It has two important features from the point of view of the vertical loading. First, at the level of the design waterline, the vertical surface normal is zero right behind the stem. When moving along the design waterline from the stem towards the fore shoulder of the ship, the vertical surface normal becomes larger. Second, the vertical surface normal becomes larger when moving towards the bottom from the design waterline. These observations mean that the magnitude of the vertical surface normal behaves in a manner that is contrary to the amplitude of the dynamic pressure

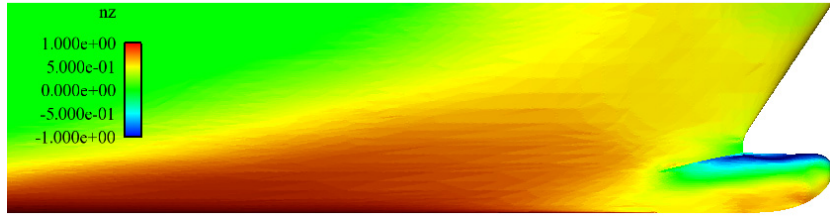


Figure 6.12. Distribution of the vertical component of the surface normal pointing inwards

(Subsection 6.1.3) in the area of the bow. As a consequence, the distributions of the vertical loading are different from the distributions of the total pressure as a result of the cancelling effect of the vertical surface normals.

Figure 6.13 compares the instantaneous distributions of the pressure with the respective distributions of the vertical loading. When the wave passes the foremost part of the bow, the difference between the level of the pressure and the vertical loading is significant ($t/t_e = 0.1 - 0.3$). The level of the vertical loading is moderate in comparison with that of the pressure. As a consequence, the changes in the level of the vertical loading are moderate too between the consecutive instants ($t/t_e = 0.1 - 0.4$), whereas the maximum values of the pressure decrease significantly during this time span. When the front of the wave continues to propagate along the bow of the ship, the differences in the level of pressure and the level of the vertical loading become less important (e.g. $t/t_e = 0.08$) and even very small (e.g. $t/t_e = 0.2$) closer to the left-hand edge of the observation area.

For a more detailed observation, Figure 6.14 allows the distributions of the pressure (red dots) and the vertical loading (blue dots) at the level of the design waterline to be compared. See Subsection 6.1.4 for a similar presentation of the pressures. When the wave passes the foremost part of the bow ($t/t_e = 0.1 - 0.3$), the distributions of the total and vertical loading have two significant differences. First, the level of the vertical loading is much lower than that of the pressure, which was already shown in Figure 6.13. Second, the shapes of the distributions are different. The vertical loading decreases towards the stem, while the pressure is at a rather high level between the location of the front of the wave and the stem. When the front of the wave moves forward along the hull, the difference between the level of the pressure and of the vertical loading becomes more moderate

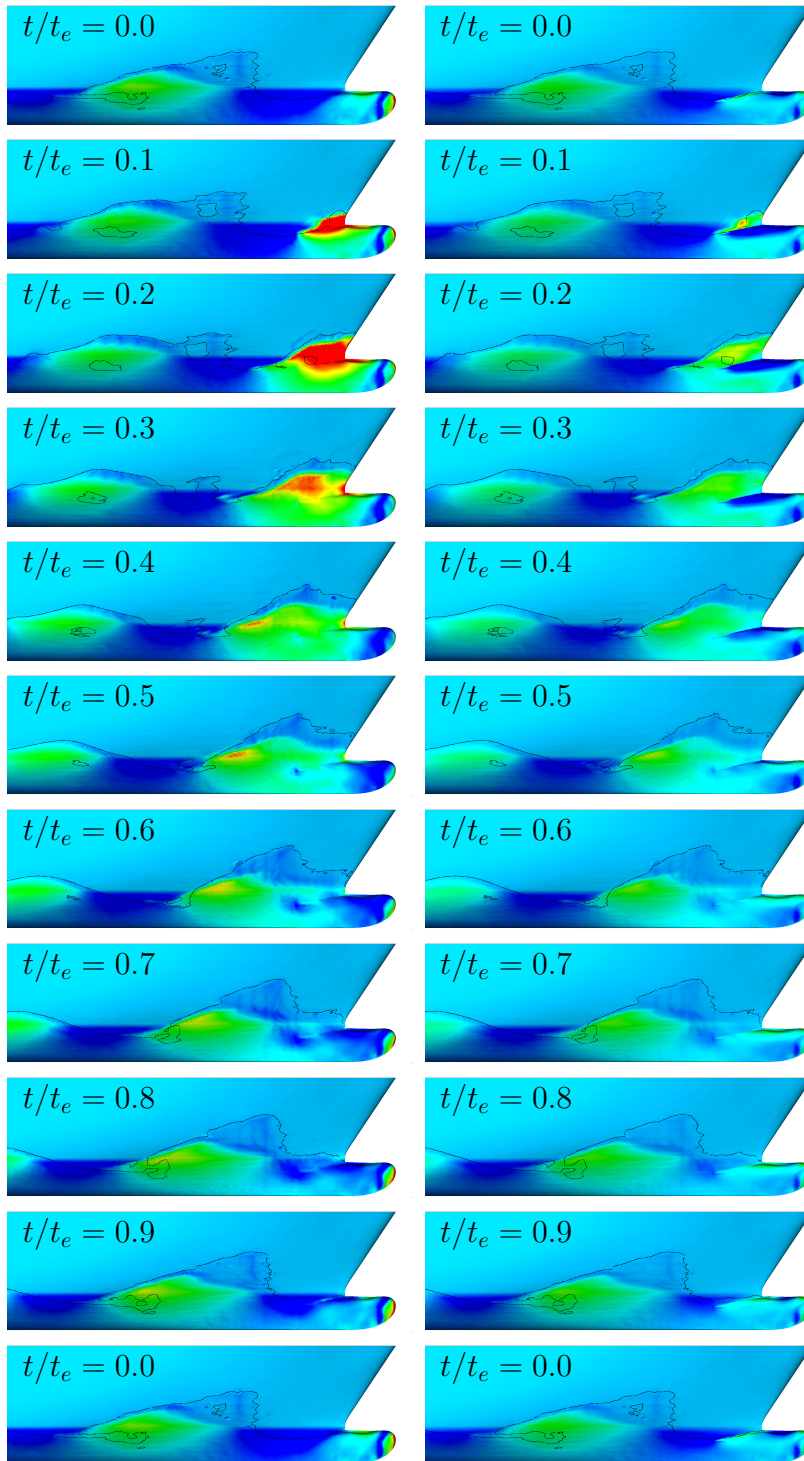


Figure 6.13. Left: distributions of pressure. Right: distributions of vertical loading. From top to bottom: $t/t_e = 0.0 - 0.9$ and $t/t_e = 0.0$. The uppermost and the lowermost subfigures are similar.

(e.g. $t/t_e = 0.50$). Then the level of the vertical loading is slightly lower. Further, the shapes of the distributions of the pressure and the vertical loading become similar, even though the shapes still differ right behind the stem. When the front of the wave moves closer to the fore shoulder of the ship, the amplitude of the vertical loading becomes much smaller than that of the pressure (e.g. $t/t_e = 0.8$ closer to the left-hand edge of the observation area).

All in all, the changes in the level of the vertical loading between the different instants are much more moderate than the changes in the level of the pressure. The reason is that the vertical loading in the foremost part of the bow is less important than the pressure.

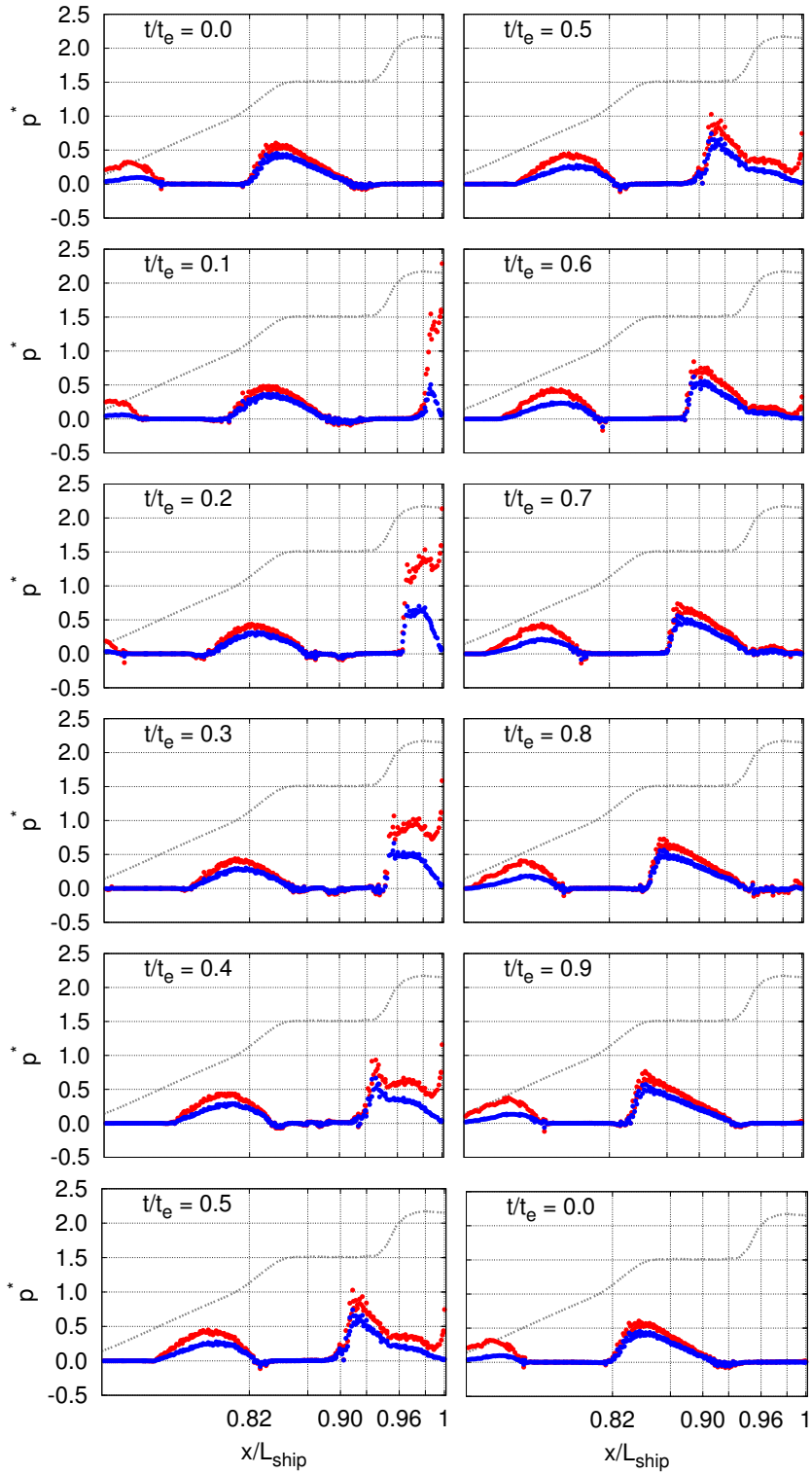


Figure 6.14. Instantaneous distributions of pressure p (red) and of $p \cdot n_z$ (blue) at the level of the design waterline. Entrance angle at the design waterline (grey).

6.2.2 Vertical loading and its second harmonic contribution at certain stations in the area of the bow

This subsection continues the analysis of the vertical loading by observing it more closely at certain stations in the area of the bow.

The focus is on the vertical force histories and the local vertical loads at six stations, which are indicated in Table 6.2, and in Figure 6.14 as vertical lines. Table 6.3 summarises the data to be analysed in this subsection. As for the vertical force at each of these stations, the unfiltered and two low-pass filtered time histories are presented in order to point out how the contribution of the second harmonic vertical force can be seen in the unfiltered time history of the vertical force. The second harmonic component of the force is especially interesting here, because it resonates with the two-node vertical mode of the hull in the wave conditions that were selected. As for the local vertical loads, the aim is to explain which features result in the second harmonic vertical force at the station under observation. This explanation utilises Figure 6.18, which gives the rise times $t_{rise,90\%}$ of the local vertical loads and the instants when these rises start. The results in Figure 6.18 give an overall idea of the distributions of these two quantities. Individual time histories may include details, which the analysis (Subsection 3.3.8) cannot take into account.

Table 6.2. The observed stations.

station	Results in Figure
$x/L_{ship} = 0.98$	Figure 6.15a,c,e,g,i
$x/L_{ship} = 0.96$	Figure 6.15b,d,f,h,j
$x/L_{ship} = 0.93$	Figure 6.16a,c,e,g,i
$x/L_{ship} = 0.91$	Figure 6.16b,d,f,h,j
$x/L_{ship} = 0.88$	Figure 6.17a,c,e,g,i
$x/L_{ship} = 0.82$	Figure 6.17b,d,f,h,j

Station $x/L_{ship} = 0.98$

The station $x/L_{ship} = 0.98$ is located in the foremost part of the bow in the vicinity of the stem.

At this station, the unfiltered time history of the vertical force shows distinctly impact-type behaviour, shown by the black line in Figure 6.15e. The rise of the force history from the minimum to the maximum level is very fast ($t_{rise,98\%}/t_e = 0.14$). The fall from the maximum to the minimum

Table 6.3. Given results for each station in Figures 6.15-6.17

Subfigure	Content
a or b	Shape of the frame and distribution of n_z
c or d	Time histories of the wave elevation on the hull and in the free flow
e or f	Unfiltered vertical force, low-pass filtered vertical force histories with the zeroth - second harmonic components and with the zeroth - first harmonic components
g or h	All the time histories of the local vertical loads $p \cdot n_z$ above $z/H_{input} = -1$ with the colours indicated in Subfigure a. Red: $z/H_{input} > 0.5$, green: $0.0 < z/H_{input} < 0.5$, blue: $-0.5 < z/H_{input} < 0.0$, pink: $-1.0 < z/H_{input} < -0.5$
i or j	All the time histories of the local vertical loads $p \cdot n_z$ below $z/H_{input} = -1$ with the colours indicated in Subfigure a. Turquoise: $-1.5 < z/H_{input} < -1.0$, black: $z/H_{input} < -1.5$

level is much slower ($t_{fall,98\%}/t_e = 0.69$). The comparison of the unfiltered force history (black line) and the low-pass filtered force history with the zeroth - second harmonic components (red line) shows that the force has an important contribution of the third - n^{th} harmonic components; see Figure 6.15e. This contribution can be seen in the very fast rise time and in the monotonic fall of the force level or, in other words, in the most impact-type features of the force history. In this respect, the force history with the zeroth - second harmonic components behaves much more smoothly. The comparison of the low-pass filtered time histories with the zeroth - first (green line) and with the zeroth - second harmonic components (red line) reveals that the second harmonic contribution of the force relates to the asymmetric behaviour of the force history; see Figure 6.15e. The second harmonic contribution makes the rise time of the force history much shorter than the fall time. Further, it contributes to the maximum values of the force history.

At this station, all the local vertical loads contribute to the second harmonic component of the vertical force. This can be seen by the fact that at each depth the rise times of the local vertical loads are much shorter than the fall times, especially below $z/H_{input} \approx 0.5$; see all colours except red in Figures 6.15g and 6.15i. The rise times of the local loads $t_{rise,90\%}$ are mainly less than 15% of the encounter period and even less than 10% between $-1 < z/H_{input} < 0.5$; see Figure 6.18a. Above $z/H_{input} \approx 0.5$ (red lines in Figure 6.15g), the time histories of the local vertical loads are more symmetric, but they are located asymmetrically within the encounter period and contribute to the maximum values of the force history. The pressure peaks between $-0.5 < z/H_{input} < 0.5$ (green and blue lines) are not relevant for the second harmonic vertical force at this station. Further, the local vertical loads between $-1.0 < z/H_{input} < -0.5$ (pink lines) partly cancel their effect.

Station $x/L_{ship} = 0.96$

The station $x/L_{ship} = 0.96$ is located slightly behind the previous station $x/L_{ship} = 0.98$ in the foremost part of the bow, where the local entrance angle is the largest.

At the station $x/L_{ship} = 0.96$, the time history of the vertical force, shown by a black line in Figure 6.15f, is different from the one at the previous station $x/L_{ship} = 0.98$. At this station, the rise of the force from the minimum level to the maximum level is slower ($t_{rise,98\%}/t_e = 0.25$) than at the

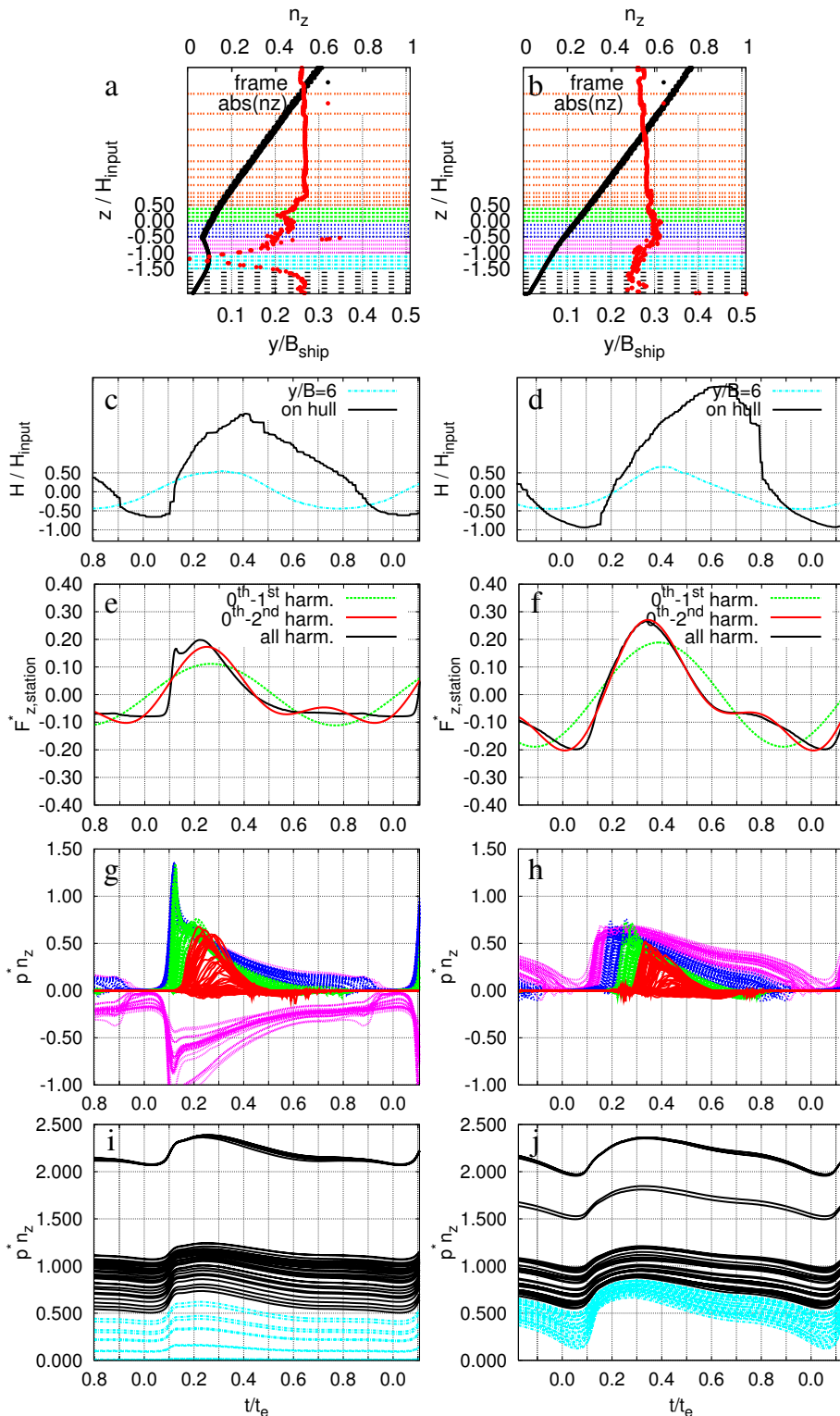


Figure 6.15. Left: $x/L_{ship} = 0.98$. Right: $x/L_{ship} = 0.96$. **a-b** Shape of the frame and distribution of n_z . **c-d** Time histories of the wave elevation on the hull and in the free flow. **e-f** Unfiltered vertical force, low-pass filtered vertical force histories with the $0^{th} - 2^{nd}$ and $0^{th} - 1^{st}$ harmonic components. **g-j** See the caption of Figure 6.16.

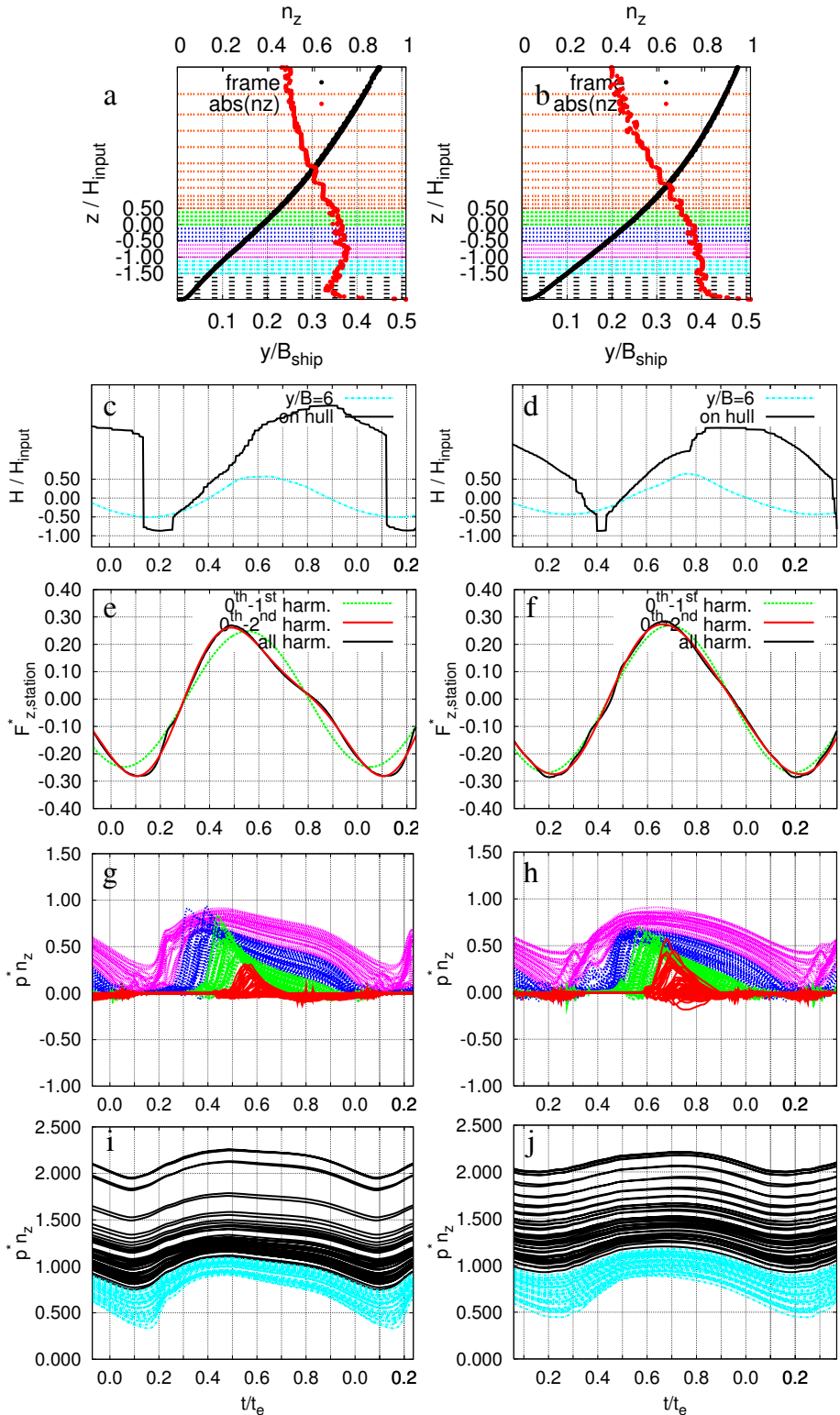


Figure 6.16. Left: $x/L_{ship} = 0.93$. Right: $x/L_{ship} = 0.91$. **a-f** See the caption of Figure 6.15. **g-h** Local vertical loads. Red: $z/H_{input} > 0.5$, green: $0.0 < z/H_{input} < 0.5$, blue: $-0.5 < z/H_{input} < 0.0$, pink: $-1.0 < z/H_{input} < -0.5$. **i-j** Turquoise: $-1.5 < z/H_{input} < -1.0$, black: $z/H_{input} < -1.5$. The line colours are indicated in Subfigures **a-b**, too. 123

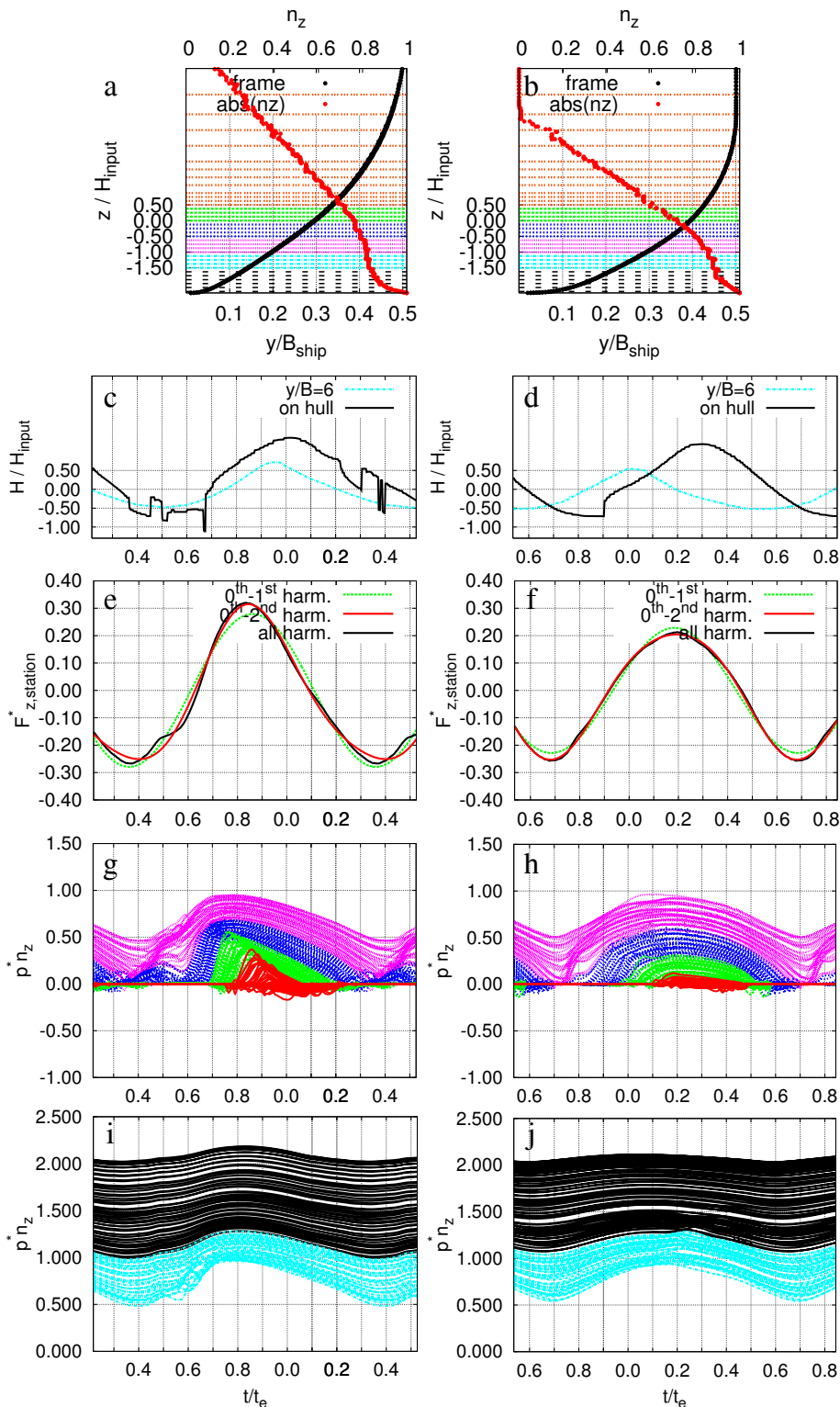


Figure 6.17. Left-hand side: $x/L_{ship} = 0.88$. Right-hand side: $x/L_{ship} = 0.82$. See the captions of Figures 6.15 - 6.16.

previous station ($t_{rise,98\%}/t_e = 0.14$) and the fall of the present force history includes a secondary hump. The distinct impact-type behaviour with the sudden changes in the force level are missing at the present station.

At the station $x/L_{ship} = 0.96$, the vertical force consists mainly of the zeroth - second harmonic components, which can be seen as the similarity of the unfiltered force history and of the low-pass filtered force history with the zeroth - second harmonic components; see Figure 6.15f. The comparison of the low-pass filtered time histories with the zeroth - second and zeroth - first harmonic components – see Figure 6.15f – reveals the contribution of the second harmonic force. Similarly to the previous station $x/L_{ship} = 0.98$, the contribution can be seen as the asymmetric behaviour of the force history. Again, the rise time is much shorter ($t_{rise,98\%}/t_e = 0.25$) than the fall time ($t_{fall,98\%}/t_e = 0.67$) and the maximum values of the force history become larger as a result of the effect of the second harmonic force. At this station $x/L_{ship} = 0.96$, all the local vertical loads contribute to the second harmonic component of the vertical force and the reasons are similar to those at the previous station $x/L_{ship} = 0.98$.

Despite the similarities to the previous station, the contribution of the second harmonic force is more important at the present station ($x/L_{ship} = 0.96$) than at the previous station ($x/L_{ship} = 0.98$). The origins of this difference are explained next. The key features to be observed are the rise and fall of the loading.

At the present station $x/L_{ship} = 0.96$, the rise of the force history is more favourable for the second harmonic vertical loading than at the previous station $x/L_{ship} = 0.98$. The rise of the force level at $x/L_{ship} = 0.96$ happens as a relatively steep but still smooth slope whereas the rise at the station $x/L_{ship} = 0.98$ happens mainly as a sudden impact. The origin of this difference lies in the different behaviour of the local vertical loads at these two stations; see Figures 6.15g-j. Two relevant features in the behaviour of the local loads can be pointed out. First, the rise of the individual local loads starts within a larger time span at the station $x/L_{ship} = 0.96$ than at $x/L_{ship} = 0.98$, the values being $t_{span}/t_e \approx 0.3$ and $t_{span}/t_e \approx 0.2$ respectively; see Figure 6.18b. Second, the rise times of the local loads are longer at $x/L_{ship} = 0.96$ ($t_{rise,90\%}/t_e < 0.2$) than at $x/L_{ship} = 0.98$ ($t_{rise,90\%}/t_e < 0.15$) below $z/H_{input} \approx -0.5$; see Figure 6.18a. The longer rise times indicate a smaller asymmetric contribution of the local loads to the force history.

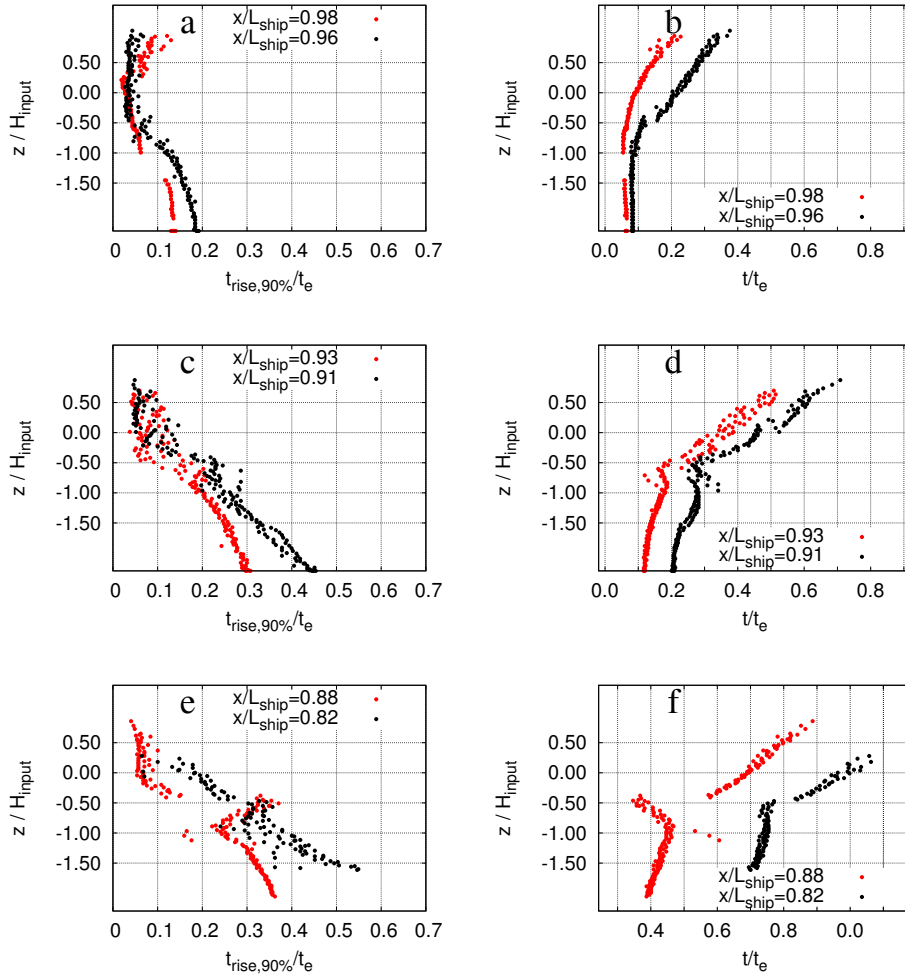


Figure 6.18. Information on the local vertical loads, whose peak-to-peak value is larger than $0.2\rho g H_{input}$. Left: rise time $t_{rise,90\%}$. Right: instant when the rise relating to $t_{rise,90\%}$ starts. **a-b** Stations $x/L_{ship} = 0.98$ and $x/L_{ship} = 0.96$. **c-d** Stations $x/L_{ship} = 0.93$ and $x/L_{ship} = 0.91$. **e-f** Stations $x/L_{ship} = 0.88$ and $x/L_{ship} = 0.82$.

At the present station $x/L_{ship} = 0.96$, the fall of the force history is more favourable for the second harmonic vertical loading than at the previous station $x/L_{ship} = 0.98$. At the present station $x/L_{ship} = 0.96$, the force history has a secondary hump in its falling part between $0.6 < t/t_e < 0.05$. At the previous station $x/L_{ship} = 0.98$, the force level returns to a low level before this respective time span (the difference from the minimum value of the force history is about 5% of the peak-to-peak amplitude of the force history). The reason for this kind of difference in the vertical forces between the present and previous stations is mostly the behaviour of the local vertical loads below $z/H_{input} \approx 0.0$. In the case of the present station, which is favourable for the second harmonic loading, the local loads continue to fall at a moderate rate between $0.6 < t/t_e < 0.05$. Furthermore, the local loads above $z/H_{input} \approx 0.0$ have negative values around $t/t_e \approx 0.7$, which results in a rather constant level of the vertical force between $0.6 < t/t_e < 0.8$. In the case of the previous station, which is less favourable for the second harmonic loading, the local loads have already reached a low level before the respective time span. Another important aspect is that, at the previous station, the loading on the upper part of the bulb cancels out the loading in the other parts of the frame. This is one reason why the vertical force falls so quickly to a low level.

Station $x/L_{ship} = 0.93$

The station $x/L_{ship} = 0.93$ is located in the area of the constant entrance angle.

At the station $x/L_{ship} = 0.93$, the vertical force history looks different from the one at the previous station $x/L_{ship} = 0.96$, shown in Figures 6.16e and 6.15f, even though they both consist practically of the zeroth - second harmonic components. At this station, the difference between the unfiltered time history and the low-pass filtered time history with the zeroth - first harmonic components is smaller than at the previous station. This indicates a less important contribution of the second harmonic vertical force.

At this station, the contribution of the second harmonic vertical force can be seen as the asymmetric behaviour of the time history in comparison with the behaviour of the low-pass filtered time history with the zeroth - first harmonic components. In other words, the rise time of the force history is shorter ($t_{rise,98\%}/t_e = 0.32$) than the fall time ($t_{fall,98\%}/t_e = 0.58$). The local vertical loads below $z/H_{input} \approx 0.5$ contribute to the second har-

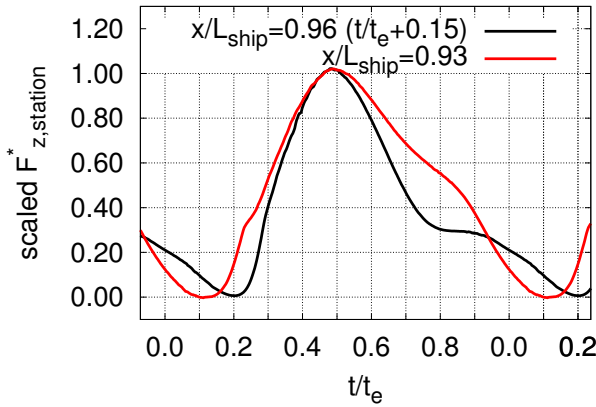


Figure 6.19. Scaled vertical forces at $x/L_{ship} = 0.96$ and $x/L_{ship} = 0.93$.

monic vertical force by having a short rise time and a longer fall time; see Figures 6.16g and 6.16i. The magnitude of the rise times $t_{rise,90\%}$ is mainly smaller than $0.3t_e$; see Figure 6.18c. Furthermore, the phase difference between the instant when the local loads at different depths start to rise is rather moderate; see Figure 6.18d.

The reason why the contribution of the second harmonic vertical force is less important at the present station $x/L_{ship} = 0.93$ than at the previous station $x/L_{ship} = 0.96$ is explained next. Figure 6.19 compares the two force histories after both of them have been scaled with their maximum amplitudes. First, the rise of the force history lasts longer ($t_{rise,98\%}/t_e = 0.32$) in the case of the smaller second harmonic vertical force at $x/L_{ship} = 0.93$ than in the case of the station $x/L_{ship} = 0.96$ ($t_{rise,98\%}/t_e = 0.25$). This relates mainly to the behaviour of the local vertical loads below $z/H_{input} \approx -0.5$ (pink, turquoise, and black lines in Figures 6.16g,i and 6.15h,j), which rise more slowly and smoothly at the station $x/L_{ship} = 0.93$ than at the station $x/L_{ship} = 0.96$. The magnitude of the rise times is $t_{rise,90\%}/t_e < 0.3$ at $x/L_{ship} = 0.93$ and $t_{rise,90\%}/t_e < 0.2$ at $x/L_{ship} = 0.96$; see Figures 6.18a and 6.18c. Further, the phase difference between the local loads at different depths is larger at the station $x/L_{ship} = 0.93$; see Figures 6.18b and 6.18d. This can be seen particularly as the different lengths of the time spans during which the local loads below $z/H_{input} \approx -0.5$ start to rise: $t_{span}/t_e \approx 0.1$ at $x/L_{ship} = 0.93$ and $t_{span}/t_e \approx 0.03$ at $x/L_{ship} = 0.96$. Second, the force level begins to fall more slowly from the maximum level to the minimum level in the case of

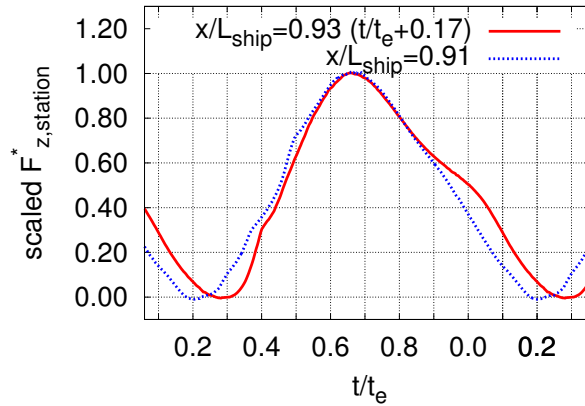


Figure 6.20. Scaled vertical forces at $x/L_{ship} = 0.93$ and $x/L_{ship} = 0.91$.

the less important second harmonic vertical force ($x/L_{ship} = 0.93$). This slower fall relates mainly to the behaviour of the local vertical loads below the design waterline $z/H_{input} \approx 0.0$ (blue, pink, turquoise, and black lines), which fall more slowly at the present station $x/L_{ship} = 0.93$ than at the previous station $x/L_{ship} = 0.96$. The shapes of the falling local loads are different between these two stations, too. All in all, the second harmonic vertical force becomes less important when the time histories of the local vertical loads become smoother and more roundish instead of having a rather linear rise and fall.

Station $x/L_{ship} = 0.91$

The station $x/L_{ship} = 0.91$ is located in the area of the constant entrance angle as the previous station $x/L_{ship} = 0.93$.

The unfiltered time history of the vertical force at the present station again looks different from the one at the previous station. At the present station, the unfiltered time history differs only slightly from the low-pass filtered time history with the zeroth - first harmonic components; see Figure 6.16f. Thus, the contribution of the second harmonic vertical force is minor. This contribution makes the rise of the time history only slightly steeper and the fall of the time history only slightly gentler in comparison with the low-pass filtered time history with the zeroth - first harmonic components. The effect of the second harmonic vertical force is so minor that it is difficult to point out specifically which features of the local vertical loads are particularly important for the second harmonic vertical force. Nevertheless, the time histories of the local vertical loads at the present

station are evidently asymmetric at this station too, which should matter in general; see Figures 6.16h and 6.16j. The asymmetry of the local loads can also be seen in the rise times, which are mostly clearly smaller than $0.5t_e$; see Figure 6.18c.

The difference in the contribution of the second harmonic vertical force between the present $x/L_{ship} = 0.91$ and the previous stations $x/L_{ship} = 0.93$ is explained next, Figure 6.20. First, in the case of the minor second harmonic vertical force ($x/L_{ship} = 0.91$), the rise of the force lasts longer. The rise time is $t_{rise,98\%}/t_e = 0.42$ at $x/L_{ship} = 0.91$ and $t_{rise,98\%}/t_e = 0.32$ at $x/L_{ship} = 0.93$. This relates to the phase differences between the local vertical loads below $z/H_{input} \approx -0.5$ (pink, turquoise, and black lines in Figures 6.16g-j). The loading closer to the bottom starts to have an effect earlier when the second harmonic vertical force is especially small. This can be seen as the different lengths of the time span during which the local loads start to rise below $z/H_{input} \approx -1.0$; see Figure 6.18d. Further, the rise times of these local loads are longer at $x/L_{ship} = 0.91$; see Figure 6.18c. Second, in the case of the minor second harmonic vertical force ($x/L_{ship} = 0.91$), the force falls linearly instead of having a secondary hump; see Figure 6.20. The origin of this linear fall is in the smooth fall of the local vertical loads below the design waterline ($z/H_{input} = 0.0$), while the respective local loads at the station $x/L_{ship} = 0.93$ fall with two slopes, which results in the secondary hump of the vertical force history.

Station $x/L_{ship} = 0.88$

The station $x/L_{ship} = 0.88$ is located in the area of the constant entrance angle, similarly to the two previous stations. The behaviour of the vertical force at the station $x/L_{ship} = 0.88$ – see Figure 6.17e – does not change greatly in comparison to the vertical force at the previous station $x/L_{ship} = 0.91$. In practice, the contribution of the second harmonic vertical force increases slightly in comparison with the previous station. In terms of local vertical loads, this may relate to the steepening of the rising parts of the time histories between $-1.5 < z/H_{input} < -0.5$ (blue, pink, turquoise, black). The matter is only slightly reflected in the rise times $t_{rise,90\%}$ presented in Figures 6.18c and 6.18e. On the other hand, it may be asked whether the related analysis captures the essential behaviour of the rising time histories around $z/H_{input} \approx -0.5$ at $x/L_{ship} = 0.88$; see Figures 6.18e and 6.18f.

Station $x/L_{ship} = 0.82$

The station $x/L_{ship} = 0.82$ is located in the area of the decreasing entrance angle where the propagating loading does not show impact-type behaviour in space; see Sections 6.1.3-6.1.4.

Figure 6.17f shows that the time history of the vertical force is rather well predicted with the zeroth - first harmonic components only. The vertical force includes a contribution of the second harmonic component, but its magnitude is minor, being of the same order as the magnitude of the second harmonic component at the station $x/L_{ship} = 0.91$. However, both the time history of the vertical force and the time histories of the local vertical loads at the present station look different in comparison to those at $x/L_{ship} = 0.91$ and also in comparison e.g. to those at the previous station at $x/L_{ship} = 0.88$. The rise and the fall times of the force history are almost similar: $t_{rise,98\%}/t_e = 0.46$ and $t_{fall,98\%}/t_e = 0.44$.

At this station, most of the time histories of the local vertical loads are symmetric or nearly symmetric; see Figures 6.17h-j. The time histories look roundish and are without especially pronounced differences between the shapes of their rising and falling parts. As a further detail, the maximum amplitudes of the local vertical loads above $z/H_{input} \approx 0.0$ are distinctly smaller than at the previous stations. Besides, this is the only one of the stations that were observed where the amplitudes of the local vertical loads approach zero towards the ship bottom; see the black lines in Figure 6.17j. All in all, the results at the present station demonstrate that the contribution of the second harmonic vertical force is minor when the time histories of the local vertical loads behave symmetrically and have roundish shapes.

6.2.3 Distribution of the amplitude of the second harmonic vertical force in the area of the bow

Subsection 6.2.2 pointed out the relevance and the origin of the second harmonic vertical force at six sections. This subsection describes the distribution of the second harmonic vertical force in the area of the bow.

Figure 6.21 gives the distribution of the amplitude of the second harmonic vertical force in the area of the bow. The locations that were analysed in the previous section are indicated on the x -axis. The distribution in Figure 6.21 shows that the amplitude of the second harmonic vertical force begins to increase strongly slightly after the stem. It reaches

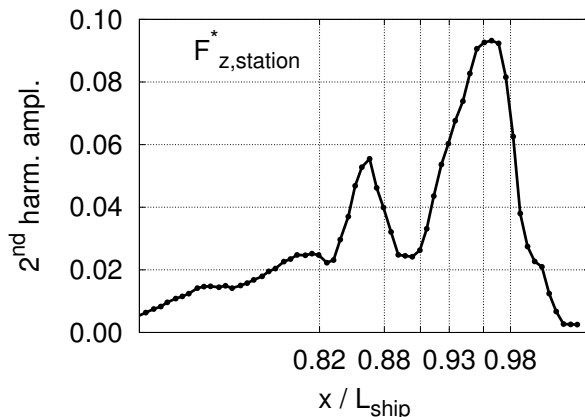


Figure 6.21. Distribution of the second harmonic vertical forces. The vertical lines illustrate the locations observed in Subsection 6.2.2.

its maximum value around $x/L_{ship} \approx 0.96$. Behind that the amplitude decreases to a low level – about 25% of the maximum value of the distribution – between $x/L_{ship} \approx 0.96$ and $x/L_{ship} \approx 0.90$. Next, the distribution has a local hump, whose maximum value is about 60% of the maximum value of the distribution. Behind $x/L_{ship} \approx 0.82$, the second harmonic amplitude decreases towards zero.

The shape of the distribution of the second harmonic vertical force can be understood on the basis of the analysis in the previous subsections. Starting from the stem, the important increase in the second harmonic vertical force relates to the impact-type behaviour of the loading. The maximum value of this force occurs behind the location of the greatest impact. It occurs at a location where the local vertical loads have impact-type features such as very short rise times and long fall times. The phase difference between local loads at different depths at that station is rather small but not as small as in the case of the impact. Behind the maximum value of the second harmonic vertical force, the decrease in the level of the force relates to the lengthening of the rise times of the individual local loads and to the lengthening of the phase difference between the individual local loads at different depths at a station. The distinct secondary hump in the distribution of the second harmonic vertical force around $x/L_{ship} \approx 0.87$ seems to relate to the steepening of the rising time histories of local loads at certain depths.

6.2.4 Accumulation of the second harmonic component of the global vertical force

This section describes how the second harmonic component of the global vertical force accumulates. See Eq. (3.16) for the definition of the cumulative force.

Figure 6.22a shows how the amplitude of the second harmonic global vertical force accumulates in the area of the bow. Between the stem and $x/L_{ship} \approx 0.92$, the amplitude increases significantly. This increase is followed by a short decrease between $x/L_{ship} \approx 0.92$ and $x/L_{ship} \approx 0.89$. Between $x/L_{ship} \approx 0.89$ and $x/L_{ship} \approx 0.82$, the second harmonic cumulative force continues to increase. Behind $x/L_{ship} \approx 0.82$, it reaches a rather established level.

The distribution of the second harmonic cumulative vertical force looks irregular with the changing lengths of the x -spans of the increasing and decreasing force level; see Figure 6.22a. Furthermore, the rate of the increase and decrease in the force level varies as a function of x too. In order to understand the origin of these irregularities, the correlation between the behaviours of the cumulative second harmonic vertical force and the distribution of the second harmonic vertical force along the length of the hull is studied next. Both the distributions of the phase and amplitude of the second harmonic vertical force are addressed.

First, the correlation between the distribution of the phase of the vertical forces and the distribution of the cumulative force is addressed. In order to do this, the locations of the local minima and maxima of the second harmonic cumulative force are indicated on the x -axis of the distribution of the phase of the second harmonic vertical forces; see Figure 6.22b. The distribution of the phase shows that the phase shifts by roughly one π between the locations of an adjacent local minimum and maximum in the distribution of the accumulative force. This is an expected observation. Thus, the different distances between the adjacent local minima and maxima originate from the different distances during which the phase of the vertical force changes by one π .

Second, the correlation between the distribution of the amplitude of the forces at the stations and the cumulative force is addressed; see Figure 6.22c. In the areas where the amplitude of a vertical force at a station is high, the change in the cumulative force is high as well, e.g. around $x/L_{ship} \approx 0.96$. In the area where the amplitude of the vertical force at a

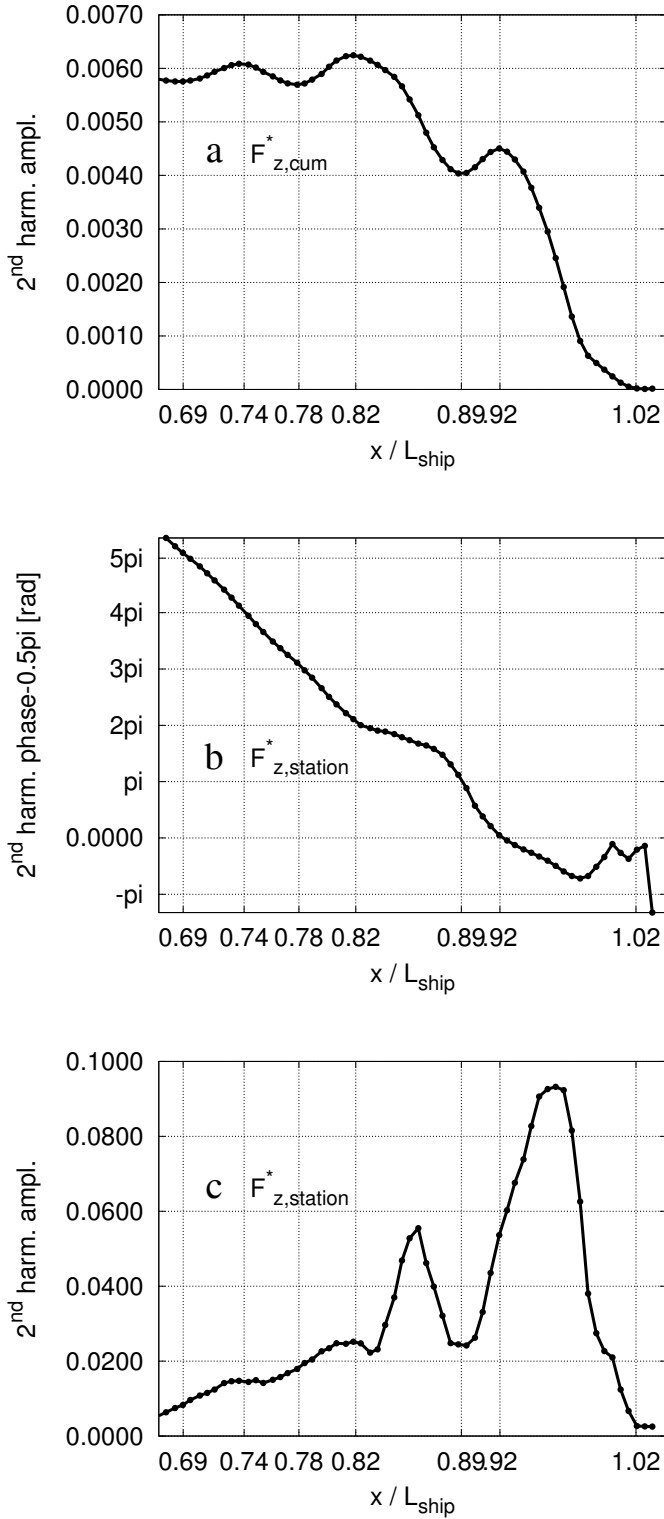


Figure 6.22. Distributions of the second harmonic vertical loading in the area of the bow **a** amplitude of the cumulative force **b** phase of the forces at the stations in relation to the phase at $x/L_{ship} = 1.0$ **c** amplitude of the forces at the stations

station is low, the change of the cumulative force is low as well, around $x/L_{ship} \approx 0.74$.

From the point of view of the resulting magnitude of the second harmonic component of the global vertical force, it is relevant to understand the joint effect of both the phase and the amplitude of the vertical force on the cumulative force. Within the same x -spans, when the cumulative force increases (especially $0.92 < x/L_{ship} < 1$ and $0.82 < x/L_{ship} < 0.89$) as a result of the phase of the vertical force at a station, the amplitudes of the vertical force at a station have their largest values. Within the x -spans of decreasing cumulative force (especially $0.89 < x/L_{ship} < 0.92$ and $0.78 < x/L_{ship} < 0.82$) as a result of the phase of the vertical force at a station, the amplitudes of the force at a station have much smaller values. This kind of behaviour also results in the amplitude of the cumulative force having a large value. The resulting amplitude could be much smaller if, for example, the relation of the distributions of the phase and amplitude of the forces at the stations were different.

So far only the area of the ship bow has been in focus. Next, Figure 6.23a-b shows the distribution of the amplitude of the second harmonic vertical force and the distribution of the respective cumulative force for the whole length of the ship. The results in these figures demonstrate that the main contribution of the loading originates from the area of the bow in a rather short area behind the stem. For instance, the magnitude of the second harmonic vertical loading within the distance of about $0.2L_{ship}$ from the fore perpendicular is roughly 94% of the respective loading of the whole ship.

Let us now consider the actual springing excitation caused by the second harmonic wave loading. The springing excitation can be described with a parameter called the generalised force. The generalised force can be obtained by multiplying the distribution of the force by the mode shape in question; see Eq. (3.17). The applied shape of the two-node vertical mode of a large cruise ship is given in Figure 6.24. This shape emphasises the importance of the loading in the area of the bow and reduces its importance further along the hull. Figure 6.23c shows that the distribution of the second harmonic component of the accumulative generalised force differs slightly from the respective distribution of the cumulative vertical force. The value of the global generalised force is about 25% smaller than the value of the global vertical force.

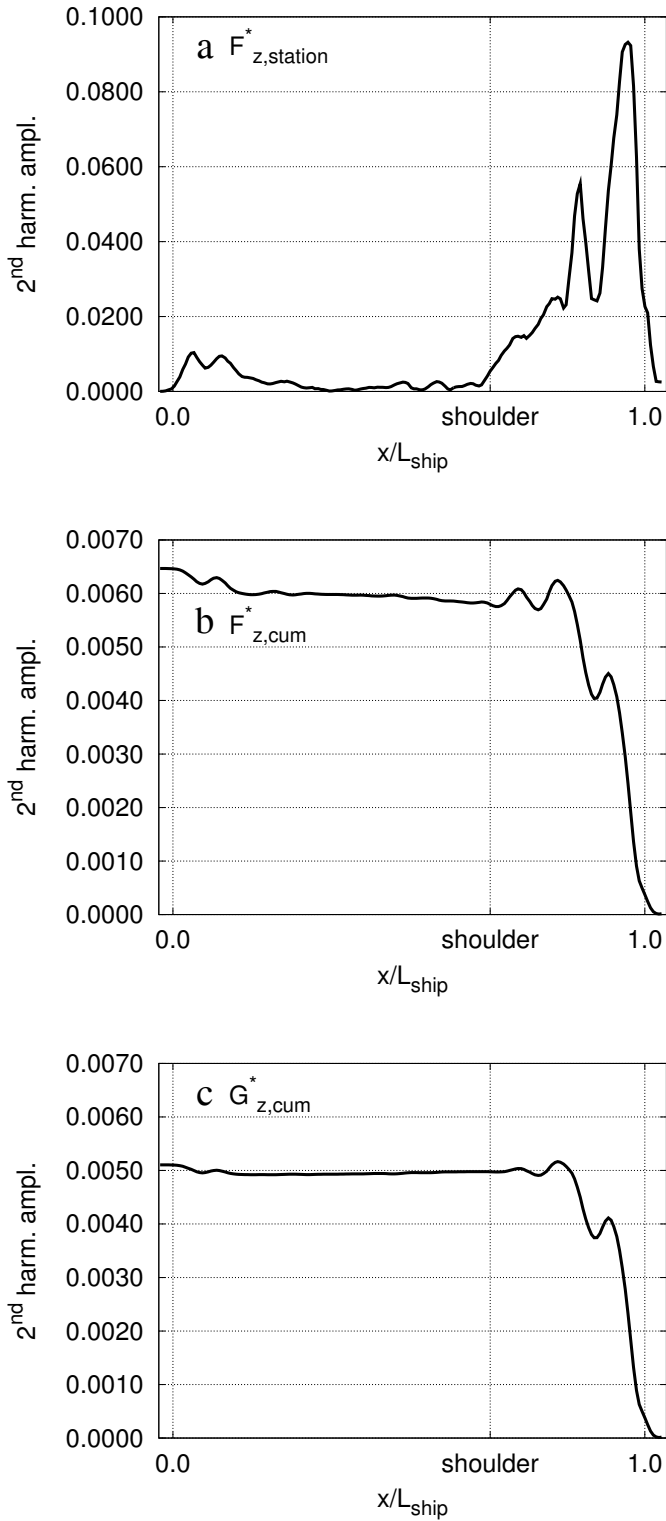


Figure 6.23. Distributions of the second harmonic vertical loading for the whole length of the hull **a** amplitude of the forces at the stations **b** cumulative force **c** cumulative generalised force

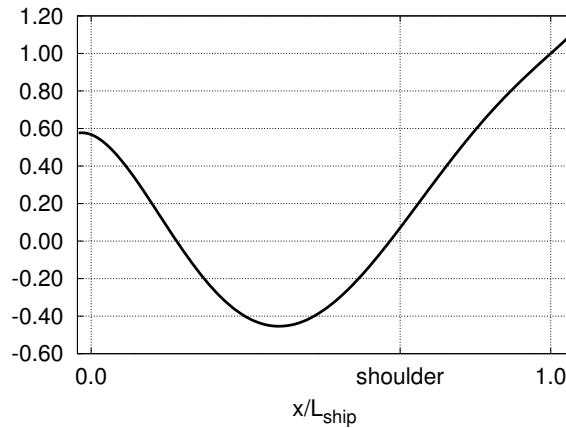


Figure 6.24. A typical shape of the two-node vertical mode of a large cruise ship

6.2.5 Summary

First, the importance of the distribution of the vertical surface normals on the vertical loading was pointed out (Subsection 6.2.1).

Second, it was shown that two features of the local loads at the stations matter for the second harmonic vertical force (Subsection 6.2.2). One of them is the ratio of the fall and rise time of individual local vertical loads. The another one is the phase difference between the local vertical loads at different depths at one station. The variation of these two features along the area of the bow can be understood on the basis of the analyses in Section 6.1. These features were at their most optimal for the second harmonic vertical force at the station which is located slightly further from the station where a large impact-type load occurs. In all, the amplitude of the second harmonic vertical force is significant for a short portion of the length of the ship (Subsection 6.2.3).

Third, it was illustrated that the distributions of both the second harmonic amplitude and the second harmonic phase of the vertical force at the stations matter for the resulting global second harmonic load (Subsection 6.2.4).

7. Discussion

7.1 On the reliability of the results

The reliability of the results was studied from the points of view of both the numerical and modelling accuracies.

The numerical accuracy of the computed wave loads was assessed by studying the effect of the resolution and the effect of the iteration number on the results. In general, the agreement of the results with the different resolutions and iteration numbers was good. In the case of the largest differences between the resolutions, the results of the medium and fine resolutions were similar and the result of the coarse resolution more different. The analysis of the local pressures showed that the fine resolution with 20 iterations was adequate for the prediction of the main characteristics of the pressure histories (Subsection 5.1.2). The analysis of the vertical force at the stations increased confidence in the reliability of the computed results. The comparison of the distributions of the second harmonic vertical force which were computed with the different resolutions and different iteration numbers confirmed that the second harmonic loading first becomes very significant behind the stem and then smaller and smaller towards the fore shoulder of the ship; see Figures 5.9 and 5.10.

On the other hand, the largest numerical uncertainty that was observed concerns the secondary hump in the distribution of the second harmonic vertical force in the area of the ship bow. Around this detail of the loading, the result of the coarse resolution differs the most from the other two results; see the distributions between $x/L_{ship} \approx 0.85$ and $x/L_{ship} \approx 0.92$ in Figure 5.10. Two observations can be made. First, the amplitude of the second harmonic loading decreases less behind the maximum value of the distribution according to the coarse resolution than according to

the other two resolutions. Second, the maximum values of the secondary hump given by the coarse resolution are smaller than those predicted by the other two resolutions. On the other hand, Figure 5.10 shows that the result of the coarse resolution may have some iterative error regarding the maximum values of the secondary hump. These observations on the secondary hump of the distribution of the second harmonic vertical force may seem to be non-essential as the main trend of the decreasing second harmonic vertical force at the stations towards the fore shoulder is captured by all three resolutions. However, the analysis in Subsection 6.2.4 explains how both the amplitude and phase of the force at the stations affect the resulting cumulative force; see particularly Figure 6.22. In the present case, a lesser decrease in the vertical force behind the maximum values of the distribution and smaller maximum values of the secondary hump both make the cumulative force smaller. Thus, if the actual value of the total force needs to be predicted, it is not sufficient to capture the main trend of the decreasing second harmonic vertical force towards the fore shoulder. Nevertheless, the fact that the results of the medium and fine resolutions are similar – see e.g. Figure 5.9 – increases confidence in the reliability of the results of the present fine resolution.

In general, one may ask whether a solution accuracy assessment with three resolutions is adequate to judge the numerical accuracy. In this respect, the common challenge of RANS computations is to reach the asymptotic range. In order to prove that the computed results are within the asymptotic range, more resolutions and a wider span of resolutions need to be studied. Currently, the length of the computations and the amount of available computational resources limit the number of resolutions that can be studied in practical cases of ship wave loads. Most of the previous studies on the numerical accuracy of the ship wave loads have used three resolutions too; see (Carrica et al., 2006), (Carrica et al., 2007), (Castiglione et al., 2011), (Orihara and Miyata, 2003), (Klemt, 2005), and (Deng et al., 2009). Guo et al. (2012) used four resolutions.

As for the behaviour of the waves, the solution accuracy assessment revealed that the wave height varies along the length of the numerical towing tank. It was observed that the numerical wave boundary condition creates higher harmonic waves, which may be the source of the problem. As the boundary condition that is applied is based on the first-order Stokes waves, it is possible that applying a higher-order wave condition could reduce the magnitude of the variation in the wave height. Fur-

ther, it is possible that the resolutions applied are not sufficiently fine for the propagation of these steep waves within a distance that is about ten times their own length. The observation that the coarser the resolution is, the more significant the increase in the wave height is (Subsection 5.1.1) supports this possibility. The increase in the wave height may also have something to do with the compressive discretisation scheme applied for the convective term of the volume fraction conservation equation in the case of a low Courant number. However, this topic requires further studies in order to be fully understood.

From a general point of view, the behaviour of waves in a numerical towing tank is a fundamental matter for the reliability of the computational results. The author has not found any remarks in the literature on the variation in the wave height in a numerical towing tank when interface-capturing methods are being applied. In practice, the characteristics of the wave are often presented at one location, e.g. (Sato et al., 1999), (Orihara and Miyata, 2003), (Klemt, 2005), (Deng et al., 2009). On the other hand, the ratio of the present wave and ship length is much smaller here than in the previous studies. This means that the waves need to propagate a much longer relative distance in the numerical towing tank than in the case of longer waves. Besides, the present need to simulate a long time period means that the instabilities have a longer time to propagate in the computational domain.

The challenge of generating monochromatic waves is commonly acknowledged and often discussed within experimental hydrodynamics; see e.g. (Henderson et al., 2006). A fundamental problem is that the movement of the wave maker does not correspond to the movement of the water particles in a discrete wave. This generates additional wave components; see e.g. the numerical results in (Mikkola, 2006). Within the experimental studies on springing, the challenge of generating good-quality short waves is typical; see e.g. (Hoffman and van Hooff, 1976) and (Storhaug, 2007). In the present experiments, the challenge of generating monochromatic waves was noticed, too. It was solved by analysing the wave data which were measured in front of the advancing bow and by choosing the wave encountered that were within a selected variation range.

As for the modelling accuracy of the computed results, the comparison of the computed and measured results in Section 5.3 demonstrates that the method applied here is capable of predicting local pressure histories at ten locations in the area of the bow. Both impact-type and smoother behaviour

are well captured within the observation area in the model tests. Naturally, the reliability of the modelling accuracy could be increased even further by comparing the computed and measured results at more locations. This would require more model tests with different locations of the pressure sensors to be performed.

Previously, Klemt (2005) and Orihara (2011) validated local pressure histories given by interface-capturing methods at several locations in the area of the bow. Klemt (2005) presents the results of several impact-type loads in long and steep waves and Orihara (2011) mostly smoother loads in long and low waves. Thus, from the point of view of the state of the art, this study increases confidence in the capability of interface-capturing methods to predict ship wave loads in very short and steep waves, too. From the point of view of the present study, the most important finding is that the computed results can predict the evolution of the spatial load distribution under the wave crest when the wave moves further along the hull.

All in all, the analysis in Chapter 5 demonstrates that the computed results are reliable for the analysis of the origin of the second harmonic vertical wave loads.

7.2 On the springing excitation

This study demonstrates that, in the case investigated here, the second harmonic vertical force originates mainly from the foremost part of the bow. In general, this is a logical finding, because the bow encounters the head waves first. In theory, the vertical loading could also be important in the area of the stern and at the bottom of the parallel mid-ship as a result of the transversal surface area. However, these parts of the hull are better protected from the effect of the fluctuating wave forces in head waves, particularly as the vertical motions of the ship are negligible.

The results of this study make it possible to describe which features of the local loads matter for the second harmonic loading; see Subsection 6.2.2. The second harmonic wave loads are most important in the area where the local wave loads have impact-type features. Here, the impact-type features mean that the rise times of the local loads are short and the fall times much longer. Further, the phase differences between the local loads at different depths are small at the location of one station. Behind the area of the largest second harmonic loading, a smaller secondary

hump exists too; see Figure 6.21. Its origin cannot be stated so clearly. The secondary hump indicates that the second harmonic amplitude of the vertical force at the stations is very sensitive to small changes in the local loads and in the phase differences between local loads at different depths.

The findings in Sections 6.1 make it possible to explain how the changes in the relevant features of the local loads along the length of the hull relate to the local hull form. As for the phase difference at different depths at one station, the form of the buttock lines has a significant role, because both the front of the wave and the front of the pressure distribution follow these lines; see Subsections 6.1.2-6.1.3. In the vicinity of the fore perpendicular, the buttock lines are steep and the front of the pressure distribution takes this steep shape too. The steep front of the pressure distribution means that the pressure level at different depths starts to rise almost simultaneously. Between the stem and the fore shoulder, both the buttock lines and the front of the pressure distribution become less steep, which means that the pressure level at greater depths starts to rise earlier than the pressure level around the design waterline.

As for the changes in the ratio of the rise and the fall times of local loads, similar features in the behaviour of the local loads can be observed both in the time histories of the local loads and in the instantaneous pressure distributions along the length of the hull. The correlation between the variation in the behaviour of the pressures and the local hull form is particularly distinct at the level of the design waterline; see Subsection 6.1.4. Those findings are supported by the observations on the behaviour of the free surface in front of the hull; see Subsection 6.1.5. The local entrance angle of the hull is at its largest behind the stem and becomes smaller, at first gradually and then continuously, towards the fore shoulder of the ship. In the area of the largest local entrance angle, the pressure level rises sharply within a very short distance and falls back to its minimum level very slowly. In this same area, the hull form seems to slow down the wave and the water when they pass the hull. The sharp rise in the pressure seems to relate to the piling up of the water before the front of the wave passes the hull at the level of the design waterline, which can increase the probability of a pressure impact. On the other hand, the slow return of the pressure level to its minimum value seems to relate to the piling up of the water in front of the hull after the front of the wave has passed the observed location. The effect of the hull form on the behaviour of the flow seems to reduce towards the fore shoulder of the ship. In the

area where the local entrance angle decreases continuously, the pressure distributions at the level of the design waterline have a similar shape to the upper part of the wave profile on the hull; see Subsection 6.1.4. Further, the wave passes the hull in this area rather smoothly and without distinct deformation; Subsection 6.1.5.

In the existing literature, some remarks suggest that impact-type loads could matter for second-order resonant springing. Hu et al. (2012) reported simultaneous second-order springing and whipping in the model tests of an ultra-large tanker in regular waves. Their finding indicates that the wave loads that cause second-order springing have impact-type features or slams, which caused whipping. Further, previous studies have indicated that an increase in the ship's speed or in wave steepness makes the second-order springing more important. With increasing speed and wave steepness, the impact-type loads become more probable, especially in the case of full hull forms. For instance, see the experimental results on bulk carriers in (Storhaug and Moan, 2007b) for the effect of the speed and in (Slocum and Troesch, 1983) for the effect of the wave steepness. In addition, Manderbacka et al. (2008) reported that local second harmonic wave loads and the breaking of the oncoming waves in the bow area of a cruise ship occur simultaneously in short oblique waves, which may indicate the possibility of impact-type loads, too.

Let us now consider the origin of an impact that can matter for the second-order springing excitation. Traditionally, the slam loads in sea-keeping are predicted with methods that are further developed and extended from Wagner's theory on the entry into the water of a keeled bottom (Wagner, 1931). When such methods are applied to ships' slams, the vertical motions of the ship and relative vertical velocity are usually underlined. The occurrence of a slam may be assessed on the basis of a threshold velocity; see e.g. (Ochi, 1964). Further, the peak impact pressure p_{peak} can be roughly estimated on the basis of the square of the relative velocity V_{rel}^2 and of a pressure coefficient C_p ; see e.g. (Lloyd, 1989):

$$p_{peak} = \frac{1}{2} C_p \rho_{water} V_{rel}^2. \quad (7.1)$$

The pressure coefficient depends on the shape of the object. In the case of a wedge with deadrise angles β above 25° , a theoretical formula may be used:

$$C_p = 1 + \left(\frac{\pi \cot \beta}{2} \right) \quad (7.2)$$

In the case investigated here, the value of the peak impact pressure itself

is not relevant. Nevertheless, the formulae (7.1)-(7.2) are applied next to check whether a similar connection can be found between the peak pressure, the relative velocity, and the hull shape.

In the present case, the vertical velocity is not large in comparison with the ship's velocity, for instance. As the motions of the ship are negligible, the vertical component of the velocity on the hull relates only to the fluctuation of the free surface. Its maximum value is about 20% of the ship's velocity V_{ship} according to the first time derivative of $h(x, t)$; see Eq. (3.11). On the other hand, the present encounter velocity of the ship and the waves $V_e = V_{ship} + L_{wave}/t_{wave}$ is large, being $V_e/V_{ship} = 1.87$ (19.25m/s on full scale). As a comparison, the threshold velocity for slamming in the present case would be much smaller $V_e/V_{ship} = 0.51$ (5.3m/s on full scale) according to Ochi (1964). Further, the front of the approaching wave in this study case is almost like a vertical wall just before it hits the stem. These observations may be interpreted in such a way that the ship bow could resemble a wedge which hits the water in its longitudinal direction. It may be asked whether the situation at the level of the design waterline could correlate to some extent with the entry into the water of a body in a vertical direction. This idea is tested by applying the formulae (7.1)-(7.2) in the longitudinal direction in the present case. The angle corresponding to the deadrise angle at the stem is about 63° . This gives $C_p \approx 1.8$, according to Eq. (7.2). In the case of the present entrance velocity and the maximum pressure given by the RANS computation, Eq. (7.1) gives $C_p \approx 0.7$. Thus, the present slamming pressure coefficient is much smaller than the value in a respective drop test would be, but it still has the same order of magnitude. It is logical that this value should be smaller in the present case because of the presence of the free surface. A part of the impact load is released immediately as the deformation of the free surface.

The previous reflection on Wagner's theorem suggests that the impact-type loads in the case investigated here may follow, to some extent, a somewhat similar regularity to the slamming loads in a classical case of a vertical entry into the water. For one thing, it suggests the importance of the longitudinal relative velocity. It is relevant to notice that the relative velocity in short waves is large in the longitudinal direction and not in the vertical direction. The results presented in Section 6.1 suggest the importance of the longitudinal flow by showing that the fronts of both the wave that is encountered and the uppermost part of the pressure distribution on the hull follow the shapes of the buttock lines, which restrict the

flow in the longitudinal direction. The importance of the longitudinal direction of the flow has not commonly been commented on in the previous springing studies. On the other hand, some previous studies on springing have presented numerical predictions that include a slamming model which are further developments of Wagner's theory, e.g. (Lee et al., 2012) and (Storhaug et al., 2003). Lee et al. (2012) reported that in their study the applied 2D slamming model (Tuitman and Malenica, 2009) gives very small slamming forces in a head wave condition that causes second-order springing of a container ship. They applied the slamming model to inclined sections ($\approx 27^\circ$ from the vertical direction) in the area of the bow. It is interesting to speculate whether their results would be different if the model were applied to, for example, waterlines instead, which would emphasise the relative velocity in the longitudinal direction.

In the present case, reflecting on Wagner's theory on slamming loading further suggests that the entrance angle of the bow matters for impact-type loads. The present results themselves underline the importance of the local entrance angle for the behaviour of the local loads at the level of the design waterline. Particularly, they show that the short rise time and the longer fall time of local loads are most important in the area of the largest entrance angle before becoming more symmetric with a decreasing local entrance angle. The previous studies have not commented directly on the effect of the local entrance angle on springing, but a previous finding supports this observation. Storhaug and Moan (2007a) touched on the effect of the shape of the waterline by conducting model tests both with a typical bow shape of a bulk carrier and with a sharp triangular bow. They reported a reduction in the second-order transfer function with the sharper bow.

The present results allow the importance of the three-dimensionality of the flow on the second-order springing excitation to be judged in the case investigated here. In this respect, the effect of the local entrance angle at the design waterline is one factor. Another factor is the effect of the shape of the buttock lines in the area of the bow. The buttock lines affect the phase difference between the local loads at different depths, which matters for the second harmonic amplitude of the vertical force at a station. Having the combined importance of the local entrance angle at the design waterline and of the shape of the buttock lines in the area of the bow makes this flow case highly three-dimensional. The literature includes some remarks which may indicate the interest in the rela-

tionship of the three-dimensionality of the flow and springing excitation. Vidic-Perunovic (2010) pointed out the importance of the linear hydrodynamic excitation resulting from diffracted waves on springing, which also demonstrates the importance of the three-dimensional effects. In practice, some authors have recently predicted second-order springing with three-dimensional methods for hydrodynamic loading; see (Kim et al., 2012), (Lee et al., 2012), and (Oberhagemann and el Moctar, 2012).

As a further detail, the present results show that the bow bulb steepens the approaching wave; see Section 6.1. This steepening may make the effect of the impact-type loading more important and thereby increase the second harmonic loading. The previous springing studies on different ship types do not support the possibility that a bow bulb would increase springing. Storhaug and Moan (2007a) tested in model experiments the effect of the bow bulb on the springing of a bulk carrier in ballast condition in irregular waves. They report that the effect of the bulb on the vibration damage is small. Bell and Taylor (1968) presented full-scale measurements on a tanker with and without a ram bow. They report that detailed comparisons are not possible as a result of differences in the sea states, but that the increase in the level of vibration with the speed of the ship followed a similar pattern with and without the ram bow.

All in all, the results of this study demonstrate that the major deformation of the free surface can matter for the second-order springing excitation. This finding may bring into question whether the traditional sea-keeping methods are capable of predicting ship springing. The existing literature includes reflections on the same topic, e.g. (Storhaug et al., 2003).

8. Conclusions and recommendations for future work

This study shows that a RANS solver with a VOF method can predict ship wave loads at a detailed level in very short and steep waves when the discretisation resolutions, for instance, are carefully selected. This finding was confirmed with a solution accuracy assessment and with comparisons of the computed results against the measured data. The case investigated here differs from most of the cases in the previous literature in the shortness of the waves that were encountered. Thus, from the point of view of the state of the art, this study increases confidence in the capability of interface-capturing methods to predict ship wave loads. In general, having reliable computed predictions on wave loads at a detailed level opens up new opportunities for learning more about their origin.

This study demonstrates that the vertical second harmonic wave loading originates in the foremost part of the ship bow in the case investigated here. The analysis of the results reveals that two features of local loading matter for the development of the second harmonic total loading along the length of the hull. These features are the ratio of the rise and fall times of individual local loads and the phase difference between local loads at different depths at a station. The second harmonic wave loading is at its largest when the ratio of the rise and fall times is small and when a small phase difference exists between the loading at different depths.

This study explains how the local properties of the hull form affect the local loading in the case that was investigated. The bow bulb contributes by acting like a shallow beach, which makes the approaching wave very steep before it hits the stem. The local entrance angle correlates with the rise and fall of the local pressures at the level of the design waterline. A larger entrance angle makes the rise time shorter and the fall time longer. A corresponding behaviour was observed in the behaviour of the free surface in front of the buttock lines, too. The front of the propagating

wave and the related pressure distribution follow the shape of the buttock lines. Thus, the shapes of the buttock lines explain the phase difference between the local loading at different depths, especially in the foremost part of the hull.

The findings on the origin of the second harmonic wave loading and their relation on the local hull form that are presented here are believed to be original in the context of the existing knowledge on springing excitation. Nevertheless, they are compatible with the general ideas of springing relating to the fullness of a bow and the steepness of waves.

In future work, the generality of the findings on springing excitation should be studied. Firstly, the second harmonic wave loads with a similar hull form in different wave heights should be studied. Second, several hull forms and different ship types (different critical ratios of wave and ship lengths) should be analysed to learn how general these particular findings on the effect of the hull form are for the second harmonic wave loads. Both head and oblique waves should be considered. Moreover, in realistic sea states, second harmonic wave loads are not the only source of excitation. Therefore, the relation between the hull form and the other excitation types in regular waves needs to be studied. Finally, the origin of springing excitation in irregular waves needs to be addressed. Learning more about the wave loads on a rigid hull can help in gaining a better understanding of the origin of springing excitation. Furthermore, depending on the type of ship, studying how the springing vibration itself affects the exciting wave loads can be important too. Understanding the origin of resonant springing excitation should help gain a better understanding of the relation of springing- and slamming-type loading, too. The combination of these two effects has often been mentioned in recent publications.

References

- Bell, A.O. and Taylor, K.V., "Wave-excited hull vibration, Measurements on a 47,000-d.w.t. tanker," *Shipping World and Shipbuilder*, 1968, pp. 412–426.
- Carrica, P.M., Fu, H., and Stern, F., "Computations of self-propulsion free to sink and trim and of motions in head waves of the KRISO Container Ship (KCS) model," *Applied Ocean Research*, Vol. 33, 2011, pp. 309–320.
- Carrica, P.M., Wilson, R.V., Noack, R.W., and Stern, F., "Ship motions using single-phase level set with dynamic overset grids," *Computers & Fluids*, Vol. 36, 2007, pp. 1415–1433.
- Carrica, P.M., Wilson, R.V., and Stern, F., "Unsteady RANS simulation of the ship forward speed diffraction problem," *Computers & Fluids*, Vol. 35, 2006, pp. 545–570.
- Castiglione, T., Stern, F., Bova, S., and Kandasamy, M., "Numerical investigation of the seakeeping behaviour of a catamaran advancing in regular head waves," *Ocean Engineering*, Vol. 38, 2011, pp. 1806–1288.
- Chapra, S.C. and Canale, R.P., *Numerical methods for engineers*, McGraw-Hill, Inc., Singapore, 1988, 2nd ed.
- Deng, G.B., Personal communication March 18, 2014.
- Deng, G.B., Queutey, P., and Visonneau, M., "Seakeeping prediction for a container ship with RANS computation," 22nd *Chinese Hydrodynamic Conference*, Chengdu, China, 2009.
- el Moctar, O., Oberhagemann, J., and Schellin, T.E., "Free surface RANS method for hull girder springing and whipping," *Transactions of the Society of Naval Architects and Marine Engineers*, Vol. 119, 2011, pp. 48–66.
- Goodman, R.A., "Wave-excited main hull vibration in large tankers and bulk carriers," *Transactions of the Royal Institute of Naval Architects*, 1971, pp. 167–184.
- Guo, B.J., Steen, S., and Deng, G.B., "Seakeeping prediction of KVLCC2 in head waves with RANS," *Applied Ocean Research*, Vol. 35, 2012, pp. 56–67.
- Hänninen, S.K., Mikkola, T., and Matusiak, J., "Computational and experimental study on local ship loads in short and steep waves," *Journal of Marine Science and Technology*, Vol. 19, No. 1, 2014, pp. 103–115.

- Hänninen, S.K., Mikkola, T., and Matusiak, J., “On the numerical accuracy of the wave load distribution on a ship advancing in short and steep waves,” *Journal of Marine Science and Technology*, Vol. 17, No. 2, 2012, pp. 125–138.
- Henderson, D.M., Patterson, M.S., and Segur, H., “On the laboratory generation of two-dimensional, progressive, surface waves of nearly permanent form on deep water,” *Journal of Fluid Mechanics*, Vol. 559, 2006, pp. 413–427.
- Hino, T., ed., *The Proceedings of CFD Workshop Tokyo 2005*, National Maritime Research Institute, 2005.
- Hoffman, D. and van Hooff, R.W., “Feasibility study of springing model tests of a Great Lakes bulk carrier,” *International Shipbuilding Progress*, 1973, pp. 72–86.
- Hoffman, D. and van Hooff, R.W., “Experimental and theoretical evaluation of springing on a Great Lakes bulk carrier,” *International Shipbuilding Progress*, Vol. 23, 1976, pp. 173–193.
- Hu, J.J., Wu, Y.S., Tian, C., Wang, X.L., and Zhang, F., “Hydroelastic analysis and model tests on the structural responses and fatigue behaviours of an ultra-large ore carrier in waves,” *Proceedings of the Institution of Mechanical Engineers, Part M: Journal of Engineering for the Maritime Environment*, Vol. 226, No. 2, 2012, pp. 135–155.
- Kalske, S., “Application of Ray Theory in Prediction of Wave Excitation for Cruise Ships in Short Waves,” Tech. Rep. AALTO-AM-19, Department of Applied Mechanics, School of Science and Technology, Aalto University, 2010.
- Kim, J.H., Kim, Y., Kang, B.C., and Kim, Y., “Ship springing analysis for very large container ship,” *International Journal of Offshore and Polar Engineering*, Vol. 22, No. 3, 2012, pp. 217–224.
- Klemt, M., “RANSE simulation of ship seakeeping using overlapping grids,” *Ship Technology Research*, Vol. 52, 2005, pp. 65–81.
- Kyowa, “Product information,” Available at http://www.kyowa-ei.co.jp/eng/product/sensors/pressure/pgm_g.html, .
- Larsson, L., Stern, F., and Visonneau, M., eds., *A workshop on Numerical Ship Hydrodynamics*, Vol. II, Chalmers University of Technology, Gothenburg, Sweden, 2010.
- Lee, Y., White, N., Wang, Z., Zhang, S., and Hirdaris, S., “Comparison of springing and whipping responses of model tests with predicted nonlinear hydroelastic analyses,” *International Journal of Offshore and Polar Engineering*, Vol. 22, No. 3, 2012, pp. 209–216.
- Lloyd, A.R., *Seakeeping: Ship behaviour in rough weather*, Ellis Horwood Limited, Chichester, England, 1989.
- Manderbacka, T., Tenovuo, K., and Matusiak, J., “Model experiments of springing-type wave loads on a cruise vessel,” 8th *International Conference on HydroDynamics*, Nantes, France, 2008.
- Mikkola, T., “Time Accurate Simulation of a Plunger Type Wave Maker Using Unstructured Finite Volume Solver with Surface Tracking,” 26th *Symposium on Naval Hydrodynamics*, Rome, Italy, 2006.

- Miyake, R., Matsumoto, T., Zhu, T., and Abe, N., “Experimental studies on the hydroelastic response due to springing using a flexible mega-container ship model,” 8th *International Conference on HydroDynamics*, Nantes, France, 2008.
- Moe, E., Holtmark, G., and Storhaug, G., “Full scale measurements of the wave induced hull girder vibrations of an ore carrier trading in the North Atlantic,” *RINA International Conference, Design & Operation of Bulk Carriers*, London, UK, 2005, pp. 57–85.
- Newman, J.N., *Marine Hydrodynamics*, The MIT Press, Cambridge, Massachusetts, 1977.
- Numeca, “Theoretical Manual FINETM / Marine v2.3,” , 2011a.
- Numeca, “User manual FINETM/Marine v2.3, Documentation v2.3b,” , 2011b.
- Oberhagemann, J. and el Moctar, O., “Numerical and experimental investigations of whipping and springing of ship structures,” *International Journal of Offshore and Polar Engineering*, Vol. 22, No. 2, 2012, pp. 108–114.
- Oberhagemann, J., el Moctar, O., and Schellin, T.E., “Fluid-structure coupling to assess whipping effects on global loads of a large containership,” 27th *Symposium on Naval Hydrodynamic*, Seoul, Korea, 2008.
- Oberhagemann, J., Holtmann, M., el Moctar, O., Schellin, T.E., and Kim, D., “Stern slamming of a LNG carrier,” *Journal of Offshore Mechanics and Arctic Engineering*, Vol. 131, 2009, pp. 031103–1–031103–10.
- Ochi, M.K., “Prediction of occurrence and severity of ship slamming at sea,” 5th *Symposium on Naval Hydrodynamics, Ship motions and drag reduction*, 1964, pp. 545–596.
- Orihara, H., “Comparison of CFD simulations with experimental data for a tanker model advancing in waves,” *International Journal of Naval Architecture and Ocean Engineering*, Vol. 3, 2011, pp. 1–8.
- Orihara, H. and Miyata, H., “Evaluation of added resistance in regular incident waves by computational fluid dynamics motion simulation using an overlapping grid system,” *Journal of Marine Science and Technology*, Vol. 8, 2003, pp. 47–60.
- Queutey, P. and Visonneau, M., “An interface capturing method for free-surface hydrodynamic flows,” *Computers & Fluids*, Vol. 36, 2007, pp. 1481–1510.
- Sato, Y., Miyata, H., and Sato, T., “CFD simulation of 3-dimensional motion of a ship in waves: application to an advancing ship in regular heading waves,” *Journal of Marine Science and Technology*, Vol. 4, 1999, pp. 108–116.
- Shao, Y.L. and Faltinsen, O.M., “A numerical study of the second-order wave excitation of ship springing in infinite water depth,” *Proceedings of the Institution of Mechanical Engineers, Part M: Journal of Engineering for the Maritime Environment*, Vol. 226, No. 2, 2012, pp. 103–119.
- Slocum, S. and Troesch, A.W., “Non-linear ship springing experiments,” Tech. Rep. 226, Department of Naval Architecture and Marine Engineering, College of Engineering, The University of Michigan, 1983.

- Storhaug, G., "Experimental investigation of wave induced vibrations and their effect on the fatigue loading of ships," Ph.D. thesis, Department of Marine Technology, Faculty of Engineering Science and Technology, Norwegian University of Science and Technology, 2007.
- Storhaug, G. and Moan, T., "The effect of bow shape on the springing/whipping response of a large ocean-going vessel - investigated by an experimental method," *26th International Conference on Offshore Mechanics and Arctic Engineering, OMAE2007*, San Diego, California, United States of America, 2007a.
- Storhaug, G. and Moan, T., "Springing/whipping response of a large ocean-going vessel - investigated by an experimental method," *10th International Symposium on Practical Design of Ships and Other Floating Structures*, Houston, Texas, United States of America, 2007b.
- Storhaug, G., Moe, E., and Holtsmark, G., "Measurements of wave induced hull girder vibrations of an ore carrier in different trades," *Journal of Offshore Mechanics and Arctic Engineering*, Vol. 129, 2007, pp. 279–289.
- Storhaug, G., Vidic-Perunovic, J., Rüdinger, F., Holtsmark, G., Helmers, J.B., and Gu, X., "Springing/whipping response of a large ocean going vessel - A comparison between numerical simulations and full-scale measurements," *3rd International Conference on Hydroelasticity in Marine Technology*, Oxford, UK, 2003.
- Troesch, A.W., "Ship springing - An experimental and theoretical study," Tech. Rep. 219, Department of Naval Architecture and Marine Engineering, The University of Michigan, 1980.
- Troesch, A.W., "Effects of nonlinearities on hull springing," *Marine Technology*, Vol. 21, No. 4, 1984, pp. 356–363.
- Tuitman, J.T. and Malenica, S., "Fully coupled seakeeping, slamming, and whipping calculations," *Proceedings of the Institution of Mechanical Engineers, Part M: Journal of Engineering for the Maritime Environment*, Vol. 223, 2009, pp. 439–456.
- Vidic-Perunovic, J., "Springing response due to bidirectional wave excitation," Ph.D. thesis, Department of Mechanical Engineering, Technical University of Denmark, 2005.
- Vidic-Perunovic, J., "Towards the prediction of hull springing response," *ASME 2010, 29th International Conference on Ocean, Offshore and Arctic Engineering, OMAE2010*, Shanghai, China, 2010.
- Vidic-Perunovic, J., "Ship springing response in finite water depth," *Journal of Ship Research*, Vol. 56, No. 2, 2012, pp. 80–90.
- Vidic-Perunovic, J. and Jensen, J.J., "Non-linear springing excitation due to a bidirectional wave field," *Marine Structures*, Vol. 18, 2005, pp. 332–358.
- Visonneau, M., Queutey, P., Leroyer, A., Deng, G.B., and Guilmineau, E., "Ship motions in moderate and steep waves with an interface capturing method," *8th International Conference on HydroDynamics*, Nantes, France, 2008.

- Wackers, J., Koren, B., Raven, H.C., van der Ploeg, A., Starke, A.R., Deng, G.B., Queutey, P., Visonneau, M., Hino, T., and Ohashi, K., "Free-surface viscous flow solution methods for ship hydrodynamics," *Archives of Computational Methods in Engineering*, Vol. 18, 2011, pp. 1–41.
- Wagner, H., "Landing of seaplanes," Technical memorandum 622, National Advisory Committee for Aeronautics, 1931.
- Zwart, P.J., Godin, P.G., Penrose, J., and Rhee, S.H., "Simulation of unsteady free-surface flow around a ship hull using a fully coupled multi-phase flow method," *Journal of Marine Science and Technology*, Vol. 13, 2008, pp. 346–355.

A. Turbulence model

The turbulence model applied here, Menter's *STT* $k - \omega$ model with wall functions, is described in this appendix. The description follows Numeca International (2011a). It is presented in a differential form. The model uses Wilcox's $K - \omega$ model near solid walls and the standard $K - \epsilon$ model, in a $K - \omega$ formulation, near boundary layer edges and in free-shear layers. The turbulent kinetic energy is denoted as K and the specific dissipation rate of the turbulent frequency as ω . The eddy viscosity μ_t is defined as

$$\mu_t = \frac{\rho K / \omega}{\max \{1, \Omega F_2 / (a_1 \omega)\}} \quad \text{with} \quad a_1 = 0.31. \quad (\text{A.1})$$

The auxiliary function F_2 is a function of wall distance d as follows:

$$F_2 = \tanh \left(\left[\max \left\{ 2 \frac{\sqrt{K}}{0.09 d \omega}, \frac{500 \mu}{\rho d^2 \omega} \right\} \right]^2 \right). \quad (\text{A.2})$$

The transport equations of K and ω are defined as

$$\frac{\partial \rho K}{\partial t} + \frac{\partial}{\partial x_j} \left(\rho U_j K - (\mu + \sigma_k \mu_t) \frac{\partial K}{\partial x_j} \right) = \tau_{t_{ij}} S_{ij} - \beta^* \rho \omega K \quad (\text{A.3})$$

$$\begin{aligned} \frac{\partial \rho \omega}{\partial t} + \frac{\partial}{\partial x_j} \left(\rho U_j \omega - (\mu + \sigma_\omega \mu_t) \frac{\partial \omega}{\partial x_j} \right) &= \\ &= P_\omega - \beta \rho \omega^2 + 2(1 - F_1) \frac{\rho \sigma_{\omega 2}}{\omega} \frac{\partial K}{\partial x_j} \frac{\partial \omega}{\partial x_j}. \end{aligned} \quad (\text{A.4})$$

The production term P_ω is approximated as

$$P_\omega \equiv 2\gamma\rho(S_{ij} - \omega S_{nn}\delta_{ij}/2)S_{ij} \cong \gamma\rho\Omega^2. \quad (\text{A.5})$$

In boundary layer zones, the model coefficients of the original $K - \omega$ model are blended with the transformed $K - \epsilon$ model in the free-shear layer and free-stream zones with the auxiliary blending function F_1 , which is defined as

$$\begin{aligned} F_1 &= \tanh \left(\left[\min \left\{ \max \left[\frac{\sqrt{K}}{0.09 d \omega}, \frac{500 \mu}{\rho d^2 \omega} \right], \frac{4\rho\sigma_{\omega 2}k}{CD_{k\omega}d^2} \right\} \right]^4 \right) \\ \text{with} \quad CD_{k\omega} &= \max \left\{ \frac{2\rho\sigma_{\omega 2}}{\omega} \frac{\partial K}{\partial x_j} \frac{\partial \omega}{\partial x_j}, 10^{-20} \right\}. \end{aligned} \quad (\text{A.6})$$

The constants of the STT $K - \omega$ model are

$$a_1 = 0.31 \quad \beta^* = 0.09 \quad \kappa = 0.41 \quad (\text{A.7})$$

The model coefficients β , γ , σ_k and σ_ω are defined by blending the coefficients of the original $K - \omega$ model, denoted as ϕ_1 , with those of the transformed $K - \epsilon$ model, denoted as ϕ_2 , as follows:

$$\phi = F_1\phi_1 + (1 - F_1)\phi_2 \quad \text{where} \quad \phi = \{\beta, \gamma, \sigma_k, \sigma_\omega\} \quad (\text{A.8})$$

The coefficients of the original models are defined for the inner model as

$$\begin{aligned} \sigma_{k1} &= 0.85 & \sigma_{\omega1} &= 0.500 & \beta_1 &= 0.0750 \\ \gamma_1 &= \beta_1/\beta^* - \sigma_{\omega1}\kappa^2/\sqrt{\beta^*} = 0.553 \end{aligned} \quad (\text{A.9})$$

and for the outer model as

$$\begin{aligned} \sigma_{k2} &= 1.00 & \sigma_{\omega2} &= 0.856 & \beta_2 &= 0.0828 \\ \gamma_2 &= \beta_2/\beta^* - \sigma_{\omega2}\kappa^2/\sqrt{\beta^*} = 0.440. \end{aligned} \quad (\text{A.10})$$

The free-stream values are set to

$$\omega_\infty = \frac{U_{ship}}{L_{ship}} \quad \mu_{t\infty} = 10^{-3}\mu_t \quad K_\infty \equiv \frac{\mu_{t\infty}\omega_\infty}{\rho}. \quad (\text{A.11})$$

Wall boundary conditions are

$$K = 0 \quad \omega = 10 \frac{6\mu}{\beta\rho(y_1)^2}. \quad (\text{A.12})$$

B. Second harmonic vertical force at the stations

This appendix compares the distributions of the second harmonic amplitude of the vertical force at the stations when the amplitudes are calculated with Equations (3.24) and (3.25). The results in Figure B.1 show that Equations (3.24) and (3.25) give similar second harmonic amplitudes in practice.

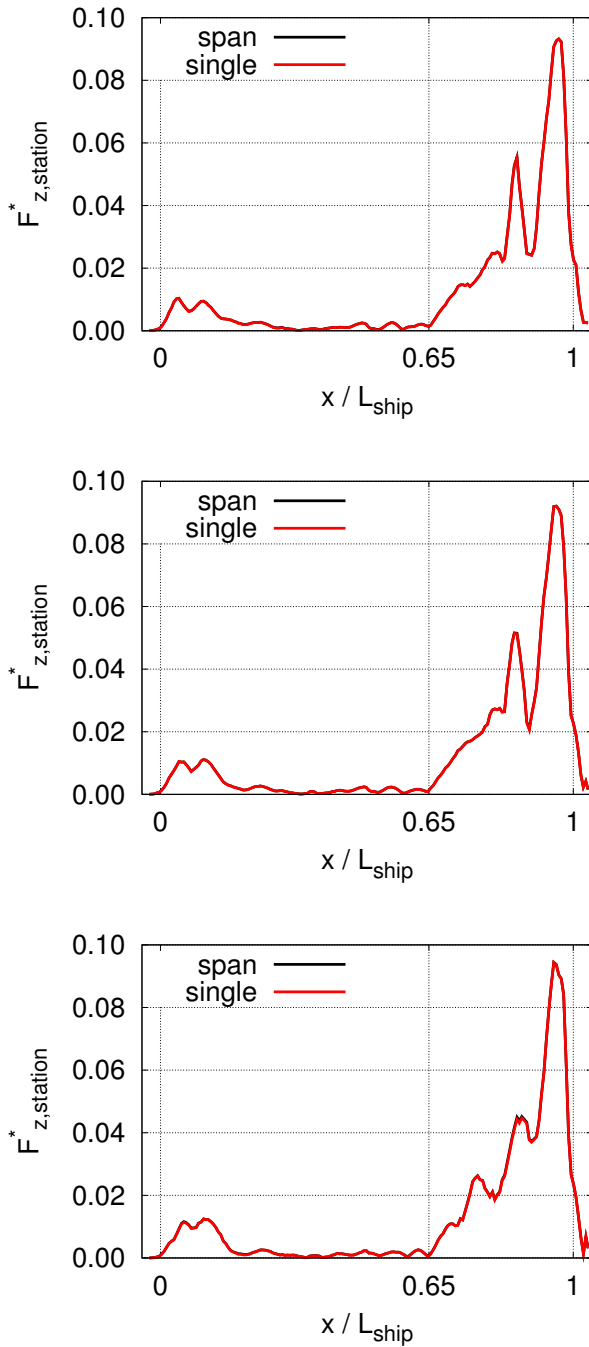


Figure B.1. Distributions of the second harmonic amplitude of the vertical force at stations. Black line: Equation (3.25). Red line: Equation (3.24). From top to bottom: fine, medium, and coarse resolutions with 20 iterations.

C. Instantaneous pressure distributions at the level of the design waterline

This appendix gives the instantaneous pressure distributions with the three resolutions at the level of the design waterline. The results in Figure C.1 show that the resolution does not have a significant effect on the results.

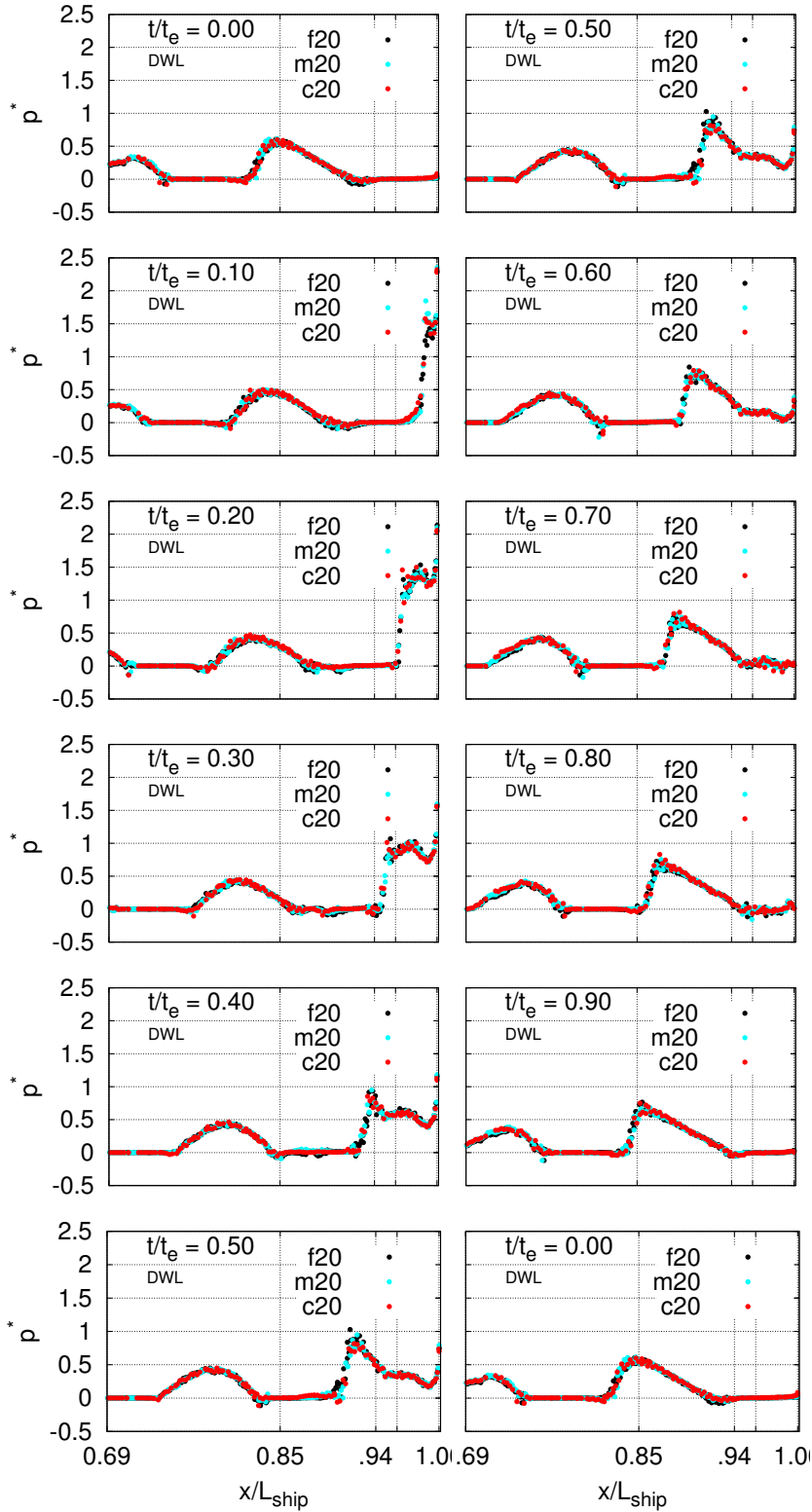


Figure C.1. Pressure distributions at the level of the design waterline. Black dots: fine resolution. Turquoise dots: medium resolution. Red dots: coarse resolution. Number of iterations: 20.

D. Pressure histories at six stations in the area of the bow

This appendix gives the time histories of the local pressures at six stations in the area of the bow with the three resolutions. The results show that the three resolutions predict similar main characteristics of the pressure histories.

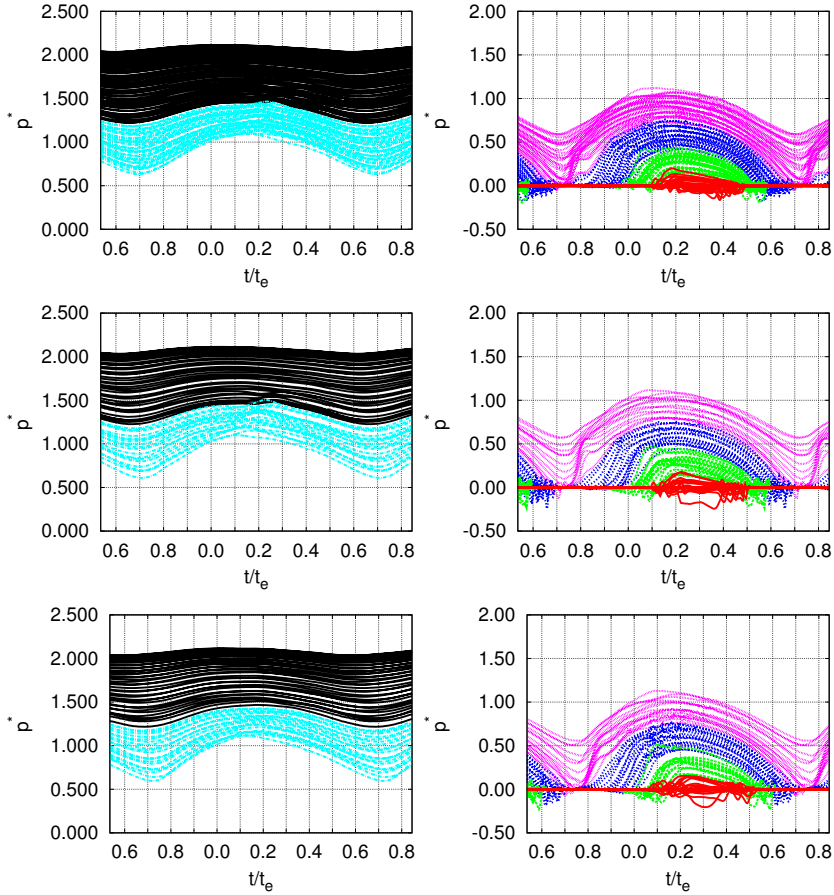


Figure D.1. $x/L_{ship} = 0.82$. Left: pressure histories below $z/H_{input} = -1.5$ with black lines and between $-1.5 < z/H_{input} < -1.0$ with light blue lines. Right: pressure histories between $-1.0 < z/H_{input} < -0.5$ with pink lines, between $-0.5 < z/H_{input} < 0.0$ (DWL) with blue lines, between $0.0 < z/H_{input} < 0.5$ with green lines and above $z/H_{input} = 0.5$ with red lines. From top to bottom: fine, medium, and coarse resolutions with 20 iterations.

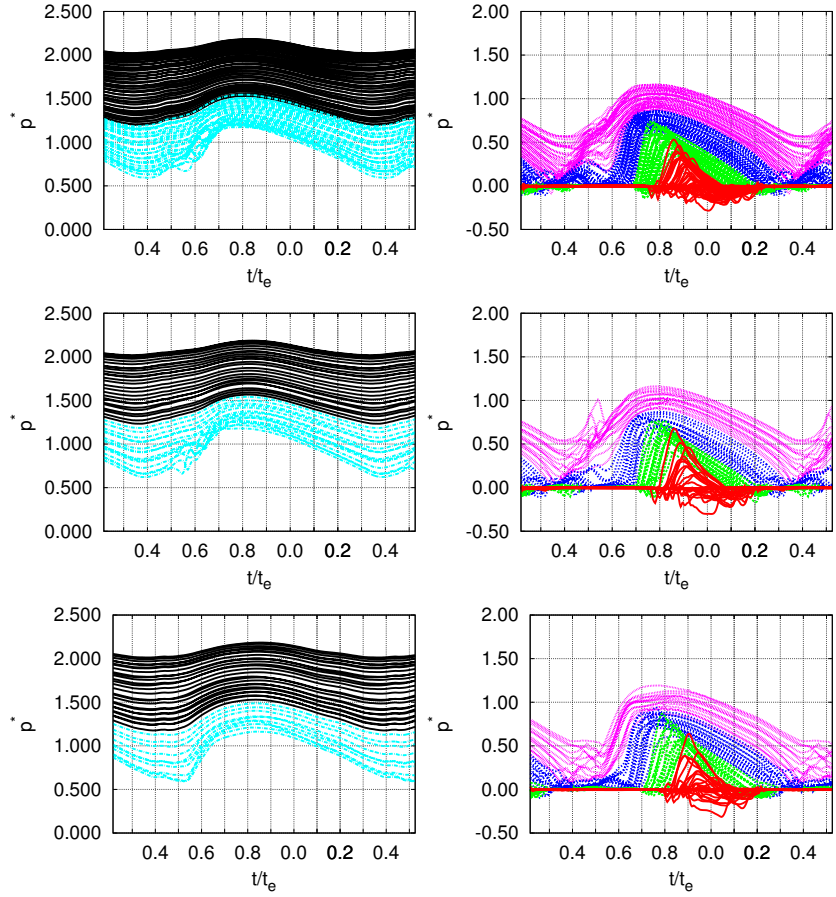


Figure D.2. $x/L_{ship} = 0.88$. See the caption of Figure D.1.

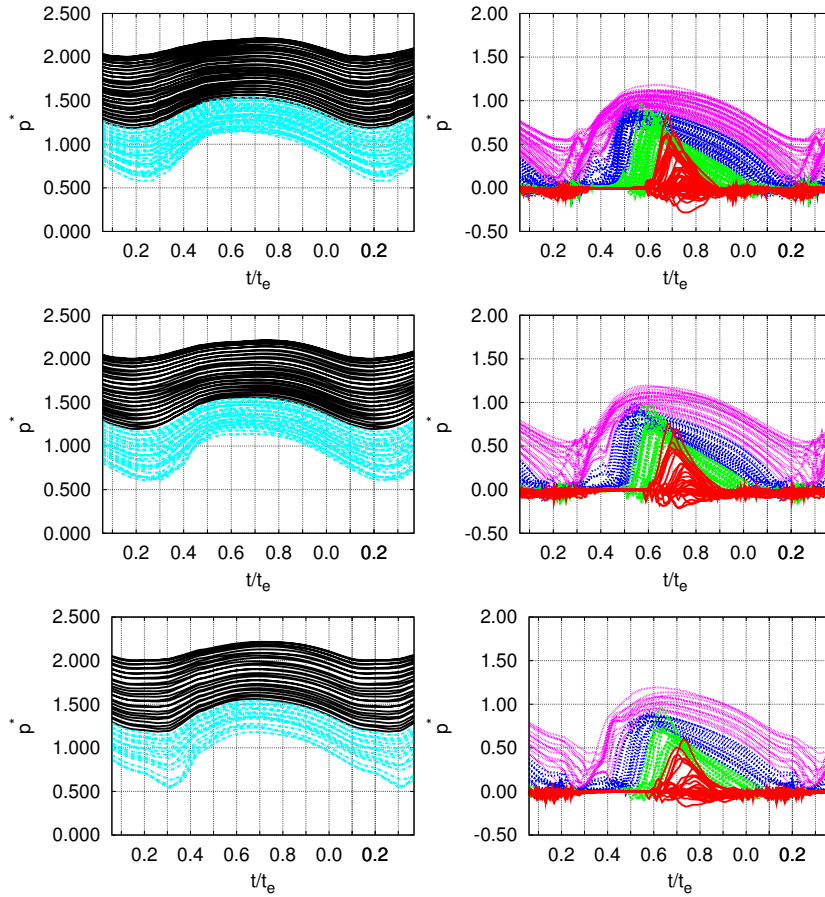


Figure D.3. $x/L_{ship} = 0.91$. See the caption of Figure D.1.

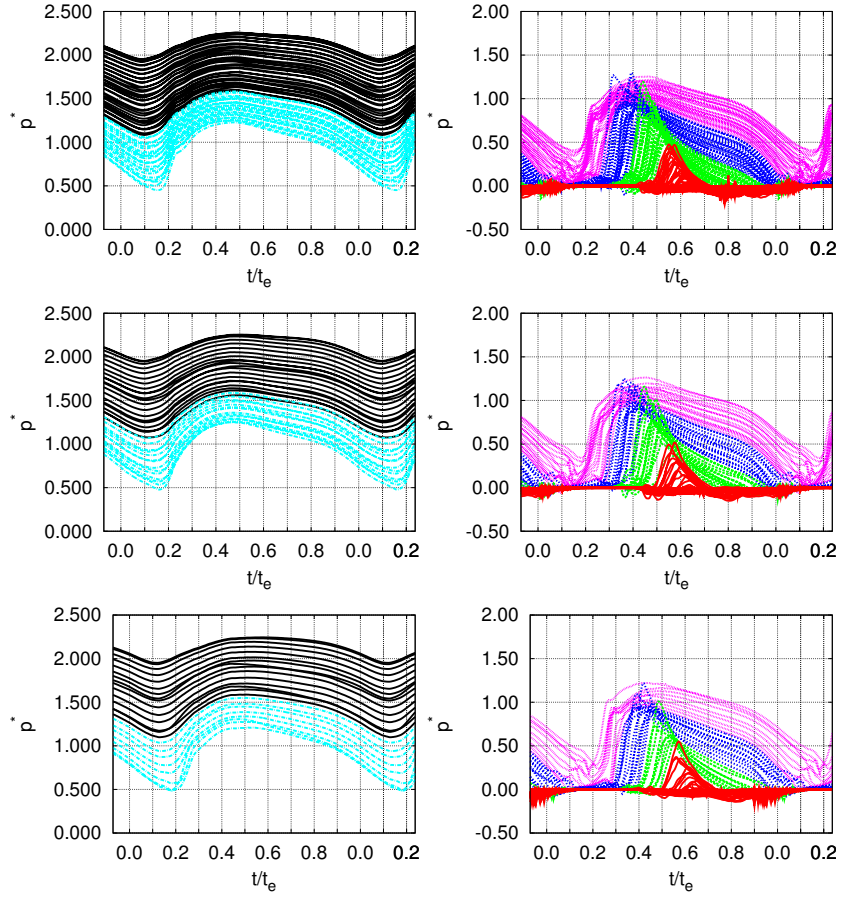


Figure D.4. $x/L_{ship} = 0.93$. See the caption of Figure D.1.

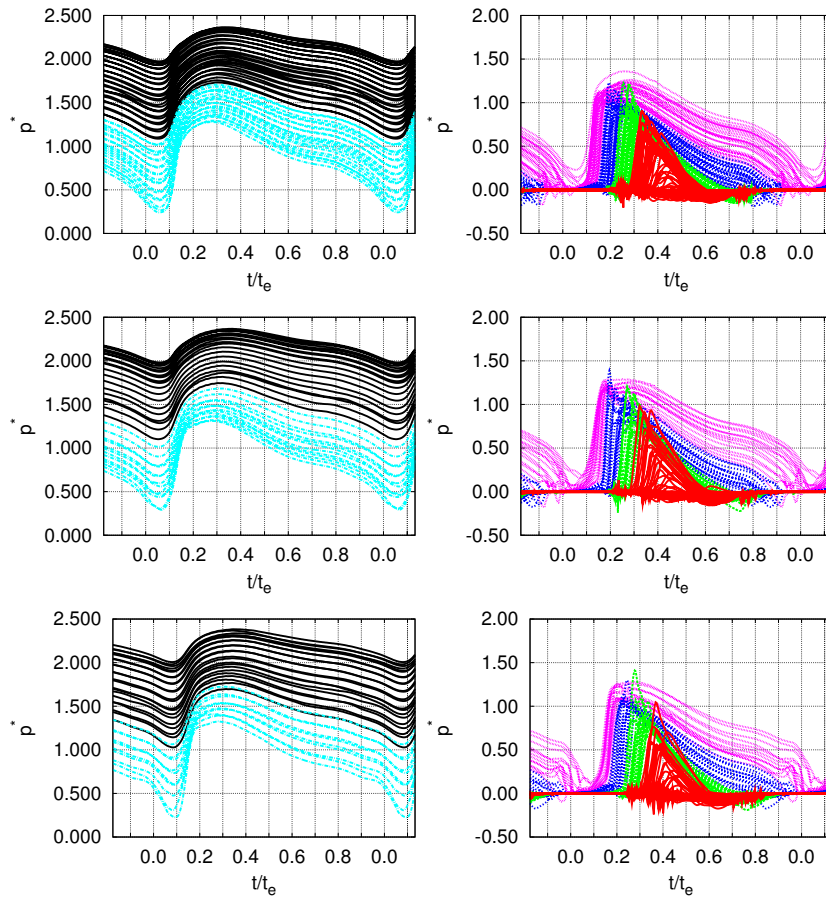


Figure D.5. $x/L_{ship} = 0.96$. See the caption of Figure D.1.

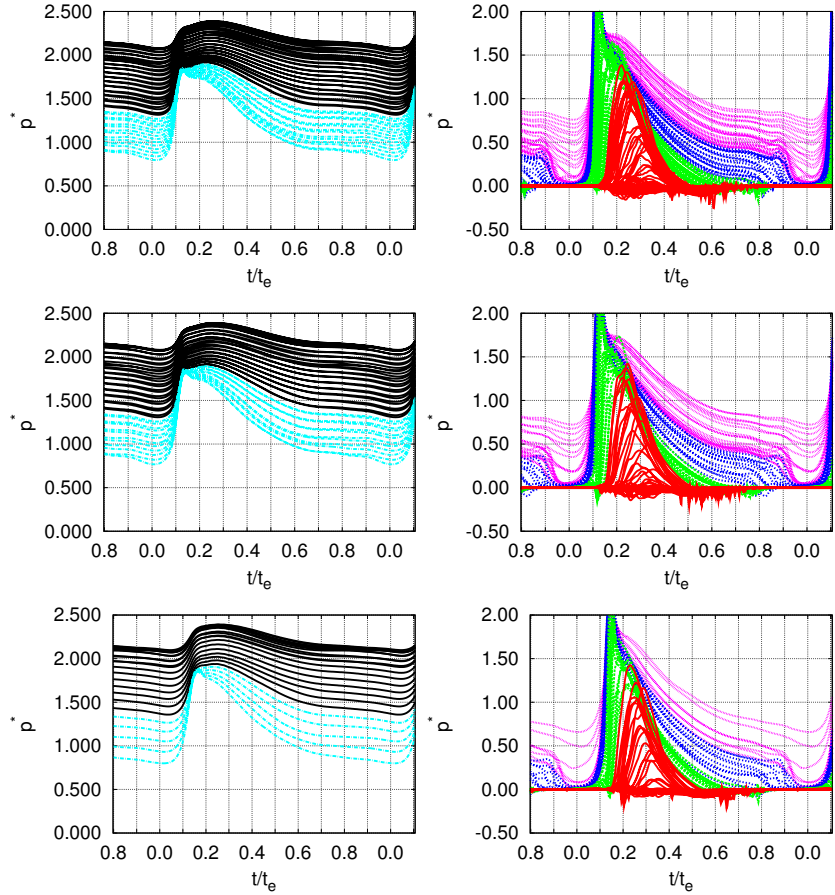
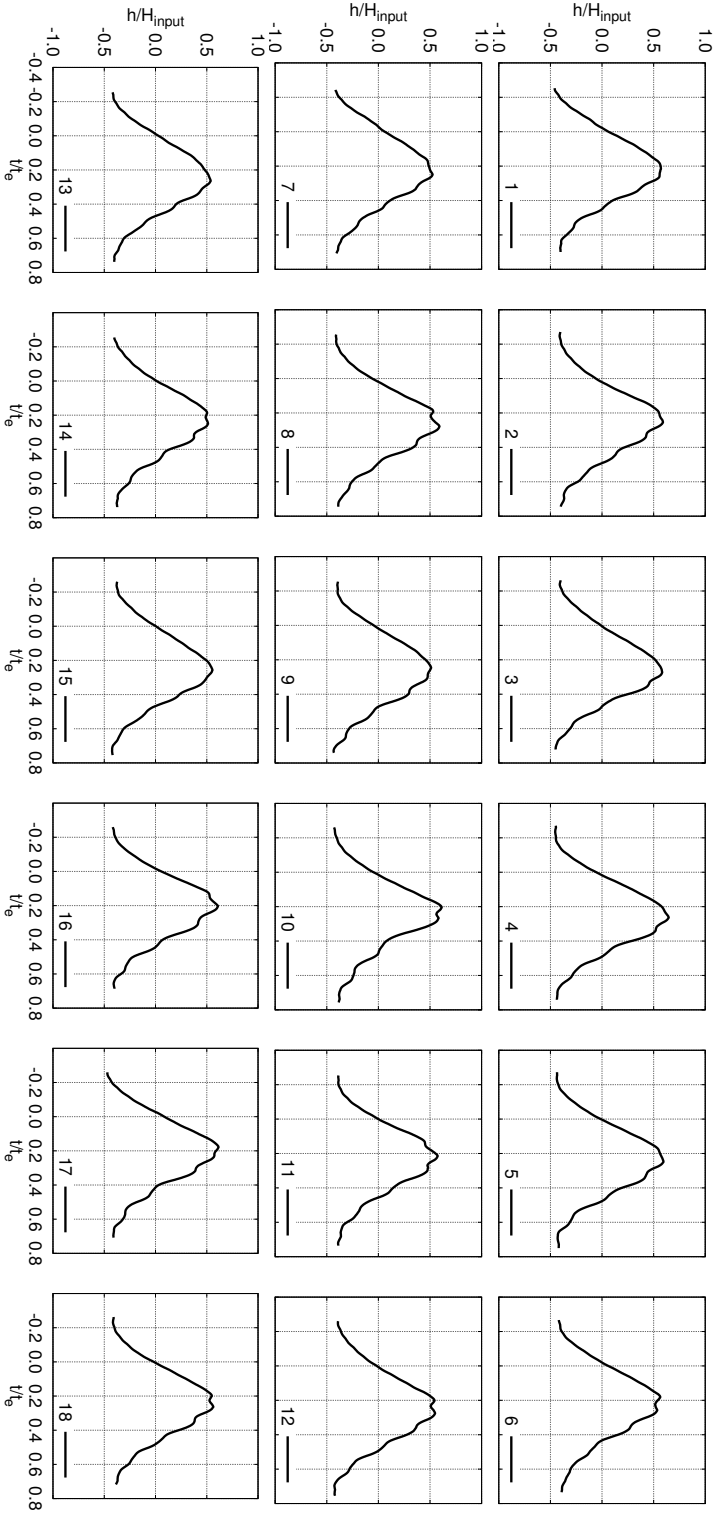


Figure D.6. $x/L_{ship} = 0.98$. See the caption of Figure D.1.

E. Measured waves

This appendix gives the wave signals of all the selected encounters separately.

Figure E.1. Selected waves encountered. (1/4)



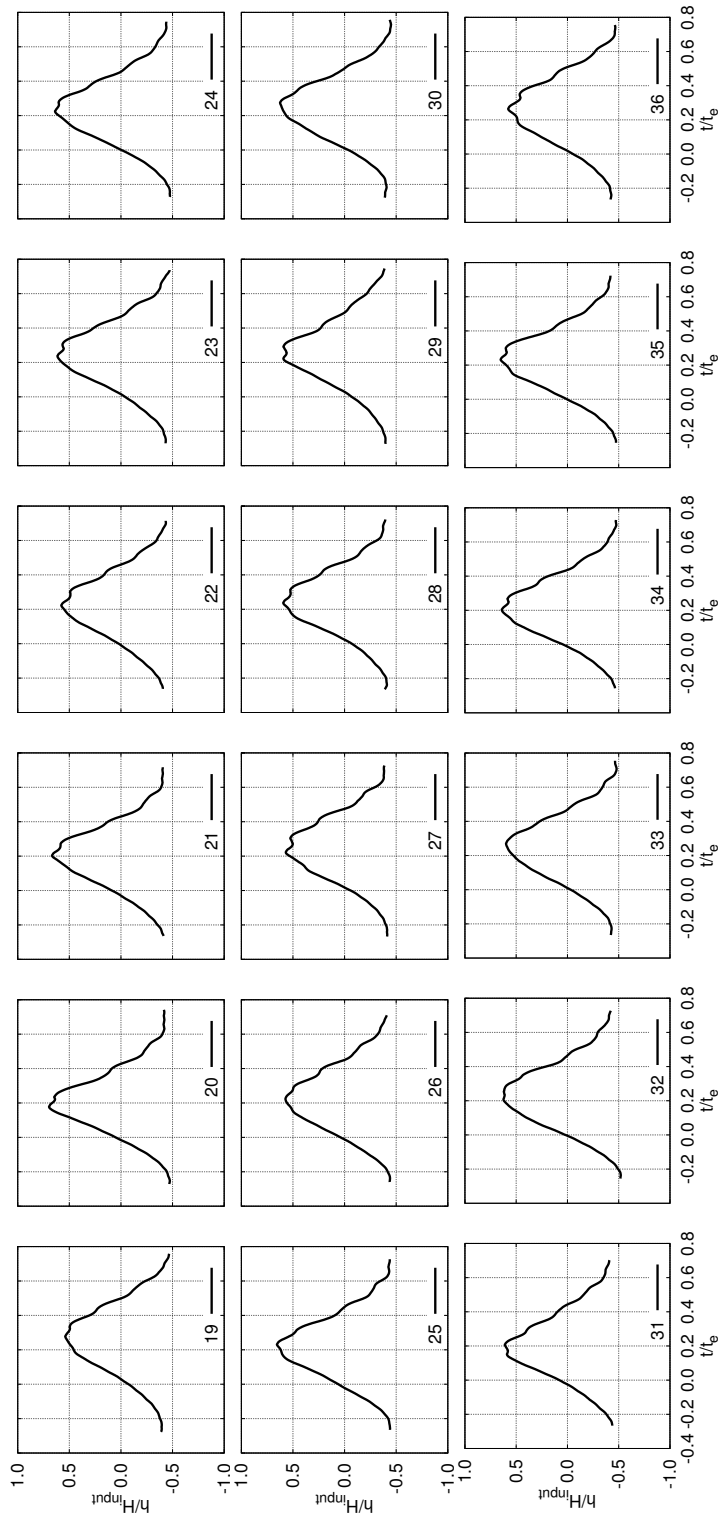
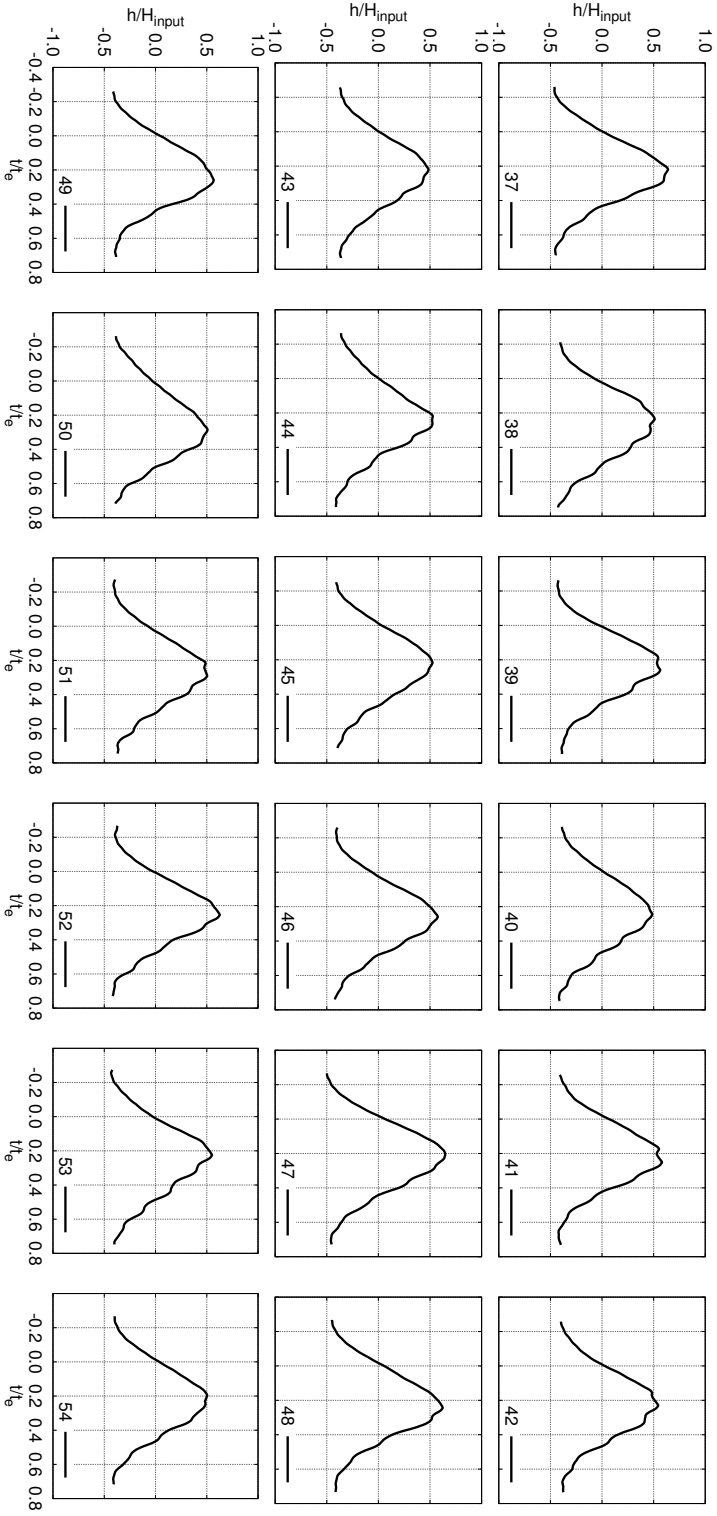


Figure E.2. Selected waves encountered. (2/4)

Figure E.3. Selected waves encountered. (3/4)



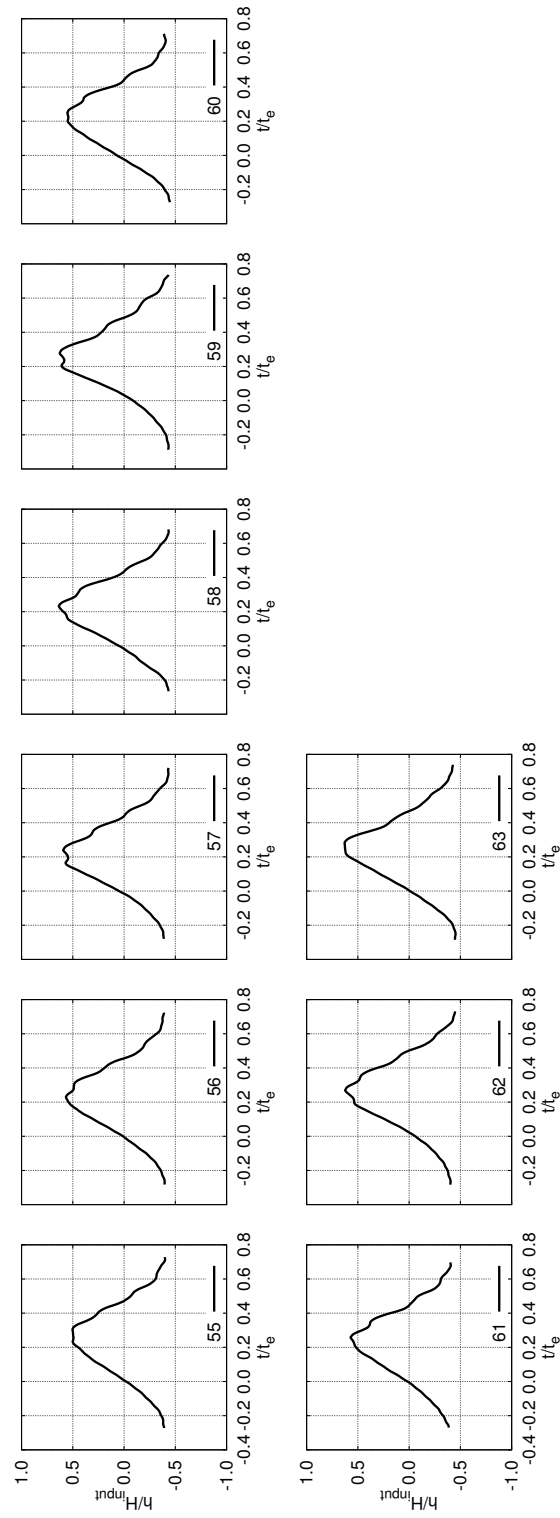


Figure E.4. Selected waves encountered. (4/4)

F. Measured pressures

This appendix gives the pressure signals of the selected encounters separately (red line). The corresponding wave signals (black line) are given, too.

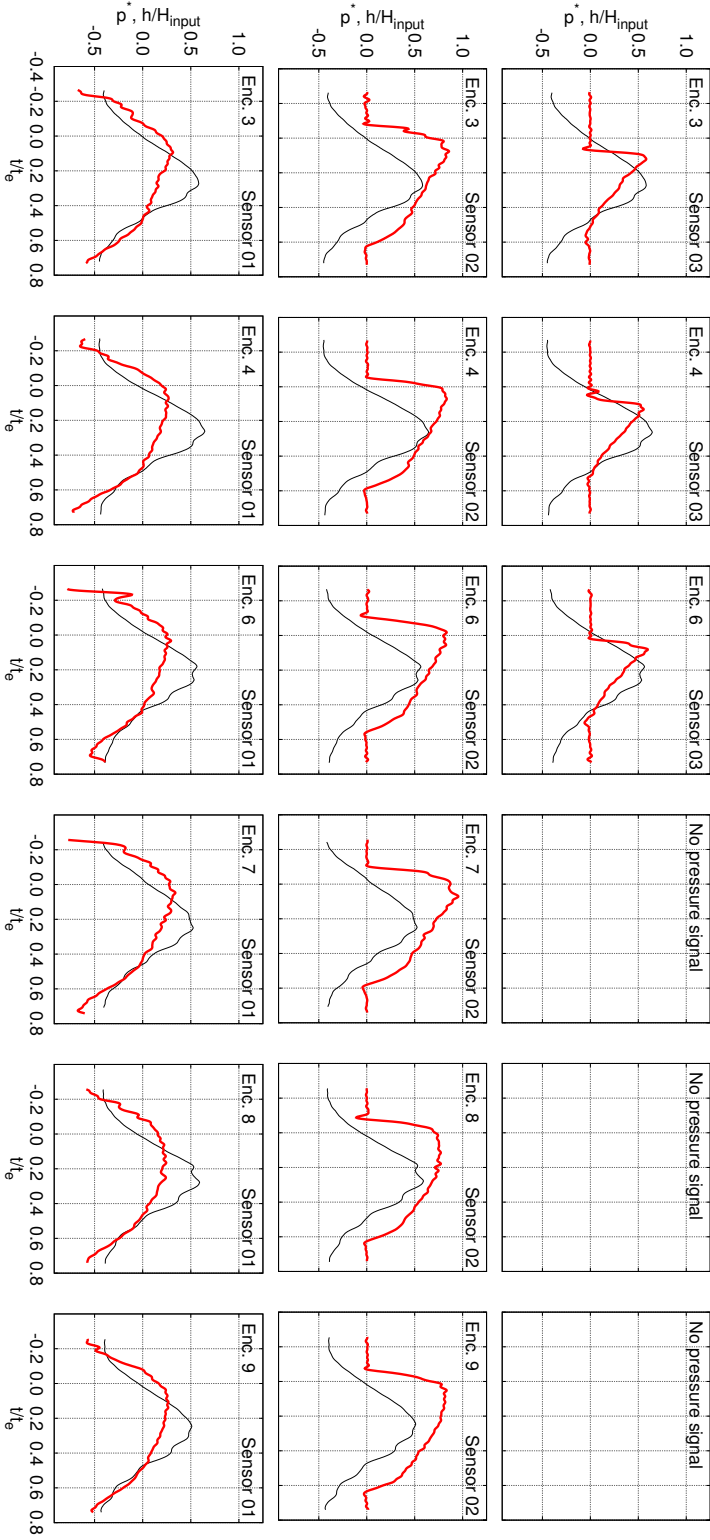


Figure F.1. Station $x/L_{ship} = 0.93$: fast rise time at Sensor 02. (1/9)

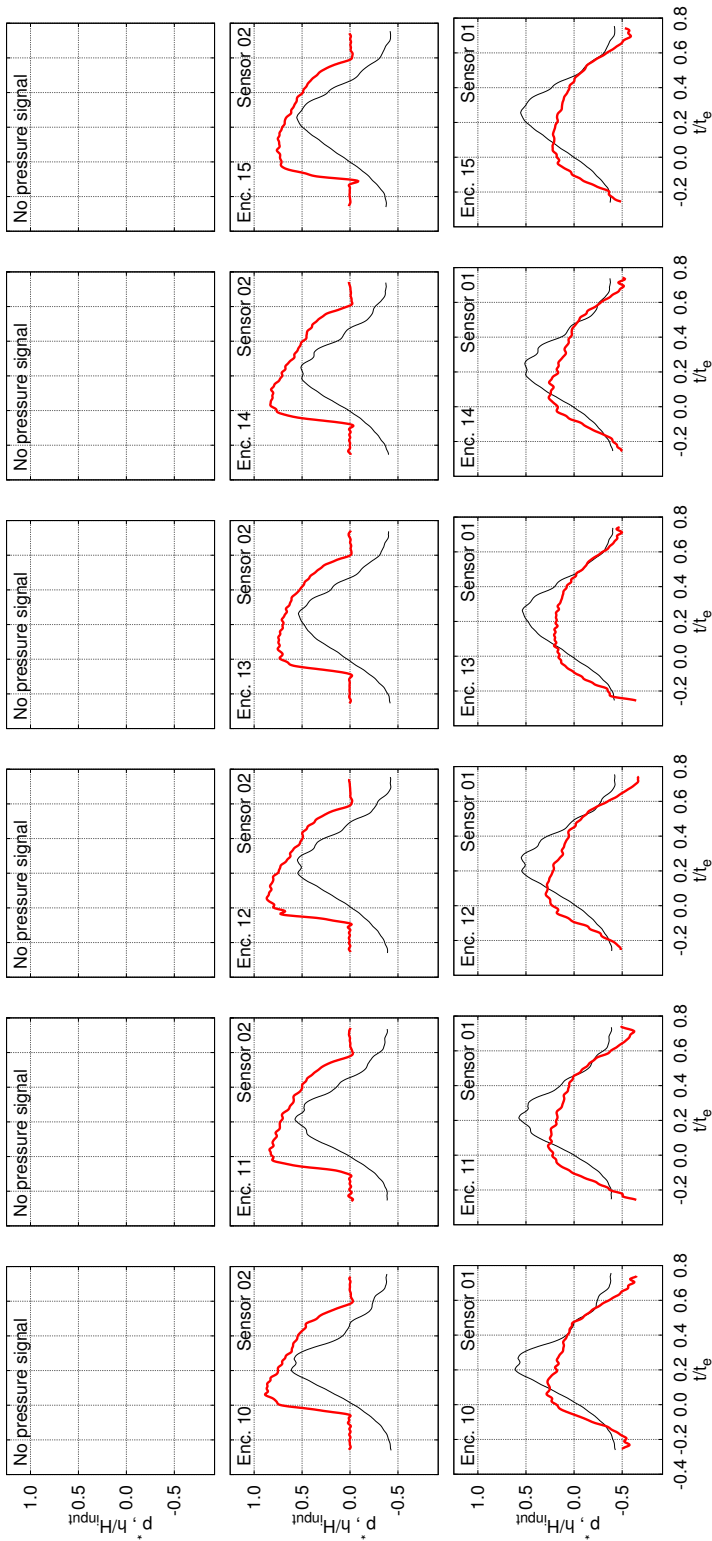


Figure F.2. Station $x/L_{ship} = 0.93$; fast rise time at Sensor 02. (2/9)

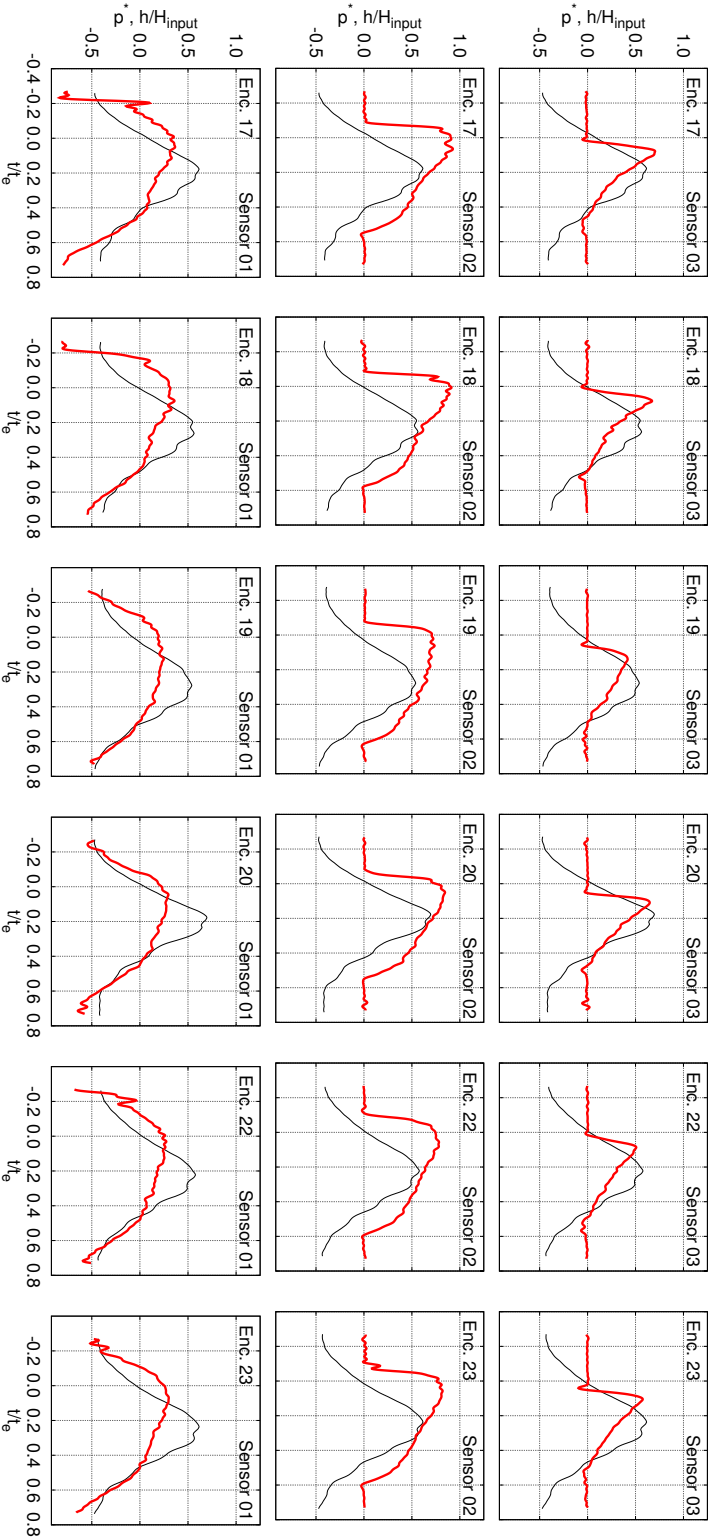


Figure F.3. Station $x/L_{ship} = 0.93$; fast rise time at Sensor 02. (3/9)

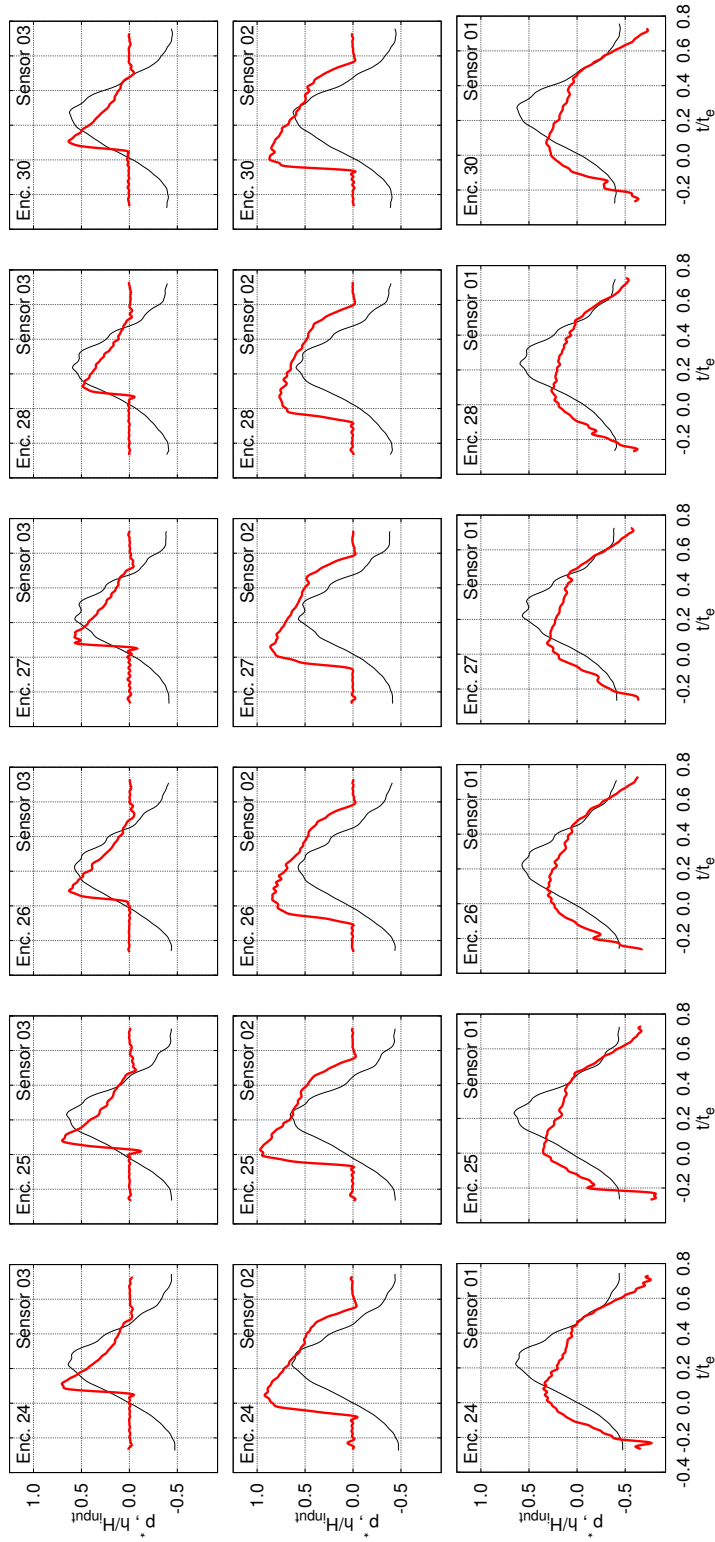


Figure F.4. Station $x/L_{ship} = 0.93$; fast rise time at Sensor 02. (4/9)

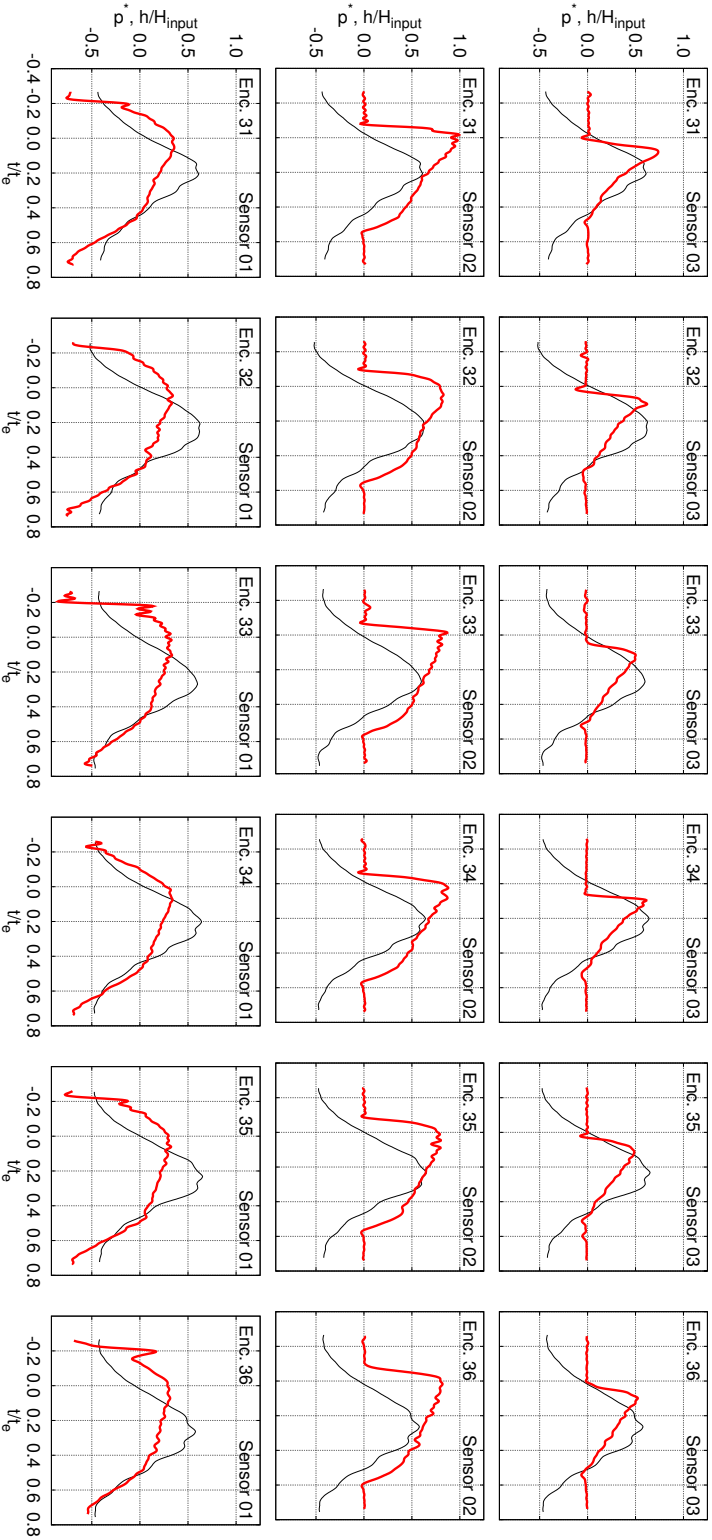


Figure F5. Station $x/L_{ship} = 0.93$; fast rise time at Sensor 02. (5/9)

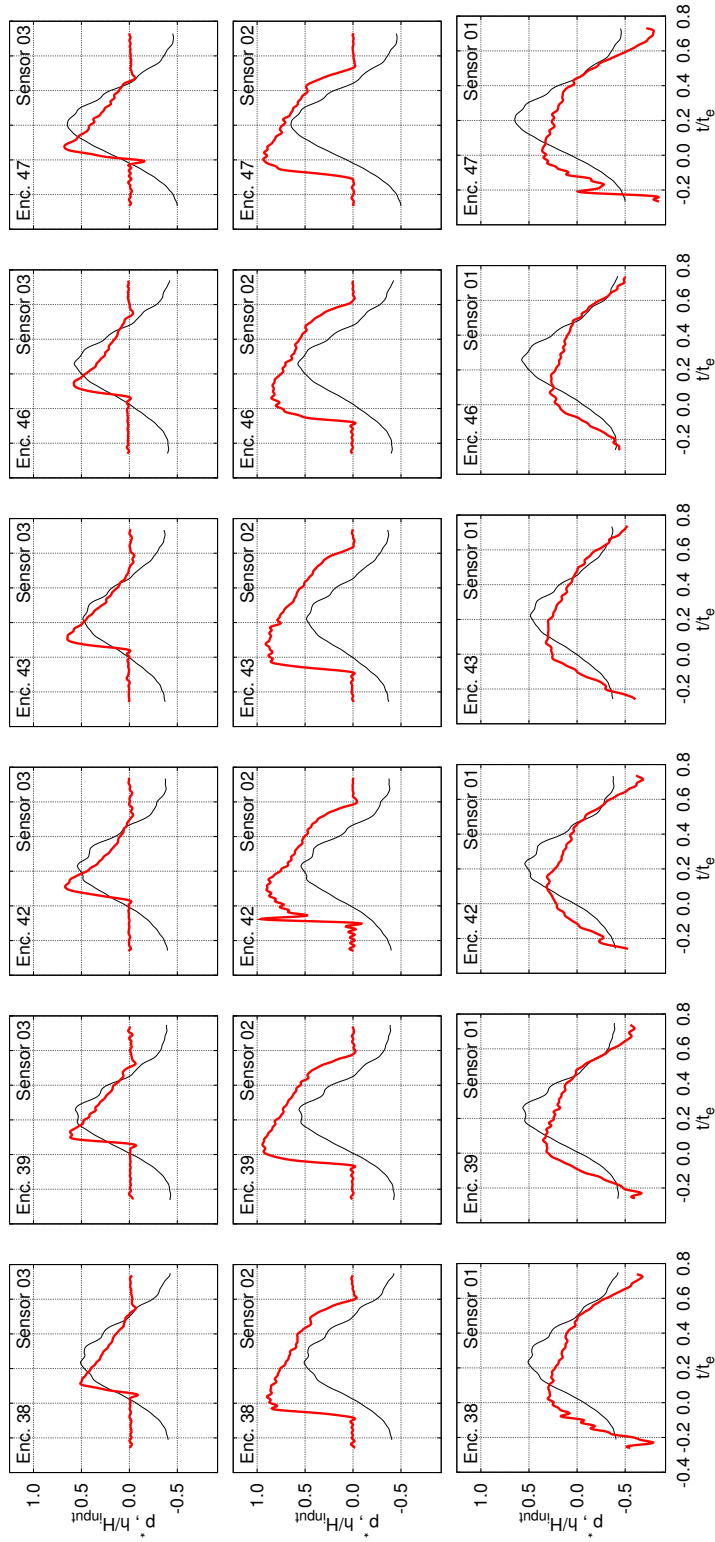


Figure F.6. Station $x/L_{ship} = 0.93$; fast rise time at Sensor 02. (6/9)

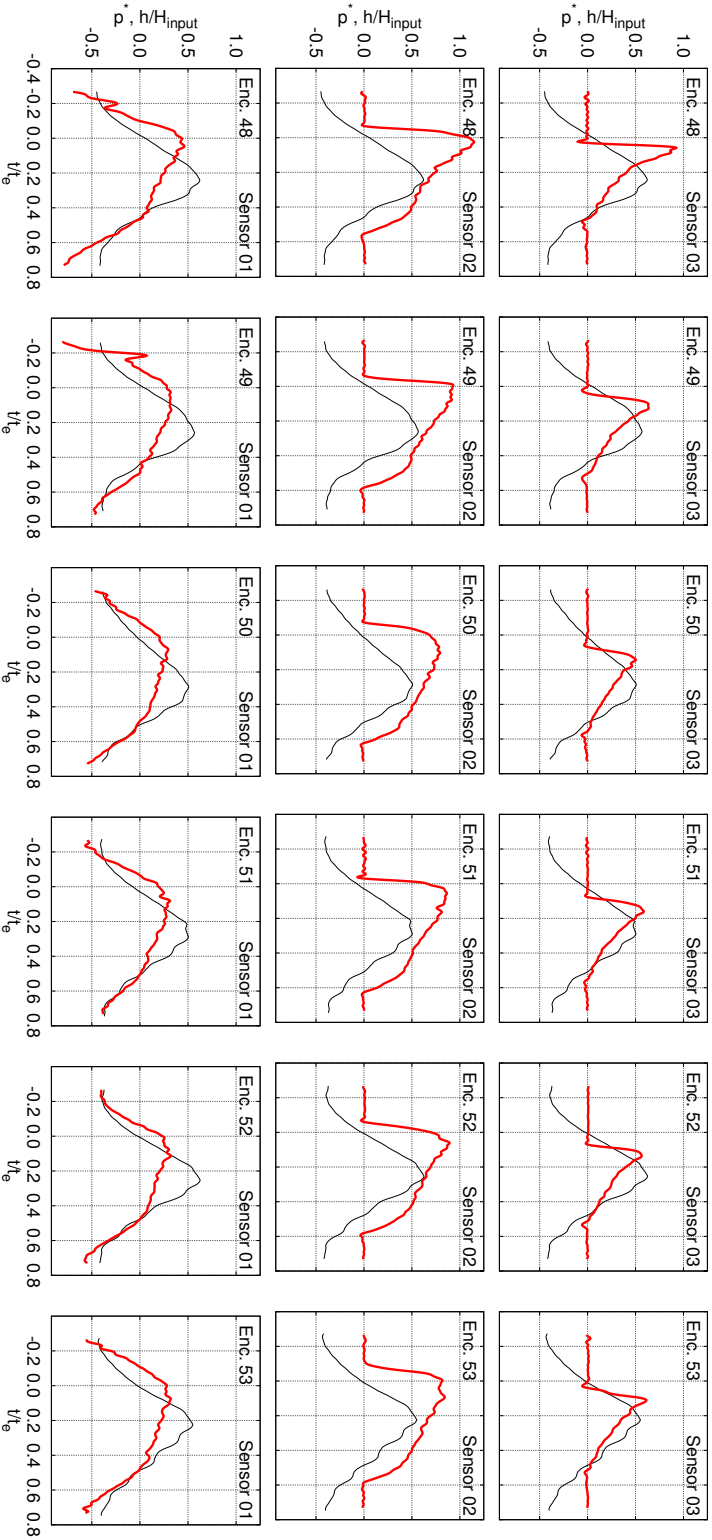


Figure F.7. Station $x/L_{ship} = 0.93$; fast rise time at Sensor 02. (7/9)

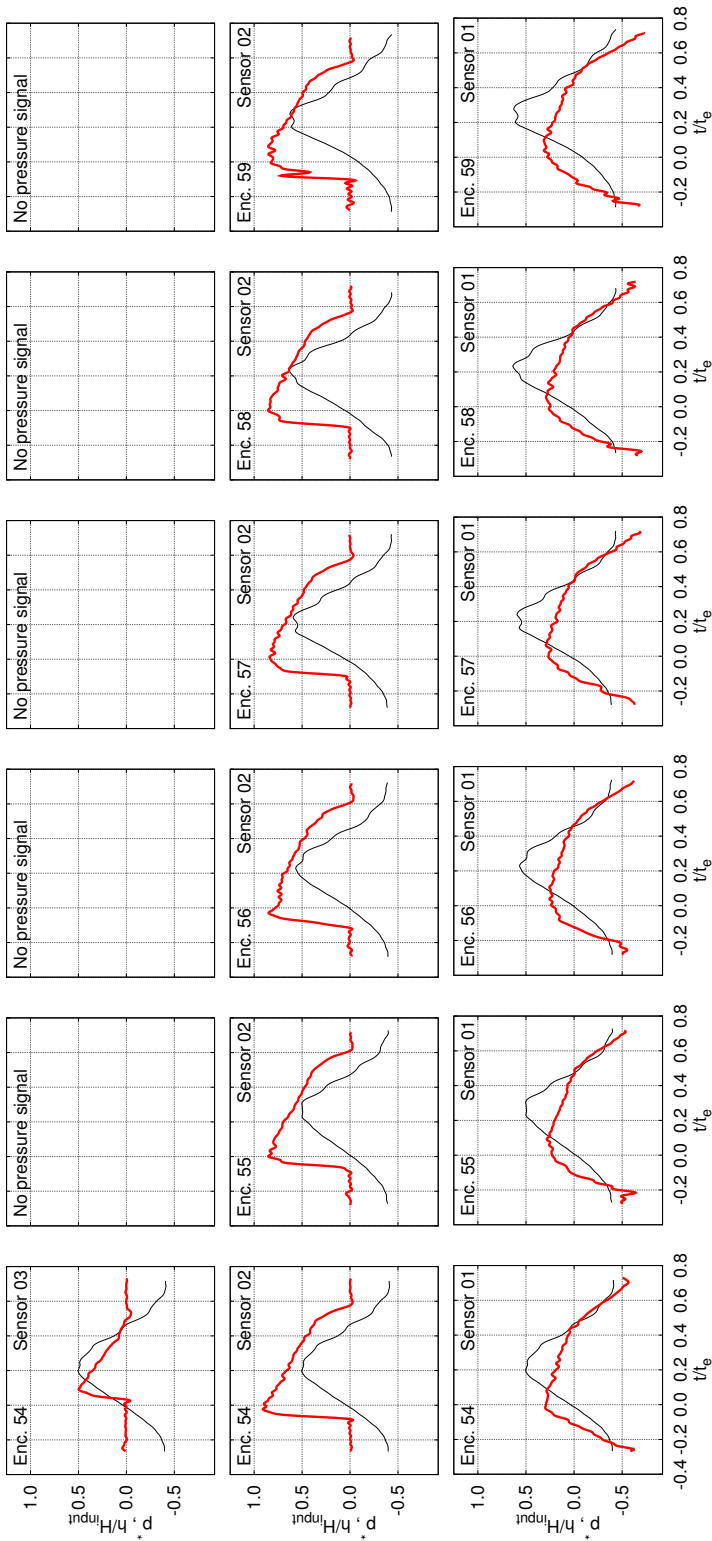


Figure F.8. Station $x/L_{ship} = 0.93$; fast rise time at Sensor 02. (8/9)

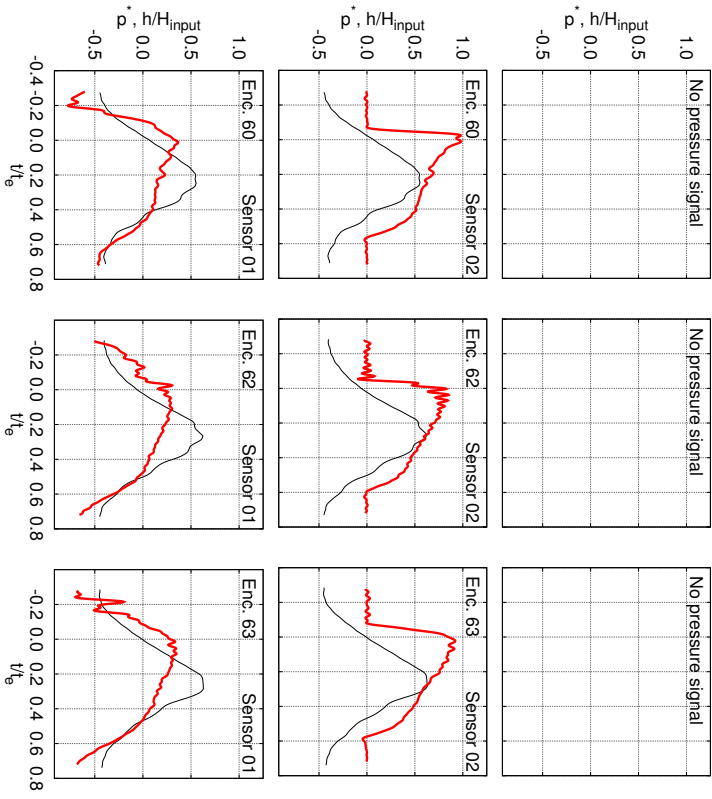


Figure F.9. Station $x/L_{ship} = 0.93$; fast rise time at Sensor 02. (9/9)

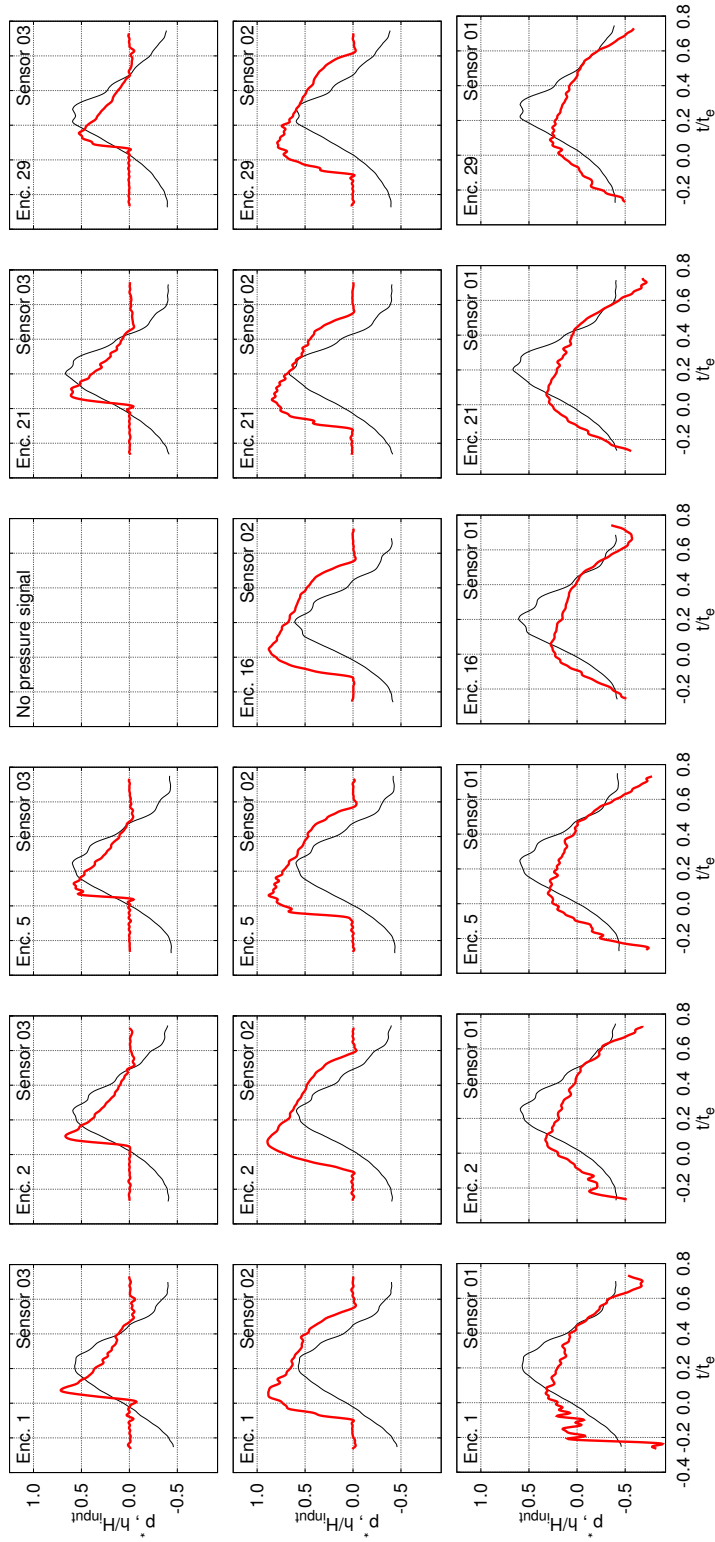


Figure F.10. Station $x/L_{ship} = 0.93$; medium rise time at Sensor 02. (1/2)

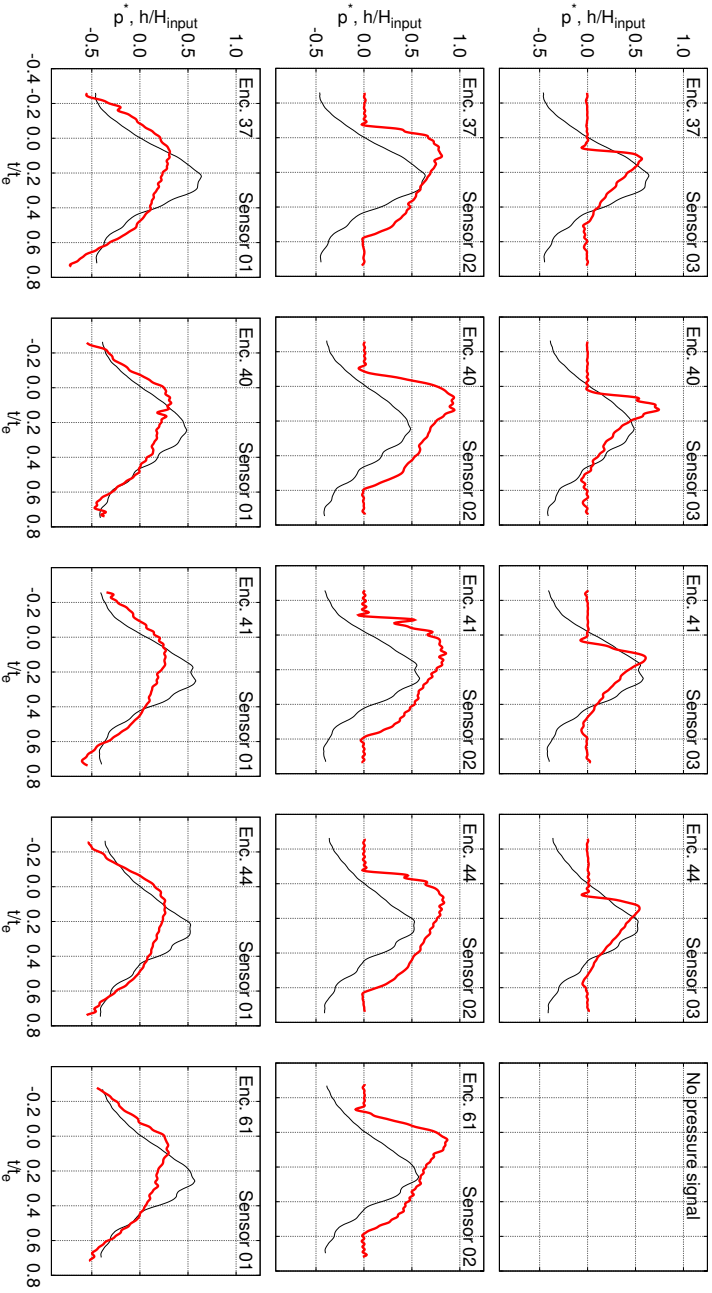


Figure F.1.1. Station $x/L_{stip} = 0.93$: medium rise time at Sensor 02. (2/2)

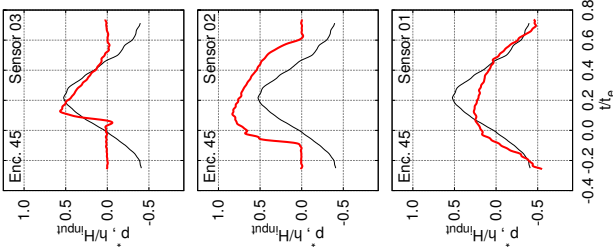


Figure F.12. Station $x/L_{ship} = 0.93$: slow rise time at Sensor 02. (1/1)

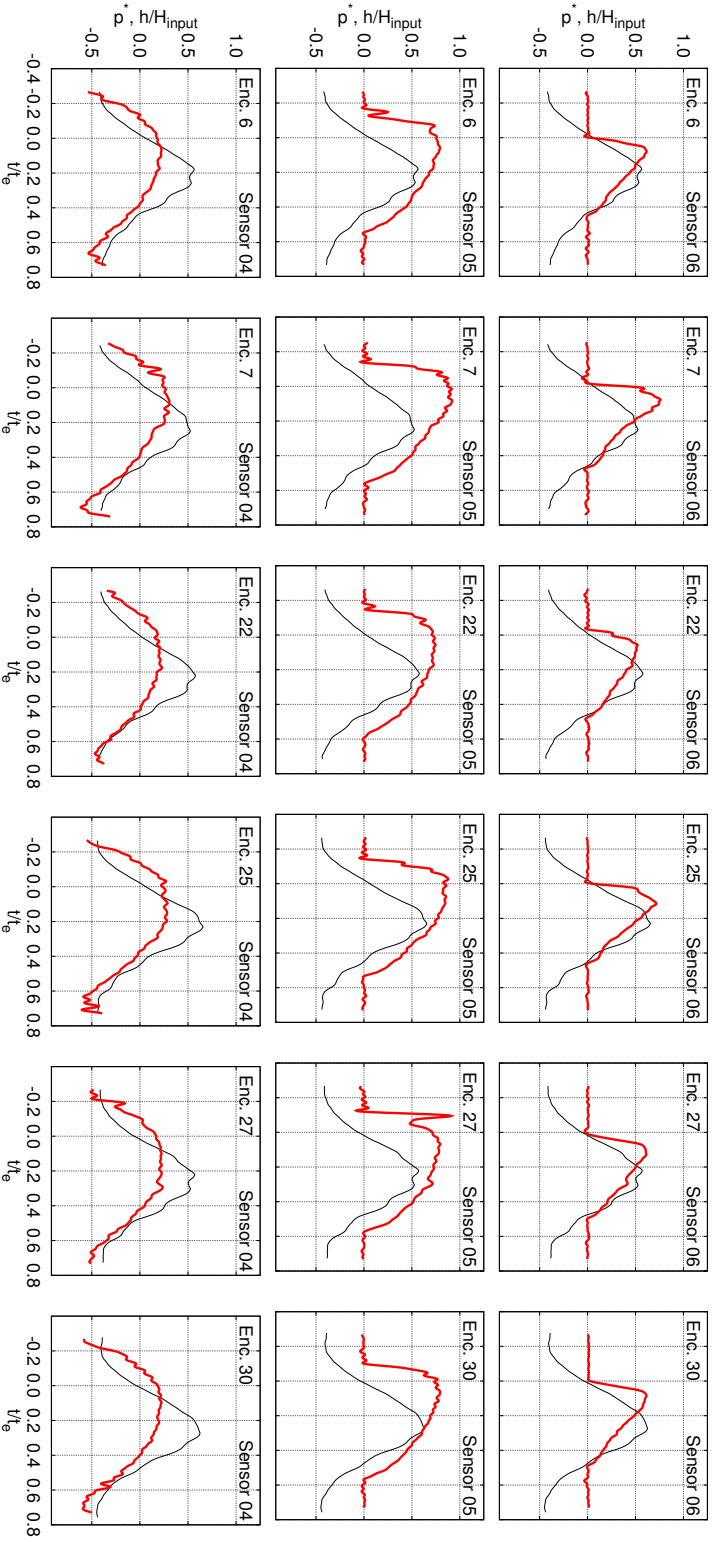


Figure F.13. Station $x/L_{stip} = 0.90$: fast rise time at Sensor 05. (1/4)

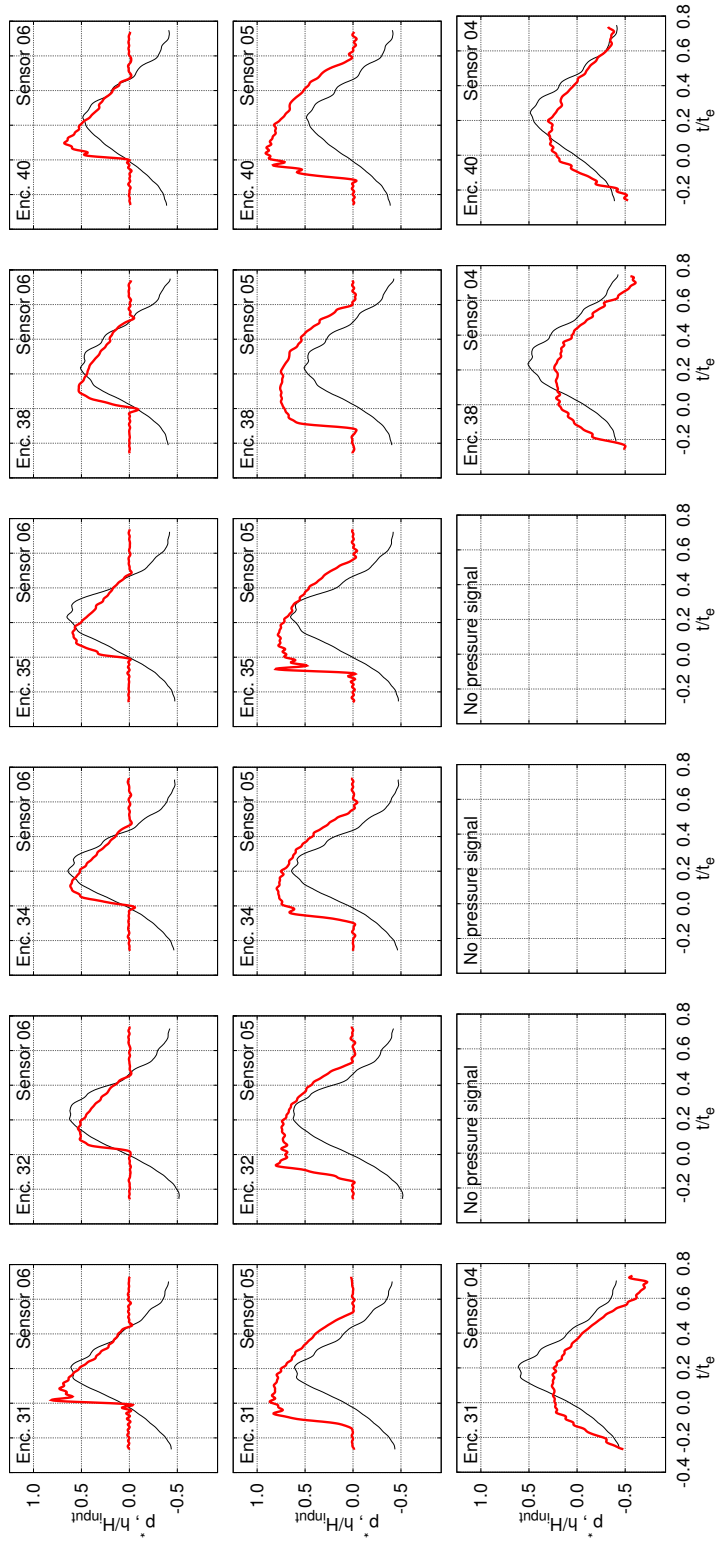


Figure F.14. Station $x/L_{ship} = 0.90$: fast rise time at Sensor 05. (2/4)

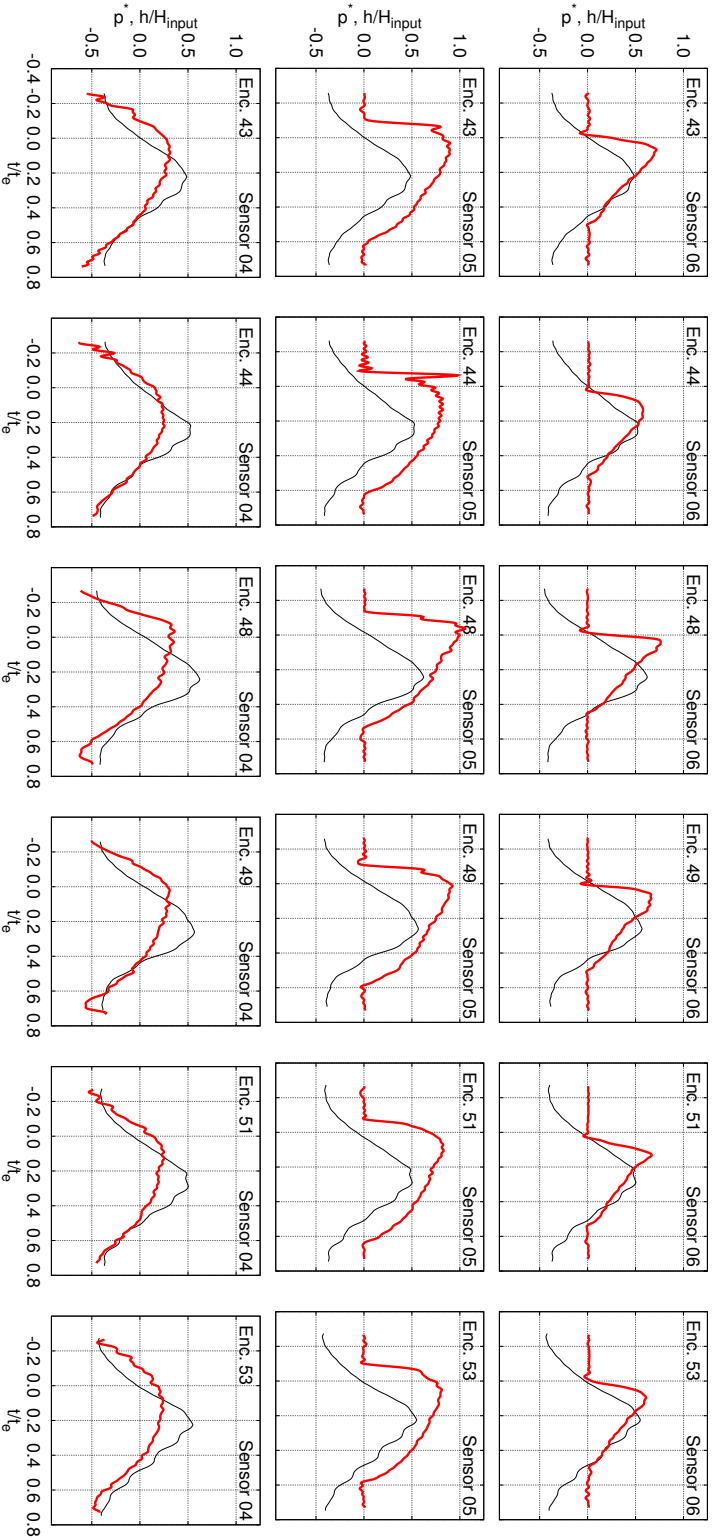


Figure F.15. Station $x/L_{stip} = 0.90$: fast rise time at Sensor 05. (3/4)

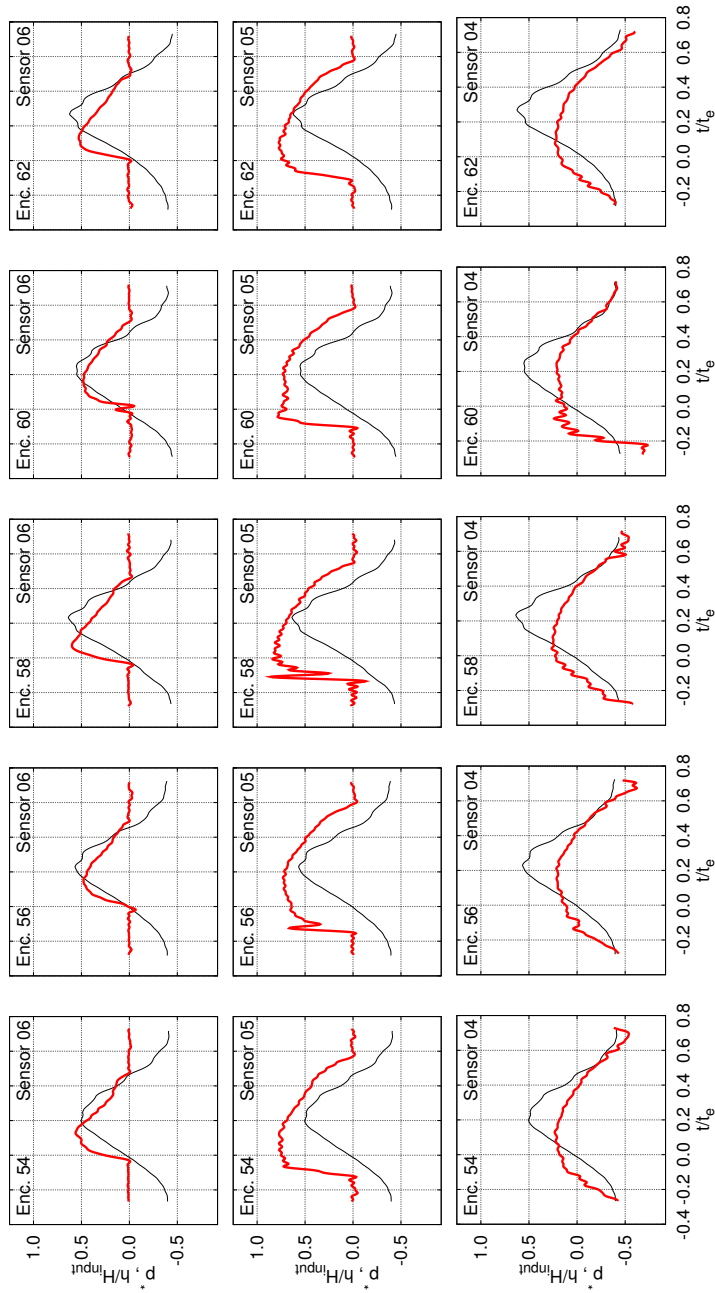


Figure F.16. Station $x/L_{ship} = 0.90$: fast rise time at Sensor 05. (4/4)

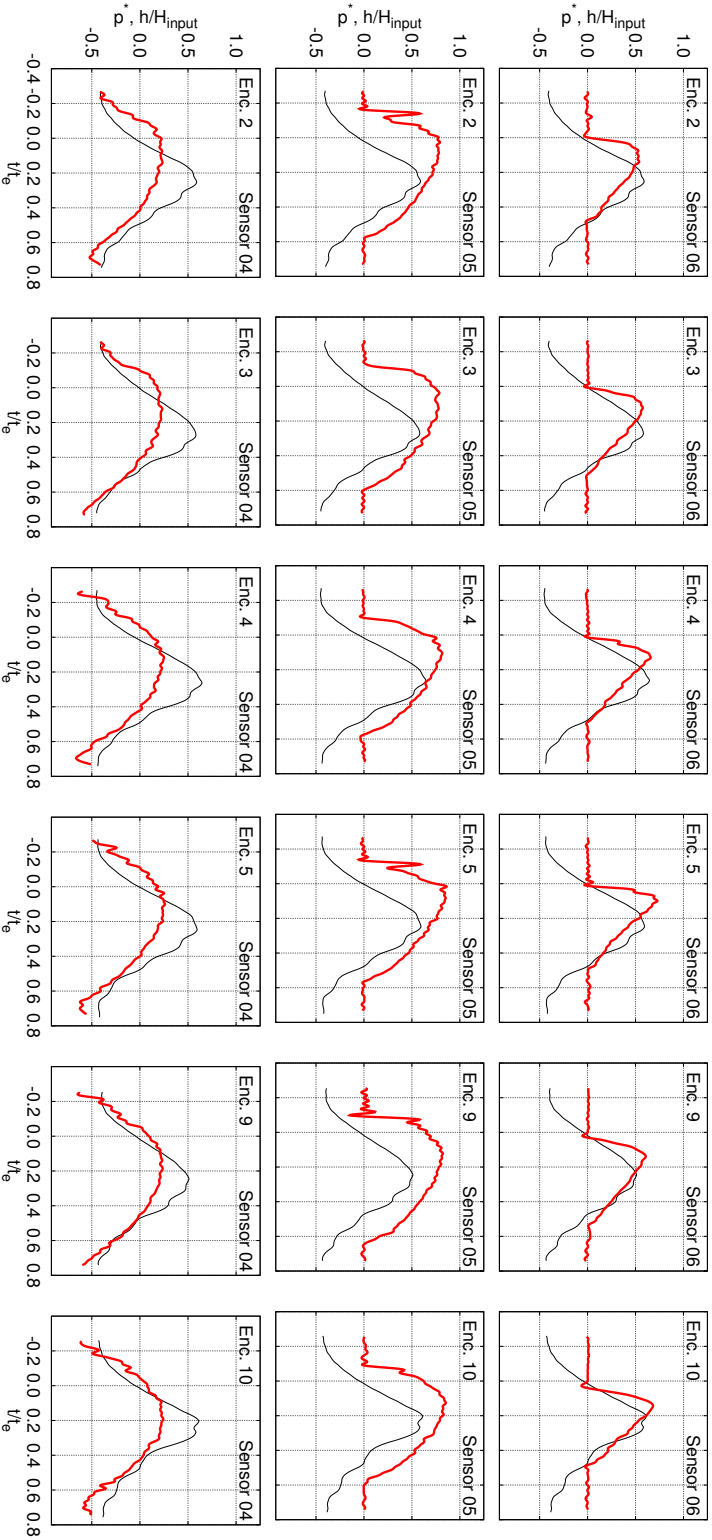


Figure F.17. Station $x/L_{stip} = 0.90$: medium rise time at Sensor 05. (1/6)

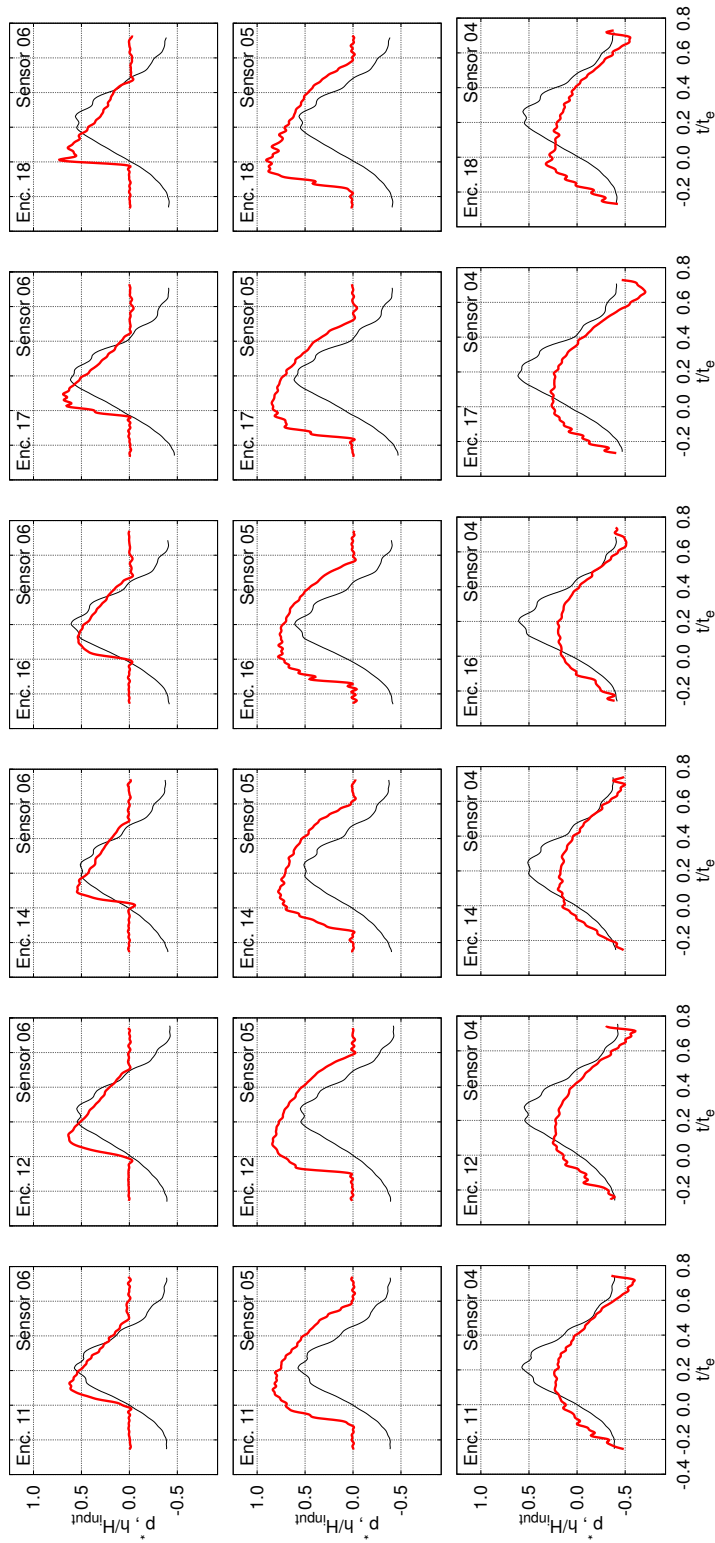


Figure F.18. Station $x/L_{ship} = 0.90$: medium rise time at Sensor 05. (2/6)

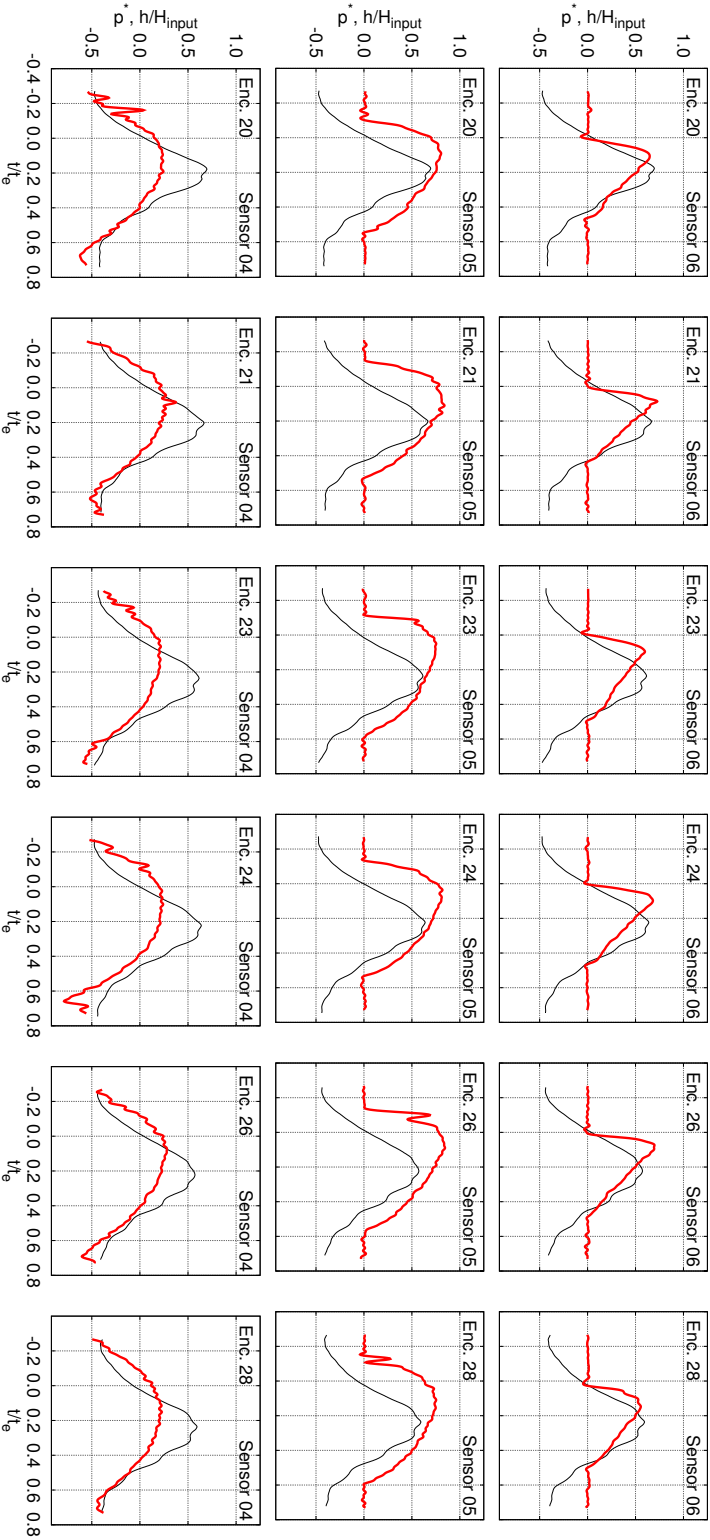


Figure F.19. Station $x/L_{stip} = 0.90$: medium rise time at Sensor 05. (3/6)

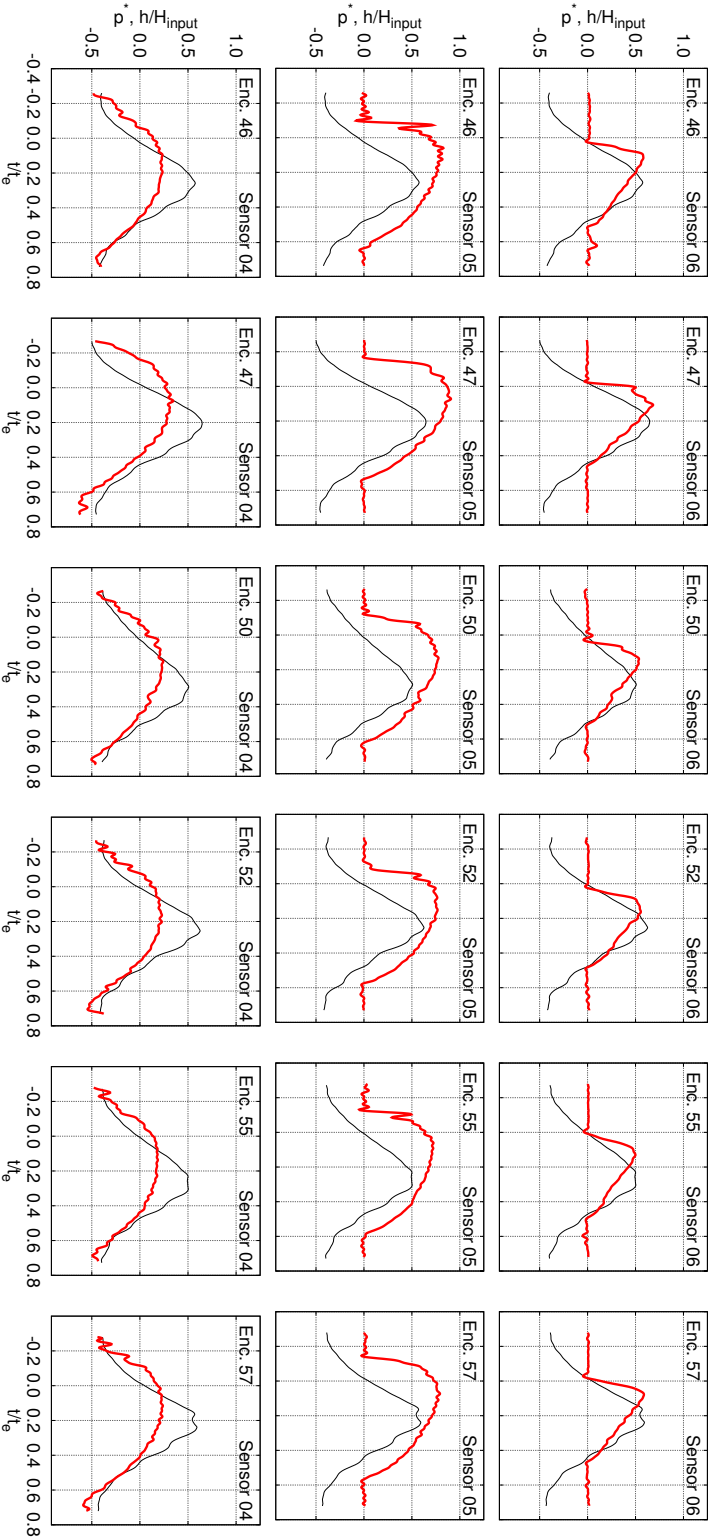


Figure F21. Station $x/L_{stip} = 0.90$: medium rise time at Sensor 05. (5/6)

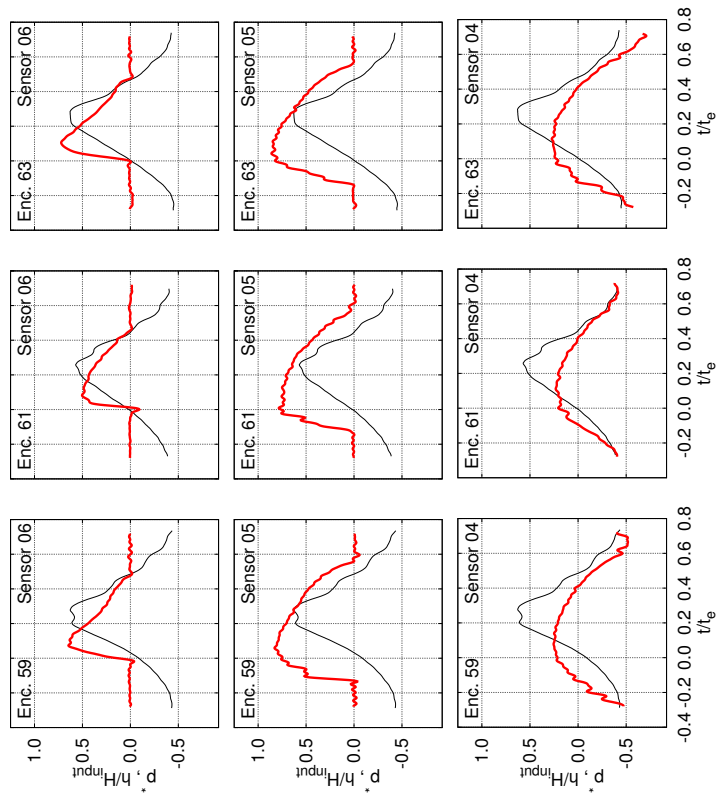


Figure F.22. Station $x/L_{ship} = 0.90$: medium rise time at Sensor 05. (6/6)

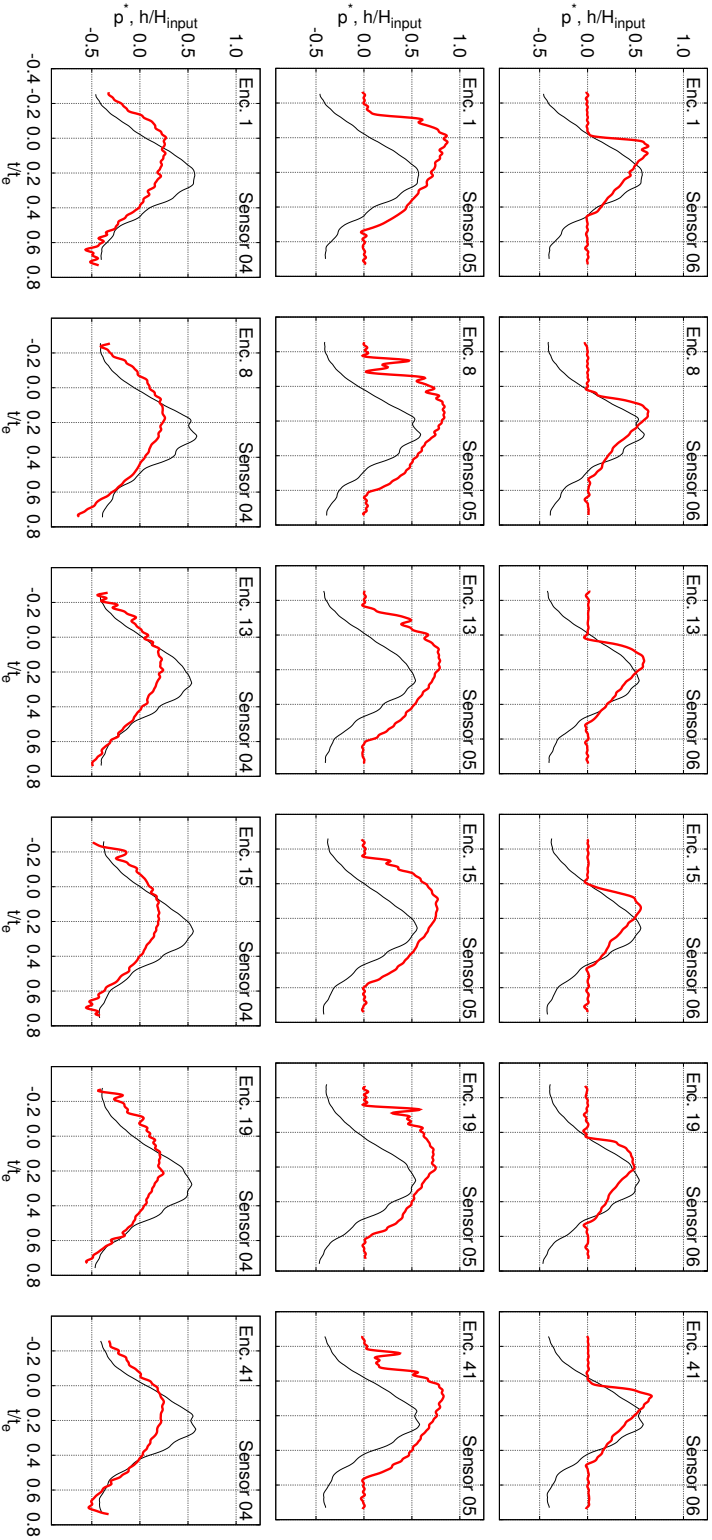


Figure F.23. Station $x/L_{stip} = 0.90$: slow rise time at Sensor 05. (1/2)

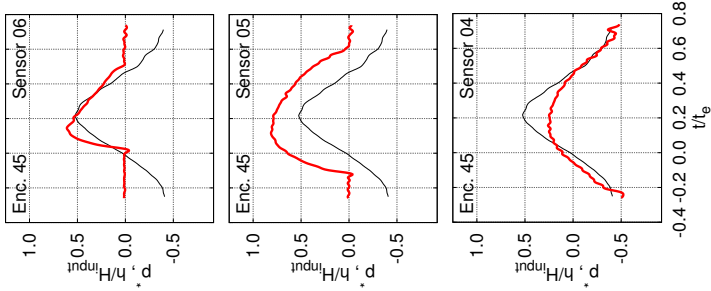


Figure F.24. Station $x/L_{ship} = 0.90$; slow rise time at Sensor 05. (2/2)

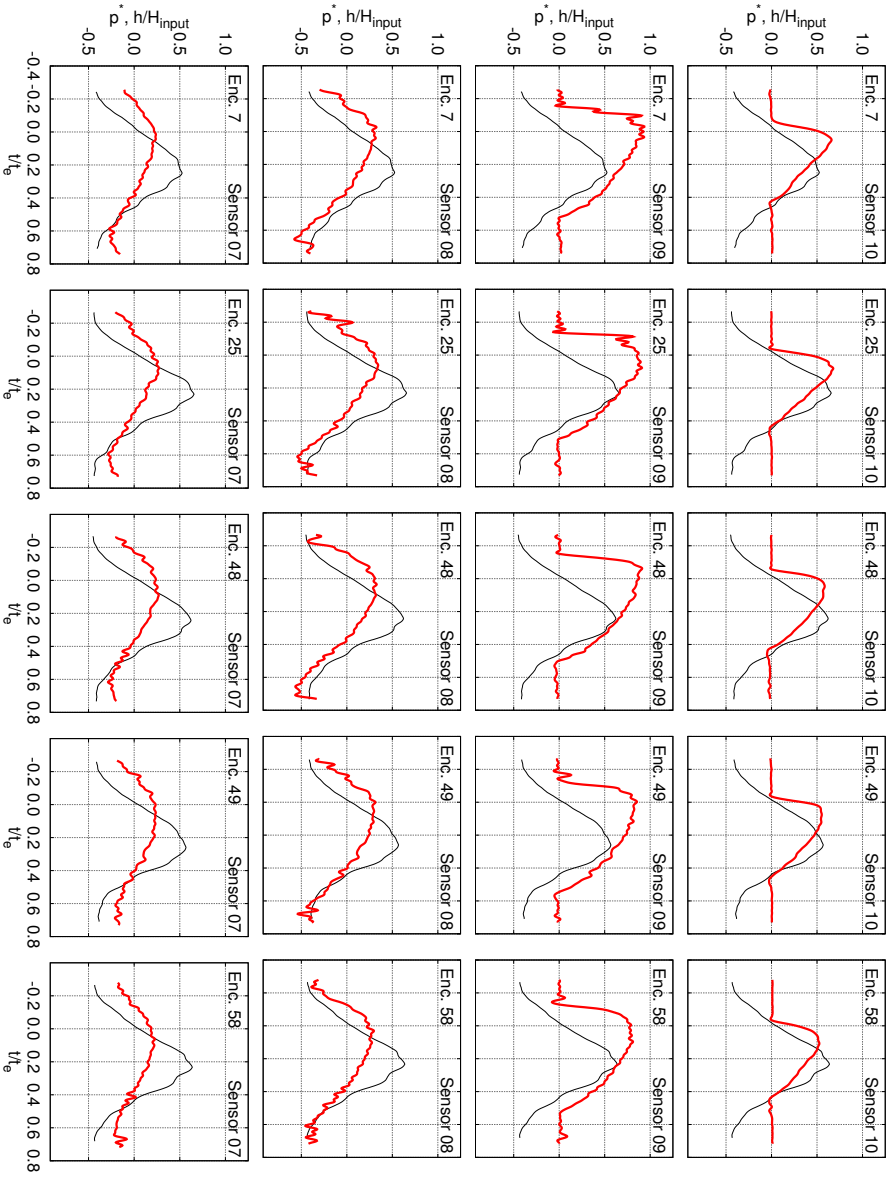


Figure F.25. Station $x/L_{shIP} = 0.88$; fast rise time at Sensor 09. (1/1)

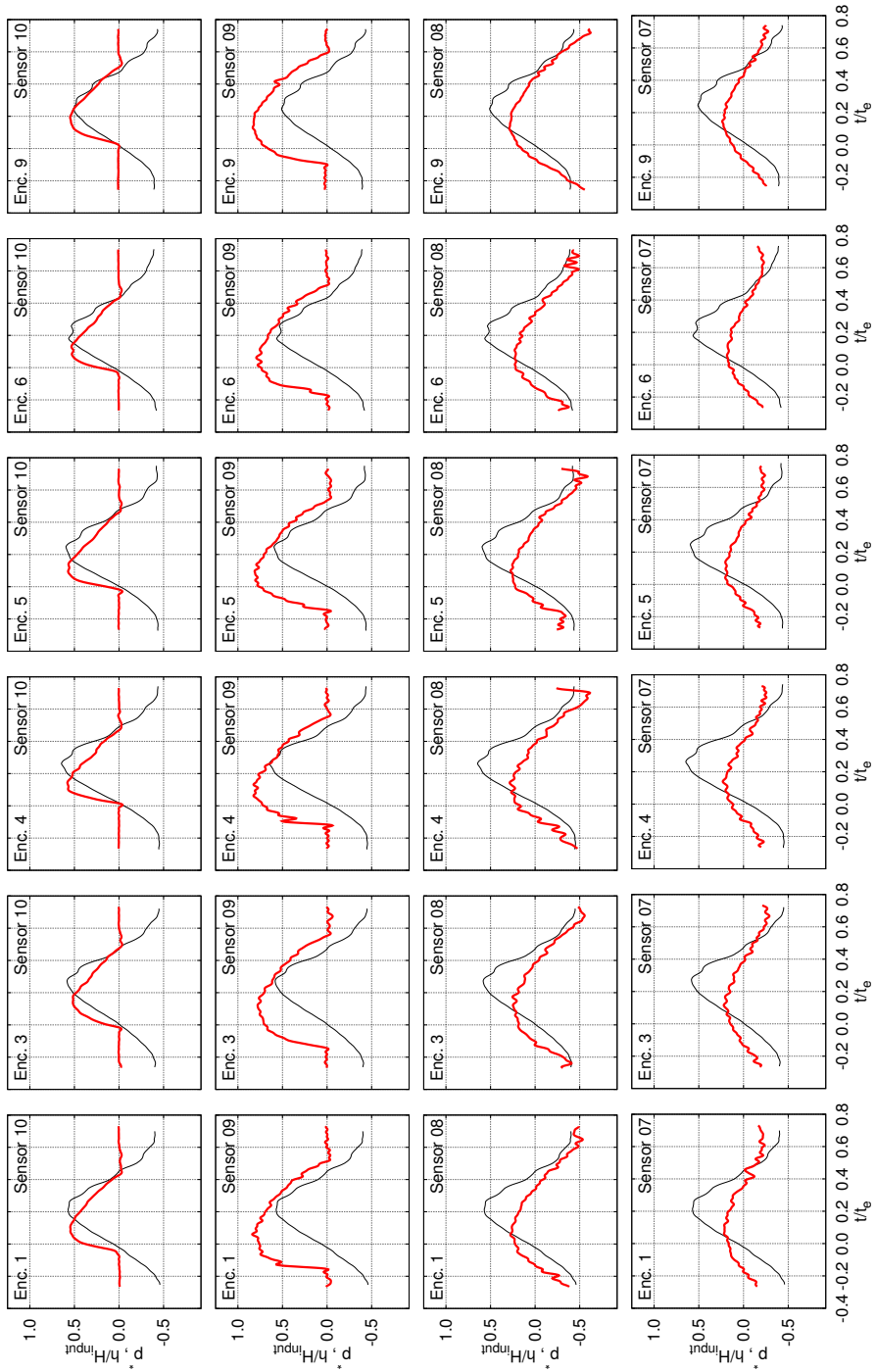


Figure F.26. Station $x/L_{ship} = 0.88$: medium rise time at Sensor 09. (1/5)

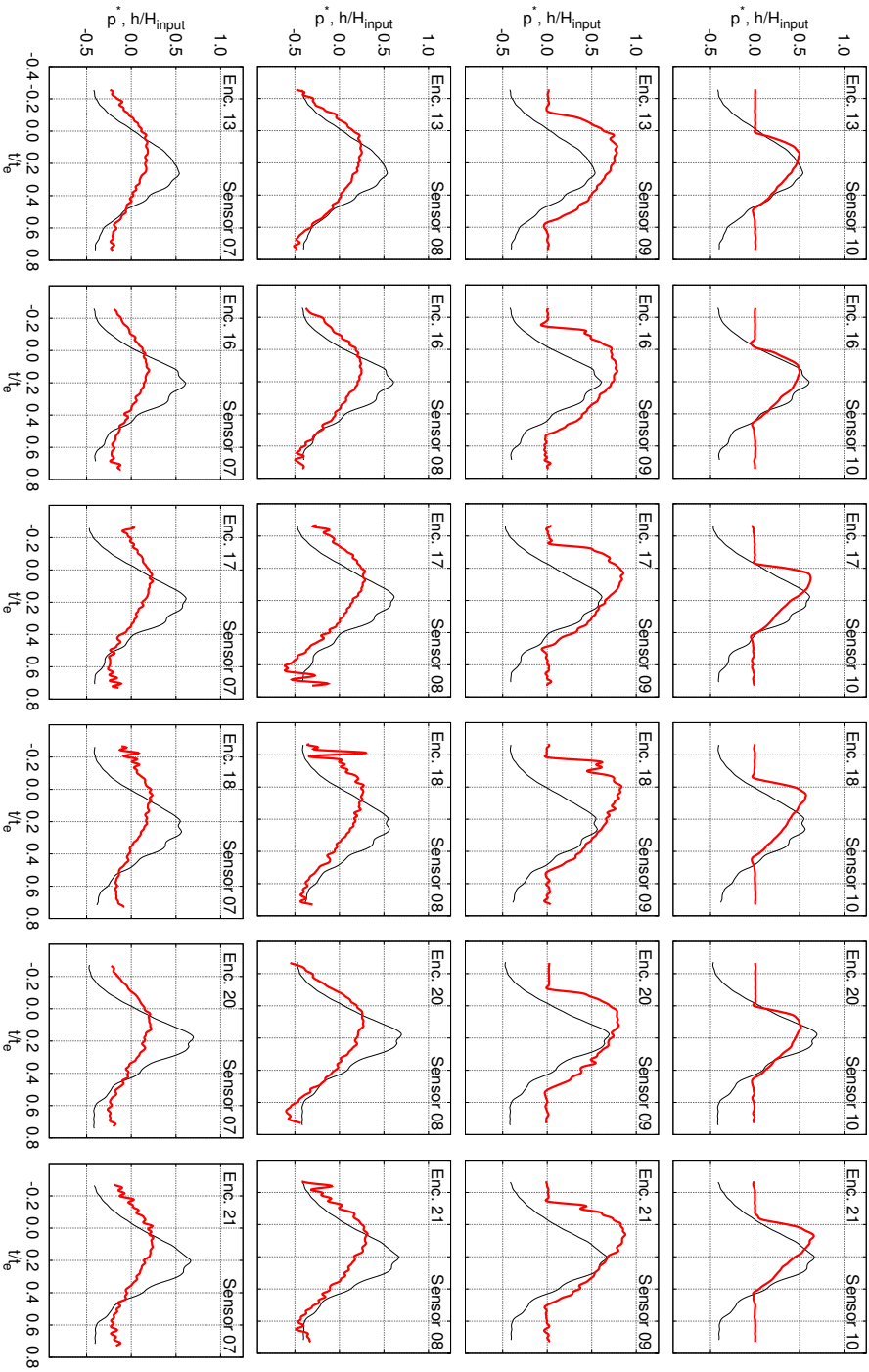


Figure F27. Station $x/L_{shIP} = 0.88$; medium rise time at Sensor 09. (2/5)

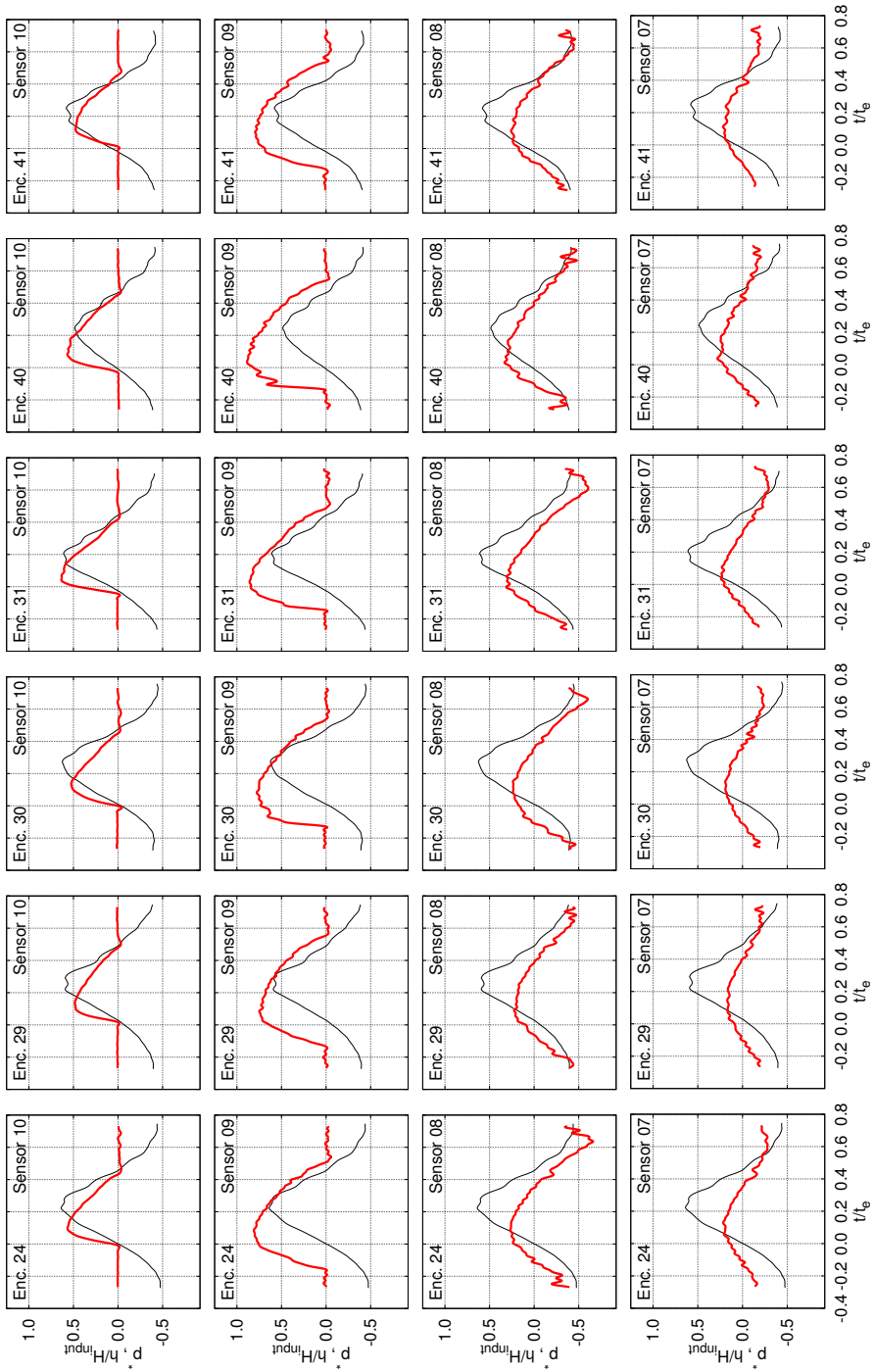


Figure F.28. Station $x/L_{ship} = 0.88$: medium rise time at Sensor 09. (3/5)

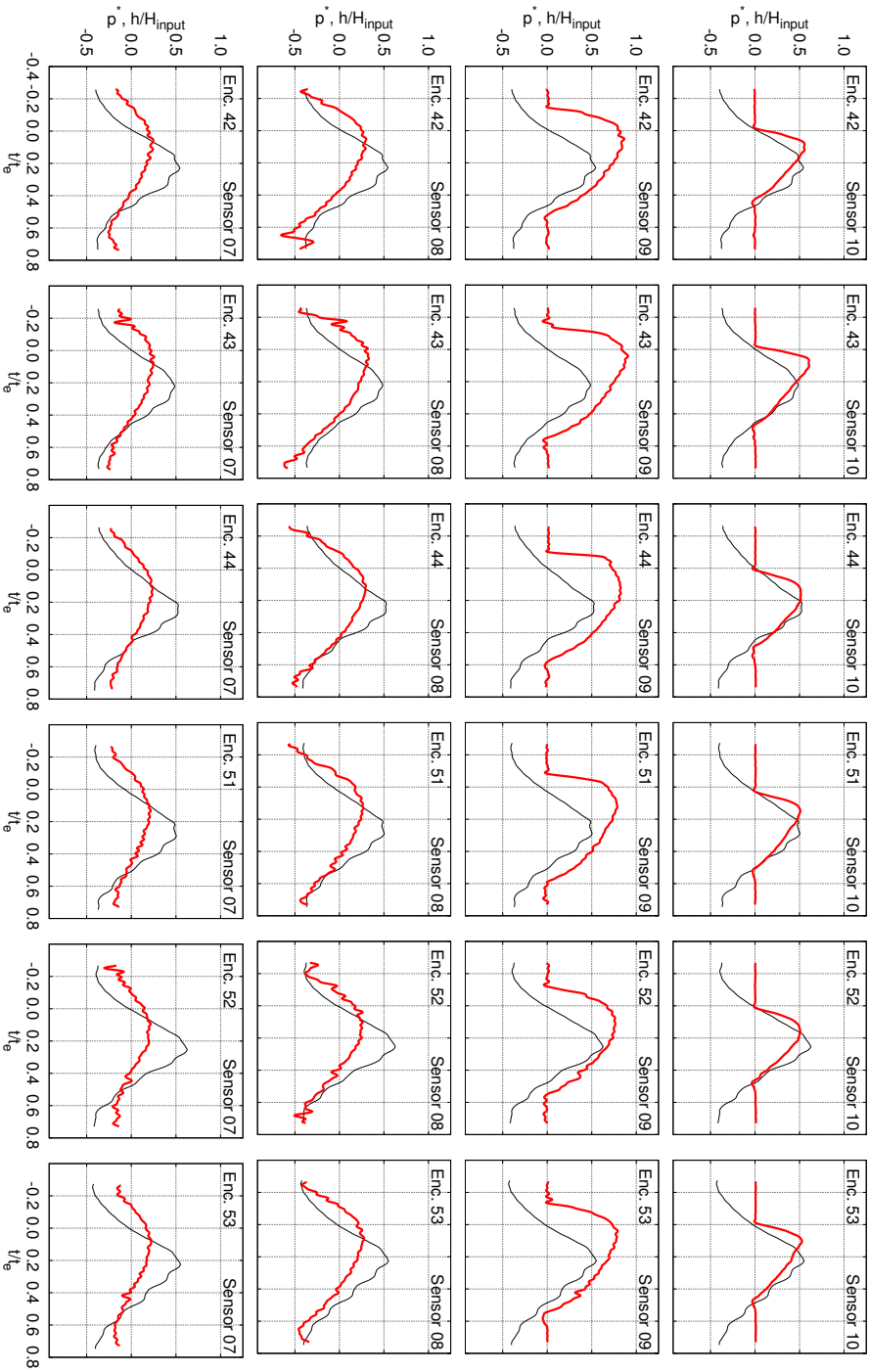


Figure F29. Station $x/L_{shIP} = 0.88$; medium rise time at Sensor 09. (4/5)

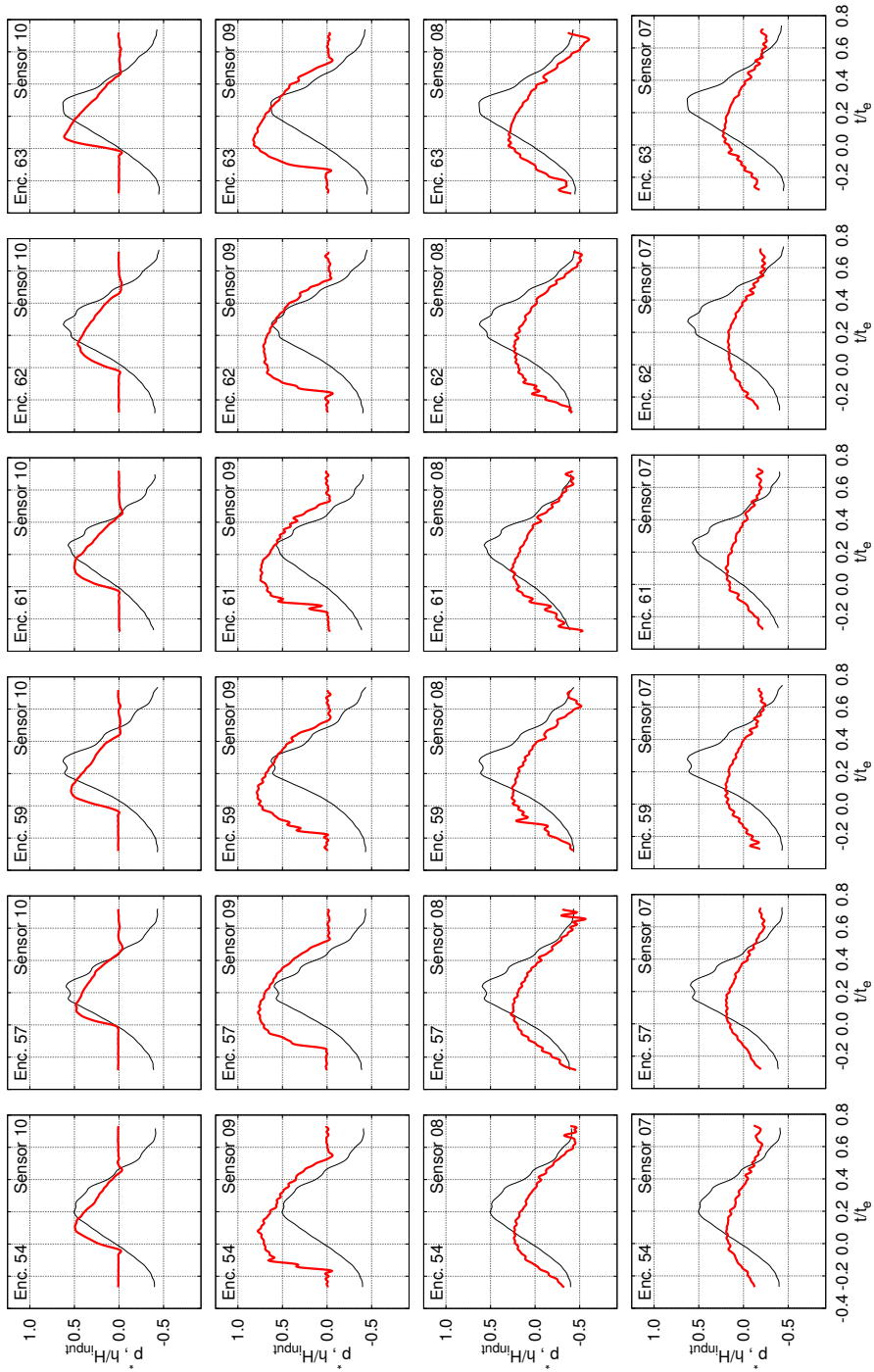


Figure F.30. Station $\alpha/L_{ship} = 0.88$: medium rise time at Sensor 09. (5/5)

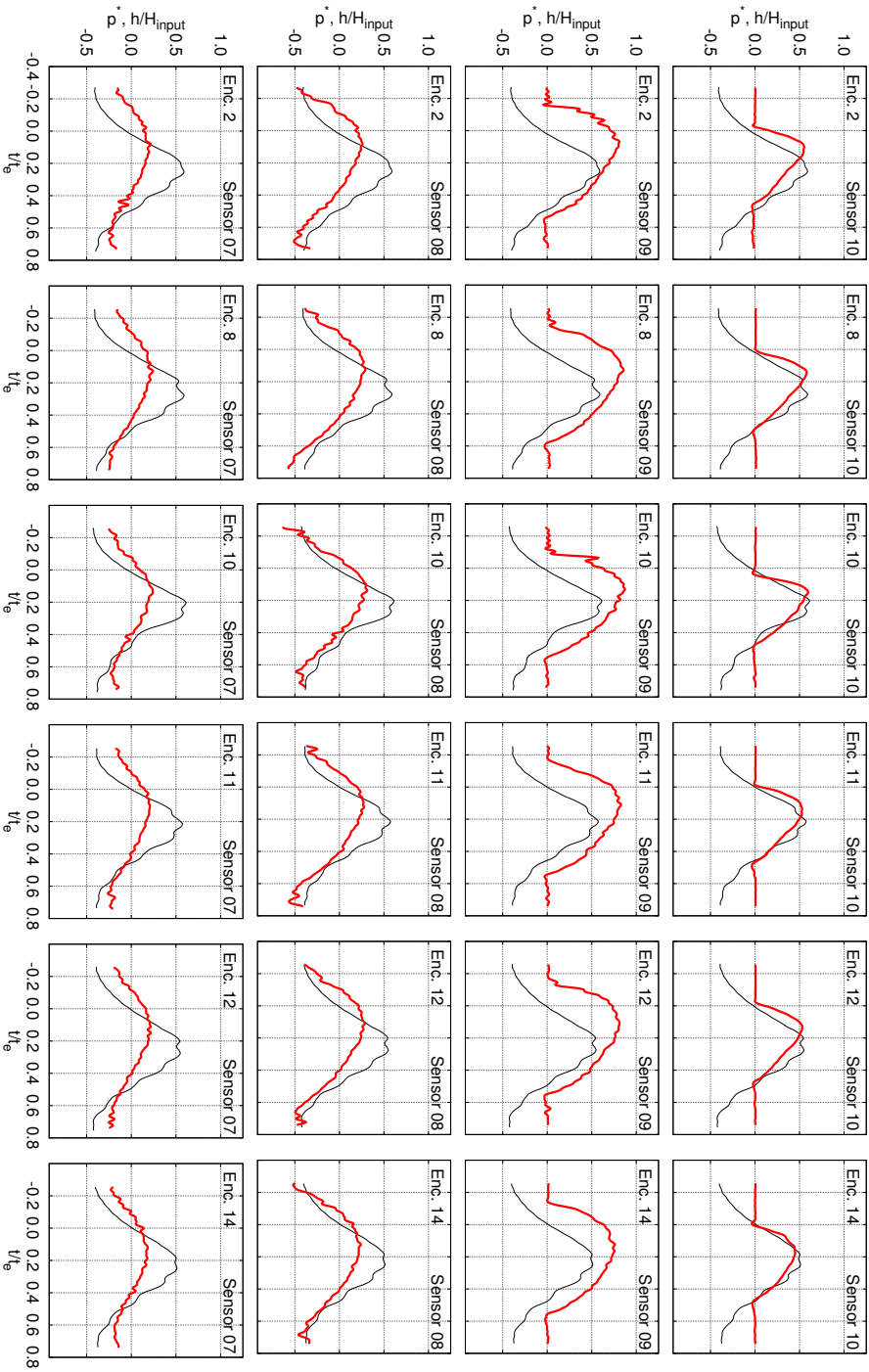


Figure F.31. Station $x/L_{shIP} = 0.88$; slow rise time at Sensor 09. (1/5)

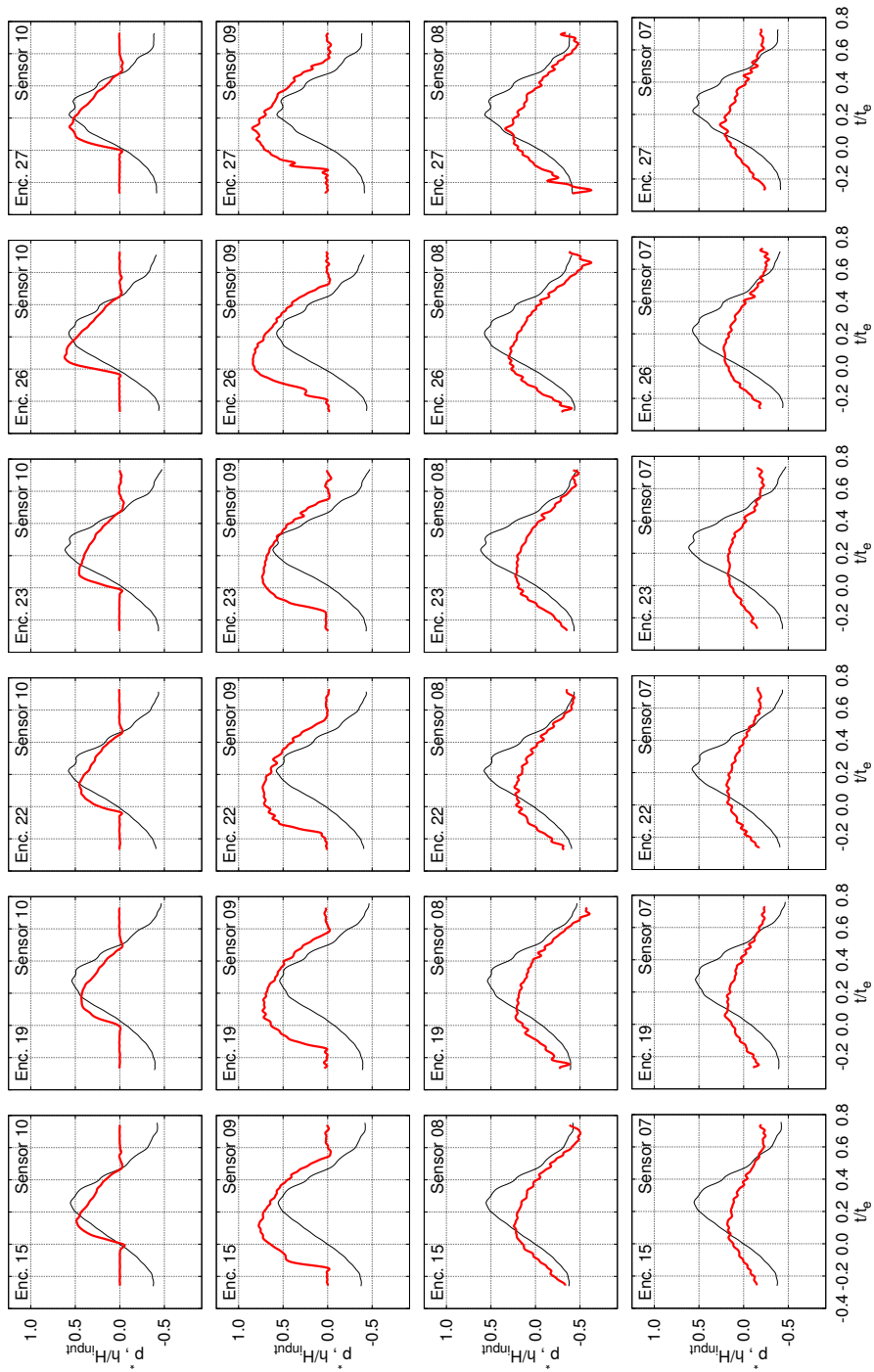


Figure F.32. Station $\alpha/L_{ship} = 0.88$: slow rise time at Sensor 09. (2/5)

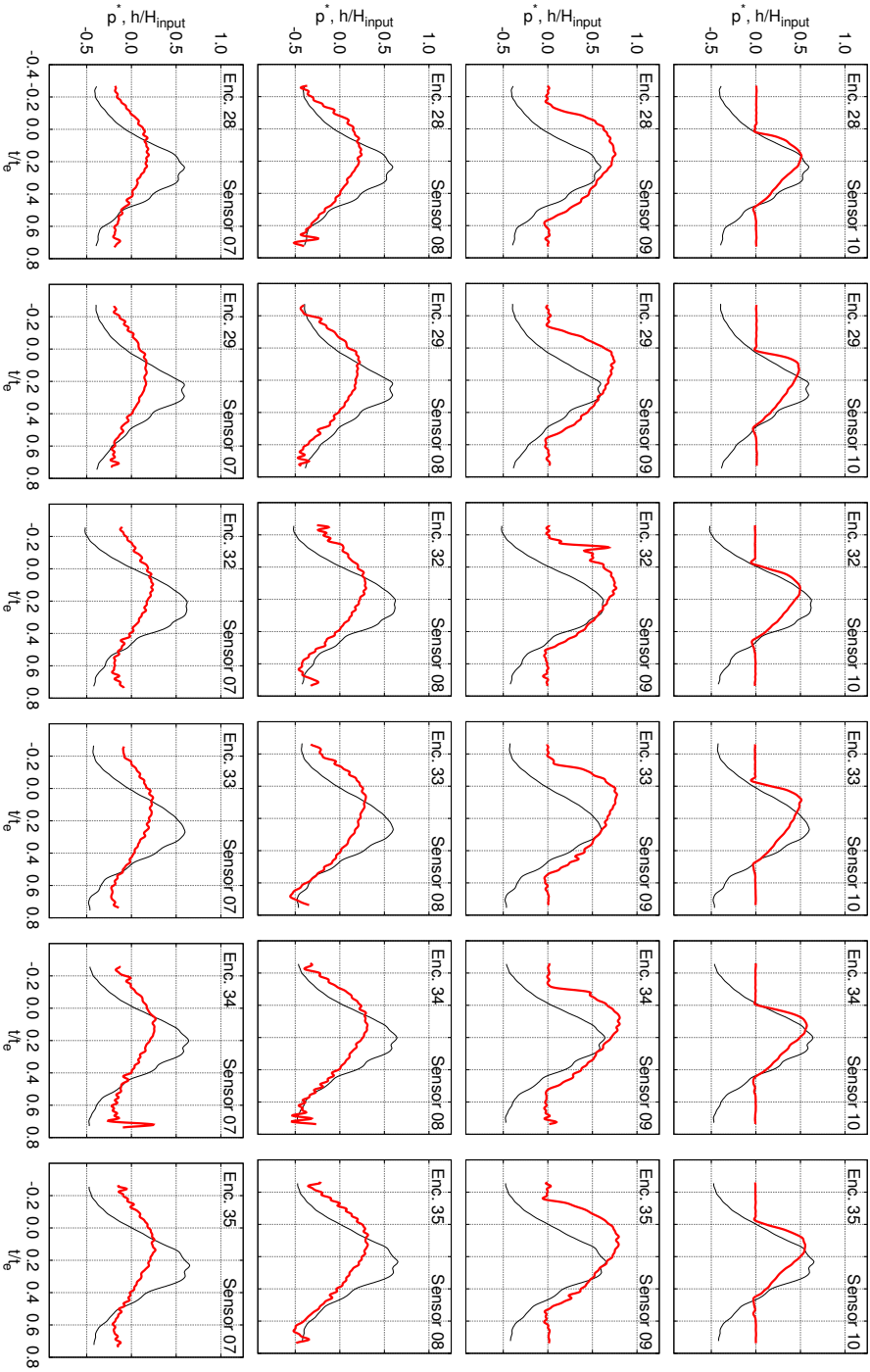


Figure F.33. Station $x/L_{shIP} = 0.88$; slow rise time at Sensor 09. (3/5)

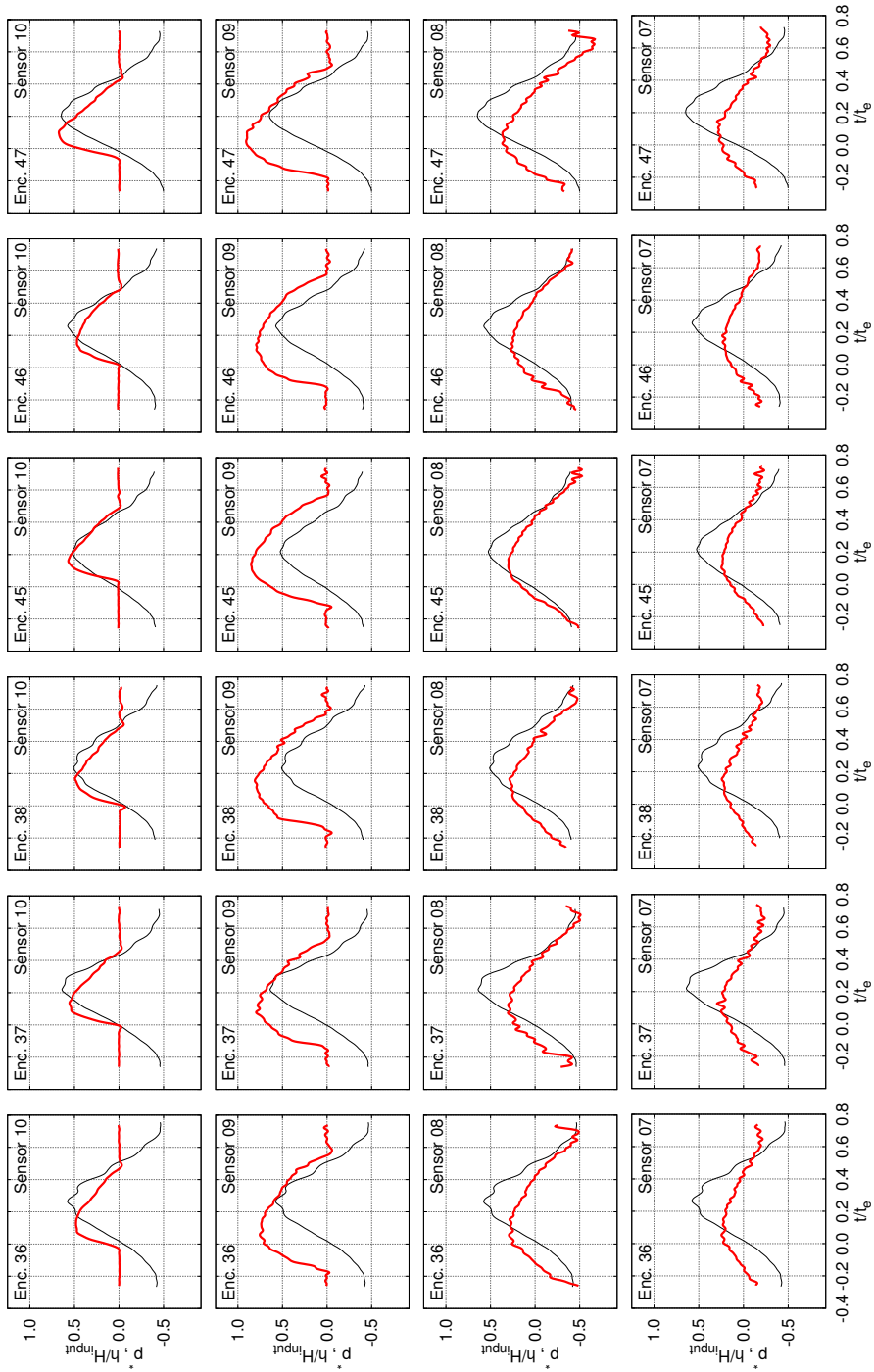


Figure F.34. Station $\alpha/L_{ship} = 0.88$: slow rise time at Sensor 09. (4/5)

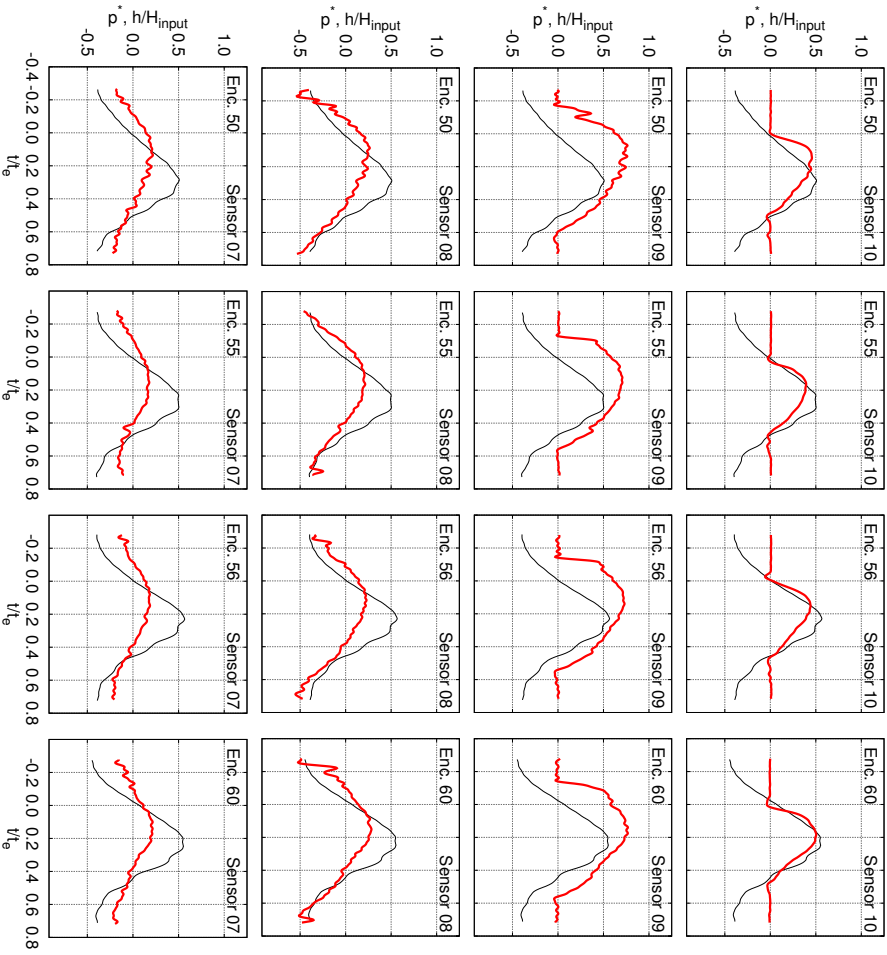


Figure F.35. Station $x/L_{stip} = 0.88$; slow rise time at Sensor 09. (5/5)

Ship springing means the resonant wave-induced vibration of a ship hull. Springing can endanger the comfort of the passengers in cruise ships and cause the fatigue damage of ships in general. In the case of large ships, the complete avoidance of springing is not possible, because the lowest eigenmodes of their hull resonate with the waves in any case. One way to reduce the level of springing vibration is to design a hull form, which minimises the wave loads that can excite springing. However, the existing knowledge that enables such a hull design is very limited.

In this study, the correlation between local hull form and springing excitation is explained for one study case. Both computations and dedicated model tests were conducted and utilised.



ISBN 978-952-60-5668-5
ISBN 978-952-60-5671-5 (pdf)
ISSN-L 1799-4934
ISSN 1799-4934
ISSN 1799-4942 (pdf)

Aalto University
School of Engineering
Department of Applied Mechanics
www.aalto.fi

**BUSINESS +
ECONOMY**

**ART +
DESIGN +
ARCHITECTURE**

**SCIENCE +
TECHNOLOGY**

CROSSOVER

**DOCTORAL
DISSERTATIONS**